

**APPLICATIONS OF *IN SITU* ¹⁴C TO GLACIAL LANDSCAPES IN
SWEDEN AND ANTARCTICA**

by

Alexandria Jo Koester

A Dissertation

Submitted to the Faculty of Purdue University

In Partial Fulfillment of the Requirements for the degree of

Doctor of Philosophy



Department of Earth, Atmospheric, and Planetary Sciences

West Lafayette, Indiana

May 2023

THE PURDUE UNIVERSITY GRADUATE SCHOOL
STATEMENT OF COMMITTEE APPROVAL

Dr. Darryl E. Granger, Chair

Department of Earth, Atmospheric, and Planetary Sciences

Dr. Nathaniel A. Lifton

Department of Earth, Atmospheric, and Planetary Sciences

Dr. Marc W. Caffee

Department of Physics and Astronomy

Dr. Marissa M. Tremblay

Department of Earth, Atmospheric and Planetary Sciences

Dr. Arjen Stroeven

Department of Physical Geography, Stockholm University

Approved by:

Dr. Daniel Cziczo

“Have no fear of perfection; you'll never reach it.”

– Marie Curie

ACKNOWLEDGMENTS

I would like to thank my advisor, Nat Lifton, for his inspiring unrelenting perseverance, numerous scientific discussions, and light-hearted sarcasm over the last five years. Nat's commitment to track down and understand every nuance of the carbon system, his seemingly endless scientific knowledge, and thought-provoking questions have continually motivated me to be a better scientist and understand "the systematics of the system". My committee members, who have been influential in my graduate career, Darryl Granger, Marc Caffee, Marissa Tremblay, and Arjen Stroeven, helped keep me on track during the global pandemic. I want to thank Darryl for his calm demeanor and laboratory knowledge, Marc for his expertise about reaction cross-sections, and Marissa for welcoming me into her lab group meetings. I especially want to thank Arjen Stroeven, whose direct hard-hitting questions and friendly advice have been beneficial.

I want to thank the members of the MAGIC-DML team for their kindness in welcoming me to the team. I want to particularly thank Dr. Jane Andersen for her mentorship and friendship. Thank you for teaching me laboratory procedures in PRIME lab, countless data discussions, reading early manuscript drafts, and helping me improve my coding. I also want to thank Dr. Martim Mas e Braga for running Antarctic model simulations, data-model comparison discussions, and for his inspiring, hardworking, and positive attitude.

My fellow graduate students have brought me joy and friendship throughout my PhD journey. My officemates over the years, Sarah Sams, Adrian Singleton, Angus Moore, Will Odom, Lan Luo, and Xianmei Huang, have all brightened my graduate experience. I want to thank Sarah for sharing her Antarctic knowledge and infectious laugh. Adrian, for his thoughtful and calm presence and for reminding me not to take life too seriously. I want to thank Angus for his cosmogenic nuclide wisdom and unmeasurable valuable advice. Thank you to Will and Lan for teaching me how to extract ^{10}Be and ^{26}Al . Finally, thank you to Xianmei whose bright optimism and upbeat attitude was a shining light during my final year. I am especially grateful for the supportive friendships of Carlisle Wishard and Allison LaFleur.

I want to acknowledge my family, especially my parents Rita and Tim, who have always encouraged me to try harder and do my best. I wouldn't be where I am today without the love, patience, and support of my husband, Brian Higginbotham, who constantly believed in me even when I didn't believe in myself. You are my soup snake; I mean soul mate.

TABLE OF CONTENTS

LIST OF TABLES	8
LIST OF FIGURES	10
ABSTRACT	14
CHAPTER 1. INTRODUCTION	15
1.1 Significance of <i>in situ</i> cosmogenic ¹⁴ C	15
1.2 Applications of <i>in situ</i> ¹⁴ C in polar regions	16
1.3 Research plan	18
1.3.1 Chapter 2: The Riukojietna ice cap, Sweden	18
1.3.2 Chapter 3: Holocene thinning of the East Antarctic Ice Sheet	19
1.3.3 Chapter 4: Calculating compositionally dependent <i>in situ</i> ¹⁴ C production rates	19
CHAPTER 2. THE RIUKOJIETNA ICE CAP LIKELY SURVIVED THE HOLOCENE THERMAL MAXIMUM BUT WAS LESS EXTENSIVE THAN TODAY	24
2.1 Introduction and Background	24
2.2 Study Site	26
2.3 Methods	27
2.3.1 Collection and extraction of cosmogenic nuclides from bedrock	28
2.3.2 Lacustrine sediment cores	28
2.3.3 Ice thickness reconstructions, bed topography, and volume calculations	29
2.4 Results	30
2.4.1 Cosmogenic nuclide concentrations and apparent exposure ages	30
2.4.2 Lacustrine records	31
2.4.3 Ice thickness reconstructions and volume	32
2.5 Discussion	32
2.5.1 Constraints on Holocene history of Riukojietna from cosmogenic nuclides	32
2.5.2 Constraints on Holocene history of Riukojietna from lacustrine sediments	33
2.5.3 Reconciling the measured cosmogenic nuclide data with the lake core record	35
Forward modeling of allowable Holocene ice cap histories at Riukojietna	38
2.5.4 Paleoclimate constraints	41
2.6 Conclusion	41

CHAPTER 3. HOLOCENE ICE SURFACE LOWERING IN WESTERN DRONNING MAUD LAND, EAST ANTARCTICA.....	62
3.1 Introduction and Background	62
3.1.1 Deglacial constraints on the East Antarctic Ice Sheet	63
3.1.2 Western Dronning Maud Land	65
3.2 Methods.....	65
3.2.1 Field strategies and sample collection	65
3.2.2 Carbon extraction and exposure age calculations.....	67
3.2.3 Ice surface elevation	67
3.2.4 Adaptive-resolution ice sheet model	68
3.3 Results.....	69
3.3.1 Jutulstraumen Drainage Basin	69
3.3.2 Veststraumen Drainage Basin.....	70
3.3.3 Holocene thinning rates from the coast to inland	72
3.3.4 Numerical model results	72
3.4 Discussion.....	73
3.4.1 Coast-to-inland LGM ice thickness trends at Jutulstraumen and Veststraumen	73
3.4.2 Deglacial thinning rates in DML	74
3.4.3 Data-model comparisons	76
3.4.4 Model limitations.....	78
3.5 Conclusions.....	79
CHAPTER 4. A SOFTWARE FRAMEWORK FOR CALCULATING COMPOSITIONALLY DEPENDENT <i>IN SITU</i> ¹⁴ C PRODUCTION RATES.....	101
4.1 Introduction.....	101
4.2 Constraining compositionally dependent <i>in situ</i> ¹⁴ C production rates.....	102
4.2.1 Geologic and experimental production rate calibrations	102
4.2.2 Theoretical production rate estimates	103
4.3 Methods.....	104
4.3.1 Software framework	104
4.3.2 Predicted compositionally dependent production rates	106
4.4 Results and Discussion	107

4.4.1	Predicted compositionally dependent production rates	107
4.4.2	Assessing uncertainty in predicted compositionally dependent production rates ...	108
4.4.3	Comparisons with previous studies	110
4.5	Conclusions.....	112
4.6	Data availability	112
CHAPTER 5. CONCLUSIONS.....		124
APPENDIX A. COSMOGENIC NUCLIDE PROCESSING		127
APPENDIX B. SWEDEN SITE DESCRIPTIONS.....		130
APPENDIX C. FORWARD MODELING OF COSMOGENIC NUCLIDE PRODUCTION UNDER ICE		133
APPENDIX D. ANTARCTIC SITE DESCRIPTIONS, MODEL SET UP, AND MODEL OUTPUTS.....		147
REFERENCES		166
VITA.....		184

LIST OF TABLES

Table 2.1. Volume of Riukojietna ice cap from ice surface reconstructions (Rosqvist and Østrem, 1989)	55
Table 2.2. Sample collection information and the measured cosmogenic nuclide concentrations.	56
Table 2.3. <i>In situ</i> ¹⁰ Be measurement data from bedrock samples in Sweden.	57
Table 2.4. <i>In situ</i> ²⁶ Al measurement data from bedrock samples in Sweden.	57
Table 2.5. <i>In situ</i> ¹⁴ C measurements from bedrock samples in Sweden.	58
Table 2.6. Input cosmogenic nuclide data from bedrock samples taken adjacent to Riukojietna Ice Cap for the online University of Washington cosmogenic calculator, v.3.	59
Table 2.7. Radiocarbon dates from core PL1-169, measured in Fall 1998. Calibrated ages derived using CALIB Radiocarbon Calibration v 8.2 (http://calib.org/calib/ ; Stuiver et al., 1993; Reimer et al., 2020).	60
Table 2.8. Reconstructed ice thicknesses above the 2016 sample sites.	60
Table 2.9. Calculated concentrations of ¹⁰ Be from muon production over time. Note that all concentrations calculated are below the ¹⁰ Be detection limit of 5.61 x 10 ⁴	61
Table 2.10. Calculated concentrations of <i>in situ</i> ¹⁴ C from muon production over time. Note that concentrations are above the ¹⁴ C detection limit of 6.20 x 10 ⁴ at ice thickness <10 m.	61
Table 3.1. Sample locations for Antarctic samples.	89
Table 3.2. Summary table of glacial striation information found from Antarctic field seasons...	91
Table 3.3. <i>In situ</i> ¹⁴ C measurements for samples from western DML.	93
Table 3.4. <i>In situ</i> ¹⁰ Be and ²⁶ Al measurements for selected samples from western DML	96
Table 3.5. Apparent exposure age results from field sites in Antarctica.	97
Table 3.6. Modern day ice stream elevations and their latitude and longitude points compared to LGM best-fit model estimates.	99
Table 4.1. <i>In situ</i> ¹⁴ C global calibration dataset formatted for production rate calibration input to University of Washington online calculator, version 3 (Balco et al., 2008; http://hess.ess.washington.edu/math/v3/v3_cal_in.html). This dataset can be copied and pasted directly into the input data block field. Data from Borchers et al. (2016), Phillips et al. (2016), Schimmelpfennig et al. (2012), and Young et al. (2014). NL gratefully acknowledges the following colleagues for providing samples from surfaces at secular equilibrium, as part of the CRONUS-Earth project (NSF EAR-0345150): Tibor Dunai (CA-05A, northern Chile), Jay Quade (SPN samples, northern Chile), John Stone (98-PCM and WBC samples, Antarctica).....	115

Table 4.2. Elemental oxide compositions (weight %) for selected silicate minerals (Barthelmy, 2014; Morimoto, 1988) and rock types (Parker, 1967) used to calculate number densities (Eq. 4.2).
..... 119

Table 4.3. Predicted modern *in situ* ^{14}C spallogenic production rates (at $\text{g}^{-1} \text{y}^{-1}$) at SLHL from neutrons and protons in minerals and rock types considered, both theoretical (P_{CDpred}) and normalized to calibrated production in quartz (P_{CD}) using the gridded R_C record of Lifton (2016) and the ($P_{\text{CD,GD}}$) using the geocentric dipolar R_{CD} record of Lifton (2016)..... 120

Table 4.4. Percentage of total theoretical predicted modern SLHL *in situ* ^{14}C production (P_{CDpred}) by element for each mineral and rock type considered..... 121

Table 4.5. Predicted modern *in situ* ^{14}C production rates at SLHL for neutron spallation from O derived from secular equilibrium concentrations (N_{SE}) at ca. 20 cm depth for different rock types (Fabryka-Martin, 1988) compared to our software framework. Note that these estimates are not normalized relative to P_{Qcal} , for straightforward comparison to Fabryka-Martin’s (1988) predictions..... 122

Table 4.6. Neutron-only SLHL *in situ* ^{14}C production based on Masarik (2002; P_{M02}) theoretical predictions for compositions considered in this work, compared to modern SLHL neutron-only production predicted here (also see Table 4.3). Note that these estimates are not normalized relative to P_{Qcal} , to enable direct comparison to Masarik’s (2002) predictions. 123

LIST OF FIGURES

Figure 1.1. Principles of prior exposure and incomplete exposure which result in apparent exposure ages. (a) The ideal case where a sample experiences complete shielding before deposition and is continuously exposed since deglaciation. (b) A sample that is exposed to cosmic rays prior to glaciation, the apparent exposure age will be older than the deglaciation age. (c) If a sample is partially shielded from cosmic rays following deglaciation, the apparent exposure age will be younger than expected. (Figure from Heyman et al., 2014). 21

Figure 1.2. Conceptual figure of complex exposure dating utilizing *in situ* ^{14}C and ^{10}Be . (I) An exposed surface sample will begin to accumulate CN, such as *in situ* ^{14}C and ^{10}Be , assuming deep erosion before deglaciation. (II) When a glacier or ice sheet advances and covers the sample under cold-based conditions (no subglacial erosion), *in situ* ^{14}C will decay significantly more quickly than ^{10}Be . (III) Once re-exposed, the concentration builds back up. However, the resulting *in situ* ^{14}C apparent exposure age will be younger than the ^{10}Be apparent exposure age. The difference (D) between the measured nuclides reflects the length of burial time. (Modified from N. Lifton, pers. comm.)..... 22

Figure 1.3. Conceptual diagram of a mountain protruding through an ice sheet acting as a “dipstick”. As an ice sheet thins around a nunatak, the top of the nunatak is exposed first, with ages getting progressively younger closer to the modern ice surface. Larger white circles indicate older exposure ages while brown circles indicate other clasts. (Modified from S. Sams, pers. comm.). 23

Figure 2.1. **(a)** Map of Scandinavia showing deglacial isochrons of the Fennoscandian Ice Sheet in kyr intervals from 20 to 11, then in 100-year intervals (Stroeven et al., 2016). **(b)** European Union Digital Elevation Model (EU-DEM) of northern Sweden/Norway depicting the location of the Riukojietna ice cap (within the box of Fig. 2). White stars represent lake records. The numbers on the contours are the deglacial isochrons in ka. 43

Figure 2.2. **(a)** Satellite image (Google, 2018) of the Riukojietna ice cap depicting the location of bedrock samples (white circles). Apparent exposure ages (in ka) are shown in white boxes. Black lines show the Late Holocene moraines. Black arrow indicates the second ice tongue at the LIA. White stars depict lakes that have been cored downstream of the ice cap. **(b)** Two bedrock samples collected directly adjacent to the ice cap (1290 m a.s.l.). **(c)** Two bedrock samples collected from a bedrock knoll that was exposed in 2011 (1240 m a.s.l.). **(d)** One bedrock sample collected adjacent to lake 1063 (1064 m a.s.l.). 44

Figure 2.3. The age-depth model output from the Bayesian accumulation (Bacon v2.3.9.1) age-modelling software (Blaauw and Christen, 2011) using three radiocarbon tie points (Table 2.3). The median is shown with the minimum and maximum estimates on either side (95% probability). 45

Figure 2.4. Bed topography of the Riukojietna ice cap constructed from interpolated GPR measurements in 2011, 2012, and 2015. Background shows 2 m LiDAR from 2015 provided by Lantmäteriet (<https://www.lantmateriet.se/>). 46

Figure 2.5. Riukojietna ice cap surface topography reconstructions for 1916, 1960, 1978, and 2015 with respect to its maximum extent during the LIA (1910). The 1960 and 1978 elevations from Rosqvist and Østrem (1989) have been adjusted to better match the 2015 LiDAR DEM of the surrounding terrain. Sample sites are shown as white dots. 47

Figure 2.6. **(a)** Ice extents from 1910, 1960, 1978, and 2015 and ice thickness reconstruction for 2015 (see Fig. 2.5). The absence of ice within the outlet glacier tongue (white patch south of the profile line) is the bedrock knob sampled for 16-003 and 16-004. **(b)** Ice profile reconstructions of the flow line in **(a)**..... 48

Figure 2.7. **(a)** Two-isotope diagram of normalized $^{26}\text{Al}/^{10}\text{Be}$ concentration ratio vs. normalized ^{10}Be concentration. Ellipses show 2σ uncertainty. **(b)** Two-isotope isochron diagram of normalized *in situ* ^{14}C concentration vs. normalized ^{10}Be concentration. Burial isochrons (dashed lines) are calculated relative to the simple exposure line. Asterisks indicate that concentrations are normalized to site-specific production rates, hence corresponding units are in yr. 49

Figure 2.8. Stratigraphy and loss on ignition (LOI) from PL1-169 **(a)** and PL3-23 **(b)** in Pajep Luoktejaure (Fig. 2). High LOI indicates high organic content, interpreted as relatively low glacial activity while low LOI indicates low organic content associated with a relatively active glacier. **(a)** Core PL-169 has 3 radiocarbon tie points (in cal ka.) and the LOI record has been interpolated using the basal lake age from the nearby lake Vuolep Allakasjaure (Fig. 2.1), to an age scale in panel **(c)**. **(d)** An interpolated composite core where 1 – 13 cm are from PL3-23 and 13 – 130 cm are from PL1-169. Blue areas shown our interpretation of ice cap activity. 50

Figure 2.9. Ice thickness reconstructions for Riukojietna from the LIA (1910 CE), 1960, 1978, and 2015 with respect to the maximum extent of the LIA (1910). A contour at 40 m thickness is shown in dashed grey. Sample sites are shown as white dots..... 51

Figure 2.10. Ice sheet model outputs directly over the bedrock sample sites through time (Riuko 16-003). The solid line is the University of Maine Ice Sheet Model (UMISM; Fastook and Chapman, 1989; Fastook, 1994; Fastook and Prentice, 1994; SKB, 2010), the blue dashed line is the Patton model (Patton et al., 2016, 2017), and the orange dotted line is the ANU model (Lambeck and Purcell, 2001; Lambeck et al., 2014). 52

Figure 2.11. Modeled *in situ* ^{14}C , ^{10}Be , and ^{26}Al accumulation (black) as a function of ice thickness (blue) based on the EXP Model (solid lines) and HTM Model (stippled lines) described in text. Panels a – c shows the results for samples Riuko-16-001 and Riuko-16-002 while d – f show results for samples Riuko-16-003 and Riuko-16-004. The bottom panels show the same scenario as the top but with subglacial erosion. 53

Figure 2.12. Same as in Fig. 2.11 but with subglacial erosion rate assumed to be 0.01 cm yr^{-1} . 54

Figure 3.1. Overview map of Dronning Maud Land showing published cosmogenic nuclide (CN) data. The black dotted line shows the LGM model extent. Inset map shows locations mentioned in text. WAIS = West Antarctic Ice Sheet, EAIS = East Antarctic Ice Sheet, EL = Enderby Land, LHB = Lützow-Holm Bay, FM = Framnes Mountains, LA = Lambert-Amery glacial system, LH: Larsemann Hills, BH = Bunger Hills, SR = Shackleton Range. The MEASURES ice flow velocity by Rignot and Scheuchl (2017). RAISED Paleo ice extents from Bentley et al. (2014). (Modified from Andersen et al., 2020). 80

Figure 3.2. **(a)** Exposure age data from Veststraumen drainage basin and **(b)** Jutulstraumen drainage basin. Exposure ages in boxes are in elevation order from highest to lowest. Flowlines through ice streams are used in Fig. 3.6. White circles are erratics, white squares are bedrock, and yellow circles are Suganuma et al., (2022) ^{10}Be sample locations. 81

Figure 3.3. **(a)** Elevation vs. ^{10}Be and ^{26}Al cosmogenic nuclide data from the study sites compared to *in situ* ^{14}C showing that most of the ^{10}Be and ^{26}Al do not indicate last glacial maximum signal. **(b)** Elevation vs. *in situ* ^{14}C concentrations compared to saturation (solid line). Erratics are circles and bedrock are squares in both panels..... 82

Figure 3.4. Thinning rates determined from iceTEA (Jones et al., 2019) on selected nunataks. Data along Jutulstraumen are split into samples directly influenced by the main channel of Jutulstraumen (a) and by the Penck glacier (b). Thinning rates from the Veststraumen coast are calculated using all the samples from Basen and Fossilryggen (c). Blue data are *in situ* ^{14}C exposure age while black are ^{10}Be data..... 83

Figure 3.5. Density count histogram (i.e., count divided by bin width) for LGM-to-present ice-surface elevation differences (in m) over selected nunataks in the Veststarumen and Jutulstraumen catchment, using the entire ensemble of model runs (n=100, white bars) and a subset that is constrained by ice-core and cosmogenic-nuclide elevation-change estimates (n=27, blue bars). Elevation change intervals denote the 25th to 75th percentile of the constrained distribution. Grey zone marks the minimum thickening based on ^{14}C ages. (Fig. by M. Mas e Braga)..... 84

Figure 3.6. Different estimates of elevation change since the LGM based on the best experiment (IPSL-CM5A-LR_sld06) for the **(a)** Veststraumen catchment and **(b)** Jutulstraumen catchment. Solid lines indicate elevation change along each ice stream (cf. Fig. 3.2) for the best constrained run (dashed lines show the 5th and 95th percentiles of the ensemble of 27 simulations). Circles use the nearest point over the present-day ice stream as the reference, but take the LGM surface elevation from the best-performing simulation over the sample's elevation per se (circles). (Fig. by M. Mas e Braga, modified by A. Koester)..... 86

Figure 3.7. Summary figure of Holocene thinning rates across Dronning Maud Land. Ice surface lowering based solely on ^{10}Be (left) are from 1. Framenes Mtns (Macintosh et al., 2007); 2. Enderby Land (White and Fink, 20014); 3. Lutzow-Holm Bay (Kawamata et al., 2020); 4. Lutzow-Hom Bay (Yamane et al., 2011); 5. Suganuma et al., 2022; 6. Jutulstraumen (Andersen et al., 2020). Ice surface lowering based on *in situ* ^{14}C from this study include 7. Jutulstraumen and 8. Plogbreen (Basen and Fossilryggen sites). The eustatic sea level is shown in black compared to the modeled regional sea level change at the grounding line of Jutulstraumen (Suganuma et al., 2022). The thin lines are relative sea levels based on different earth models and the bold line represents the best model (Suganuma et al., 2022). The map of Antarctica (c) shows the study location by number. 87

Figure 3.8. The difference in elevation between our best fit model (see Appendix D) and Suganuma et al. (2022)'s best fit model for the Jutulstraumen basin (Fig. by M. Mas e Braga). 88

Figure 4.1. Measured (Reedy, 2013) (panels **a** and **b**) and modeled (panels **c** and **d**) neutron and proton reaction excitation functions for *in situ* ^{14}C production from various targets. The lines are linearly interpolated between points. Note that modeled predictions for ^{23}Na (JENDL/HE-2007;

Fukahorit et al., 2002; Watanabe et al., 2011) suggest the highest production of all nuclides considered. 113

Figure 4.2. Predicted theoretical SLHL production of *in situ* ^{14}C (P_{CDpred}) in minerals (a) and rocks (b) relative to that in pure quartz (dashed grey line). The color of each symbol reflects the element that contributes the highest proportion of production after oxygen and silica. 114

Figure 4.3. Modeled neutron (a) and proton (b) cross-sections for ^{23}Na from JENDL/HE-2007 (Na_J , solid line) compared to the spliced TENDL-2019 at energies ≤ 0.2 GeV and JENDL/HE-2007 > 0.2 GeV ($^{23}\text{Na}_T$, dashed line). Differential neutron and proton fluxes at SLHL (J_N and J_P , respectively; Sato et al., 2008) are plotted in their respective panes to illustrate the combined effect of excitation function and flux on *in situ* ^{14}C production. 114

ABSTRACT

Reconstructing past glacier and ice-sheet extents is important to better understand how glacial systems have responded to past climate changes in hope of constraining predictions of their responses to ongoing anthropogenic climate warming. As such, the most recent period of climatic variations, from the Last Glacial Maximum (LGM, ca. 21 ka) through today, is of great interest as a prominent example of how ice has reacted to past climatic warming events. Surface exposure dating utilizing cosmogenic nuclides can directly constrain when past ice deglaciated in current and former glacial landscapes. Numerous studies have utilized long-lived cosmogenic radionuclides (i.e., ^{10}Be , ^{26}Al) in polar regions to reconstruct glacial systems. However, due to prevalent non-erosive cold-based ice, prior nuclides from pre-LGM can be preserved.

The research described in this dissertation applies *in situ* cosmogenic ^{14}C (*in situ* ^{14}C), an emerging geochronometer, to polar glacial landscapes in Sweden and Antarctica to constrain the timing and rate of glacial ice retreat. *In situ* ^{14}C more closely reflects the post-LGM deglacial signal in polar regions because it is less likely to preserve prior nuclides (inheritance) under minimally erosive ice. Our cosmogenic ^{10}Be – ^{26}Al – ^{14}C concentrations near the Riukojietna ice cap, the last remaining ice cap in Sweden, combined with a sedimentary record from a proximal proglacial lake, indicate the ice cap likely survived during a warm period in the Holocene, but was less extensive than today. The *in situ* ^{14}C exposure data from nunataks in western Dronning Maud Land (DML), East Antarctica indicate significant coastal thickening (up to 850 m) not predicted by models to date. In addition, this work dates the timing of post-LGM ice surface lowering in two drainage basins in western DML. These results demonstrate the significant contribution of *in situ* ^{14}C in polar regions.

In addition to applications of *in situ* ^{14}C in polar regions, this work also describes the development of a compositionally dependent *in situ* ^{14}C production rate calculator. The ability to extract *in situ* ^{14}C from samples which quartz cannot be separated (either quartz-poor or fine-grained) would allow new avenues of research. The computational framework will be a useful tool in efforts to broaden the utility of *in situ* ^{14}C to quartz-poor and fine-grained rock types.

CHAPTER 1. INTRODUCTION

1.1 Significance of *in situ* cosmogenic ^{14}C

Cosmogenic nuclides (CNs) have revolutionized studies of Quaternary geomorphology. CNs are rare nuclides produced *in situ* in minerals near the Earth's surface by cosmic ray bombardment (Gosse and Phillips, 2001). CNs build up predictably over time in an exposed surface through spallation and muon reactions. An exposure age can be calculated by measuring the concentration (atoms g^{-1}) of rare CNs in a sample and utilizing the production rate at that site (atoms $\text{g}^{-1} \text{yr}^{-1}$) and isotopic decay rate for radionuclides, assuming continuous exposure and no erosion. Measured concentrations can also be interpreted in terms of an erosion rate, assuming steady-state erosion. However, the work in this thesis focuses on exposure ages, thus erosion rates are outside the scope of this research. The most commonly measured CNs are ^{10}Be ($t_{1/2} = 1.39 \text{ My}$ (Chmeleff et al., 2010; Korschinek et al., 2010) and ^{26}Al ($t_{1/2} = 705 \text{ ky}$ (Nishiizumi, 2004)) which are typically extracted from the mineral quartz, due to its simple composition and resistance to weathering. ^{10}Be and ^{26}Al are excellent geochronometers for reconstructing geomorphic processes on thousand-year to million-year timescales. They are especially beneficial for detecting complex exposure histories over long time spans. However, over the last 50 – 100 ka, they become less useful to studying complex exposure due to their long half-lives.

In situ cosmogenic ^{14}C (*in situ* ^{14}C) is also produced in the quartz mineral lattice through interactions with cosmic rays (Gosse and Phillips, 2001). This radionuclide is unique among commonly measured cosmogenic nuclides because its short half-life (5.7 ky) makes it sensitive to exposure since the global Last Glacial Maximum (LGM; 21 ka; Clark et al., 2009). Its short half-life predicts that *in situ* ^{14}C decays rapidly in 5-7 half-lives (~30 – 40 kyr) to background levels when rocks are shielded and can more reliably constrain the post-LGM deglacial signal than long-lived radionuclides. Over the last 20 years, various methods have been developed to reliably extract *in situ* ^{14}C from quartz (e.g., Lifton et al., 2001; Hippe et al., 2009; Lifton et al., 2015b; Fülöp et al., 2019; Goehring et al., 2019), leading to a recent increase in its applications (e.g., Anderson et al., 2008; Briner et al., 2014; Nichols et al., 2019; Pendleton et al., 2019; Koester et al., 2020; Hippe et al., 2021). Polar regions generally have low erosion rates due to prevalent cold-based ice that can preserve landscapes over glacial cycles (e.g., Miller et al., 2006; Altmaier et al.,

2010; Marrero et al., 2018; Balter et al., 2020). For this reason, nuclide inventories from long-lived radionuclides may not be reset and thus can contain previous periods of exposure, leading to complex exposure over post-LGM deglaciation. Therefore, *in situ* ^{14}C is a powerful tool in the polar regions for reconstructing post-LGM deglaciation compared to long-lived radionuclides.

1.2 Applications of *in situ* ^{14}C in polar regions

Global temperatures have risen in the last century at least 1°C above pre-industrial levels and they are likely to increase another 1.5°C between 2030 and 2052 (IPCC, 2022). Although the climate has warmed in the past, current warming trends are unprecedented since the 1950s in the context of paleoclimate reconstructions (Arias et al., 2021). Paleoclimatic evidence extends modern instrument-based observations back in time to provide the long-term context of current climate trends. Changes in the cryosphere give insight into the long-term trends of climate change relating to regional and global sea level changes (Gulev et al., 2021). The Arctic and Antarctic are ideal locations to study past ice behavior because they respond directly to orbital forcing of global warming and/or cooling in the Northern Hemisphere (Hays et al., 1976; Alley et al., 2002; Kawamura et al., 2007). Reconstructing former extents of ice sheets and glaciers allows further inferences about past climate conditions which can be used for future predictions of the effects of ongoing anthropogenic warming.

CNs are useful in glacial geomorphology because they can help to infer the timing of maximum glacial extent (at scales ranging from individual glaciers to ice sheets), timing of retreat or advance of ice, and past rates of ice surface lowering, particularly where other dateable material is lacking. Thick ice cover ($>100\text{ m}$) can shield the bedrock surface from cosmic rays while simultaneously eroding any prior CN accumulations, resetting the CN concentrations in the bedrock to background levels and restarting the cosmogenic nuclide clock when the surface is re-exposed to cosmic radiation. Removal of 4 m of rock below a glacier will erode close to 99% of the ^{10}Be inventory but only 89% of the *in situ* ^{14}C inventory (Hippe, 2017). However, the rapid decay of *in situ* ^{14}C under ice contributes to nuclide loss (Hippe, 2017). In such a scenario, the concentration of a CN in glacially eroded bedrock or a transported erratic is proportional to the deglaciation age at that site assuming a single continuous exposure period.

However, complications can arise when applying cosmogenic radionuclides to glacial landscapes. For instance, cold-based ice is non-erosive and can preserve landscapes, violating the

continuous exposure assumption. In this case, CN concentrations in the bedrock surface are not fully reset by erosion, leaving a signal of prior exposure (i.e., inherited nuclides) and leading to an erroneously old exposure age (Heyman et al., 2011; Fig. 1.1). On the other hand, complex exposure histories can arise that can lead to a deglaciation age younger than expected (Heyman et al., 2011). After deglaciation, a sample could get buried and become partly or fully shielded, which decreases production while simultaneously decaying away radionuclides which reduces the overall concentration. A sample could also experience erosion after deglaciation. Erosion will decrease the overall concentration, leading to an erroneously young exposure age. In polar regions, bedrock is less likely to be affected due to low erosion rates.

Measuring two or more CNs with different half-lives can often constrain complex exposure histories, especially when dealing with non-erosive ice that is frozen to its bed (Granger, 2006). In this situation, two-isotope plots are useful for constraining whether samples have undergone continuous exposure (with or without steady erosion), or if they have experienced complex histories of exposure and burial (Fig. 1.2). For instance, pairing *in situ* ^{14}C with ^{10}Be extracted from bedrock samples taken directly in front of the Rhône Glacier in Switzerland showed that the glacier was smaller or larger than present at various times during the Holocene (Goehring et al., 2011).

Although using CNs to date the maximum extents of glaciers and ice sheets and their retreat are common (e.g., Marsella et al., 2000; Balco et al., 2002; Bromley et al., 2016; Corbett et al., 2017), recently they have also been used to reconstruct past ice surface lowering for modern ice sheets (e.g., Stone et al., 2003) and former ice sheets (e.g., Goehring et al., 2008). The thinning rate of an ice sheet can be inferred from measuring CN concentrations in samples collected along an altitudinal transect along mountains protruding through the ice (nunataks) – the so-called ‘dipstick method’ (Fig. 1.3). This method assumes that as an ice sheet thinned, the top of the nunatak would be exposed first, while samples from near the current ice surface would be exposed most recently – resulting in higher concentrations near the summit and progressively lower concentrations with decreasing elevation. Thus, exposure ages derived from these samples will similarly decrease with decreasing altitude.

Recent studies have demonstrated that *in situ* ^{14}C is a powerful tool for constraining Holocene and latest Pleistocene glacial histories in polar regions. Glacial ice in polar regions is commonly frozen to the bed (cold-based) and these regions more generally exhibit low erosion

rates (e.g., 0.1 – 0.5 mm/ka)(Marrero et al., 2018), which can preserve glacial landscapes over glacial-interglacial cycles. Therefore, measured concentrations of long-lived or stable cosmogenic nuclides (i.e., ^{10}Be , ^{26}Al , ^{36}Cl , ^{21}Ne , ^3He) in polar settings may contain inventories from prior exposure periods. Applications of *in situ* ^{14}C in the Arctic (Briner et al., 2014; Young et al., 2021) and the Antarctic (Johnson et al., 2019; Nichols et al., 2019) have demonstrated that *in situ* ^{14}C is able to quantify rates of post-LGM retreat where long-lived nuclides often cannot.

1.3 Research plan

This thesis applies CNs to glaciated zones in polar regions, focusing primarily on *in situ* ^{14}C , to reconstruct post-LGM ice histories. The following three chapters cover different applications of *in situ* ^{14}C . The first two chapters focus on applications in polar environments, while the third addresses a need identified while processing samples collected from Antarctica.

1.3.1 Chapter 2: The Riukojietna ice cap, Sweden

Chapter 2 investigates the post-LGM history of the Riukojietna ice cap, the last remaining ice cap in Sweden. Evidence of past glacier retreat in Sweden relies on indirect methods to indicate when glaciers were active vs. inactive and does not constrain their relative size. By obtaining *in situ* ^{14}C , ^{10}Be , and ^{26}Al concentrations from two recently exposed bedrock outcrops adjacent to the ice cap and a bedrock outcrop bordering an adjacent proglacial lake, it is possible to directly constrain the size of the ice cap during the Holocene. The results of this study have implications for how climate change (i.e., temperature, precipitation) during the Holocene, especially the Holocene Thermal Maximum (HTM), impacted the ice cap.

The cosmogenic nuclide results from the bedrock samples adjacent to the ice cap experienced previous period(s) of exposure during the Holocene, indicating the ice cap was as small or smaller than present. In addition, laminated intervals in a sediment core from a proglacial lake further downstream (Pajep Luoktejaure) suggest the ice cap likely survived the HTM. Although our sampled sites were exposed, we postulate that the ice cap may have persisted during the HTM in a configuration similar to the present. This chapter represents a prepublication manuscript in preparation for *Quaternary Science Reviews* and is a collaboration between A. Koester, A. Stroeven, G. Rosqvist, J. Andersen, C.A. Wahlström, and N. Lifton.

1.3.2 Chapter 3: Holocene thinning of the East Antarctic Ice Sheet

Chapter 3 presents *in situ* ^{14}C exposure ages from mountains protruding through the margin of the EAIS along two marine-terminating ice streams in western Dronning Maud Land (DML) to constrain ice surface lowering since the LGM. Past ice sheet surface lowering rates are largely absent from western Dronning Maud Land in East Antarctica, presenting a knowledge gap in how this sector of the Antarctic ice sheet retreated during the last deglaciation. The exposure ages were used to validate ice thickness reconstructions for the LGM using an ensemble of high-resolution ice sheet model experiments. Exposure data and model results indicate significant coastal thickening of the EAIS at the LGM that have not been predicted by models to date in DML.

Exposure data indicate significant coastal thickening of the ice sheet during the LGM upwards of 850 m, while estimated inland thickening below the escarpment ranges from ca. 100 to 400 m. Our best-fit high-resolution model shows significant amount (800 – 900 m) of coastal thickening, in agreement with the exposure dating. This study points to the need for high-resolution modeling to integrate cosmogenic data into a spatially integrated reconstruction of EAIS response to climate change. This chapter is a prepublication manuscript prepared for *The Cryosphere* and represents a collaboration from the Mapping, Measuring and Modeling Antarctic Geomorphology and Ice Change in Dronning Maud Land (MAGIC-DML) team, with specific support from M. Mas e Braga who contributed model set up and outputs and J. Andersen, N. Lifton, and A. Stroeven who contributed to writing and editing.

1.3.3 Chapter 4: Calculating compositionally dependent *in situ* ^{14}C production rates

Chapter 4 presents a software framework to calculate compositionally dependent *in situ* ^{14}C production rates for a range of silicate rock and mineral compositions. A subset of samples collected from Antarctica and Sweden contained little to no quartz, or the quartz was too fine-grained for *in situ* ^{14}C to be extracted using existing techniques. *In situ* ^{14}C measurements are currently limited to relatively coarse-grained (typically sand-sized or larger, crushed/sieved to sand-size) quartz-bearing rock types, but while such rocks are common, they are not ubiquitous. Thus, one research goal was to develop robust extraction methods for *in situ* ^{14}C from non-quartz whole-rock samples. The ability to extract and interpret *in situ* ^{14}C from quartz-poor and fine-grained rocks would thus open its unique applications to a broader array of landscapes.

As a first step toward this goal, a MATLAB[®]-based software framework was developed to quantify spallogenic production of *in situ* ¹⁴C from a broad range of silicate rock and mineral compositions. Production from oxygen dominates the overall *in situ* ¹⁴C signal, accounting for >90% of production for common silicate minerals and rock types at sea-level and high latitudes (SLHL). This work confirms that Si, Al, and Mg are important targets, but also predicts greater production from Na than from those targets. Predicted production rates drop as compositions become more mafic (particularly Fe-rich). This framework should thus be a useful tool in efforts to broaden the utility of *in situ* ¹⁴C to quartz-poor and fine-grained rock types, but future improvements in measured and modeled excitation functions would be beneficial. This chapter represents a collaboration between A. Koester and N. Lifton and was published in *Geochronology* in January 2021.

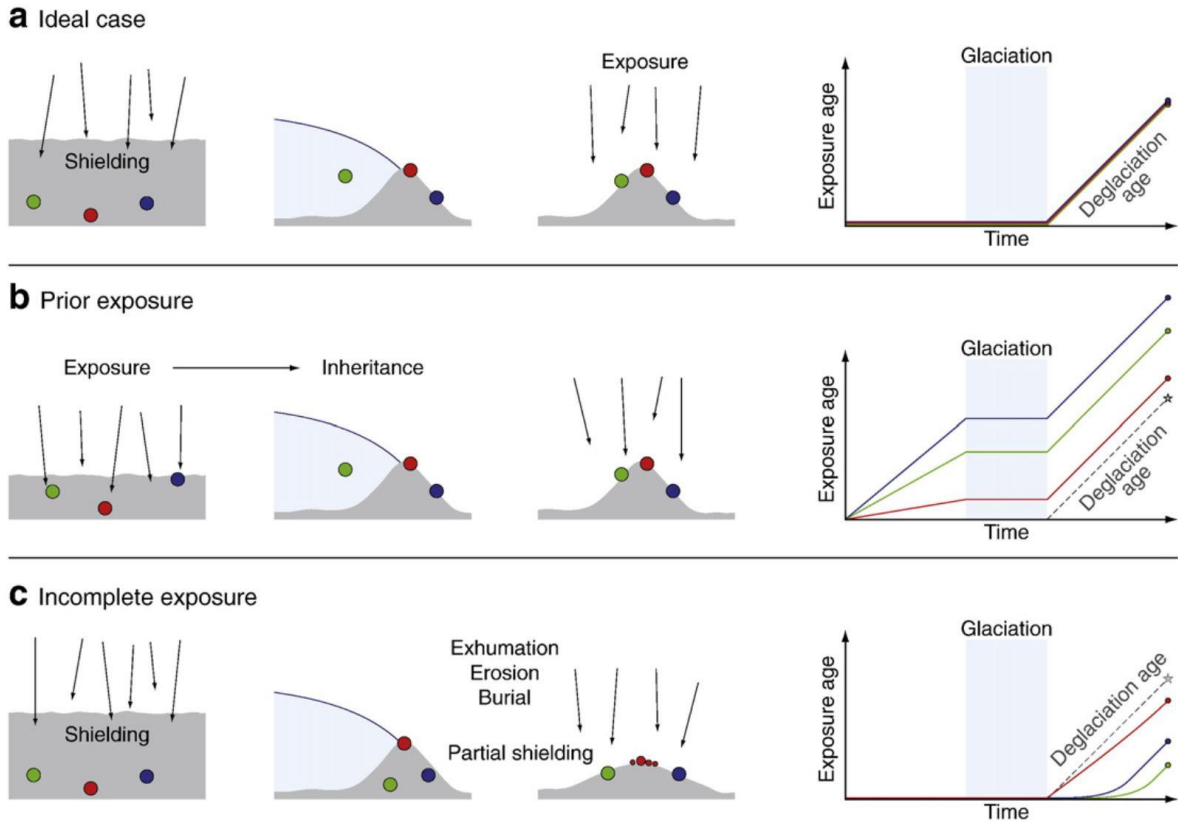
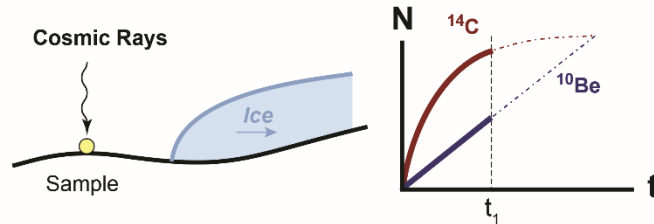
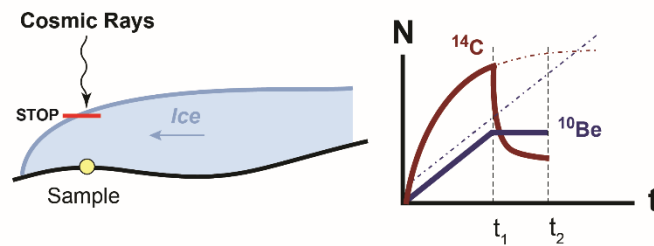


Figure 1.1. Principles of prior exposure and incomplete exposure which result in apparent exposure ages. (a) The ideal case where a sample experiences complete shielding before deposition and is continuously exposed since deglaciation. (b) A sample that is exposed to cosmic rays prior to glaciation, the apparent exposure age will be older than the deglaciation age. (c) If a sample is partially shielded from cosmic rays following deglaciation, the apparent exposure age will be younger than expected. (Figure from Heyman et al., 2014).

I. Deglaciation: surface exposure



II. Glaciation: burial by Ice



III. Deglaciation: 2nd surface exposure

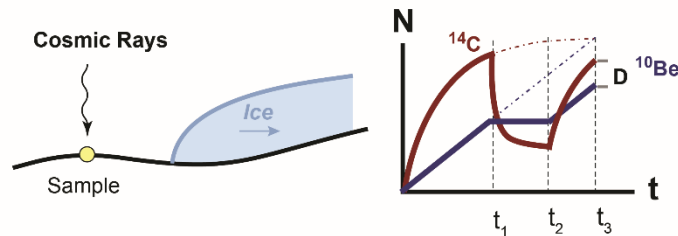


Figure 1.2. Conceptual figure of complex exposure dating utilizing *in situ* ^{14}C and ^{10}Be . (I) An exposed surface sample will begin to accumulate CN, such as *in situ* ^{14}C and ^{10}Be , assuming deep erosion before deglaciation. (II) When a glacier or ice sheet advances and covers the sample under cold-based conditions (no subglacial erosion), *in situ* ^{14}C will decay significantly more quickly than ^{10}Be . (III) Once re-exposed, the concentration builds back up. However, the resulting *in situ* ^{14}C apparent exposure age will be younger than the ^{10}Be apparent exposure age. The difference (D) between the measured nuclides reflects the length of burial time. (Modified from N. Lifton, pers. comm.)

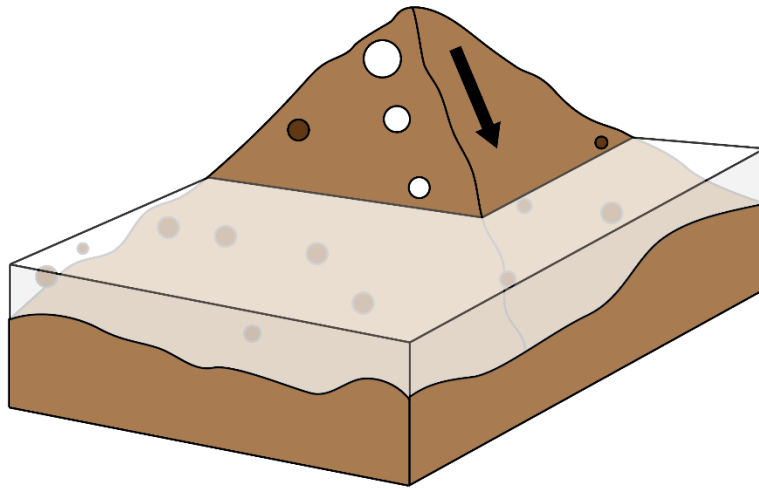


Figure 1.3. Conceptual diagram of a mountain protruding through an ice sheet acting as a “dipstick”. As an ice sheet thins around a nunatak, the top of the nunatak is exposed first, with ages getting progressively younger closer to the modern ice surface. Larger white circles indicate older exposure ages while brown circles indicate other clasts. (Modified from S. Sams, pers. comm.).

CHAPTER 2. THE RIUKOJETNA ICE CAP LIKELY SURVIVED THE HOLOCENE THERMAL MAXIMUM BUT WAS LESS EXTENSIVE THAN TODAY

2.1 Introduction and Background

Mountain glaciers and ice caps are reliable indicators of regional climate change on decadal timescales because their mass balances are sensitive to changes in winter precipitation and summer ablation (Grudd, 1990; Oerlemans and Fortuin, 1992; Oerlemans, 2005). Indeed, worldwide, glaciers have retreated at accelerating rates during the 20th century (WGMS, 2022) and are projected for continued decline throughout the 21st century due to increased global temperatures (Oerlemans et al., 1998; Hock et al., 2019). Within this observed contemporary framework, we explore whether glaciers were as small as, or smaller than, today also during the Holocene Thermal Maximum (HTM; 8 – 5 thousand years ago [ka]) (Wastegård, 2022) as inferred from proglacial lacustrine sediment records (Snowball and Sandgren, 1996; Nesje et al., 2000; Rosqvist et al., 2004; Larocca and Axford, 2022).

Lakes are widespread features in deglacial landscapes, forming in bedrock basins or impounded by moraines. A common method to reconstruct the timing of glacier retreat and subsequent activity is to investigate the sediment record deposited in proglacial lakes (Karlén, 1988; Snowball and Sandgren, 1996; Nesje et al., 2000; Andersson et al., 2010). Typically, glacial sediments (glacial flour) indicate an active glacier while organic-rich sediments (gyttja) indicate deposition during a period of glacial inactivity or absence (Jansson et al., 2005). This is because basal sliding is required for a glacier to erode its substrate and produce glacial flour (i.e., a warm-based glacier). However, several factors influence the sedimentation rate into proglacial lakes such as subglacial erosion rates, intermediate sediment storage, and transportation processes within the catchment (Leonard, 1986; Rubensdotter and Rosqvist, 2003; Jansson et al., 2005). The relationship between glacial sediment accumulation and glacier size remains undetermined and a proglacial lacustrine record does therefore not provide direct constraints on glacier extent (Jansson et al., 2005; Nesje, 2009).

Cosmogenic nuclides such as ^{10}Be ($t_{1/2} = 1.39 \text{ My}$ (Chmeleff et al., 2010; Korschinek et al., 2010)) and ^{26}Al ($t_{1/2} = 705 \text{ ky}$ (Nishiizumi, 2004)) are only produced when near-surface minerals are exposed to incident cosmic radiation. In glacial landscapes, the buildup of cosmogenic

radionuclides in a rock surface is governed by the rate of spallation and muon reactions while removal is governed by radioactive decay and rock surface erosion (Gosse and Phillips, 2001). When a bedrock surface is buried by thick ice (e.g., >100 m), production is minimal, and the nuclides simply decay at known rates. The timing of the last deglaciation of Scandinavia has been determined using radiocarbon-dated oldest (lacustrine) sediments, the Swedish Time Scale varve chronology (Kleman et al., 1997; Stroeven et al., 2016) and the postglacial accumulation of ^{10}Be and ^{26}Al (Fabel et al., 2002, 2006; Goehring et al., 2008; Stroeven et al., 2011, 2016; Cuzzone et al., 2016). Although these nuclides are often valuable for deglaciation reconstructions, they are unable to resolve complex periods of burial and re-exposure arising from latest Pleistocene and Holocene glacial fluctuations due to their long half-lives. *in situ* cosmogenic ^{14}C (*in situ* ^{14}C) has a short half-life (5.7 ky), making it a powerful tool for constraining Holocene and latest Pleistocene glacier histories, especially in concert with ^{10}Be and/or ^{26}Al . Such studies have been done in the European Alps (Goehring et al., 2011; Wirsig et al., 2016; Schimmelpfennig et al., 2022), on Greenland and Baffin Island (Briner et al., 2014; Young et al., 2021), in Antarctica (Johnson et al., 2019; Nichols et al., 2019), and in Norway (Rand and Goehring, 2019).

Following the demise of the Fennoscandian Ice Sheet (FIS; Fig. 2.1) after the Last Glacial Maximum (LGM, ~22 ka), there appear to have been many glacier advances in the Scandinavian Mountains. Existing climate reconstructions from Fennoscandian lakes indicate a maritime climate with a strong zonal atmospheric circulation during the early Holocene (11.7 – 8.2 ka) (Hammarlund et al., 2003; Seppä et al., 2005). Glaciers shrank or melted away completely during the early Holocene, after ~10.2 to 7 ka (Nesje et al., 2008; Larocca and Axford, 2022). It has been proposed that some glaciers in Norway disappeared during the mid-Holocene due to either increased summer temperatures or reduced winter precipitation (Bjune et al., 2005; Nesje et al., 2008). Although older literature suggests that Swedish glaciers retreated and advanced multiple times during the HTM (Karlén, 1976, 1981; Karlén et al., 1995), evidence for such advances have not been found in subsequent studies (Snowball and Sandgren, 1996; Rosqvist et al., 2004). Conditions during the HTM were drier and had higher summer temperatures than today of 1.5 °C (Barnekow, 2000; Seppä et al., 2005; Nesje et al., 2008; Jonsson et al., 2010). Subsequently, an overall cooling trend occurred in the late Holocene (Bigler et al., 2003; Seppä et al., 2005). The late Holocene cooling trend most likely resulted in a positive mass balance on Scandinavian glaciers, with glaciers readvancing and producing increased volumes of glacial material

(Karlén et al., 1995; Matthews and Dresser, 2008). All glaciers in Scandinavia advanced during the Little Ice Age (LIA; 1300 - 1850). Most Swedish glaciers are thought to have reached their maximum Holocene position as late as the beginning of the 18th century (Karlén, 1988), thus potentially eradicating evidence from glacial advances during earlier phases of the Holocene (Jansson et al., 2005).

Here, we aim to constrain the former size of Riukojietna, a rapidly retreating thin (<100 m) ice cap located in northern Sweden (Fig. 2.1). We do this by combining indirect evidence of glacial extent from proglacial lacustrine records with direct evidence from cosmogenic nuclide chronometry (^{14}C , ^{10}Be , ^{26}Al). We can then evaluate the sensitivity of Riukojietna to Holocene climate change.

2.2 Study Site

Riukojietna is a small, flat, polythermal ice cap located on the Swedish-Norwegian border (Fig. 2.1), covering a granite/schist plateau (Holmlund et al., 1996). In 1989, the ice cap had an area of 4.6 km² which spanned elevations between 1140 and 1456 m a.s.l., and its thickness ranged between 105 and 36 m (Rosqvist and Østrem, 1989). However, the ice cap has since diminished, covering 2.8 km² in 2015 while spanning less than 283 m vertically between the ice divide and snout (Table 2.1). The ice cap flows radially outwards from its highest point and is impounded by bedrock ridges to the south and northeast. Currently, Riukojietna has one outlet glacier tongue that terminates on a steep rise on the northeast end near Lake 1063 (Fig. 2.2). Till cover in the catchment area is thin and blocky and vegetation consists of grass heath and mosses.

The terminus of the eastern flank of Riukojietna has been mapped since 1963 and its mass balance has been monitored annually since 1986. Two topographic maps were constructed based on aerial photography from 1960 and 1978 showing ice cap surface contours and extent (Rosqvist and Østrem, 1989). The eastern terminus calved into Lake 1063 (Fig. 2.2) before 1960 but retreated up-valley after 1975. Ice volume has been decreasing significantly during the 20th century due to a dominantly negative annual mass balance (WGMS, 2022). Because it is relatively low-lying and spans an unusually narrow elevation interval (compared to most valley glaciers in the region), Riukojietna is assumed to be highly sensitive to climate change (Rosqvist and Østrem, 1989).

Although thin, the ice cap has been thick enough through its history to produce pressure melting at the base, enabling sediment delivery to downstream lakes. Four lakes on the eastern

side of the ice cap receive glacial meltwater; ordered by their elevation (in m a.s.l.), they are lakes 1063, 1009, Pajep Luoktejaure (913), and 903 (Fig. 2.2). Snow melt contributes additional water in spring and early summer. Lakes at this latitude and altitude are generally ice-covered from October to June. The lakes act as a series of traps for sediment derived from glacial erosion and soil erosion from the stream banks or the wider catchment. Today, the color of the downstream lakes indicates input from glacial sediment (Fig. 2.2). Karlén (1981) cored two of the lakes downstream of Riukojietna, Lake 1009 and Pajep Luoktejaure, to determine their Holocene sediment accumulation histories. Karlén (1981) noted that Pajep Luoktejaure had accumulated twice as much sediment as Lake 1009, despite a low influx of glacial flour. From the variations in relative densities and organic content of the sediments in lakes 1009 and Pajep Luoktejaure, Karlén (1981) proposed that Riukojietna was inactive and/or small between 10.9 ± 0.4 (Si-2860) and 2.7 ± 0.1 (Si-2895) cal ka and subsequently reactivated (calibrated using the online CALIB rev. 8; Stuiver and Reimer, 1993; Reimer et al., 2020).

Terminal moraines are largely absent in the blocky terrain surrounding Riukojietna. The most prominent lateral/end moraine is located to the southeast of Lake 1063 (Fig. 2) and indicates that the ice cap advanced to this position at least once during the Holocene. Karlén (1975) used lichenometry on *R. geographicum* and *R. alpicola* to infer a depositional age of c. 1910 for that terminal moraine (Pohjola et al., 2005), which is similar to other lichenometry-dated LIA moraines in the region (Karlén and Denton, 1973; Karlén, 1976). Moraines indicate that a second outlet glacier used to extend to the southwest (Fig. 2.2; southwest of samples Riuko-16-001 & Riuko-16-002), and a glacially molded hanging valley extends from the current ice cap margin to the southeast, aligned with streamlined glaciofluvial landforms and lineations downstream.

2.3 Methods

We combine cosmogenic nuclide chronometry, lacustrine sediment records, ice reconstructions, and modeling of complex exposure histories to evaluate the Holocene history of Riukojietna. Each method is described in detail below.

2.3.1 Collection and extraction of cosmogenic nuclides from bedrock

We set out to investigate the post-LGM deglacial and Holocene ice burial history of the Riukojietna ice cap. To constrain this, we collected five bedrock samples in 2016 from three locations near Riukojietna (Fig. 2.2) and measured concentrations of *in situ* ^{10}Be , ^{26}Al , and ^{14}C (Table 2.2). The nuclide inventories ideally would be able to indicate if these locations were recently deglaciaded, exposed during previous warm periods in the Holocene, and for how long they have been buried by ice in-between exposure periods. Two samples from granitic bedrock were collected immediately adjacent to the ice cap (<2 m from the modern ice; Riuko-16-001 & Riuko-16-002). Two samples were taken from a granitic bedrock knob protruding through the outlet glacier tongue (Riuko-16-003 & Riuko-16-004) that was exposed in 2011. The last sample was collected from a bedrock outcrop adjacent to Lake 1063 (Riuko-16-005). (See Appendix A for cosmogenic nuclide separation and extraction information; Table 2.2; Table 2.3, Table 2.4).

2.3.2 Lacustrine sediment cores

Pajep Luoktejaure has a relatively even bathymetry with one deeper section (12 m) in its northern part. Sediment cores PL1-PL5 were retrieved from the deepest part of the lake in April 1998 using a modified Livingstone piston corer (90 mm diameter). The top 23 cm of unconsolidated sediments were retrieved by an additional gravity corer (PL3-23). PL-5 was kept unopened for reference. Visual inspection and results from measurements of loss-on-ignition (LOI) determined at 550 °C at 1 cm resolution of PL 1 – 4 showed the same general stratigraphy for common sections. PL1-169 was the longest core (down to 169 cm below the lake floor) and the only one representing the early phase of lake development; the composite stratigraphic description of Pajep Luoktejaure is based on this core and surface core PL3-23.

Sedimentary structures and grayscale density of cores PL1-169, PL2-133, and PL3-23 were determined by X-ray radiography and subsequent image analysis providing information of relative density (Rosqvist et al., 2004). However, there were problems with the reference calibration for sediment density, therefore it is not shown. Line transects (1 mm width) of grayscale density values were taken at a resolution of 0.3 mm. Grain size distribution was analyzed in a Sedigraf 5100 on 1 cm slices of specific sedimentary structures in cores PL1-169 and PL2-133.

Age control is provided by three AMS ^{14}C -dates from PL1-169, one of which was based on a terrestrial plant macrofossil and two on 1-cm-thick bulk sediment samples (Table 2.7). The samples were radiocarbon dated at the Ångström Laboratory, Uppsala University, Sweden. We assumed the top of the core stopped accumulating 100 years ago before collected (i.e., 1898). The basal radiocarbon age from PL1-169 is from bulk radiocarbon and is older than the regional ~ 10 ka deglacial age estimated from Stroeve et al. (2016). We instead use the basal sediment age of 9.8 ± 0.2 cal ka constrained by a terrestrial macrofossil from a nearby lake (~ 20 km NE), Vuolep Allakajaure (Fig. 2.1; 8740 ± 100 ^{14}C yr B.P.; Ua-16628; Rosqvist et al., 2004), in our age-depth modelling. Calibration to cal ka was performed using CALIB Radiocarbon Calibration v 8.2 (<http://calib.org/calib/>; Stuiver and Reimer, 1993; Reimer et al., 2020), and the Bayesian accumulation (Bacon v2.3.9.1) age-modelling software (Blaauw and Christen, 2011) was used to derive the age-depth model (Fig. 2.3).

2.3.3 Ice thickness reconstructions, bed topography, and volume calculations

Detailed ice surface topography maps were constructed from aerial photographs taken in 1960 and 1978 to determine the average mass balance of Riukojietna (Rosqvist and Østrem, 1989). These two maps were scanned and georeferenced in QGIS software to derive the ice cap surface elevation during these time periods (Wahlström, 2016). The ice cap topography was additionally mapped during the summer of 2014 and spring 2015 using two differential GPS (dGPS) rover units. The subglacial bedrock topography was constrained with ground penetrating radar (GPR) towed behind a snowmobile in the spring of 2011, 2012, and 2015 (Fig. 2.4). We use these data sources to track ice cap area and volume changes relative to a 2 m-resolution LiDAR digital elevation model (DEM) from 2015 provided by Lantmäteriet (<https://www.lantmateriet.se/>).

The elevations of fixed bedrock points on the 1960 and 1978 maps were compared to the recent LiDAR DEM to evaluate their accuracies, and differences were calculated. These differences were interpolated using kriging in Surfer 11 to create misfit values across the glacier surface. The resulting spatial pattern of misfit is used to correct the altitudes derived from the 1960 and 1978 maps to better match ice surface elevations to the 2015 LiDAR DEM (Fig. 2.5).

The perimeter of the presumed LIA glacial extent (1910) was mapped from two orthophotos (1960, 1978) and integrates the location of the eastern terminal moraine. There is no evidence from the LiDAR or satellite imagery for a western terminal moraine, mentioned by Schytt

(1963), to constrain the LIA ice cap extent on the Norwegian side. Due to a lack of a visual moraine, the 1910 extent on the western side is slightly more expanded than the 1960 extent by 50 – 100 m. The 1910 ice surface was calculated for the central flow line (Fig. 2.6) using the reconstructed bed topography, a target maximum elevation of 1490 m a.s.l., and an adjustable yield stress following Benn and Hulton (2010). The surface elevations were interpolated in Surfer 11 using kriging to create a LIA ice surface reconstruction.

For each of the four time slices, Surfer 11 was used to calculate the volume and average ice thickness of Riukojietna using the difference between the ice surface DEM and the bed topography DEM (Table 2.1, Table 2.8).

2.4 Results

2.4.1 Cosmogenic nuclide concentrations and apparent exposure ages

The ^{10}Be concentrations in bedrock samples Riuko-16-001 to Riuko-16-005 range from $8.8 \pm 0.4 \times 10^4$ to $2.2 \pm 0.1 \times 10^5$ atoms g^{-1} , while the ^{26}Al concentrations range from $6.4 \pm 0.3 \times 10^5$ to $1.5 \pm 0.1 \times 10^6$ atoms g^{-1} (Table 2.3; Table 2.4). When plotted on a two-isotope diagram, the ^{10}Be - ^{26}Al results of the five samples bedrock samples overlap with the simple exposure line at 1σ (Fig. 2.7a). The corresponding apparent exposure ages for ^{10}Be and ^{26}Al range between 6.1 ± 0.3 ka and 14.7 ± 0.4 ka (Fig. 2.2; Table 2.3; Table 2.4). Because ^{10}Be and ^{26}Al apparent exposure ages for the same samples overlap within 1σ , we focus on the ^{10}Be values in the remainder of the paper. The two samples collected on the recently emerged bedrock knob at ~1240 m a.s.l. (Riuko-16-003 and Riuko-16-004) have ^{10}Be apparent exposure ages of 6.1 ± 0.3 and 6.4 ± 0.4 ka, respectively (Table 2.3). The oldest apparent ^{10}Be exposure ages of 12.0 ± 0.3 and 14.7 ± 0.4 ka, respectively, occur at the highest elevation site, adjacent to the current ice cap margin (~1290 m a.s.l.; Riuko-16-001 and Riuko-16-002). Sample Riuko-16-005, collected near Lake 1063, has an apparent ^{10}Be exposure age of 7.9 ± 0.4 ka (Fig. 2.2).

The measured *in situ* ^{14}C concentrations range from $1.3 \pm 0.1 \times 10^5$ to $2.3 \pm 0.1 \times 10^5$ atoms g^{-1} (Table 2.5). The ^{14}C - ^{10}Be two-isotope diagram shows that only sample Riuko-16-005 plots between the simple exposure and steady state erosion line, indicating continuous exposure (Fig. 2.7b). The corresponding *in situ* ^{14}C apparent exposure age of 7.7 ± 0.4 ka agrees with its ^{10}Be apparent age within 1σ (Fig. 2.2; Table 2.3; Table 2.5). We thus take the weighted mean ^{14}C - ^{10}Be

exposure age of 7.8 ± 0.1 ka (1σ) as the deglacial age for that location. The remaining samples (Riuko-16-001 – Riuko-16-004) plot in the complex exposure field of the ^{14}C - ^{10}Be plot, and apparent exposure ages are not relevant (Fig. 2.7b).

2.4.2 Lacustrine records

The bottom of core PL1-169 from 169 to 116 cm depth is characterized by homogenous glacial silt and clay (Fig. 2.8a). Between 116 and 85 cm depth, glacial input increases with finely laminated sediments of silt and clay. The laminations are interbedded with a section of high organic content between 107 and 94 cm depth that contains diffuse laminations. Between 85 and 9 cm depth, the core contains a high proportion of homogenous organic material (gyttja). The uppermost 9 cm of PL1-169 consists of finely laminated silts and clays.

Surface core PL3-23 spans the uppermost 23 cm of the stratigraphy in Pajep Luoktejaure. This is important because due to the loose character the uppermost sediment at least 5 cm was lost during core extraction. The bottom of the core has a mix of silt/clay and organic material. Well-preserved laminations are observed between 13 and 3 cm while the top of the core contains loose organic material (Fig. 2.8b).

Results from grain size distribution analyses at 14 levels in cores PL1-169 and PL2-131, show that 90% of the glacial particles at these levels consist of clay and silt. The X-ray imagery and gray scale density analysis reveal that the sediments between 116 cm and 85 cm depth and between 9 and 0 cm depth (PL1-169) are finely (mm's) laminated and have a higher density than the sequence between 85 and 10 cm depth.

The LOI at the bottom of PL1-169 remains a few percent between 169 and 116 cm (Fig. 4a). Subsequently, the LOI slowly increases at 104 cm to a maximum of 15.9% at 95 cm. The LOI sharply decreases at 93 cm to a low of 7.2%, then increases to 17% at 85 cm. The LOI remains high until it sharply decreases at 8 cm and varies between c. 5% and 8 % until the top.

The LOI results from PL3-23 show a decrease in organic content towards the surface followed by a sharp increase in the uppermost 3 cm (Fig. 4b). From the bottom of the core to 10 cm depth, LOI progressively decreases in a pattern similar to that seen in the top 8 cm of core PL1-169 (cf. Fig. 2.8a, b). Between 10 and 3 cm sediment depth LOI is at a minimum, <5%, and sharply increases to surface values of 17% in the uppermost 3 cm (Fig. 2.8b).

Three radiocarbon dates were obtained from PL1-169, with the oldest (116 cm depth; 11.0 ± 0.1 cal ka) and youngest (9 cm depth; 1.8 ± 0.1 cal ka) ages derived from bulk sediment and the intermediate age (90 cm depth; 4.5 ± 0.1 cal ka) derived from a terrestrial plant macrofossil (Fig. 2.8; Table 2.7). To present PL1-169 LOI variations in a temporal framework (Fig. 2.8c), we make use of a terrestrial plant macrofossil-based age from the bottom of lacustrine sediment record in nearby Vuolep Allakasjaure (Fig. 1a; 9.8 ± 0.2 cal ka; Rosqvist et al., 2004) as a substitute for our bulk-sediment age at 116 cm depth, and the two youngest radiocarbon tie points (at 90 and 9 cm depth) to create an age-depth model (Fig. 2.3). When core PL3-23 LOI record is spliced into the core PL1-169 LOI record (representing the top 11 cm of the joint record; Fig. 2.8d), the average sedimentation rate of the laminated sections (9 – 0 cm, 116 – 85 cm) is ca. $0.05 \text{ mm year}^{-1}$ and the sedimentation rate of the organic rich section (85 – 10 cm) is ca. 0.3 mm year^{-1} .

2.4.3 Ice thickness reconstructions and volume

Ice thickness reconstructions for the past century are shown in Fig. 2.9. At the end of the LIA (CE 1910), Riukojietna covered an area of 6.7 km^2 and had a volume of 0.36 km^3 (Table 2.1). Since 1910, both ice extent and volume have decreased by $>58\%$ and $>64\%$, respectively (Table 2.1; Fig. 2.9). The change in volume between 1960 (0.26 km^3) and 2015 (0.13 km^3) corresponds to an average reduction of $0.0024 \text{ km}^3 \text{ year}^{-1}$. Based on these reconstructions, we estimate that the ice thickness above our three cosmogenic sample locations was $<35 \text{ m}$ during the last century prior to exposure (Table 2.8). Our reconstructed ice thickness at the summit of Riukojietna during the LIA is 94 m , in agreement with the LIA summit thickness of c. 93 m estimated by Pohjola et al. (2005).

2.5 Discussion

2.5.1 Constraints on Holocene history of Riukojietna from cosmogenic nuclides

The cosmogenic nuclide results directly constrain the size of Riukojietna. As noted in section 4.1, the agreement between ^{10}Be - ^{14}C exposure ages at 1 sigma for sample Riuko-16-005 (1064 m a.s.l.) indicates continuous exposure at that site since deglaciation, strengthening the interpretation that the ice likely never expanded past Lake 1063 after $\sim 8 \text{ ka}$ (Fig. 2.2). This

agreement also indicates that the Fennoscandian Ice Sheet eroded sufficient bedrock at that site to reset the cosmogenic nuclide signal produced prior to the LGM.

While the ^{10}Be - ^{26}Al two-isotope plot of the two samples on the bedrock knob (Riuko-16-003 and Riuko-16-004; ~1240 m a.s.l.) is consistent with continuous exposure (Fig. 2.7a) the samples plot significantly below the continuous exposure field in the ^{10}Be - ^{14}C two-isotope plot (Fig. 2.7b), indicating a complex exposure history. If one assumes no inherited component prior to post LGM-exposure, their position on this plot is consistent with a cumulative burial duration of 4 – 5 kyr. However, it is important to note their position is also consistent with a small, inherited ^{10}Be component that displaces the point to the right of the simple exposure curve.

The ^{10}Be inventories at the highest elevation site (Riuko-16-001 and Riuko-16-002; ~1290 m a.s.l.) suggest additional contributions from pre-LGM exposure, since the ^{10}Be apparent ages (11-15 ka) exceed the regional deglaciation age of ~9.9 ka by several ky (Stroeven et al., 2016; Fig. 2.2, Table 2.3). Like the bedrock knob samples, these samples also plot in the complex exposure field of the ^{10}Be - ^{14}C two-isotope plot (Fig. 2.7b), consistent with ca. 4-5 kyr of burial in the simplest interpretation. However, the strong evidence of an inherited component in these samples suggests again that their position on this plot is due largely to the inherited ^{10}Be signal.

2.5.2 Constraints on Holocene history of Riukojietna from lacustrine sediments

Although Karlén (1981) presents data from cores collected from Pajep Luoktejaure and Lake 1009, that study lacks enough detail to allow a straightforward comparison with our data. Therefore, we focus here solely on the Pajep Luoktejaure cores we collected.

The linkage between Pajep Luoktejaure stratigraphy and Riukojietna glacial activity is somewhat complicated for two reasons. The first is that the age-depth model (Section 2.4.2; Fig. 2.3) exhibits significant uncertainties, on the order of up to a few ky, particularly in the deeper portions of the core. Thus, although we make glacial activity interpretations based on median ages derived from this model, one should consider these as estimates. The second complexity is topographic, because in the dominant northeastern outlet glacier drainage from Riukojietna, Lakes 1063 and 1009 act as sediment traps upstream of Pajep Luoktejaure (Fig. 2.2). It is evident from the darkening of lake colors in Fig. 2.2 that even in its retreated position today the ice cap is contributing glacial sediments to the series of three proglacial lakes and the amount of sediment reaching each lake progressively decreases downstream. The buffering effect of this drainage

system might thus be expected to dampen, and perhaps even delay, sedimentary responses to changing glacial conditions upstream of Pajep Luoktejaure. Fortunately, the southeastern tongue of our LIA reconstruction of Riukojietna lies within a glacially molded hanging valley that currently is drained by small streams entering both Lake 1009 and Pajep Luoktejaure. However, there are significant streamlined glaciofluvial landforms downstream of and aligned with this valley that indicate likely dominant past drainage directly into Pajep Luoktejaure (Fig. 2.2). Therefore, in the discussion below we infer that the Pajep Luoktejaure sedimentary record directly reflects glacial input from that tongue during extended ice cap configurations, while recessional configurations favor sediments perhaps more equably contributed from both drainages.

The basal section of Pajep Luoktejaure (169-116 cm depth; Fig. 2.8) consists of non-laminated clay/silt and likely represents the subglacial sediments that survived beneath (and were compacted by) the FIS. Laminated sediments began accumulating at 116 cm depth and indicate a seasonal input of meltwater from the Riukojietna ice cap after the northern FIS margin had separated from Riukojietna by ~9.9-9.8 ka (Fig. 2.1; Stroeven et al., 2016). The section is 31 cm thick (116-85 cm depth) but contains a 13 cm-thick interval with relatively higher organic content and more diffuse laminations (~108-95 cm; Fig. 2.8a). However, it is important to note that the age model does not allow us to determine the sedimentation rate for this organic rich segment and have instead assumed the same sedimentation rate throughout the lamination section. The interval may indicate ice cap retreat or a thin/small ice cap between 7.5 and 6.5 cal ka, however the age-depth model limits our ability to interpret exact numbers (Fig. 2.8d). By analogy to the LIA ice cap configuration (Fig. 2.5), we assume that when the ice cap was larger at ~8 ka, the southeastern tongue also contributed sediment-laden meltwater directly to Pajep Luoktejaure, creating the observed laminations. LOI values gradually increase from a few percent at 116 cm to a maximum of ~15% at 95 cm depth. The slow increase of LOI likely represents increased organic productivity in the lake due to a decrease in glacial sediment and likely also increasing inputs of organic material from vegetation development in the catchment following Riukojietna ice cap retreat.

Laminations become more pronounced again between 95 and 85 cm depth (~5.5 – 4.5 cal ka), indicating increasing glacial input until ca. 4.5 cal ka B.P. (Fig. 2.8d). These laminations suggest that Riukojietna survived throughout the HTM, despite the warming climate (Seppä et al., 2005; Nesje et al., 2008; Jonsson et al., 2010). Thereafter, the input of glacial material appears

to decrease significantly and laminations disappear, indicating a decrease in glacial activity and the establishment of more suitable conditions for organic productivity in Pajep Luoktejaure.

Finely laminated silts and clays in the top section of PL1-169 and PL3-23 indicate an expansion of Riukojietna during late Holocene cooling, starting ca. 1.8 ± 0.1 cal ka. We interpret the subsequent increase of organic content in the uppermost 3 cm of the sediment sequence in core PL3-23 as likely resulting from ice cap retreat from its LIA extent. In summary, within the caveats of the age-depth model, we interpret the lake record as suggesting increased glacial activity between 9.8 and 8 cal ka, 5.5 and 4.5 cal ka, and from 1.8 cal ka until ca. 1910.

2.5.3 Reconciling the measured cosmogenic nuclide data with the lake core record

A key goal of this study was to utilize the downstream lake sediment record to inform the ice cap history inferred from *in situ* cosmogenic nuclides. The cosmogenic nuclide signals directly reflect the presence or lack of ice and/or glacial erosion, while the lake sediments represent only an indirect proxy of the ice cap state. As such, it's important to consider the influences on lake sedimentation in this environment. One influence on the sedimentation rate in proglacial lakes is the rate of subglacial erosion, which in turn is affected by temperature at the ice-bed interface and overburden pressure. Riukojietna is a polythermal glacier (Pohjola et al., 2005), such that parts of the ice cap are wet-based (erosive) while other parts are frozen to the bed (non-erosive). Spatial variation in subglacial erosion likely reflects this distribution beneath the ice cap, which can also shift over time due to changes in ice thickness and configuration. While a more intense erosion regime under a much thicker former FIS would be expected generally to reset near-surface cosmogenic nuclide inventories, the observed nuclide inheritance at our highest site (Riuko-16-001 and Riuko-16-002) suggests spatially variable erosion consistent with polythermal conditions. Furthermore, it is conceivable that some fraction of the lake sediments could be derived from loose sediments remobilized from the glacier forefield during ice cap retreat, which would not directly reflect subglacial erosion. We reiterate that although the Riukojietna ice cap is thin at present, glacial sediment is visible in downstream lakes (Fig. 2), indicating that the thin ice can still produce glacial sediments. With these caveats in mind, we attempt to constrain potential exposure and burial scenarios for the cosmogenic nuclide samples using the proglacial lake signal as input to a forward model.

Forward modeling set up

We explore potential effects of temporal variations in ice cap extent and thickness on our bedrock cosmogenic nuclide inventories using a forward model implemented in MATLAB (Appendix C) which is constrained by evidence from our cosmogenic nuclide data (Section 2.5.1) and lacustrine record (Section 2.5.2). The model considers depth-dependent production of ^{10}Be , ^{26}Al , and ^{14}C in bedrock from subaerial exposure, incomplete shielding beneath thin ice, and effects of subglacial erosion, for both spallogenic and muogenic production mechanisms. We evaluate goodness of fit based on whether the modeled cosmogenic nuclide falls within 2σ of the measured cosmogenic nuclide concentrations.

We calculate the total production rate at the sample under prescribed ice thickness histories (P_{tot} , at $\text{g}^{-1} \text{yr}^{-1}$) for each site using the LSDn scaling framework (Lifton et al., 2014) and account for the depth-dependence of spallogenic and muogenic production due to ice thickness and erosional histories for 100-yr time steps over a modeled deglaciation since 20 ka. We account for erosion using a Lagrangian framework, which tracks the production changes in the sample as it moves towards the surface over time, including ice-shielding effects (e.g., Knudsen et al., 2019). In practice this involves back-calculating sample depths within the bedrock according to the subglacial erosion rate, time step, and model duration, beneath time-dependent ice thicknesses, such that the sample ends up at the ground surface at present. If erosion is not specified, only the shielding effects of the ice-thickness history over the ground surface are modeled.

The spallogenic production rate for each nuclide with depth is calculated following the equation:

$$P_{sp_cor,i}(t) = P_{sp,i} * e^{-\left(\frac{\rho_{ice} * z_{ice}(t)}{\Lambda_{sp,ice}} + \frac{\rho_{rock} * z_{rock}(t)}{\Lambda_{sp,rock}}\right)} \quad \text{Eq.1}$$

where $P_{sp,i}$ is the site-specific spallation production rate of nuclide i at the ground surface (at $\text{g}^{-1} \text{yr}^{-1}$), ρ_{ice} is the density of ice (0.92 g cm^{-3}), $z_{ice}(t)$ is the prescribed ice thickness over time (cm), $\Lambda_{sp,ice}$ is the spallation attenuation length for ice (140 g cm^{-2}), $\Lambda_{sp,rock}$ is the spallation attenuation length for rock (150 g cm^{-2}) (Lifton et al., 2014; Marrero et al., 2016; Phillips et al., 2016), ρ_{rock} is rock density (2.65 g cm^{-3}), and $z_{rock}(t)$ is the sample depth within the bedrock over time (cm). We calculate the depth-dependence of muon production for each nuclide over time using Model 1a of Balco (2017). This code accounts for depth-dependent changes in the energy spectrum of the muon flux per the formulation of Heisinger et al. (2002b, 2002a) with resulting effects on nuclide production. We calculate the total production ($P_{tot,i}$) at each depth (time) interval by summing the spallogenic and muogenic production.

The cosmogenic nuclide concentrations of nuclide i are then calculated from 20 ka to present following the equation:

$$N_i = [N_{i,0} * e^{-\lambda_i dt}] + \left[\frac{P_{tot,i}}{\lambda_i} * (1 - e^{-\lambda_i dt}) \right] \quad \text{Eq. 2}$$

where N_i is the concentration of nuclide i (at g^{-1}), $N_{i,0}$ is the concentration of nuclide i (at g^{-1}) produced from the previous time step (0 at 20 ka), λ_i is the decay constant of nuclide i , $P_{tot,i}$ is the total production rate at the sample depth for nuclide i (at $\text{g}^{-1} \text{yr}^{-1}$), and dt is the 100-yr time step.

We estimated uncertainties in the model output by accounting for the production rate uncertainty in each nuclide, as well as an assumed 10% uncertainty in ice thickness estimates, via a simple Monte Carlo method using 1000 iterations. Since the production rate estimates and their uncertainties are means and standard deviations, we draw a production rate randomly for each iteration from a normal distribution characterized by the calibrated mean and standard deviation. For each iteration we also draw randomly from a uniform distribution of the reconstructed ice thickness $\pm 10\%$. We then run the forward model for 1000 iterations and store the predicted modern nuclide concentrations from each iteration. Finally, we calculated the mean and standard deviation of the predicted modern values for each nuclide and plot the results $\pm 2\sigma$.

In situ ^{14}C exhibits a higher proportion of total production by muons than either ^{10}Be or ^{26}Al , with ca. 20% of total production of *in situ* ^{14}C at the ground surface (Sea level high latitude; SLHL) from muons, compared to $\sim 2\%$ surface production by muons for both ^{10}Be and ^{26}Al (Lupker et al., 2015; Balco, 2017). To evaluate shielding of muon production at our sample sites, we considered the detection limits of each nuclide as 2 standard deviations of their respective procedural blank uncertainties. Therefore, the detection limit for ^{10}Be and ^{14}C are 5.61×10^4 atoms and 6.20×10^4 atoms, respectively (Table 2.9; Table 2.10). Ice needs to be < 10 m for *in situ* ^{14}C to rise above our detection limit over periods greater than 10 kyr (Table 2.10). Although at present Riukojietna is thin (30-100 m; Holmlund et al., 1996), the ice cap thickness can shield subglacial bedrock from cosmogenic nuclide production according to our calculated detection limit.

Effects of subglacial erosion are incorporated via an optional erosion rate of 0.01 cm yr^{-1} typical of thin temperate plateau glaciers on crystalline bedrock (Hallet et al., 1996), tied to a specified minimum ice thickness threshold for erosion to occur. However, constraints are lacking on the ice thickness required to reach pressure-melting conditions in this setting. We evaluated minimum erosional thresholds of 10, 20, and 30 m with respect to the resulting cosmogenic nuclide concentrations and found little difference in predicted concentrations when the threshold is

between 10 and 30 m with our modeled scenarios. Since we take our maximum ice thickness during the Holocene as 33 m, based on the LIA thickness reconstruction, we set the minimum erosional threshold at 30 m.

We implement deglacial ice reconstructions from three different ice sheet models between 20 and 10 ka: the University of Maine Ice Sheet Model (UMISM) (Fastook and Chapman, 1989; Fastook and Prentice, 1994; Fastook, 1994), the Patton model (Patton et al., 2016, 2017), and the ANU model (Lambeck and Purcell, 2001; Lambeck et al., 2014)(Fig. 2.10). The UMISM output agrees with other thermodynamic ice sheet models of the FIS (Huybrechts et al., 1996; Payne et al., 2000). The estimated ice thickness at 20 ka is 901 m and declines to 0 m by 10.3 ka. However, Stroeven et al. (2016) estimate the local deglaciation of the FIS to be ~9.9 ka (Fig. 2.1), consistent with the basal age of 9.8 ± 0.2 cal ka for Pajep Luoktejaure (Rosqvist et al., 2004). Therefore, we assume the ice cap extended over Lake 1063 until 8 ka as evidenced by the ^{10}Be - ^{14}C mean exposure age from sample Riuko-16-005 (7.8 ± 0.1 ka) and assume our sample sites were covered with LIA maximum thickness estimates from 9.8 ka to 7.8 ka. During the Holocene, we assume a maximum ice thickness (33 m) corresponding to the reconstructed ice thickness over our samples during the LIA (the coldest period in this time interval; Table 2.8).

Forward modeling of allowable Holocene ice cap histories at Riukojietna

We compared two end-member scenarios for bedrock exposure in the forward model. We first assumed a scenario using evidence of past and observed Riukojietna extents – the LIA moraine and 1910 extent, and the continuously exposed sample Riuko-16-005. We assume that the bedrock samples closest to the ice cap (Riuko-16-001 through Riuko-16-004) experienced rapid exposure after 7.8 ± 0.1 ka (i.e., within 100 years), following the pattern of glacier retreat from the LIA (1910) limit slightly beyond sample site Riuko-16-005 through 2011, with LIA readvance at ca. 1.8 cal ka per the lake record, and retreat since 1910 per our reconstruction (Section 2.3.3.) (Table 2.8). We refer to this model as the Exposure (EXP) model. Next, we tested the simplest scenario that is consistent with both the full lake record and cosmogenic nuclide records. We use the presence or absence of laminated sediments from the Pajep Luokejaure composite core record to infer when the ice cap was active vs. inactive, respectively (Section 2.5.2) and assume the same LIA readvance ca. 1.8 cal ka and post-1910 retreat as the EXP model. We refer to this model as the Holocene Thermal Maximum (HTM) model. We then compare ^{14}C and

^{10}Be inventories in our bedrock samples to those calculated assuming the EXP and HTM models with a thin (33 m) ice cover over the sampled sites (Fig. 2.11). For these initial scenarios, we assume no subglacial erosion, and no inherited components.

The *in situ* ^{14}C EXP model predictions for Riuko-16-001 and Riuko-16-002 are consistent with the measured concentrations, suggesting full exposure between 8 and 1.8 ka followed by thin ice cover (~33 m) until retreat after the LIA (EXP Model; Fig. 2.11a). However, the predicted ^{10}Be concentrations for samples Riuko-001 and Riuko-002 in the EXP model are well below the measured concentrations, implying 50-60% of the measured ^{10}Be concentration is inherited (Fig. 2.11b), consistent with the inference from the disagreement between the apparent ages and the Stroeven et al. (2016) deglacial age. The *in situ* ^{14}C EXP prediction for Riuko-16-003 and Riuko-16-004 slightly overestimates the measured *in situ* ^{14}C inventories, but still agrees within uncertainty with the measurements (EXP Model; Fig. 2.11d). The ^{10}Be prediction under the EXP scenario for Riuko-16-003 and Riuko-16-004 also agrees with the measured ^{10}Be concentrations, suggesting no significant inheritance at that site (Fig. 2.11e). The agreement between all modeled nuclides (^{14}C , ^{10}Be , ^{26}Al ; Figs. 2.11) suggests this scenario is plausible.

The *in situ* ^{14}C HTM model predictions for Riuko-16-001 and Riuko-16-002 fall significantly below the measured values (Fig. 2.11a) but overlap within uncertainty with the measured *in situ* ^{14}C inventories for Riuko-16-003 and Riuko-16-004 (HTM Model; Fig. 2.11d). However, the disagreement between model predictions and measured ^{14}C concentrations for the two sets of samples under the same exposure history indicates the HTM scenario is not plausible. Since the ice cap is small and the two sets of samples are not widely separated, thus one would not expect widely different exposure histories to affect the two sites – a conclusion supported by our post-LIA ice thickness reconstructions (Fig. 2.9; Table 2.8). Furthermore, the predicted ^{10}Be concentrations for samples Riuko-16-001 through Riuko-16-004 using the HTM model all fall significantly below the measured concentrations, again indicating that the HTM model does not adequately explain those results (HTM Model; Fig. 2.11).

Between the two simple scenarios, the EXP better fits the *in situ* ^{14}C for samples Riuko 16-001 and Riuko 16-002 while it is difficult to distinguish between the two model scenarios for Riuko 16-003 and Riuko 16-004. Although our two bedrock sites have different geomorphic settings, both sites have recently emerged beneath the ice cap indicating the ice cap responds rapidly to changing conditions. It stands to reason that both sites would have had similar retreat

histories. Therefore, it follows that the sites experienced similar exposure history, albeit with slightly different ice shielding, as shown by our ice cap reconstructions (Fig. 2.9; Table 2.8). Because the EXP model has a better fit to the *in situ* ^{14}C from samples Riuko 16-001 and Riuko 16-002 and samples Riuko 16-003 and Riuko 16-004 overlap within uncertainty of the *in situ* ^{14}C , the simplest scenario is to prefer the EXP model over the HTM model.

Including effects of subglacial erosion in the modeling only lowers predicted concentrations in all cases, worsening fits to the measurements in nearly all cases for all nuclides (Fig. 2.12). The only samples for which erosion might be plausible are Riuko-16-003 and Riuko-16-004 for *in situ* ^{14}C (Fig. 2.12d), but the ^{10}Be predictions exhibit worse agreement with measurements (Fig. 2.12e). Erosion at this site might be more likely given its location within the Riukojietna main outlet glacier, but that would require ~30% of the measured ^{10}Be concentration to be inherited from a prior exposure period. Erosion would shift the plotted sample in the ^{10}Be - ^{14}C two-isotope plot (Fig. 2.7b) from the right to the left, following the burial line toward the origin.

All things considered, the EXP scenario with no erosion yields the best agreement with all the cosmogenic nuclide measurements, contrary to HTM predictions from the Pajep Luoktejaure core record. However, in the above scenarios, we deduce the ice history from a combination of the cosmogenic nuclide results, reasoning based on observed geomorphology and plausible ice cap behavior, and the presence of laminated sediments at specific times based on our age-depth model median estimates. Our interpretation is guided most strongly by the first two of these lines of evidence, directly reflecting conditions at the ice cap. However, as noted in section 2.4.3, the lake age-depth model is only based on three radiocarbon tie points, leading to large uncertainties (on the order of 2-4 ky maximum-minimum), especially deeper within the lake core due to the low accumulation rate (Fig. 2.3). These large uncertainties lower confidence in the age of the transition between the 116-107 cm laminated section and overlying higher organic content sediments, potentially allowing for alternate interpretations of when the ice cap covered our sites. On the other hand, the macrofossil age of 4.5 ± 0.1 cal. ka firmly dates laminations at the HTM, indicating the presence of the ice cap. It is important to note that we are modeling exposure history at our sample sites – measured concentrations are most consistent with continuous exposure between ca. 8 and 1.8 ka. However, exposure of our sites during the HTM does not negate the possibility that the ice cap could have been present in a similar configuration to modern or smaller. For instance, our sites were exposed in 2011 but the ice cap is still present and contributing sediment downstream through

Lakes 1063 and 1009, and into Pajep Luokejaure. Therefore, considering all the evidence we suggest Riukojietna survived the HTM but was likely as small or smaller than today.

2.5.4 Paleoclimate constraints

From our cosmogenic nuclides results and lake record we infer that Riukojietna covered the uppermost lake until c. 8 ka after which it retreated. The Pajep Luoktejaure sediment record reveals that the ice cap reached an advanced position again at c. 4.5 ka. The nearby glacier record from Vuolep Allakasjaure also shows evidence for an increase in glacier activity, and the reconstructed oxygen isotopic composition of precipitation from the same site confirm cold summer conditions at that time (Rosqvist et al., 2004). Several glaciers in northern Norway were also reactivated at this time (Bakke et al., 2010; Wittmeier et al., 2015; Jansen et al., 2016). The shift towards cooler climate occurring from c. 5 ka likely reduced ablation season temperature forcing an increase in mass balance (e.g., Marcott et al., 2013; Sjögren, 2021; Wastegård, 2022). After this event Riukojietna retreated and thinned significantly as there is no input of glacier derived sediments in the lake until after c. 2 ka. Other pro-glacial records reveal some glacier activity also during this period (e.g., Snowball and Sandgren, 1996; Rosqvist et al., 2004; Jansen et al., 2016). The difference in response of Riukojietna relative to other cirque/valley glaciers is likely due to its low surface gradient, which makes its areal extent sensitive to small changes in equilibrium line altitude (ELA) (e.g., Anderson et al., 2008).

The ice cap was reactivated again at 1.8 cal. ka as evidenced by the laminations downstream in Pajep Luokejaure. It likely remained active until the end of the LIA, assuming that the uppermost organic rich sediment without laminations represents the recessional phase over the past c. 100 years. The ~2-ka advance was probably triggered by a significant lowering of ablation season temperatures. A pronounced cooling from 2 ka has indeed been recorded in carbonate and diatom oxygen isotope records from several lakes in the area (i.e., Lake Tibetanus, Lake 850, Vuolep Allakasjaure; Fig. 2.1) (Shemesh et al., 2001; Rosqvist et al., 2004, 2007).

2.6 Conclusion

We sampled five bedrock outcrops directly adjacent to the Riukojietna ice cap in northern Sweden for *in situ* ^{14}C , ^{10}Be , and ^{26}Al measurements. Results of these *in situ* cosmogenic nuclide

analyses were then compared to a sediment record from a proglacial lake downstream of the ice cap. We also utilized ice surface reconstructions from 1910, 1960, 1978, and 2015 to track the thickness and extent changes over the last century and used these results in concert with nuclide measurements and lake sediment interpretations in a forward model to constrain possible exposure scenarios at our sample sites. ^{10}Be concentrations from our highest elevation site (1290 m a.s.l.) include a signal inherited from pre-LGM exposure due to apparent exposure ages that are significantly older than the local deglaciation age (~9.9 ka; Stroeven et al., 2016). The presence of laminations in proglacial lake Pajep Luokejaure suggests the ice cap was active from ca. 9.8-6.5, 5.5-4.5, and 1.8 cal. ka to ca. 1910. The first two lamination intervals suggest that Riukojietna was likely active during the HTM despite increased temperatures. However, our cosmogenic nuclide forward model scenarios are most consistent with continuous exposure at our sampled sites between ca. 8 and 1.8 cal. ka. Although the cosmogenic nuclide measurements indicate that those sites were exposed throughout the HTM, it is conceivable that the ice cap persisted through that time with a modern or smaller configuration, contributing sediments to the proglacial lakes as it does today. To gain a better picture of the ice cap's influence on glacial sediment, future work should focus on sediment cores from Lake 1063 (and perhaps Lake 1009) to provide a more direct record of Riukojietna's past behavior.

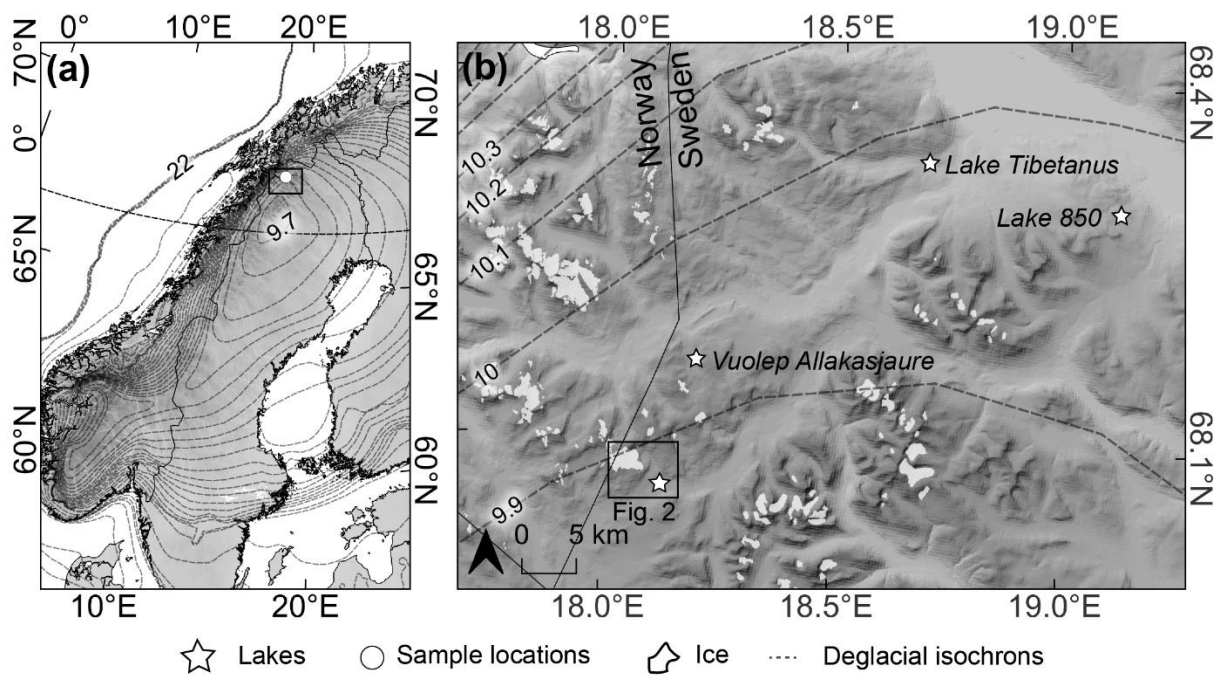


Figure 2.1. **(a)** Map of Scandinavia showing deglacial isochrons of the Fennoscandian Ice Sheet in kyr intervals from 20 to 11, then in 100-year intervals (Stroeven et al., 2016). **(b)** European Union Digital Elevation Model (EU-DEM) of northern Sweden/Norway depicting the location of the Riukojietna ice cap (within the box of Fig. 2). White stars represent lake records. The numbers on the contours are the deglacial isochrons in ka.

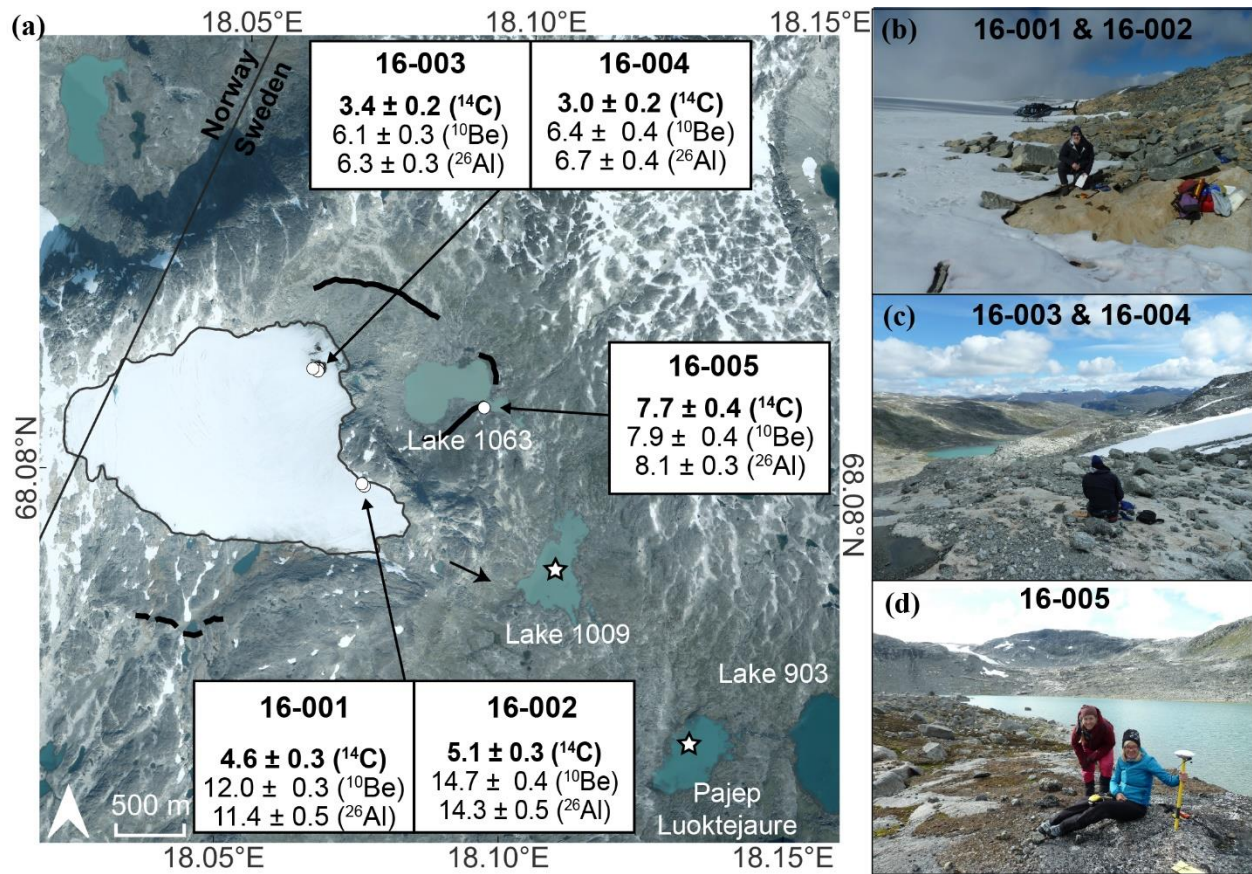


Figure 2.2. **(a)** Satellite image (Google, 2018) of the Riukojietna ice cap depicting the location of bedrock samples (white circles). Apparent exposure ages (in ka) are shown in white boxes. Black lines show the Late Holocene moraines. Black arrow indicates the second ice tongue at the LIA.

White stars depict lakes that have been cored downstream of the ice cap. **(b)** Two bedrock samples collected directly adjacent to the ice cap (1290 m a.s.l.). **(c)** Two bedrock samples collected from a bedrock knoll that was exposed in 2011 (1240 m a.s.l.). **(d)** One bedrock sample collected adjacent to lake 1063 (1064 m a.s.l.).

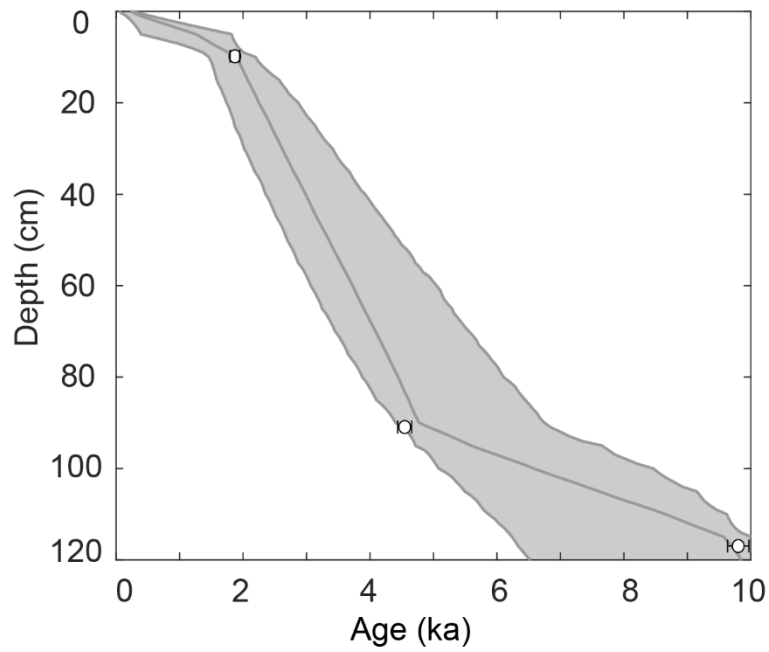


Figure 2.3. The age-depth model output from the Bayesian accumulation (Bacon v2.3.9.1) age-modelling software (Blaauw and Christen, 2011) using three radiocarbon tie points (Table 2.3). The median is shown with the minimum and maximum estimates on either side (95% probability).

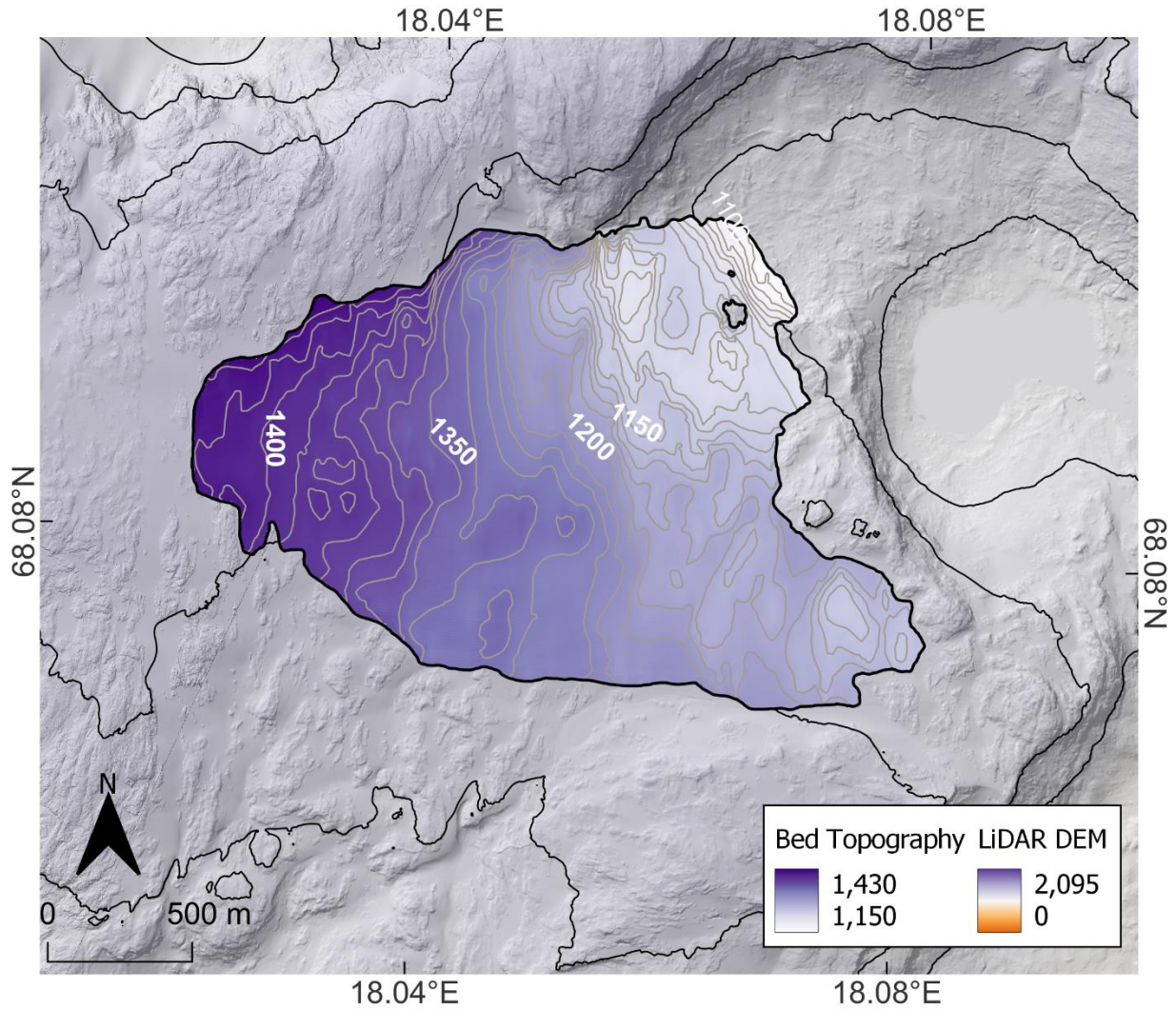


Figure 2.4. Bed topography of the Riukojieta ice cap constructed from interpolated GPR measurements in 2011, 2012, and 2015. Background shows 2 m LiDAR from 2015 provided by Lantmäteriet (<https://www.lantmateriet.se/>).

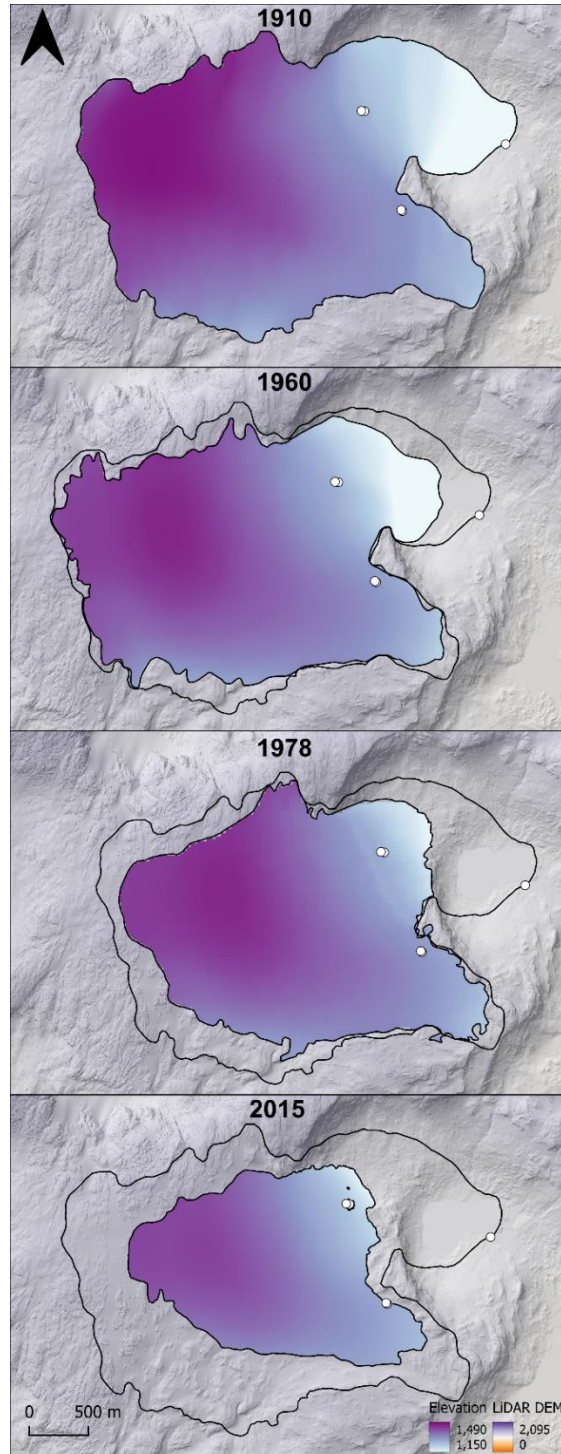


Figure 2.5. Riukojietna ice cap surface topography reconstructions for 1916, 1960, 1978, and 2015 with respect to its maximum extent during the LIA (1910). The 1960 and 1978 elevations from Rosqvist and Østrem (1989) have been adjusted to better match the 2015 LiDAR DEM of the surrounding terrain. Sample sites are shown as white dots.

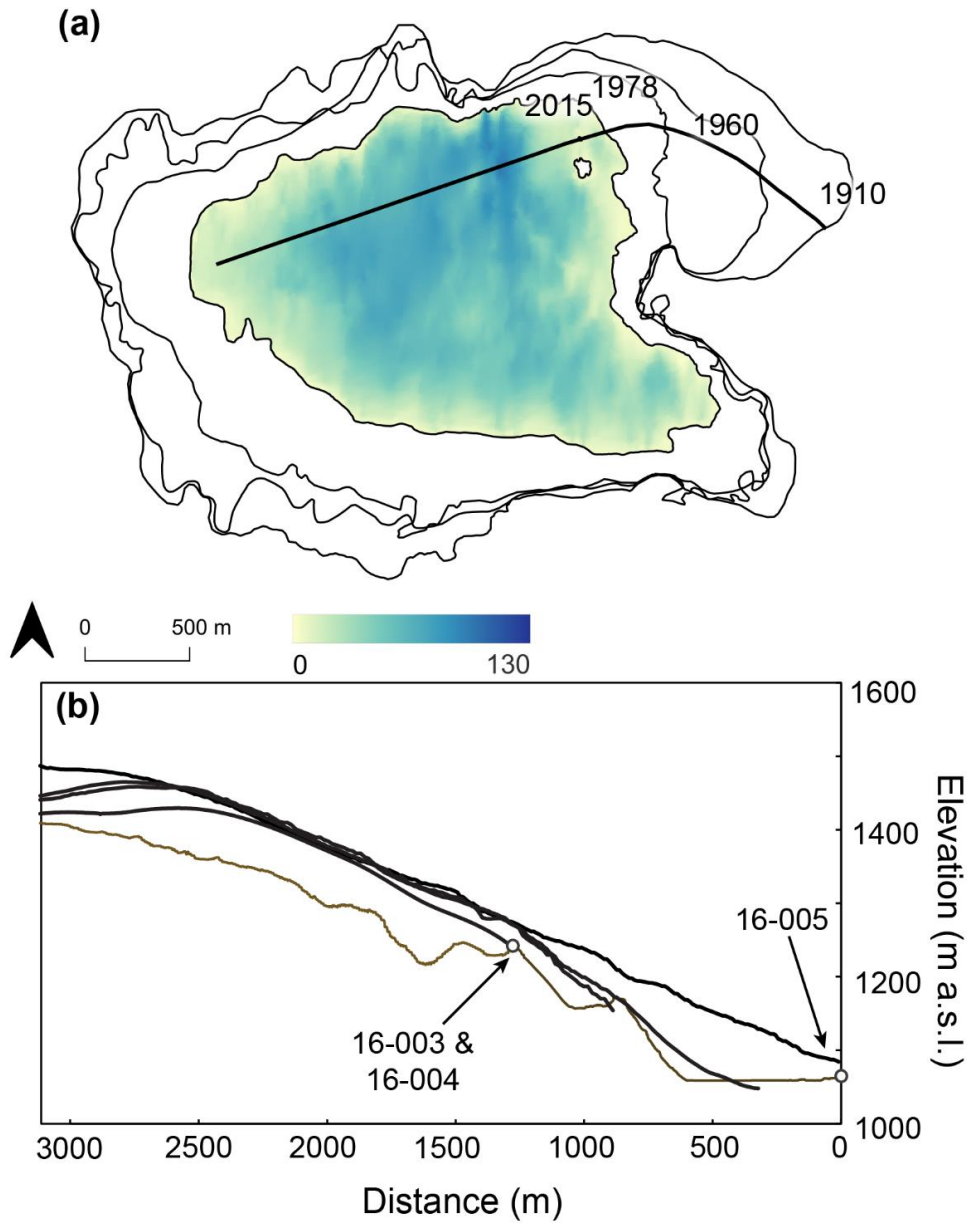


Figure 2.6. **(a)** Ice extents from 1910, 1960, 1978, and 2015 and ice thickness reconstruction for 2015 (see Fig. 2.5). The absence of ice within the outlet glacier tongue (white patch south of the profile line) is the bedrock knob sampled for 16-003 and 16-004. **(b)** Ice profile reconstructions of the flow line in **(a)**.

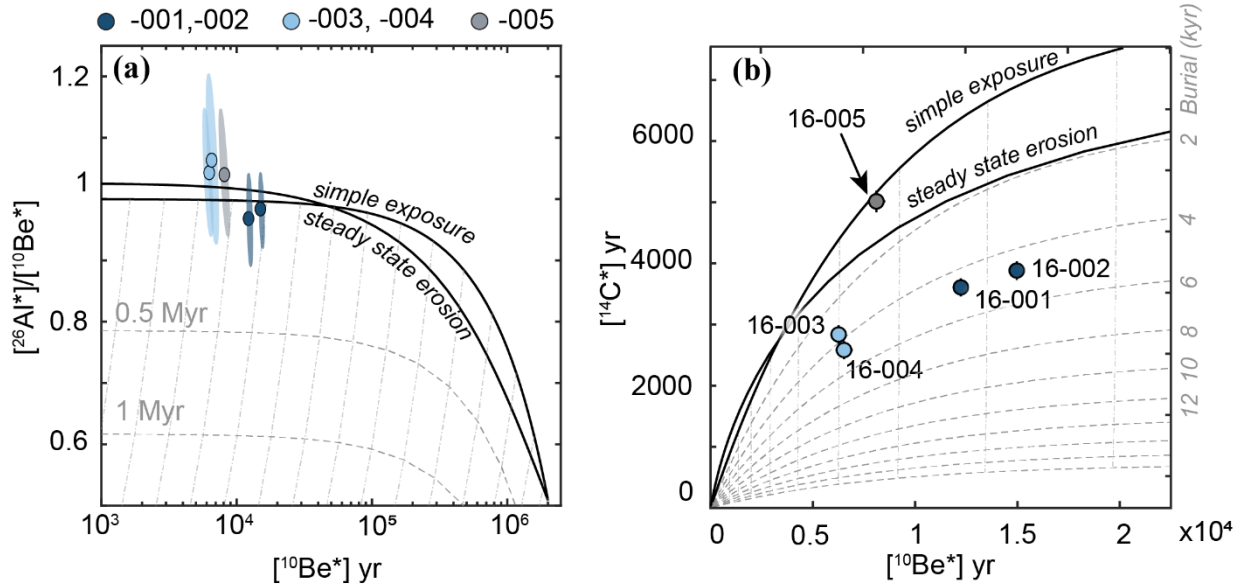


Figure 2.7. **(a)** Two-isotope diagram of normalized $^{26}\text{Al}/^{10}\text{Be}$ concentration ratio vs. normalized ^{10}Be concentration. Ellipses show 2σ uncertainty. **(b)** Two-isotope isochron diagram of normalized *in situ* ^{14}C concentration vs. normalized ^{10}Be concentration. Burial isochrons (dashed lines) are calculated relative to the simple exposure line. Asterisks indicate that concentrations are normalized to site-specific production rates, hence corresponding units are in yr.

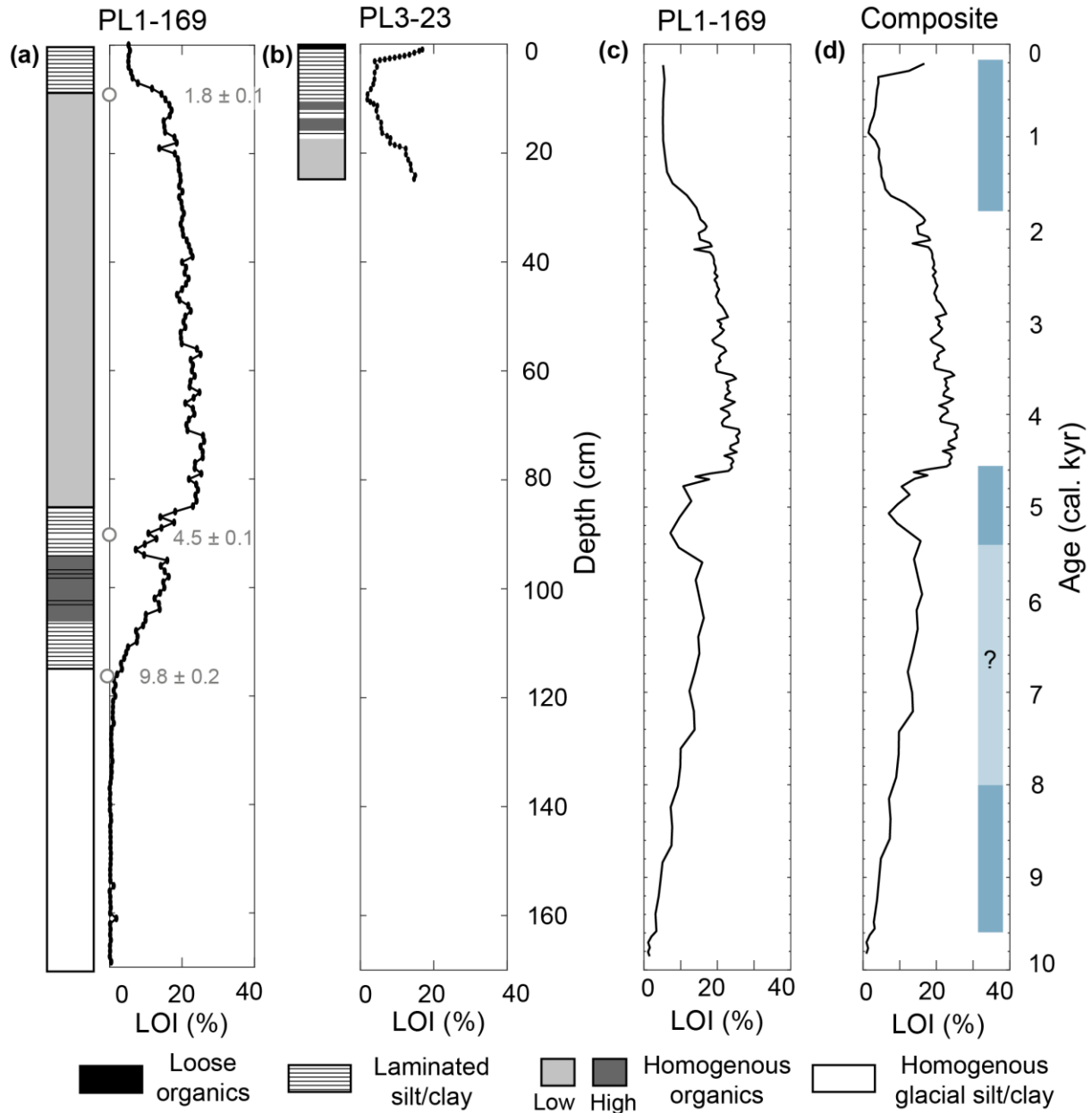


Figure 2.8. Stratigraphy and loss on ignition (LOI) from PL1-169 (a) and PL3-23 (b) in Pajep Luoktejaure (Fig. 2). High LOI indicates high organic content, interpreted as relatively low glacial activity while low LOI indicates low organic content associated with a relatively active glacier. (a) Core PL-169 has 3 radiocarbon tie points (in cal ka.) and the LOI record has been interpolated using the basal lake age from the nearby lake Vuolep Allakasjaure (Fig. 2.1), to an age scale in panel (c). (d) An interpolated composite core where 1 – 13 cm are from PL3-23 and 13 – 130 cm are from PL1-169. Blue areas shown our interpretation of ice cap activity.

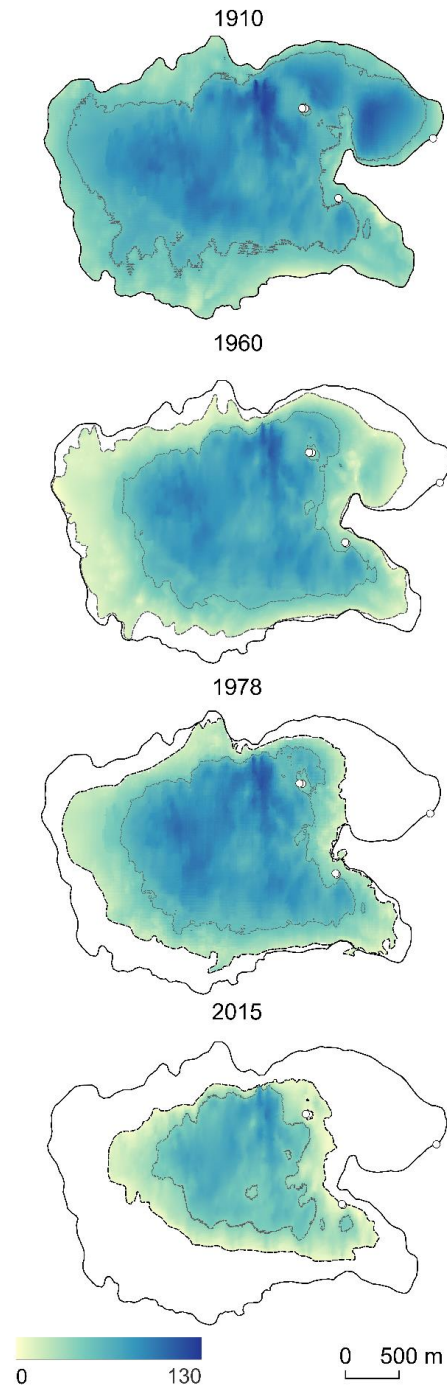


Figure 2.9. Ice thickness reconstructions for Riukojietna from the LIA (1910 CE), 1960, 1978, and 2015 with respect to the maximum extent of the LIA (1910). A contour at 40 m thickness is shown in dashed grey. Sample sites are shown as white dots.

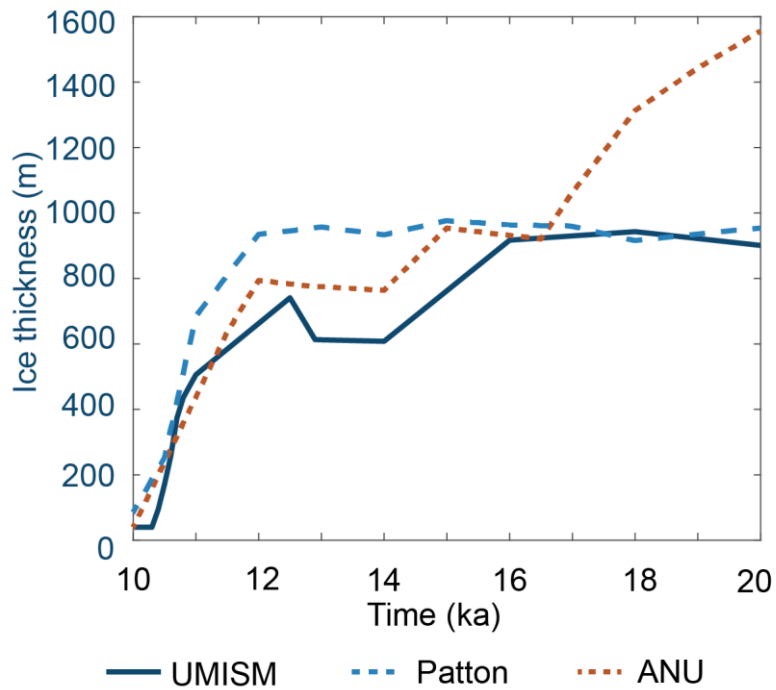


Figure 2.10. Ice sheet model outputs directly over the bedrock sample sites through time (Riuko 16-003). The solid line is the University of Maine Ice Sheet Model (UMISM; Fastook and Chapman, 1989; Fastook, 1994; Fastook and Prentice, 1994; SKB, 2010), the blue dashed line is the Patton model (Patton et al., 2016, 2017), and the orange dotted line is the ANU model (Lambeck and Purcell, 2001; Lambeck et al., 2014).

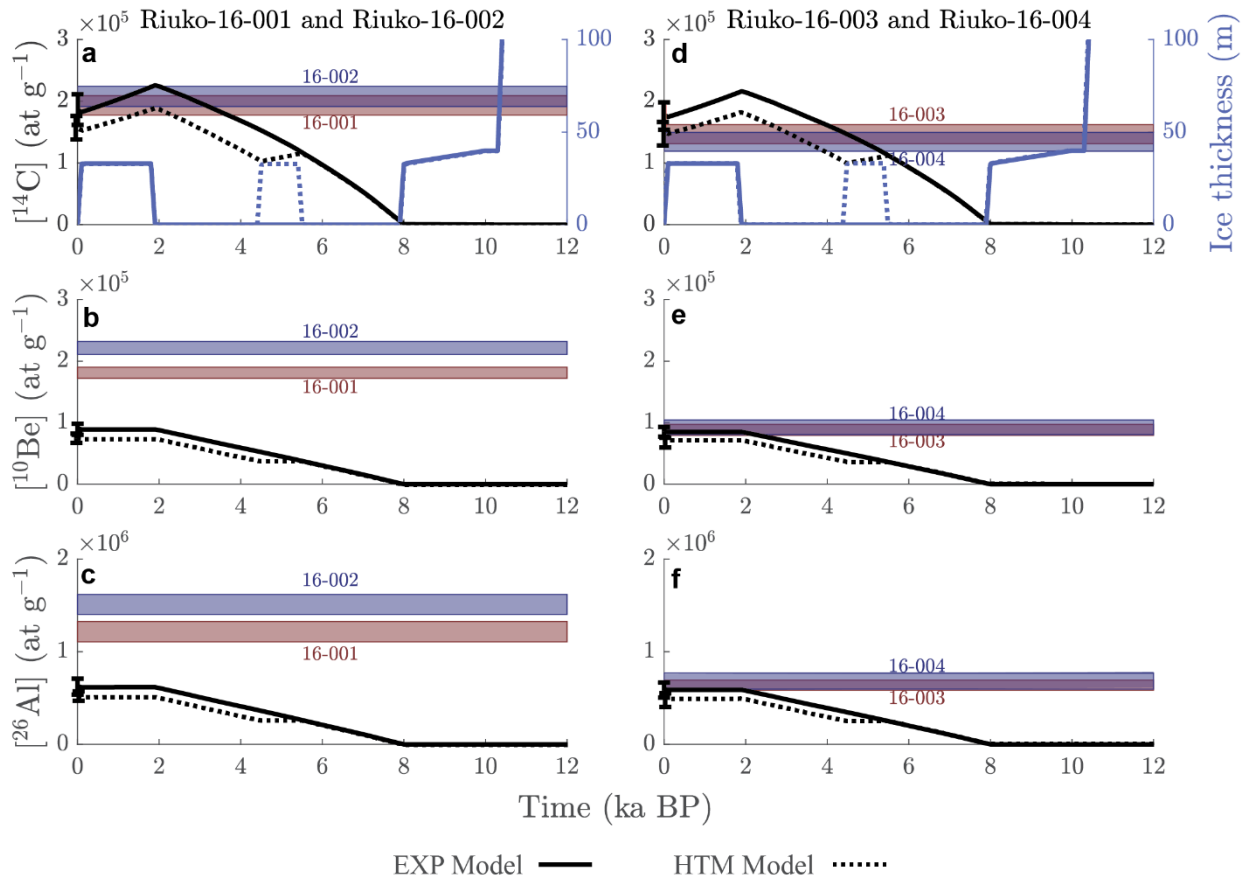


Figure 2.11. Modeled *in situ* ^{14}C , ^{10}Be , and ^{26}Al accumulation (black) as a function of ice thickness (blue) based on the EXP Model (solid lines) and HTM Model (stippled lines) described in text. Panels a – c shows the results for samples Riuko-16-001 and Riuko-16-002 while d – f show results for samples Riuko-16-003 and Riuko-16-004. The bottom panels show the same scenario as the top but with subglacial erosion.

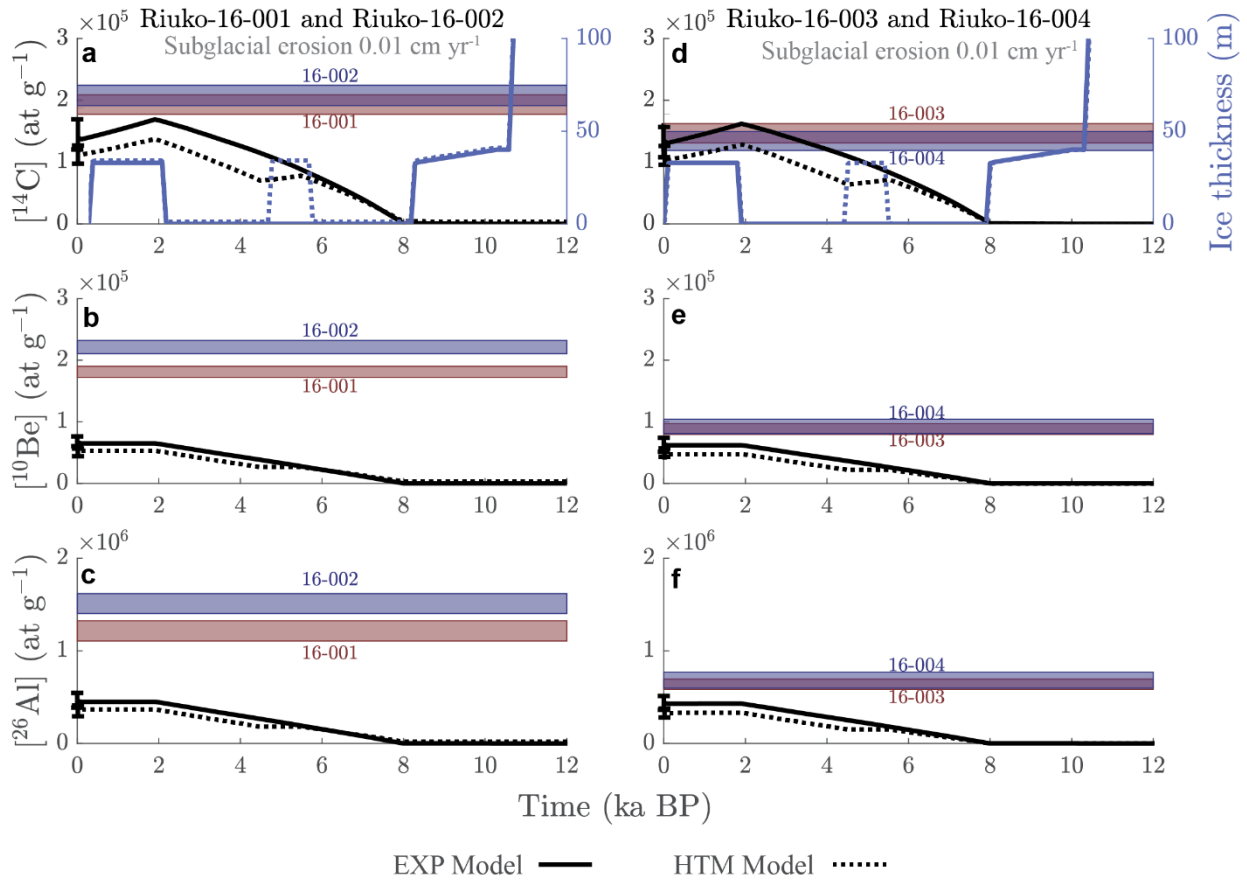


Figure 2.12. Same as in Fig. 2.11 but with subglacial erosion rate assumed to be 0.01 cm yr⁻¹.

Table 2.1. Volume of Riukojietna ice cap from ice surface reconstructions (Rosqvist and Østrem, 1989)

Year	1910	1960	1978	2015
Area (km ²)	6.7	5.5	4.6	2.8
Volume (km ³)	0.36	0.26	0.22	0.13
Min altitude (m a.s.l.)	1058	1058	1122	1146
Max altitude (m a.s.l.)	1488	1468	1459	1429
Elevation span (m)	430	410	337	283
Average thickness (m)	54	47	47	46
Volume change in % (from 1910)		0.28	0.39	0.64

Table 2.2. Sample collection information and the measured cosmogenic nuclide concentrations.

Sample ID	Latitude (°N)	Longitude (°W)	Elevation (m a.s.l.)	Sample thickness (cm)	Density (g cm ⁻³)	Shielding	[¹⁰ Be] ^a (x10 ⁵ at g ⁻¹)	[²⁶ Al] ^b (x10 ⁶ at g ⁻¹)	[¹⁴ C] ^c (x10 ⁵ at g ⁻¹)
16-001	68.08005	18.07339	1291	1.5	2.65	0.99	1.8108 ± 0.0452	1.2158 ± 0.0543	1.9319 ± 0.079
16-002	68.08013	18.07315	1288	1.2	2.65	0.99	2.2137 ± 0.0534	1.5105 ± 0.0538	2.0783 ± 0.083
16-003	68.08749	18.06473	1238	1.5	2.65	0.99	0.8825 ± 0.0442	0.6391 ± 0.0037	1.4664 ± 0.0778
16-004	68.08751	18.06409	1242	1.3	2.65	0.99	0.9250 ± 0.0590	0.6833 ± 0.0043	1.3417 ± 0.0764
16-005	68.08550	18.09376	1064	1.4	2.65	1	0.9918 ± 0.0531	0.7169 ± 0.0287	2.2776 ± 0.0798

^a ¹⁰Be concentrations were corrected with the procedural blank of $0.2911 \pm 0.4195 \times 10^{-15}$ ¹⁰Be atoms.

^b ²⁶Al concentrations were corrected with the procedural blank of $0.6883 \pm 0.9919 \times 10^{-15}$ ²⁶Al atoms.

^c ¹⁴C concentrations were corrected with the mean procedural blank of $1.5119 \pm 0.3133 \times 10^5$ ¹⁴C atoms.

Table 2.3. *In situ* ^{10}Be measurement data from bedrock samples in Sweden.

Sample ID	PLID ^{10}Be ^a	Sample Mass (g)	^9Be Carrier (mg)	Measured $^{10}\text{Be}/^9\text{Be}$ Ratio ($\times 10^{-15}$)	$[^{10}\text{Be}]$ ^b ($\times 10^5$ at g^{-1})	^{10}Be Age (ka)
Riuko 16-001	201800926	30.34	0.264115	311.5750 ± 7.7524	1.8108 ± 0.0452	12.0 ± 0.3
Riuko 16-002	201800927	30.05	0.265266	375.5540 ± 9.0373	2.2137 ± 0.0534	14.7 ± 0.4
Riuko 16-003	201800928	16.99	0.264324	85.1944 ± 4.2297	0.8825 ± 0.0442	6.1 ± 0.3
Riuko 16-004	201800929	14.99	0.263592	79.0089 ± 5.0036	0.9250 ± 0.0590	6.4 ± 0.4
Riuko 16-005	201800930	18.00	0.268927	99.6275 ± 5.3042	0.9918 ± 0.0531	7.9 ± 0.4
COQTZP2-AK	202001610	5.19	0.2642196	722.1939 ± 16.8787	24.5427 ± 0.5740	-
Cblk-4723	202001609	-	0.265161	0.2911 ± 0.4195	-	-

^a PLID = Prime Lab ID^b ^{10}Be concentrations were corrected with $(0.2911 \pm 0.4195) \times 10^{-15}$ Table 2.4. *In situ* ^{26}Al measurement data from bedrock samples in Sweden.

Sample ID	PLID ^{26}Al ^a	Sample Mass (g)	Native Aluminum ^b (mg)	^{27}Al Carrier ^c (mg)	Measured $^{26}\text{Al}/^{27}\text{Al}$ Ratio ($\times 10^{-15}$)	$[^{26}\text{Al}]$ ^d ($\times 10^6$ atoms g^{-1})	^{26}Al Age (ka)	$^{26}\text{Al}/^{10}\text{Be}$
Riuko 16-001	202001612	30.34	0.5430	0.8718	1168.5400 ± 52.7673	1.2158 ± 0.0543	11.4 ± 0.5	6.71
Riuko 16-002	202001613	30.05	1.7350	-	1172.0500 ± 41.7613	1.5105 ± 0.0538	14.3 ± 0.5	6.82
Riuko 16-003	202001614	16.99	0.1800	1.2844	333.8200 ± 14.4347	0.6391 ± 0.0037	6.3 ± 0.3	7.23
Riuko 16-004	202001615	14.99	0.1250	1.2961	323.5660 ± 20.3612	0.6833 ± 0.0043	6.7 ± 0.4	7.38
Riuko 16-005	202001616	18.00	0.2730	1.2836	371.9830 ± 14.8891	0.7169 ± 0.0287	8.1 ± 0.3	7.22
COQTZP2-AK	202001617	5.19	0.0790	1.2623	2814.6299 ± 96.9346	16.2221 ± 0.5588	-	6.61
Cblk-4723	202001618	-	-	1.7006	0.6883 ± 0.9919	-	-	-

^a PLID = Prime Lab ID^b Native aluminum is measured by Inductively-coupled plasma optical emission spectrometry (ICP-OES) at PRIME Lab^c Aluminum carrier is added if native aluminum is < 1.5 mg^d ^{26}Al concentrations were corrected with $(0.6883 \pm 0.9919) \times 10^{-15}$

Table 2.5. *In situ* ^{14}C measurements from bedrock samples in Sweden.

Sample ID	PLID ^a	Sample Mass (g)	C yield (μg)	Diluted C Mass (μg)	$\delta^{13}\text{C}$ ($\text{‰}_{\text{VPDB}}^{\text{b}}$)	$^{14}\text{C}/^{13}\text{C}$ ($\times 10^{-12}$)	$^{14}\text{C}/\text{total}^{\text{c}}$ ($\times 10^{-14}$)	^{14}C ($\times 10^5$ atoms)
Riuko 16-001	201800926	5.0838	19.2 ± 0.3	280.3 ± 3.4	-42.96 ± 0.2	7.1909 ± 0.1295	7.4133 ± 0.1367	9.8213 ± 0.4010
Riuko 16-002	201800927	5.0259	14.4 ± 0.2	285.6 ± 3.5	-43.48 ± 0.2	7.5576 ± 0.1423	7.7960 ± 0.1501	10.4450 ± 0.4148
Riuko 16-003	201800928	4.6797	4.9 ± 0.1	296.4 ± 3.6	-44.18 ± 0.2	5.3491 ± 0.9611	5.4634 ± 0.1014	6.8623 ± 0.3641
Riuko 16-004	201800929	4.8272	4.9 ± 0.1	294.4 ± 3.6	-44.24 ± 0.2	5.1368 ± 0.1052	5.2392 ± 0.1110	6.4766 ± 0.3691
Riuko 16-005	201800930	5.0366	6.7 ± 0.1	295.5 ± 3.6	-44.38 ± 0.2	8.1367 ± 0.1216	8.3989 ± 0.1282	11.4710 ± 0.4021
Blank Data								
PB1-03232021	202101468	-	4.1 ± 0.1	307.7 ± 3.7	-43.82 ± 0.2	1.2488 ± 0.0737	1.1455 ± 0.0779	1.8138 ± 0.1252
PB1-03252021	202101469	-	4.0 ± 0.1	298.0 ± 3.6	-44.6 ± 0.2	1.2531 ± 0.0644	1.1479 ± 0.0680	1.7716 ± 0.1071
PB1-04032021	202101473	-	5.9 ± 0.1	293.9 ± 3.6	-43.73 ± 0.2	0.9846 ± 0.0052	0.8654 ± 0.0554	1.3157 ± 0.0857
PB1-04062021	202101474	-	3.5 ± 0.1	296.2 ± 3.6	-43.91 ± 0.2	1.1538 ± 0.0484	1.0437 ± 0.0513	1.5920 ± 0.0806
PB1-04152021	202101478	-	2.6 ± 0.1	297.4 ± 3.6	-44.41 ± 0.2	0.7731 ± 0.0054	0.6423 ± 0.0566	0.9825 ± 0.0874
PB1-04292021	202101479	-	4.2 ± 0.1	297.5 ± 3.6	-44.37 ± 0.2	1.1447 ± 0.0466	1.034 ± 0.0493	1.5958 ± 0.0785
Blank mean								1.5119 ± 0.3133

Table 2.5 continued

^{14}C] ^b ($\times 10^5$ atoms g^{-1})	^{14}C Age (ka)
1.9319 ± 0.079	4.6 ± 0.3
2.0783 ± 0.083	5.1 ± 0.3
1.4664 ± 0.0778	3.4 ± 0.2
1.3417 ± 0.0764	3.0 ± 0.2
2.2776 ± 0.0798	7.7 ± 0.4

^a PLID = Prime Lab ID^b Measured relative to Vienna PeeDee Belemnite^c Mean procedural blank of $(1.5119 \pm 0.3133) \times 10^5$ ^{14}C atoms subtracted.

Table 2.6. Input cosmogenic nuclide data from bedrock samples taken adjacent to Riukojietna Ice Cap for the online University of Washington cosmogenic calculator, v.3.

Sample ID	Latitude	Longitude	Elevation	Pressure	Sample thickness	Density	shielding	erosion	date of sample collection
16-001	68.08005	18.073385	1291	std		1.5	2.65	0.999492	0 2016;
16-002	68.08013	18.07315	1288	std		1.2	2.65	0.999492	0 2016;
16-003	68.08749	18.064733	1238	std		1.5	2.65	0.99718	0 2016;
16-004	68.08751	18.064093	1242	std		1.3	2.65	0.99718	0 2016;
16-005	68.0855	18.093758	1064	std		1.4	2.65	1	0 2016;
16-001	Al-26	quartz	1215780	54920	KNSTD;				
16-002	Al-26	quartz	1510494	53820	KNSTD;				
16-003	Al-26	quartz	639046	27810	KNSTD;				
16-004	Al-26	quartz	683377	43120	KNSTD;				
16-005	Al-26	quartz	716987	28780	KNSTD;				
16-001	C-14	quartz	193189	7888	;				
16-002	C-14	quartz	207832	8254	;				
16-003	C-14	quartz	146639	7781	;				
16-004	C-14	quartz	134170	7647	;				
16-005	C-14	quartz	227756	7984	;				
16-001	Be-10	quartz	1810780	4510	07KNSTD;				
16-002	Be-10	quartz	221370	5330	07KNSTD;				
16-003	Be-10	quartz	88250	4410	07KNSTD;				
16-004	Be-10	quartz	92500	5900	07KNSTD;				
16-005	Be-10	quartz	99180	5310	07KNSTD;				

Table 2.7. Radiocarbon dates from core PL1-169, measured in Fall 1998. Calibrated ages derived using CALIB Radiocarbon Calibration v 8.2 (<http://calib.org/calib/>; Stuiver et al., 1993; Reimer et al., 2020).

Sample Name	Depth (cm)	Material	¹⁴C age BP	d¹³C PDB	Calibrated Age (cal yr BP)	± 1 σ	± 2 σ
Ua-14024	9	bulk	1920 ± 70	-27.08	1839	76	150
Ua-14025	90	macrofossil	4024± 85	-27.48	4514	109	221
Ua-14026	116	bulk	9650 ± 160	-26.87	10969	108	449

Table 2.8. Reconstructed ice thicknesses above the 2016 sample sites.

	1910 surface (m)	1960 surface (m)	1978 surface (m)	2015 surface (m)
Riuko 16-001/2	35	25	19	0
Riuko 16-003/4	33	32	30	0

Table 2.9. Calculated concentrations of ^{10}Be from muon production over time. Note that all concentrations calculated are below the ^{10}Be detection limit of 5.61×10^4 .

Ice thickness (m)	P10mu^a (at g ⁻¹)	P10sp^b (at g ⁻¹)	P10tot^c (at g ⁻¹)	10000 (x 10 ² at)	20000 (x 10 ² at)	30000 (x 10 ² at)	40000 (x 10 ² at)	50000 (x 10 ² at)
0	0.1219	15.0560	15.1780	1.2159	4.8514	10.8884	19.3089	30.0952
5	0.0769	0.7013	0.7782	0.7668	3.0595	6.8668	12.1773	18.9797
10	0.0526	0.0327	0.0853	0.5245	2.0928	4.6972	8.3297	12.9828
20	0.0291	7.09×10^{-5}	0.0292	0.2906	1.1593	2.6020	4.6143	7.1918
33	0.0170	2.44×10^{-8}	0.0170	0.1699	0.6781	1.5218	2.6987	4.2063
50	0.0105	7.23×10^{-13}	0.0105	0.1050	0.4189	0.9402	1.6672	2.5986
100	0.0046	3.48×10^{-26}	0.0046	0.0454	0.1812	0.4066	0.7211	1.1239

^a Site specific total muon production calculated using model 1A from Balco (2017).

^b Site specific total spallation production.

^c Total site specific total production is the muon and spallation production added together.

Table 2.10. Calculated concentrations of *in situ* ^{14}C from muon production over time. Note that concentrations are above the ^{14}C detection limit of 6.20×10^4 at ice thickness <10 m.

Ice thickness (m)	P14mu^a (at g ⁻¹)	P14sp^b (at g ⁻¹)	P14tot^c (at g ⁻¹)	10000 (x 10 ⁴ at)	20000 (x 10 ⁴ at)	30000 (x 10 ⁴ at)
0	5.4529	54.8030	60.2560	15.7751	20.4509	21.8368
5	3.2763	2.5525	5.8288	9.4783	12.2876	13.1203
10	2.1140	0.1189	2.2329	6.1158	7.9285	8.4658
20	1.0156	2.58×10^{-4}	1.0158	2.9381	3.8090	4.0671
33	0.4906	8.89×10^{-8}	0.4906	1.4193	1.8400	1.9647
50	0.2443	2.63×10^{-12}	0.2443	0.7068	0.9163	0.9784
100	0.0715	1.27×10^{-25}	0.0715	0.2069	0.2682	0.2864

^a Site specific total muon production calculated using model 1A from Balco (2017).

^b Site specific total spallation production.

^c Total site specific total production is the muon and spallation production added together.

CHAPTER 3. HOLOCENE ICE SURFACE LOWERING IN WESTERN DRONNING MAUD LAND, EAST ANTARCTICA

3.1 Introduction and Background

Modeling how ice sheets respond to climate warming has become vital for the prediction of the future sea-level impact from Antarctica (DeConto et al., 2021; Stokes et al., 2022). The East Antarctic Ice Sheet (EAIS) contains 52.2 m sea level equivalent (SLE) of water (Morlighem et al., 2020). However, it has been assumed to have been stable for ~8.1 million years due to being grounded above sea level (Sugden et al., 1995) and thus is less well studied. Although ice mass loss is dominated by the West Antarctic Ice Sheet (WAIS), the EAIS has also contributed to sea level rise (SLR) since the 1970s, though some sectors have slightly thickened inland (Rignot et al., 2019). A majority of ice loss in Antarctica is through dynamic thinning, whereby marine-terminating ice shelves thin at the base driven by increased ocean temperatures, which reduces their buttressing effect on the interior ice leading to subsequent ice surface lowering (e.g., Gudmundsson et al., 2019). Modeling how ice sheets respond to climate shifts is vital for predicting future sea-level rise from the Antarctic Ice Sheet (AIS) (DeConto et al., 2021; Stokes et al., 2022). Therefore, understanding how the EAIS responded to past climate warming can improve numerical model projections of future changes of the AIS overall. The response of the EAIS during the most recent geological period of climate warming, the Last Glacial Maximum (LGM; ~27–20 ka, Marine Isotope Stage 2 (MIS2)) to present, provides an excellent case to evaluate the importance of rising sea levels, changes in ocean temperatures, and rising atmospheric temperatures for model projections.

Cosmogenic radionuclides such as ^{10}Be ($t_{1/2} = 1.39$ My; Chmeleff et al., 2010; Korschinek et al., 2010) and ^{26}Al ($t_{1/2} = 705$ ky; Nishiizumi, 2004) are rare nuclides produced when near-surface minerals are exposed to incident cosmic radiation (Gosse and Phillips, 2001). The production of cosmogenic nuclides decreases rapidly with depth in bedrock, therefore glacial erosion can remove nuclides from prior exposure periods (Heyman et al., 2011). In general, the concentration of rare cosmogenic nuclides in glacially transported erratics and glacially eroded bedrock is proportional to the deglaciation age at that site. For instance, dating boulders on a moraine can date the lateral retreat of an ice sheet. The thinning history can be reconstructed by exposure dating erratics/bedrock along elevation profiles on nunataks. Exposure dating on

nunataks adjacent to marine-terminating ice streams is a crucial area in reconstructing ice surface lowering associated with ice-ocean interactions. These reconstructions provide a minimum thickness constraint for numerical model inputs, which are essential to refine and enhance ice-sheet dynamics in models. For example, large ensemble models reconstructing the AIS at the LGM show little thickening of the ice sheet over the polar plateau in Dronning Maud Land in East Antarctica (Whitehouse et al., 2012a; Abe-Ouchi et al., 2015), despite geomorphic evidence that the ice sheet was upwards of 1000 m thicker near the coast (Lintinen, 1996; Lintinen and Nenonen, 1997; Swithinbank, 1959). It is important to note that the coarse resolution (>30 km) of these large ensemble models cannot generally capture the influences of individual nunataks.

Although there are several reconstructions of ice surface lowering in Dronning Maud Land (DML) using exposure dating (Altmaier et al., 2010; Yamane et al., 2011; Suganuma et al., 2014; Andersen et al., 2020; Suganuma et al., 2022), the Holocene history is poorly constrained in western DML. Due to widespread cold-based, non-erosive ice in Antarctica, surface rocks may retain a component of long-lived cosmogenic nuclides accumulated during exposure prior to the last glacial cover (so-called inherited nuclides) (Hall, 2009). Although cover by non-erosive ice may not remove long-lived nuclides like ^{10}Be or ^{26}Al from a surface, *in situ* ^{14}C will decay to background levels for intervals longer than ~ 30 ky because of its short half-life (5.7 kyr). Therefore, *in situ* ^{14}C is an excellent chronometer to constrain post-LGM deglacial exposure histories in environments covered by cold-based ice.

In this study, we further refine Holocene thinning rates through use of *in situ* ^{14}C results from nunataks protruding through the EAIS. We collected samples along the Jutulstraumen ice stream in western Dronning Maud Land, with similar data from the Veststraumen ice stream to the west. Samples were located broadly along coast-to-inland transects to attempt to capture spatial trends in thinning. Further, we use *in situ* ^{14}C data to evaluate an ensemble of high-resolution ice-sheet model experiments to test plausible ice thickness distributions at the LGM in our study area. Our data-model comparison allows us to eliminate models that underestimate or overestimate ice thickness at the LGM given different basal sliding and ice rheology assumptions. Setting

3.1.1 Deglacial constraints on the East Antarctic Ice Sheet

The EAIS reached its maximum extent at the end of the LGM ($\sim 27\text{--}20$ ka) (Clark et al., 2009). Ice core records indicate interior domes thinned by 110-120 m in response to climate

cooling (Parrenin et al., 2007; Buizert et al., 2021). On the other hand, offshore records show that ocean-terminating margins advanced to the continental shelf break in most sectors at the LGM, although in some places the grounding line location remains poorly constrained (Anderson et al., 2002; Bentley et al., 2014; Weber et al., 2011; Fig. 3.1). An expansive coastal shelf and a thinner ice sheet implies that extensive sea-ice cover and colder ocean temperatures could have reduced inland precipitation, leading to surface lowering in the interior (Prentice and Matthews, 1991; Suganuma et al., 2014; Yamane et al., 2015).

A more extensive coastal shelf also implies that the coastal ice would be thicker at the LGM. Geomorphic evidence in western DML indicates a thicker-than-present ice sheet either at the LGM or before. In the Jutulstraumen drainage system, glacial erratics on nunataks have been interpreted to indicate ice surface lowering of 800 m (Swithinbank, 1959) while glacial striae have been interpreted to indicate 1000 m of ice surface lowering at Risemedet (~12 m east of the station Troll) (Lunde, 1961). In the Veststraumen drainage system, glacial striae on Vestfjella and Fossilryggen (Jonsson, 1988) combined with fresh lodgement till found on Basen suggests the LGM ice was 700 m thicker than present (Lintinen, 1996). Further, radiocarbon dated mounds from stormy petrel colonies nesting at Skuafjellet nunatak in Vestfjella indicate active nests since 8200 ¹⁴C BP (Lintinen and Nenonen, 1997; uncorrected for reservoir effects) indicating 200 m of ice thinning since the LGM. Although compelling geomorphic evidence indicates a higher LGM surface, without tighter geochronological constraints it is difficult to know the timing and rate of ice surface lowering.

The timing and rate of ice thinning during the last deglaciation can be inferred from exposure dating (largely ¹⁰Be and ²⁶Al) among the EAIS sectors (Fig. 3.1). For instance, some areas show evidence of deglaciation beginning as early as 18 ka (Lambert-Amery glacial system; White et al., 2011) while other sectors show variable thinning during the early to mid-Holocene. In Mac Robertson Land, exposure ages along the Framnes Mountains revealed coastal thinning of at most 350 m since 13 ka (Mackintosh et al., 2007). In Enderby Land, a study of the Rayner Glacier revealed >300 m of ice thinning from 9-6 ka and >10 km of retreat (White and Fink, 2014). In Lützow-Holm Bay, the ice surface lowered up to 400 m between ~9 and 5 ka and retreated inland by 10 km, potentially driven by marine ice sheet instability caused by warmer ocean temperatures from Circumpolar Deep Water (Yamane et al., 2011; Kawamata et al., 2020). Suganuma et al. (2022) finds rapid thinning of ~100 m between 8-5 ka inland from the Jutulstraumen ice stream.

Andersen et al. (2020) concluded that ~35-120 m of thinning occurred along Jutulstraumen during the Holocene. Finally, *in situ* ^{14}C data from the Shackleton Range near the Weddell Sea indicates the ice surface was >310 to 655 m thicker than present during the LGM (Nichols et al., 2019).

3.1.2 Western Dronning Maud Land

The coastal region of Dronning Maud Land (DML) is characterized by a 1,500 km long escarpment of up to 3 km a.s.l.-high coastal mountains, separating the polar plateau from the coastal ice shelf (Fig. 3.1; Fretwell et al., 2013). The escarpment acts as a barrier that simultaneously obstructs ice flow to the coast (Rignot et al., 2011) and blocks moisture from reaching the interior polar ice sheet (van de Berg et al., 2006). Outlet glaciers flow through and around the escarpment and combine into marine-terminating ice shelves.

Our study area is separated into two drainage sectors influenced by two major ice streams. The first area is the Jutulstraumen drainage system (~238,000 km²) where the escarpment is dissected by the NE-SW orientated Jutul-Penck Graben system (Huang and Jokat, 2016) that connects the interior polar plateau to the Lazarev Sea. The Jutulstraumen ice stream drains into the Fimbul Ice Shelf at a maximum velocity of 750 m yr⁻¹ (Rignot and Scheuchl, 2017). The maximum water depth below the Fimbul Ice Shelf is ~900 m (Fretwell et al., 2013). The second focus of this study is the Riiser-Larsen drainage system (~329,000 km²) where outlet glaciers draining the polar plateau converge into the Veststraumen ice stream that drains into the Riiser-Larsen Ice Shelf at a maximum velocity <230 m yr⁻¹ (Rignot and Scheuchl, 2017). The maximum water depth near the Veststraumen grounding line is 800 m and slopes upwards toward the continental margin (Fretwell et al., 2012).

3.2 Methods

3.2.1 Field strategies and sample collection

In this study, we targeted two coast-to-inland transects of nunataks to study the potential variability of ice surface lowering histories between the escarpment and the coast. We reconstructed ice thinning histories by measuring cosmogenic nuclides along elevation transects from nunataks protruding from the ice sheet. Our strategy for field collection assumed that ice thinning after the LGM occurred simultaneously across the ice stream, exposing nunataks on either

side. We targeted nunataks along the ice streams on transects from the coast inland toward the escarpment. Where possible at each nunatak, we collected samples along an elevation profile from high elevations to low elevations near the modern ice surface to measure the cosmogenic nuclide concentrations, assuming that the highest elevation was exposed first.

We targeted quartz-bearing rocks, although it proved difficult to find suitable samples due to prevalent mafic rock types in Jutulstraumen (Groenewald et al., 1995). Glacial erratics resting directly on (striated) bedrock surfaces were prioritized. Sample lithology, thickness, shielding, and surface orientation were recorded. The elevation and GPS position are especially important in Antarctica because accurate altitudes are needed for cosmogenic nuclide exposure ages. We used a handheld GPS paired with a Trimble Net R7 differential GPS (dGPS) base at a lower elevation and an identical rover dGPS unit for sample sites. In addition, the barometric pressure was recorded continuously at the base camp and at each sample site with a base/rover pair of Kestrel 5000 environmental meters to interpolate between the dGPS base and rover stations. We compared our field dGPS measurements to the Reference Elevation Model of Antarctica (REMA, 8 m spatial resolution with vertical errors <2 m, Howat et al., 2022). We use the dGPS- and barometrically constrained elevations to calculate exposure ages but use REMA to find the relative elevations of the ice surface surrounding our samples. Glacial striations were noted in the field when present at each sampled nunatak (Fig. 3.2; Table 3.1; Table 3.2).

Samples were collected along the western side of the Jutulstraumen ice stream (n=14) plus one site on the eastern side (n=4; Table 3.1). Geomorphic descriptions of each Jutulstraumen nunatak were detailed in Andersen et al. (2020); therefore, we only give a brief overview here. We sampled two nunataks on the western side of the Jutulstraumen ice stream closer to the grounding line (Straumsnutane, Gråsteinen) and one nunatak on the eastern side (Sverdrupfjella). Nunataks along the southwestern portion around Jutulstarumen drainage area are influenced by the Penck glacier, and include Viddalskollen, Ystenut, and Huldreslottet. (See Appendix D for more detailed descriptions).

We also sampled nunataks surrounding the Veststraumen ice stream (n =19; Table 3.1). The samples in the Veststraumen region fall into three categories, those that were sampled below and along the top margin of a ca. 500-m-high escarpment, and samples that lie in the transition zone between the two. We only sampled two nunataks near the coast (Basen and Fossilryggen) that are influenced by the smaller nearby Plogbreen ice stream, scattered nunataks at the base of the

escarpment (Vardeklettane, Cottontoppen Junior), samples in the transition zone (Månesigden, Bowrakammen, Milorgfjella) and two locations on the Heimefrontfjella escarpment (Ristinghortane, Milorgfjella High). Geomorphic descriptions of these locations from satellite imagery can be found in Newall et al. (2020) and in Appendix D.

3.2.2 Carbon extraction and exposure age calculations

We separated quartz at Purdue University following the standard Purdue Rare Isotope Measurement Laboratory (PRIME lab) mineral separation procedures (<https://www.physics.purdue.edu/primelab/labs/mineral-separation-lab/procedure.php>). Carbon-14 was extracted at Purdue University using an automated Carbon Extraction and Graphitization System (CEGS) modified from Goehring et al. (2019) and following procedures modified from those described in that study (Table 3.3). Beryllium-10 and ^{26}Al were extracted following a similar procedure described in Andersen et al. (2020; Table 3.4). (See Appendix A for laboratory methods for nuclide extraction and exposure age calculation).

3.2.3 Ice surface elevation

To estimate the amount of ice surface lowering in our study areas, the elevation of the current ice surface relative to our sample elevation is necessary. Our field sites span a large area across two differing ice streams; thus, we systematically estimated the local ice surface elevation based on results from recent modeling by Mas e Braga et al. (2021). That study demonstrated how nunataks can obstruct ice flow, leading to a systematic perturbation of ice surface elevation differences upstream and downstream of a nunatak. Mas e Braga et al. (2021) suggested that the ice surface measured from the nunatak perpendicular to the ice flow direction generally yields an elevation consistent with that of the unperturbed ice surface farther from the nunatak. Therefore, for each sample location we extracted the lowest elevation point on the ice surface perpendicular to ice flow at each nunatak from REMA, subtracted our sample elevation, and reported an estimate of ice surface lowering. The ice surface elevation is reported relative to the middle (lowest) point of the closest ice stream perpendicular to ice flow at each nunatak.

3.2.4 Adaptive-resolution ice sheet model

Reconstructing past ice sheet configurations is essential to informing projected ice sheet dynamic changes and calibrating numerical ice sheet models. Therefore, data-model comparisons (DMC) utilizing reliable records that reconstruct ice surface change are vital to verify numerical ice sheet models of Antarctica. Large ensemble models of Antarctica show little thickening at the LGM ice sheet in DML over our sample sites (Whitehouse et al., 2012a; Abe-Ouchi et al., 2015). However, these models have coarse resolutions (>30 km), However, the resolution of these models is too coarse (>20 km) to properly capture the sampled nunataks and resolve the ice flow around them. We therefore perform an ensemble of high-resolution experiments using the ice flow model Úa (Gudmundsson, 2020), with a regional domain that covers the Jutulstraumen and Veststraumen drainage basins (Fig. 3.1). An irregular finite-element mesh covers the domain with 10 km resolution across the ice sheet interior, scaling down to 1 km near the grounding lines and 500 m near nunataks. All simulations were performed using the Shallow Shelf Approximation (SSA) of the Stokes momentum equations on a finite-element mesh, following a similar procedure to Suganuma et al. (2022) but including the *in situ* ^{14}C exposure ages from this study (see Appendix B for details).

The initial conditions for all experiments use the present-day BedMachine Antarctica ice geometry (Morlighem et al., 2020). Estimates of the spatial distribution of rheology and basal sliding are obtained through an inversion procedure using surface velocity measurements following similar studies (Rignot et al., 2011; Rosier et al., 2021; De Rydt et al., 2021), but modified to account for uncertainties in the model parameters, considering the different characteristics of ice rheology at the LGM, and basal sliding over the modern continental shelf (see Appendix B). LGM ice sheet geometries are reproduced through a range of LGM climate forcings from General Circulation Models from the CMIP5 and CMIP6 projects, combined with a range of values for ice rheology and basal sliding. In total, 100 experiments were performed, of which 27 experiments were considered to represent plausible LGM geometries based on the exposure ages presented in this study and estimates of the magnitude of inland thinning (Buizert et al., 2021). Estimates of ice-surface elevation change were obtained as the modeled LGM ice surface elevation at the sample site minus the present-day ice surface elevation at the reference point over the ice stream. A detailed description of the model setup can be found in Appendix B.

3.3 Results

Exposure age results from Jutulstraumen are discussed along a 200 km transect from samples collected from near the grounding line to near the escarpment. Samples in Veststraumen were collected from a few locations near the coast and then at various locations along the escarpment. In the following results section, all exposure ages are *in situ* ^{14}C unless otherwise specified.

3.3.1 Jutulstraumen Drainage Basin

Apparent *in situ* ^{14}C exposure durations span from 9.6 ± 0.3 to 1.0 ± 0.1 ka ($\pm 1\sigma$ internal error; Fig. 3.2; Fig. 3.3; Table 3.3; Table 3.5) and the samples cover an elevation range from 1970 to 741 m a.s.l. Erratic and bedrock samples show a decrease in age with decreasing elevation, which is expected from a thinning ice surface. The older apparent exposure durations occur at the highest elevation sites at either end of a 200 km longitudinal transect from the grounding line (8.4 ± 0.5 ka; STR-09) to the interior (9.6 ± 0.3 ; YST-06), indicating broadly synchronous thinning along Jutulstraumen. Likewise, our samples from the east side of Jutulstraumen (Sverdrupfjella) indicate synchronous thinning with samples across the valley at Gråsteinen at ~ 4 -1 ka.

Selected ^{10}Be and ^{26}Al data from the Jutulstraumen/Penck system (Andersen et al., 2020) are shown, recalculated with the University of Washington online cosmogenic nuclide calculator (v3 UW calculator), for direct comparison with the new *in situ* ^{14}C data (Table 3.3; Table 3.4). As noted in Andersen et al. (2020), many of the ^{10}Be - ^{26}Al data indicate complex exposure over multiple glacial cycles. However, three samples have ^{10}Be exposure ages that fall within the last deglaciation (MID-05, 2.7 ± 0.2 ka; VID-04, 5.3 ± 0.3 ka; KUL-03, 11.0 ± 0.3 ka (no ^{14}C data for all three samples)). One new sample follows the same criteria as above and we include these exposure ages in our analysis (^{10}Be exposure age: STR-10, 7.0 ± 0.4 ka).

Apparent *in situ* ^{14}C measurements along nunatak slopes allow us to estimate minimum ice surface lowering from as far inland as 200 km all the way to the grounding line, as discussed below. Since the samples farthest inland are adjacent to Penck Trough rather than Jutulstraumen, we group each set of samples separately to discern potential differences in thinning patterns in the following text. The furthest inland site (Huldreslottet) indicates ~ 350 m of thinning after 1.2 ± 0.1 ka. Midbresrabben northeast from Huldreslottet and across the Penck Trough indicate ~ 280 m of thinning between 4.6 ± 0.2 and 2.3 ± 0.1 ka. At Ystenut, ice elevation estimates yield ~ 500 m of

thinning since 9.6 ± 0.3 ka from one sample taken along a low-lying ridge. Unfortunately, no other samples at that location yielded quartz, so we rely on nearby nunataks to fill in the gaps at lower elevations. For instance, samples from Viddalskollen indicate ~250 m of thinning between 5.4 ± 0.3 and 1.3 ± 0.1 . Overall, the minimum ice surface lowering along the Penck Trough indicates 500 m of gradual thinning between ~9 and 1ka.

The remaining samples are more heavily influenced by Julustraumen. Bedrock and boulder samples from Gråsteinen ~55 km from the grounding line have exposure ages between 3.5 and 1.0 ka and indicate upwards of 600 m of ice surface lowering. Sverdrupfjella, located on the opposite (eastern) side of Jutulstraumen and ~40 km from the grounding line has exposure ages between 4.3 and 1.6 ka indicating minimum Late Holocene ice surface lowering of 350 m. At Straumsnutane, three bedrock samples yield ^{14}C exposure ages of 8.4 ± 0.5 , 5.3 ± 0.3 , and 5.0 ± 0.2 ka. Another sample from the highest elevation site (929 m a.s.l.) gives a ^{10}Be exposure age of 7.0 ± 0.4 ka. Together, these data indicate ~850 m of ice loss from the Mid Holocene into the late Holocene.

3.3.2 Veststraumen Drainage Basin

Samples from the Veststraumen drainage span elevations from 2215 to 587 m a.s.l., with apparent *in situ* ^{14}C exposure ages spanning from secular equilibrium (saturation) to 5.8 ± 0.3 ka ($\pm 1\sigma$ internal error; Fig. 3.2, Table 3.3). The samples at secular equilibrium are near the summit of the Heimfrontfjella escarpment, indicating a minimum exposure age of >25-30 ka. Apparent exposure ages below the escarpment range from early to mid-Holocene (12 to 5 ka) and point to contemporaneous thinning from the grounding line to the base of the escarpment. We also report ^{10}Be and ^{26}Al exposure ages from erratic samples (Fig. 3.2). As in the Jutulstraumen drainage basin, nearly all the ^{10}Be and ^{26}Al erratic samples indicate complex exposure or exposure ages that are not post-LGM (Table 3.5). However, two samples at Fossilryggen have Holocene ^{10}Be apparent exposure ages (discussed below).

Two striated bedrock samples from Ristinghortane on the escarpment have *in situ* ^{14}C apparent exposure ages of 19.3 ± 1.3 ka and 16.5 ± 1.0 ka (17RH-01 and 17RH-02, respectively). Field observations indicate the samples were approximately 20-50 m above the adjacent ice surface, although 17RH-02 was collected within 1 m of the current snow line, consistent with the observed age relationship. The exposure ages of these two bedrock samples are consistent with ice

thinning after the LGM. These samples are influenced by a nearby outlet glacier, Kibergdalen, that drains from the polar plateau into Veststraumen. Visible but discontinuous striations (Table 3.1; Fig. 3.2) are consistent with current flow direction. The other site on the escarpment, Milorgfjella High, yielded *in situ* ^{14}C measurements near saturated concentrations. However, one erratic sample at Milorgfjella High has an exposure age of 23.2 ± 2.1 ka (17MH-03). Therefore, the *in situ* ^{14}C exposure data above and just below the escarpment at high elevations indicates that these sites were exposed soon after the end of the LGM.

Although Månesigden and Bowrakammen are located within the transition zone below the escarpment, the bedrock samples at both locations are saturated, perhaps because they are on ridges adjacent to small outlet glaciers. However, one erratic sample at Månesigden (MAB-04; 17.7 ± 1.0) has a post-LGM exposure age. In contrast, *in situ* ^{14}C apparent exposure ages from bedrock along two nunataks below the escarpment, Vardeklettane and Cottentoppen Junior, are 12.3 ± 0.6 ka (CJ-01) and 12.7 ± 0.5 ka (VK-02) and 8.6 ± 0.3 ka (VK-01; Fig. 3). These samples indicate 80 m of thinning between ~ 13 and 9 ka. On the eastern side of Heimefrontfjella in a transition zone, one erratic from Arntzenrustene, a small nunatak adjacent to a Milorgfjella outlet glacier, gives an exposure age of 11.3 ± 0.4 ka (Fig. 3.2). There are no other samples at lower elevations on the east side, therefore we can only constrain that <100 m of thinning occurred after ~ 11 kyr.

The samples collected near the coast are younger than the samples from the transition zone and the top of the escarpment. The erratic samples at Fossilryggen have *in situ* ^{14}C exposure ages of 9.0 ± 0.6 ka and 5.9 ± 0.3 ka. The accompanying ^{10}Be exposure ages are younger than the *in situ* ^{14}C and are also offset by ~ 3 ka (3.8 ± 0.2 ka; 17FR-02 and 6.3 ± 0.3 ka; 17FR-03). Because the *in situ* ^{14}C and ^{10}Be do not agree, these erratic samples likely do not have a simple burial and re-exposure history. It is possible that these erratics were buried under shallow ice (<10 m) and therefore were not shielded enough to cut off muon production. Under thin snow or shallow ice cover, a higher amount of muon production can outpace spallation production. A higher production rate leads to higher concentrations of *in situ* ^{14}C than ^{10}Be , resulting in older exposure ages. Ice surface lowering estimates from these samples indicate ~ 120 m of ice loss after 9 ka.

The *in situ* ^{14}C exposure ages from quartzite erratic samples from Basen overlap agree within uncertainty from 587 to 549 m a.s.l. (8.7 ± 0.5 ; BN03; 8.8 ± 0.6 ; BN04; 8.1 ± 0.6 ka; BN08). Together, these three samples show a minimum ice surface lowering of ~ 400 m beginning at ~ 8.6 kyr. Since all samples were collected along the nunatak's upper surface, we cannot constrain the

duration of thinning to the modern adjacent ice stream (Plogbreen, branching northward from the main Veststraumen body).

3.3.3 Holocene thinning rates from the coast to inland

Thinning rates were determined that best fit all exposure age data in each region using a Monte Carlo linear regression analysis using the MATLAB model iceTEA (<http://ice-tea.org>; Jones et al., 2019). We generated thinning rates with 5000 iterations through randomly sampled points using 2σ internal uncertainties. We determined linear thinning rates for samples influenced by the Jutulstraumen and the Penck to determine differences between the coast and inland. We were only able to determine thinning rates from the coast for the Veststraumen drainage basin from Basen and Fossilryggen.

The modeled thinning rates from nunataks influenced by Jutulstraumen range from 0.08-0.14 m yr⁻¹ (0.06-0.22 m yr⁻¹ in 95% confidence interval) between ~10 and 1 ka (Fig. 3.4). The thinning rates determined from samples influenced by the Penck are slightly lower, ranging from 0.03-0.05 m yr⁻¹ (0.03-0.06 m yr⁻¹ at 95% confidence) covering a similar time frame. We used the erratic samples from Basen and Fossilryggen to estimate the amount of coastal thinning near Veststraumen. The modeled thinning rate for the coastal Veststraumen samples has a range of 0.07-0.21 m yr⁻¹ at 1σ (0.05-0.87 m yr⁻¹ at 95% confidence).

3.3.4 Numerical model results

We assess the performance of each experiment by evaluating how many of the younger-than-LGM (i.e., 21 ka or less) samples presented in this study were covered by ice, and how close the thinning at the upstream end of the domain (i.e., within the polar plateau) is to an elevation-change estimate of -130 m (Buizert et al., 2021; Parrenin et al., 2007). We consider a model experiment to satisfactorily represent a LGM configuration if inland thinning at the upstream end of the domain is between -100 and -160 m, and if at least 90% of the samples were covered (i.e., $n < 5$). Applying these criteria yields a constrained ensemble of 27 simulations, out of the original 100 (See Appendix D for further details). Modeled ice surface elevation change was calculated at each nunatak by subtracting the present-day ice surface elevation (i.e., Table 3.6) from the modeled LGM ice surface elevation (Fig. 3.5).

3.4 Discussion

3.4.1 Coast-to-inland LGM ice thickness trends at Jutulstraumen and Veststraumen

Previous studies have reported a thicker-than-present EAIS surrounding DML at the LGM. For instance, adjacent to DML around the Weddell Sea, *in situ* ^{14}C data at the Shackelton Range was 310 - 655 m thicker (Nichols et al., 2019). Directly east of Jutulstraumen, a recent study utilizing ^{10}Be has found the LGM ice to be ~100 m thicker (Suganuma et al., 2022). Another recent study along Jutulstraumen yielded a maximum estimate of 200 m of thickening based on long-lived cosmogenic nuclides such as ^{10}Be , ^{26}Al , and ^{36}Cl (Andersen et al., 2020). However, our new *in situ* ^{14}C data indicates a thicker LGM EAIS in western DML than previously estimated.

The *in situ* ^{14}C data along Jutulstraumen show that LGM ice covered all sampled sites because exposure data is all post-LGM (Fig. 3.3). We find significant coastal thickening that has not been predicted by models to date. For instance, our data near the grounding line at Jutulstraumen indicates a maximum thickening of 850 m relative to the ice stream (Fig. 3.6). Inland, *in situ* ^{14}C exposure ages indicate a maximum of 300 m of ice surface lowering.

The *in situ* ^{14}C data surrounding Veststraumen show that LGM ice covered all sample sites below the escarpment while the top of the escarpment was exposed (Fig. 3.3). Exposure data estimate a minimum of 430 m of coastal thickening. Minimum estimates of LGM ice thickening in Veststraumen are smaller than previous estimates of 700 m (Lintinen, 1991; Lintinen and Neonen, 1997) and at Jutulstraumen, likely because we were unable to find suitable erratics at the nearby nunatak Plogen (700 m high; see Fig. 3.2a for location). Similarly, inland estimates at Veststraumen are a maximum of >100 m at the LGM, less than along Jutulstraumen (Fig. 3.6).

The differences in ice thickening estimates could be due to the drainage patterns from the polar plateau through the Heimfronfjella mountains. For instance, Jutulstraumen sits in a narrow channel and the drainage pattern was likely similar during the LGM where ice flow was focused at the ~40 km opening between the polar plateau ice through the escarpment mountains. However, in Veststraumen, there are many smaller outlet glaciers <10 km wide that drain ice from the polar plateau into the ice stream. There could have been variability in the smaller outlet glaciers that leads to uncertainties in the ice dynamics at the LGM surrounding Veststraumen.

The *in situ* ^{14}C data on and below the escarpment point to most of the sample sites not being covered by LGM ice. Indeed, ice core records indicate interior domes thinned by 110-120 m in

response to climate cooling during the LGM (Parrenin et al., 2007). Our exposure data from Milorgfjella high indicate that the plateau ice did not overtop the Heimefrontfjella mountains at one location and spill over the steep escarpment at that site. The samples from Ristinghortane are 25-50 m above the current ice surface and ~5 km to the center the outlet glacier Kybergdalen that drains the polar plateau. The exposure data from bedrock indicate the samples were likely covered at the LGM, but emerged soon after the LGM.

To achieve an LGM ice thickness of ca. 800 m over our coastal samples, the grounding lines for both Jutulstraumen and Veststraumen would have had to have been further offshore. The current best estimates of maximum LGM ice extent around Antarctica are from the RAISED paleo consortium (Bentley et al., 2014). These estimates suggest the LGM ice sheet may have been grounded 120-200 km offshore at DML from the current grounding line near the edge of the continental shelf, allowing the ice stream to thicken landward.

3.4.2 Deglacial thinning rates in DML

Holocene thinning began in DML around 10 ka and continues until 3 ka (Andersen et al., 2020; Kawamata et al., 2020; Mackintosh et al., 2007; Suganuma et al., 2022; White and Fink, 2014; Yamane et al., 2015) (Fig. 3.7). Our data fall within that range, though we are the first study in DML to find thinning that continues into the late Holocene. We find gradual ice surface lowering along Jutulstraumen and Penck glacier that occurred between 9.5 and 1 kyr. Thinning seems to be synchronous across the narrow channel from 200 km inland to the grounding line, as evidenced by exposure ages from Huldreslottet and Straumsnutane (inland to grounding line) and across the valley from Gråsteinen and Sverdrupfjella. The calculated thinning rates (Fig. 3.4) fall within the same range of thinning rates at the Grotfjellet and Rabben nuntaks (0.05 m yr^{-1} (0.03 – 0.10 m yr^{-1} 95% confidence) east of Jutulstraumen (Suganuma et al., 2022).

Exposure data from the Veststraumen drainage, in contrast to Jutulstraumen, indicates gradual ice surface lowering inland beginning ~12.8 kyr followed by rapid ice surface lowering between 9 and 5 ka near the coast. The inland thinning around 12 kyr could be driven by increased atmospheric temperatures between 12 and 11 kyr estimated from Dome Fuji (Stenni et al., 2010) and EDML (Kawamura et al., 2007). The spatial distribution of samples makes it difficult to draw broad conclusions across Veststraumen, except near the base of the escarpment and near the coast where we have reliable samples. Our calculated thinning rates (Fig. 3.4) at Jutulstraumen and

coastal Veststraumen have similar rates, despite the separation, indicating thinning occurred after 10 ka approximately simultaneously in both locations.

Holocene thinning rates in DML inferred from ^{10}Be exposure dating show little to no thinning after ~ 5 ka (Fig. 3.7; Macintosh et al., 2007; Yamane et al., 2011; White and Fink, 2014; Suganuma et al., 2022). These time gaps in exposure dating are sometimes found directly next to the modern ice surface and could indicate readvance of the AIS during the Holocene (e.g., Johnson et al., 2022). Many of these exposure dating studies rely on ^{10}Be and ^{26}Al , whose long half-lives can lead to inventories produced over multiple exposure episodes due to prevalent non-erosive ice in Antarctica, potentially masking more recent signals. Those studies might thus be missing a younger signal that could be obtained from *in situ* ^{14}C , as evidenced by recent work (e.g., Nichols et al., 2019) and our study. Our dataset along Jutulstraumen does not support a post-5 ka readvance of the ice stream. We cannot confirm the same for Veststraumen due to a lack of samples close to the modern ice surface.

Cosmogenic nuclide data at nearby nunataks east of Jutulstraumen, however, could potentially support readvance of the EAIS during the Holocene (Suganuma et al., 2022). The authors find thinning of the ice sheet between 8.4 - 5.7 ka on two nunataks. At the base of one of the nunataks, a moraine is dated to ~ 1.0 ka. The authors argue that the time gap between the base of the nunatak and the moraine could leave room for a potential readvance of the EAIS during the late Holocene. Although this study relies solely on ^{10}Be exposure dating, the large number ($n=15$) of Holocene exposure ages and data clustering between 10 and 5 ka suggest the data are reliable.

The discrepancies in the timing of ice sheet thinning between our Jutulstraumen dataset and that of Suganuma et al. (2022) could be explained by the differences in settings. First, our samples are taken near a fast-flowing ice stream (750 m yr^{-1} ; Rignot and Scheuchl., 2017) while the other study's nunataks are near two slower moving outlet glaciers (25 m yr^{-1} ; Rignot and Scheuchl, 2017). The difference in velocity is partially due to the width of outlet glaciers flowing through the escarpment draining the polar plateau. For instance, Jutulstraumen sits in a narrow but deep trough and the drainage pattern was likely similar during the LGM where ice flow was focused at the ~ 40 km opening between the polar plateau ice through the escarpment. Other outlet glaciers across DML are ca. 5-10 km wide. Second, our study site extends close to the grounding line (Straumsnutane) and has a more direct influence from the Fimbul ice shelf than the inland samples from Suganuma et al. (2022), implying our samples are likely more sensitive to ocean forcing. Our

sites likely didn't experience a delay in ocean forcing, compared to Suganuma et al. (2022)'s inland sites. Third, our modeling predicts a large difference in LGM thickening between the two study sites. Our best fit model predicts upwards of ~850 m near the coast and ~500 m 200 km inland along the Jutulstraumen system, while Suganuma et al. (2022) modeling predicts a maximum of 300 m of thickening at their sites east of Jutulstraumen ~100 km from the grounding line (Fig. 3.8).

Although our Jutulstraumen dataset has a different setting than Suganuma et al. (2022), they fall within the 10-3 ka range of ice thinning across DML demonstrated by that study. Thus, is likely influenced by the same forcing suggested for initial thinning during the Holocene. Suganuma et al. (2022) infer that inflow of warmer Circumpolar Deep Water (CWD) below ice shelves during a highstand in regional sea level acted as a trigger of rapid thinning. The authors calculated a regional sea level change at the Jutulstraumen grounding line based on global sea level and regional GIA (Fig. 7b) and found a highstand of 30 m above modern levels between 9 and 7 ka. The delayed timing of ice loss from DML leads to a delayed viscoelastic response, causing an overshoot of regional sea level rise (Suganuma et al., 2022). Our data support this conclusion, though we see continued ice thinning until 1.0 ka. The delayed thinning signal could be due to a slower propagation response time of the ice stream. The thinning of an outlet glacier can take thousands of years for ice surface lowering to propagate up glacier (Todd et al., 2010; White et al., 2011; White and Fink, 2014). Jutulstraumen has a narrow opening, and the lateral stress on the sides (Mas e Braga, in review) might be able to hold ice back inland while thinning occurs near the grounding line.

3.4.3 Data-model comparisons

A constrained ensemble of plausible LGM ice sheet geometries complements the exposure ages in several ways. First, it provides a dynamically consistent estimation of thickness changes during the LGM for the entire catchment basins as opposed to sparsely distributed nunataks. Second, it allows us to estimate how much the ice sheet could have thickened at each sampled site prior to sample exposure. Third, it provides a more robust way to determine which combination of model parameters and climate forcing best represents LGM conditions over our study region.

Based on the subset of 27 experiments constrained by the exposure ages presented above, we estimate the change in ice surface elevation between LGM and present for selected sampled

nunataks (Fig. 3.5). As a complement to the exposure ages, our model results predict LGM ice thicknesses throughout the model domain (and thus over the sampled sites) prior to deglaciation. In general, our constrained ensemble agrees well with the coast-to-inland gradient in the ice thinning magnitudes shown by the *in situ* ^{14}C exposure ages, consistent with the presence of this gradient during post-LGM deglaciation. The modeled ice surface elevation over Straumsnutane was 802 – 872 m above the modern Jutulstraumen elevation, while at Huldreslottet the ice surface was only 452 – 511 m higher. In many cases, the estimate of ice surface lowering based on *in situ* ^{14}C provides a minimum estimate (i.e., grey bars in Fig. 3.5) while the modeled ice surface provides a maximum estimate. However, estimates of ice thickening at the LGM overlap the *in situ* ^{14}C estimate at Straumsnutane.

A similar gradient is obtained for the Veststraumen catchment, where the constrained ensemble predicts that the sampled nunataks were covered by up to nearly 800 m at the margin (Basen, Fig. 5a) and at least 14 m at the escarpment (Millorgfjella; Fig. 3.5m). While Basen is located closest to the grounding line and influenced by Plogbreen, LGM ice thickness drops to 535 – 585 m at Fossilryggen, located only 20 km further inland. Closer to the escarpment, samples in the transition zone were covered by ~200 m of ice or less (Vardeklettane, Cottontoppen, Milorgfjella, Månesigden, Bowrakammen; Fig. 3.5). Contrasting with the estimates from *in situ* ^{14}C , the model results suggest that sample sites on the escarpment were covered by 200 – 250 m of ice (Ristinghortane, Milorgfjella High).

Previous studies have used exposure ages and derived thinning rates to constrain continental-scale model experiments (e.g., Whitehouse et al., 2012a), but their coarse resolution cannot properly represent the complex topography of the regions from where samples are taken (Mas e Braga et al., 2021). Our regional ice sheet model, on the other hand, was designed to better resolve ice flow close to and around regions of steep topography, allowing the model to represent individual sampled nunataks. This enabled us to use the exposure ages and estimates of inland thinning from a regional ice core as empirical constraints to evaluate results from an ensemble of 100 LGM experiments. Plausibility of the individual experiments within these constraints was assessed based on whether the modeled ice sheet geometries over-predicted or under-predicted ice thickness at our sites.

Our LGM numerical model results allow us to make an estimate on how much ice loss in our model domain contributed to sea level rise. Numerical model simulations of the entire

Antarctic continent from the LGM to today indicate the AIS contributed 10 – 14 m to global sea level rise (Whitehouse et al., 2012b; Golledge et al., 2014; Briggs et al., 2014; Argus et al., 2014; Pittard et al., 2022). Our best-fit model estimates 0.37 m sea level equivalent (s.l.e.) ice volume loss from our entire model domain since the LGM (Jutulstraumen: 0.17 m s.l.e.; Veststarumen: 0.20 m s.l.e.).

3.4.4 Model limitations

Performing a relatively large ensemble of model simulations allows us to quantify the uncertainty in the results due to the different climate forcings tested and model parameters varied (i.e., basal sliding over the continental shelf and ice rheology). From the full ensemble, it is possible to evaluate the model sensitivity to our choices of climate and model parameters, and by constraining the ensemble with exposure ages, we can determine what are the best estimates for the parameters tested. Our model was most sensitive to the choice of climate forcing, followed by the choice of basal sliding distribution and ice rheology (See Appendix B). Some spread in the resulting LGM geometries exist when varying the latter two parameters, but climate forcings that yielded plausible ice sheet geometries for one combination of parameters usually yielded plausible geometries for most combinations. It is worth noting that, even when considering the full ensemble, the range of climate forcings and model parameters explored yielded a similar (albeit wider) frequency distribution to the constrained ensemble (Fig. 3.5).

Despite the improvements given a higher resolution over the areas of interest, some limitations still exist in such modeling setup. First, ice rheology was varied only in magnitude, while keeping its spatial pattern similar to the inverted field based on present-day conditions, which would have made it harder for ice streams radically different from the ones currently observed in Antarctica to form. Similarly, by providing only equilibrium snapshots of LGM geometries we are not able to assess the ice surface evolution at the sampled sites prior to and after exposure, which would further highlight the benefits of having a more accurate representation of ice flow around individual nunataks. Finally, although the model resolution is as high as 400 m over the areas of interest, the original subglacial topography dataset has a resolution of 1 km (Morlighem et al., 2020). This means that some features are still smoothed, which explains why the model experiments missed the continuous exposure at Månesigden, Bowrakammen, and Ristinghortane. These three nunataks lie exactly at the hinge point just next to areas where the

experiment that performs best experienced thinning, and compared with the subglacial topography dataset, only Ristinghortane lies on a topographic high. Current efforts exist in providing subglacial topography at even higher resolutions (e.g., Leong and Horgan, 2020), based on machine learning using a deep neural network. Thus, while these efforts are useful and must be considered, expanding the available observational dataset of subglacial topography is critical for improving the performance of ice sheet models.

3.5 Conclusions

Our new *in situ* ^{14}C exposure data from nunataks within the Jutulstraumen and Veststraumen drainage systems indicate that sample locations below the Heimefrontfjella mountains were covered by LGM ice. Therefore, our data support significant coastal thickening at the LGM, likely due to the expansion of the ice sheet onto the continental shelf. ^{14}C results indicate that the Jutulstraumen ice thickened up to 850 m near the coast and ca. 300 m inland; results from Veststraumen show a similar pattern, but with only 100 m of LGM thickening inland below the escarpment. The gradual Holocene thinning observed along Jutulstraumen between 9.6 and 1.0 ka does not support the hypothesis of late Holocene readvance of the EAIS. We infer more rapid Holocene thinning near the coast of Veststraumen between 8 and 5 ka, at face value similar to other areas cited as evidence of late Holocene readvance, but sparse sample coverage limits the strength of that interpretation in our view at that location. We used an ensemble of high-resolution climate models and ice sheet parameters to predict possible LGM ice sheet geometries, and constrained plausible results using our *in situ* ^{14}C dataset and published ice core interpretations. The best-fit models predict progressive thickening from below the escarpment toward the coast, while the polar plateau ice was thinner than present.

This study also confirms the value of using *in situ* ^{14}C in Antarctica for post-LGM deglacial studies, limiting the potential influence of prior exposure often observed with longer-lived cosmogenic nuclides. Further, empirical ice thickness histories such as those presented here are critical for constraining models predicting the LGM configuration of the AIS. Such constraints are especially important for transient ice sheet models that predict future ice sheet loss from future climate projections (DeConto and Pollard, 2016; DeConto et al., 2021; Li et al., 2023).

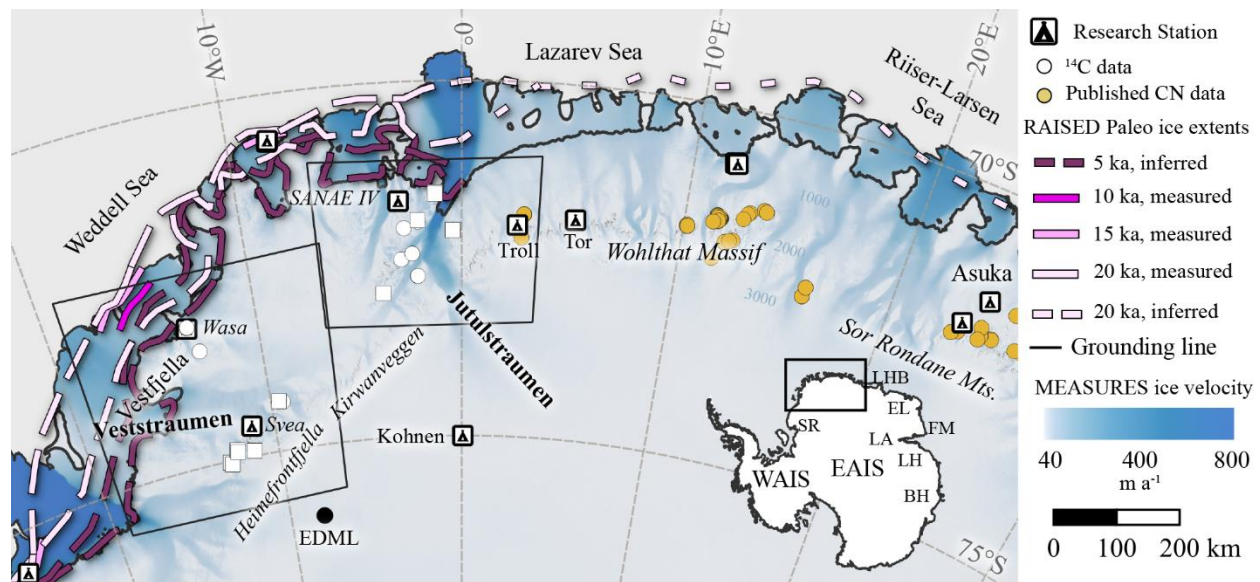


Figure 3.1. Overview map of Dronning Maud Land showing published cosmogenic nuclide (CN) data. The black dotted line shows the LGM model extent. Inset map shows locations mentioned in text. WAIS = West Antarctic Ice Sheet, EAIS = East Antarctic Ice Sheet, EL = Enderby Land, LHB = Lützow-Holm Bay, FM = Framnes Mountains, LA = Lambert-Amery glacial system, LH: Larsemann Hills, BH = Bunger Hills, SR = Shackleton Range. The MEASURES ice flow velocity by Rignot and Scheuchl (2017). RAISED Paleo ice extents from Bentley et al. (2014). (Modified from Andersen et al., 2020).

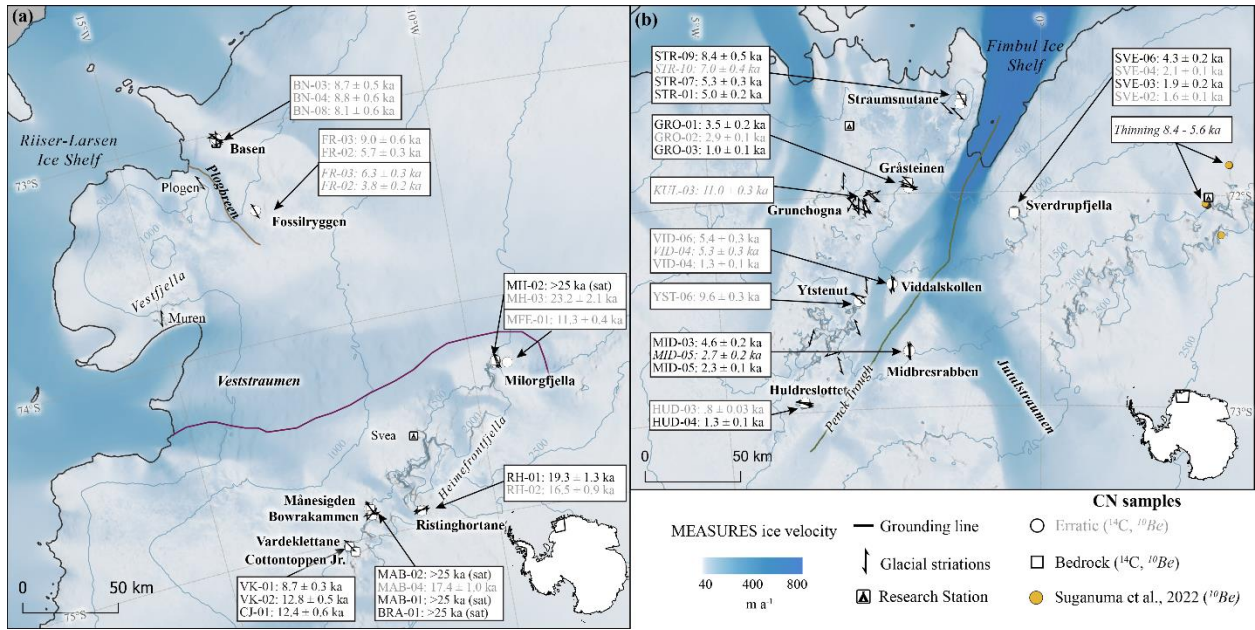


Figure 3.2. (a) Exposure age data from Veststraumen drainage basin and (b) Jutulstraumen drainage basin. Exposure ages in boxes are in elevation order from highest to lowest. Flowlines through ice streams are used in Fig. 3.6. White circles are erratics, white squares are bedrock, and yellow circles are Suganuma et al., (2022) ¹⁰Be sample locations.

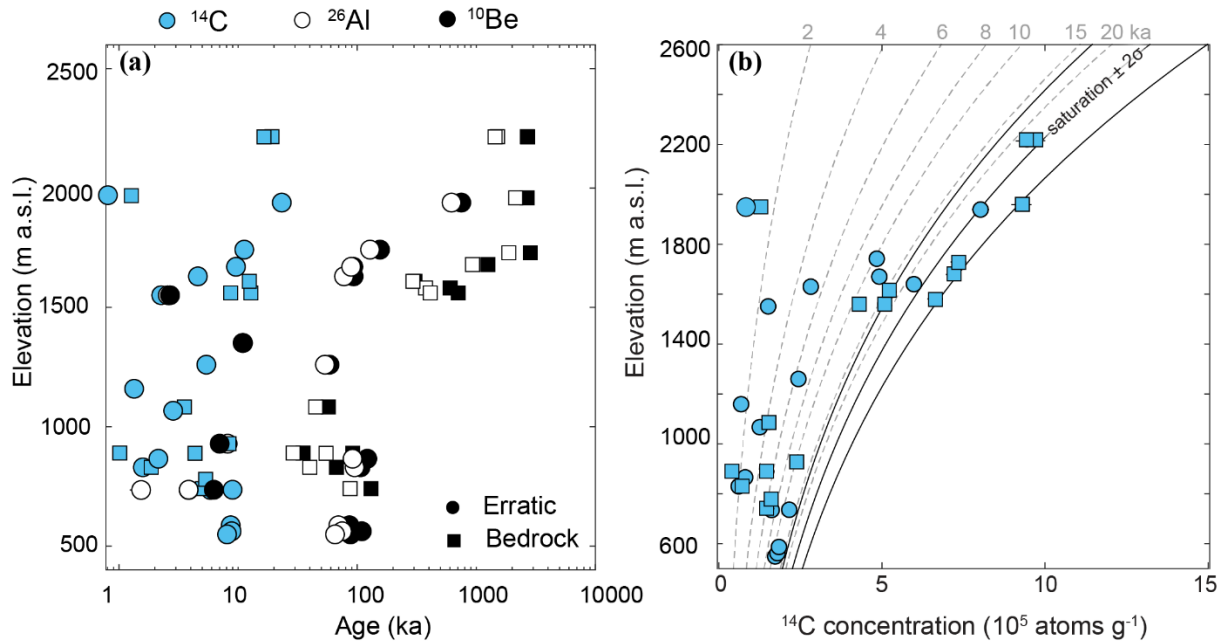


Figure 3.3. (a) Elevation vs. ^{10}Be and ^{26}Al cosmogenic nuclide data from the study sites compared to *in situ* ^{14}C showing that most of the ^{10}Be and ^{26}Al do not indicate last glacial maximum signal. (b) Elevation vs. *in situ* ^{14}C concentrations compared to saturation (solid line). Erratics are circles and bedrock are squares in both panels.

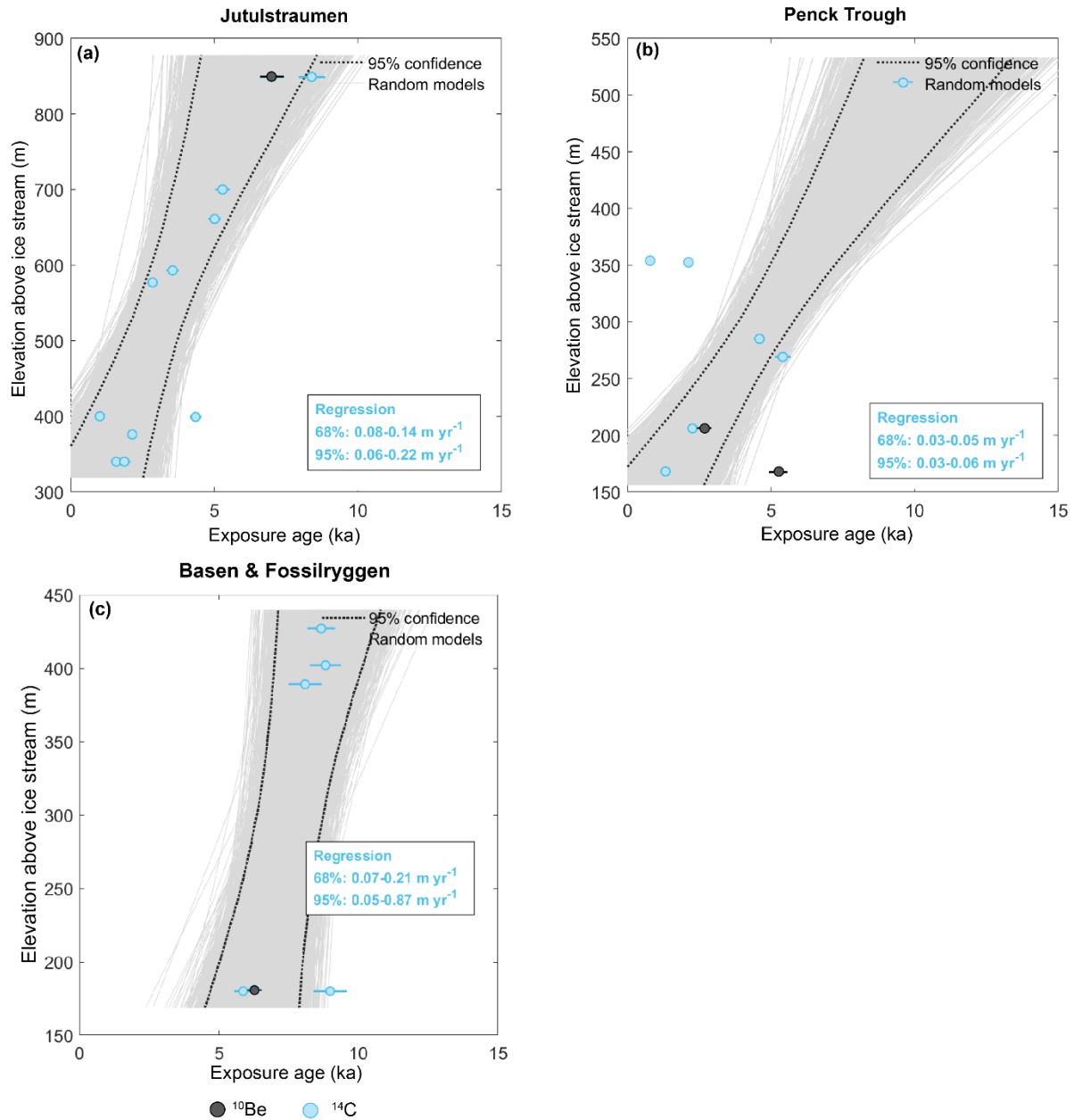


Figure 3.4. Thinning rates determined from iceTEA (Jones et al., 2019) on selected nunataks. Data along Jutulstraumen are split into samples directly influenced by the main channel of Jutulstraumen (a) and by the Penck glacier (b). Thinning rates from the Veststraumen coast are calculated using all the samples from Basen and Fossilryggen (c). Blue data are *in situ* ¹⁴C exposure age while black are ¹⁰Be data.

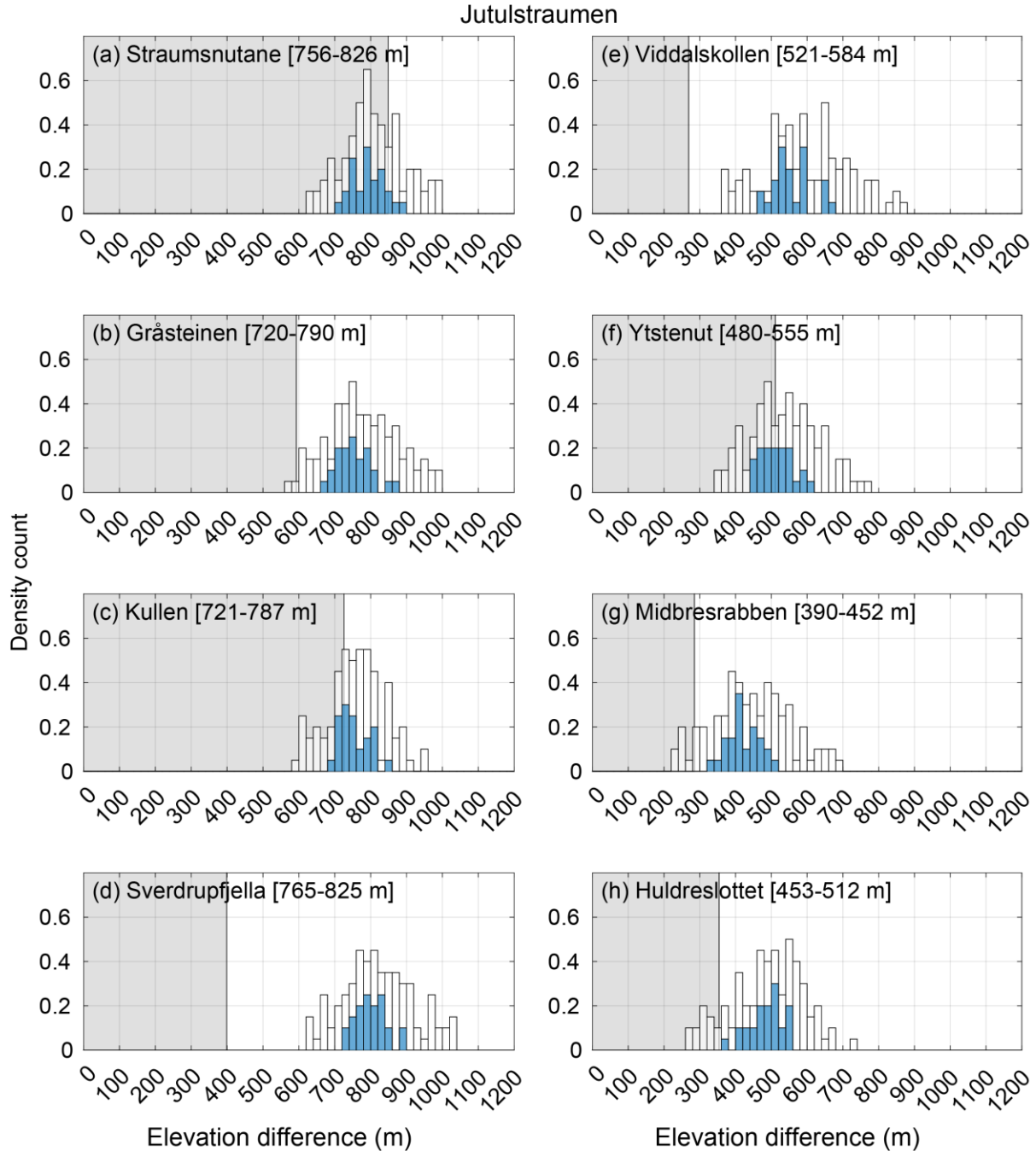


Figure 3.5. Density count histogram (i.e., count divided by bin width) for LGM-to-present ice-surface elevation differences (in m) over selected nunataks in the Veststarumen and Jutulstraumen catchment, using the entire ensemble of model runs ($n=100$, white bars) and a subset that is constrained by ice-core and cosmogenic-nuclide elevation-change estimates ($n=27$, blue bars). Elevation change intervals denote the 25th to 75th percentile of the constrained distribution. Grey zone marks the minimum thickening based on ^{14}C ages. (Fig. by M. Mas e Braga).

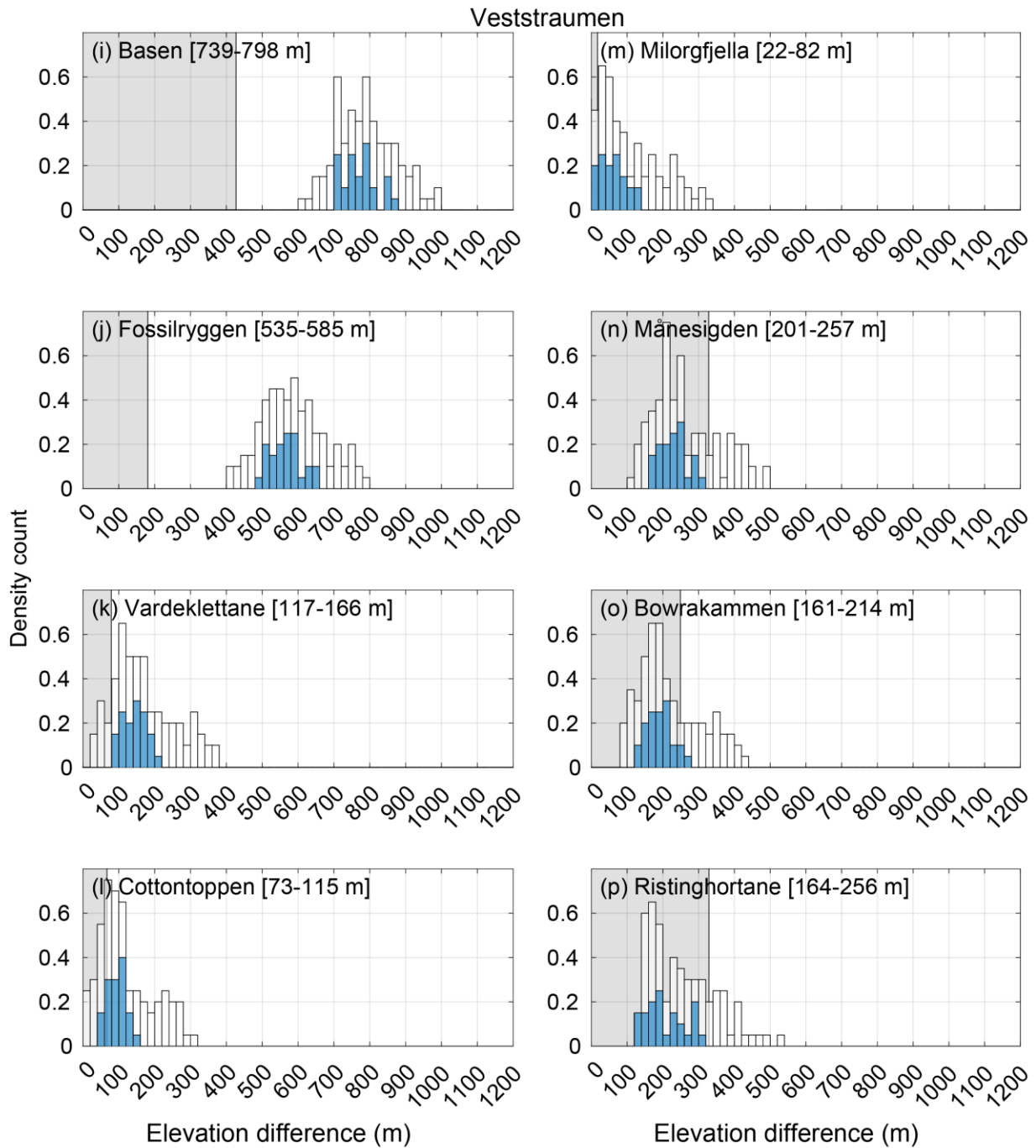


Figure 3.5 continued.

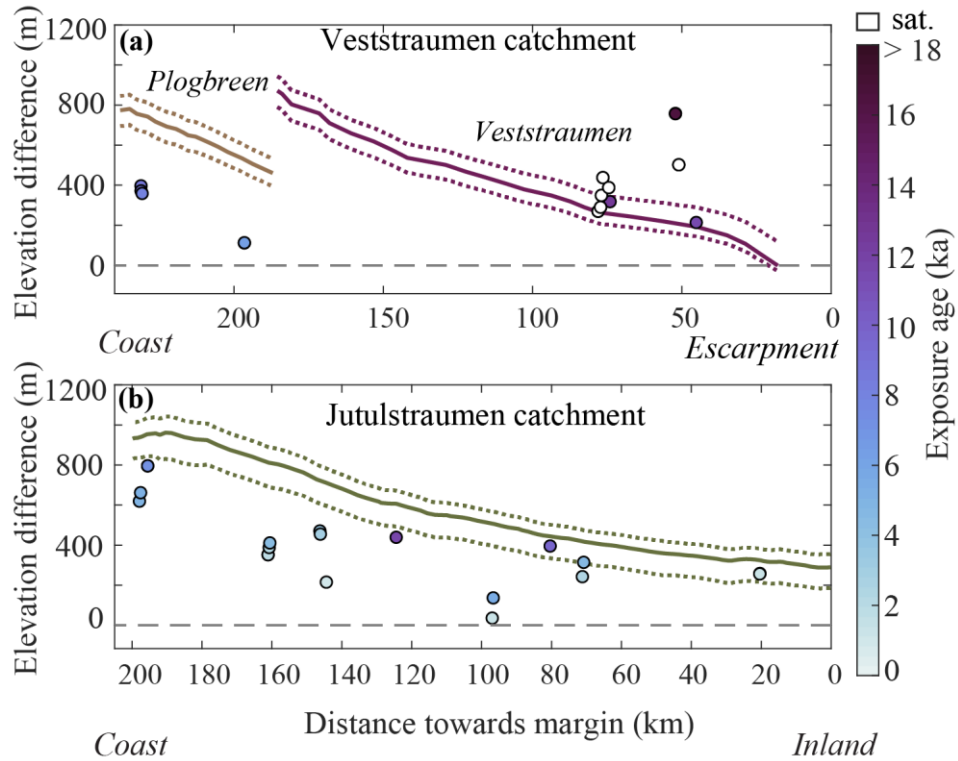


Figure 3.6. Different estimates of elevation change since the LGM based on the best experiment (IPSL-CM5A-LR_sld06) for the (a) Veststraumen catchment and (b) Jutulstraumen catchment. Solid lines indicate elevation change along each ice stream (cf. Fig. 3.2) for the best constrained run (dashed lines show the 5th and 95th percentiles of the ensemble of 27 simulations). Circles use the nearest point over the present-day ice stream as the reference, but take the LGM surface elevation from the best-performing simulation over the sample's elevation per se (circles). (Fig. by M. Mas e Braga, modified by A. Koester).

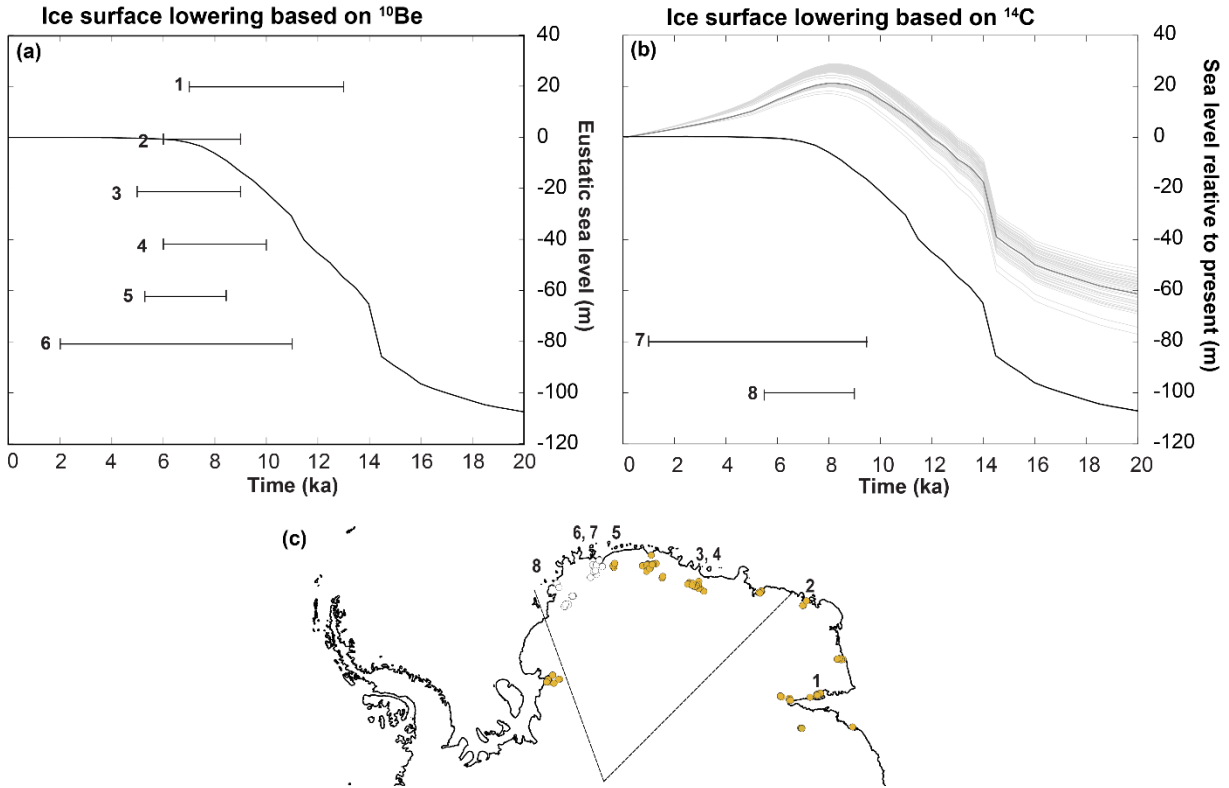


Figure 3.7. Summary figure of Holocene thinning rates across Dronning Maud Land. Ice surface lowering based solely on ^{10}Be (left) are from 1. Framenes Mtns (Macintosh et al., 2007); 2. Enderby Land (White and Fink, 20014); 3. Lutzow-Holm Bay (Kawamata et al., 2020); 4. Lutzow-Hom Bay (Yamane et al., 2011); 5. Suganuma et al., 2022; 6. Jutulstraumen (Andersen et al., 2020). Ice surface lowering based on *in situ* ^{14}C from this study include 7. Jutulstraumen and 8. Plogbreen (Basen and Fossilryggen sites). The eustatic sea level is shown in black compared to the modeled regional sea level change at the grounding line of Jutulstraumen (Suganuma et al., 2022). The thin lines are relative sea levels based on different earth models and the bold line represents the best model (Suganuma et al., 2022). The map of Antarctica (c) shows the study location by number.

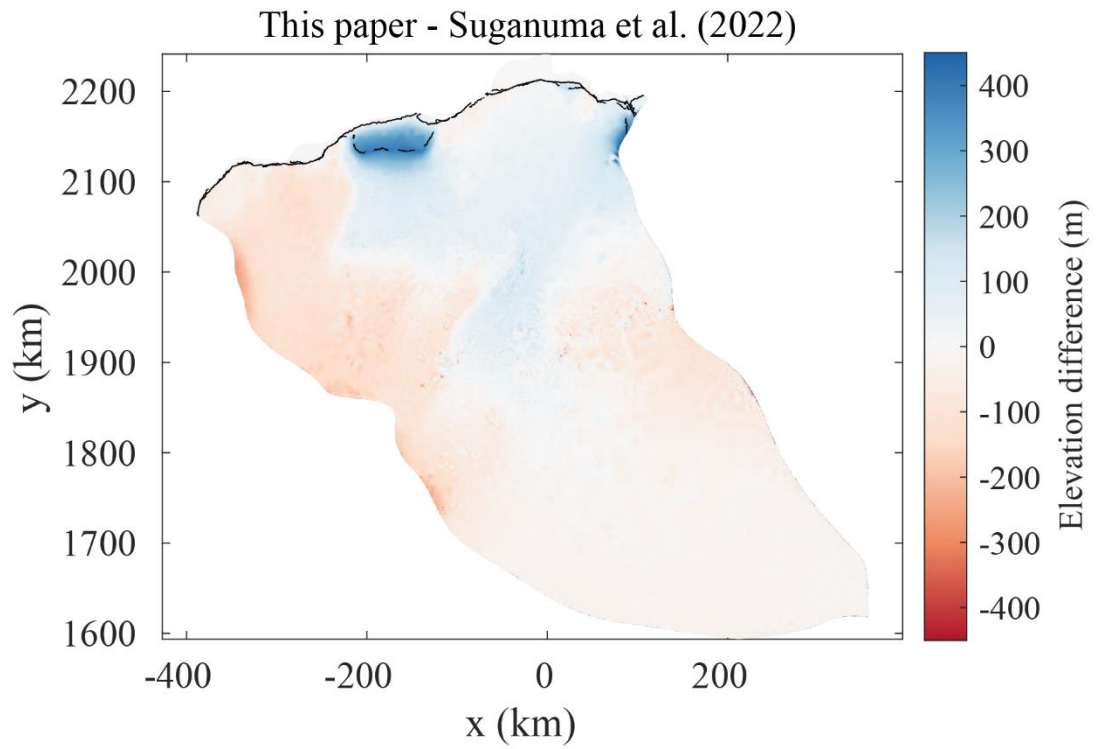


Figure 3.8. The difference in elevation between our best fit model (see Appendix D) and Suganuma et al. (2022)'s best fit model for the Jutulstraumen basin (Fig. by M. Mas e Braga).

Table 3.1. Sample locations for Antarctic samples.

Site	ID	Type ^a	Elevation (m)	Latitude	Longitude	Sample thickness (cm)	Shielding correction
Jutulstraumen Drainage Basin							
Gråsteinen	GRO-01	BR	1083	-71.9495	-2.0043	1	1
	GRO-02	ER	1067	-71.95061	-2.005607	3	0.9942
	GRO-03	BR	890	-71.97177	-1.99038	1	1
Midbresrabben	MID-03	ER	1630	-72.7364	-2.0842	7	1
	MID-05	ER	1551	-72.7348	-2.0713	6	1
Ystenut	YST-06	ER	1670	-72.4917984	-2.827147	2	1.00
Sverdrupfjella	SVE-02	ER	830	-72.0951	-0.4016	2	1
	SVE-03	BR	830	-72.0951	-0.4016	3	1
	SVE-04	ER	866	-72.0977936	-0.405136	5	1.00
	SVE-06	BR	889	-72.0993	-0.4075	3	1
Viddalskollen	VID-04	ER	1159	-72.4169235	-2.2987721	2	0.98
	VID-06	ER	1260	-72.4185	-2.3064	2	1
Straumsnutane	STR-01	BR	741	-71.5653	-1.1732	1	1
	STR-07	BR	780	-71.5677567	-1.17837	3	1
	STR-09	BR	929	-71.58659	-1.1913	6	0.99
	STR-10	ER	929	-71.5865936	-1.1913	6	0.99
Huldreslottet	HUD-03	ER	1970	-72.954483	-3.766469	2	0.99
	HUD-04	BR	1968	-72.954483	-3.766469	4	0.99
Kullen	KUL-03	ER	1351	-72.0555496	-2.647042	6	1
Veststraumen Drainage Basin							
Basen	BN-03	ER	587	-73.02774	-13.41977	5.6	1
	BN-04	ER	562	-73.026	13.415	3.5	1
	BN-08	ER	549	-73.02307	-13.39206	4.2	1
Fossilryggen	FR-02	ER	735	-73.391	13.040	2.60	1
	FR-03	ER	736	-73.39103	-13.04132	4.63	1
Milorgfjella	MFE01	ER	1742	-74.314453	-9.387043	4.4	0.86

Table 3.1 continued

Vardeklettane	VK-01	BR	1561	-75.02011	-12.75514	1	0.99
	VK02	BR	1561	-75.02011	-12.75514	3.1	0.98
Cottentoppen Junior	CJ-01	BR	1609	-75.05076	-12.66977	2.77	0.99
Ristinghortane	RH-01	BR	2215	-74.925645	-11.337693	4	1
	RH-02	BR	2214	-74.926107	-11.339867	1.4	1
Månisigden	MAB01	BR	1581	-74.868265	-12.264	2.45	0.89
	MAB02	BR	1729	-74.8714	-12.2391	4.8	1.00
	MAB04	ER	1640	-74.866834	-12.247551	6.1	1
Bowrakammen	BRA01	BR	1679	-74.89899	-12.23493	2.3	1.00
Milorgfjella	MH02	BR	1959	-74.299316	-9.586166	4.9	1
	MH03	ER	1939	-74.3036	-9.605483	7	1

^aER = erratic, BR = bedrock

Table 3.2. Summary table of glacial striation information found from Antarctic field seasons.

Sample ID	Latitude	Longitude	Direction	Notes from the field members
GRO-01	-71.9495	-2.0043	316	
GRO-03	-71.97177	-1.99038	290	Large ones, old ones?
GRO-03	-71.97177	-1.990382	274	Recent
GRO-04	-71.95941	-2.012567	290	
MID-01	-72.73612	-2.084255	350	
MID-02	-72.73755	-2.086036	355	
MID-04	-72.73464	-2.068578	360	
YST-02	-72.42213	-2.709093	354	
YST-03	-72.48321	-2.841614	310	
YST-08	-72.46958	-2.847859	280	
VID-05	-72.41869	-2.30265	350	
VID-07	-72.42432	-2.306827	10	S-N ice flow
STR-01	-71.5653	-1.1732	330	
STR-03	-71.6093	-1.39799	315	
STR-04	-71.6365	-1.23871	315	
HUD-01	-72.95664	-3.768232	110	Abundant striae
HUD-03	-72.95501	-3.766789	276	On mudstone near erratic
HUD-04	-72.95448	-3.766469	100	E-W
KUL-01	-72.05176	-2.648109	340	
KUL-04	-72.05573	-2.646835	326	
GRU-07	-72.0392	-2.86228	330	
GRU-08	-72.03876	-2.85408	315	Striations NW-SE, same direction as chatter marks
GRU-08	-72.03876	-2.85408	208	Other striation direction at site
GRU-09	-72.06422	-2.688667	350	
GRU-11	-72.06728	-2.725315	294	
SCH-03	-71.92941	-2.96068	180	Ice flowed N-S
JSP-01	-71.99707	-2.549019	253	Also 278, polished surfaces
JSP-05	-72.01262	-2.557857	308	
JSP-06	-72.00761	-2.53556	314	
17HOG-01	-72.61696	-2.882247	340	Multiple; 330-360 at sample; N of sample 30-45, 80 (fine)
17BOR-03	-72.65079	-3.606525	15	More S-N (SSE-NNW) than throughflow over ice divide
17TPK-01	-72.72968	-3.279449	73	
17MOT-01	-72.7906	-3.180104	344	
17BN-03	-73.02774	-13.41977	310	
17BN-06	-73.02307	-13.39206	305	
17VK-01	-75.02011	-12.75514	315	Very poorly developed
17RH-01	-74.92565	-11.33769	258	Very faint striae on rust-colored upper surface
17RH-02	-74.92611	-11.33987	238-258	Good but discontinuous

Table 3.2 continued

17MAB-02	-74.87140	-12.23910	328	Microstriae
17MH-02	-74.29932	-9.58617	340	
17BRA-01	-74.89899	-12.23493	220	

Table 3.3. *In situ* ^{14}C measurements for samples from western DML.

Sample Name	PLID ^a	Sample Mass (g)	C yield (μg)	Diluted Gas Mass (μg)	$\delta^{13}\text{C}$ (‰)	$^{14}\text{C}/^{13}\text{C}$ (10^{-12})	$^{14}\text{C}/\text{C}_{\text{total}}$ ^b (10^{-14})	^{14}C (10^5 atoms)	$[^{14}\text{C}]$ ^c (10^5 atoms g^{-1})
GRO-01	202101471	5.0815	6.6 ± 0.1	295.2 ± 3.6	-43.58 ± 0.2	6.0777 ± 0.1289	6.2351 ± 0.1360	8.0764 ± 0.3940	1.5894 ± 0.0775 ^d
GRO-02	202102048	3.9770	28.8 ± 0.4	272.3 ± 3.3	-43.56 ± 0.2	3.5565 ± 0.1139	3.5771 ± 0.1202	5.1427 ± 0.2060	1.2931 ± 0.0518 ^f
GRO-03	202102044	5.0512	6.4 ± 0.1	293.4 ± 3.6	-45.37 ± 0.2	1.8020 ± 0.0727	1.7242 ± 0.0767	2.3276 ± 0.1387	0.4608 ± 0.0275 ^f
MID-03	202101472	5.0704	4.2 ± 0.1	298 ± 3.6	-43.8 ± 0.2	9.9679 ± 0.1396	10.334 ± 0.1472	14.436 ± 0.4319	2.84717 ± 0.0852 ^d
MID-05	202102053	4.6866	2.2 ± 0.1	296.4 ± 3.6	-45.96 ± 0.2	4.9238 ± 0.1424	5.0054 ± 0.1499	7.2655 ± 0.2541	1.5503 ± 0.0542 ^f
YST06	202101659	5.0045	29.8 ± 0.4	271.5 ± 3.3	-42.63 ± 0.2	16.9693 ± 0.1994	17.735 ± 0.2105	24.7020 ± 0.4682	4.936 ± 0.0936 ^e
SVE-02	202102041	5.0557	19.9 ± 0.3	278.9 ± 3.4	-43.22 ± 0.2	2.4201 ± 0.0828	2.3797 ± 0.0875	3.2919 ± 0.1546	0.6511 ± 0.0306 ^f
SVE-03	202101470	4.8639	13.3 ± 0.2	286.9 ± 3.5	-40.77 ± 0.2	3.3501 ± 0.0928	3.3696 ± 0.0982	3.6208 ± 0.3528	0.7444 ± 0.0725 ^d
SVE04	202101660	5.0242	9.9 ± 0.2	290.3 ± 3.5	-44.88 ± 0.2	4.4458 ± 0.0921	4.5085 ± 0.0971	4.2723 ± 0.1865	0.8503 ± 0.0371 ^e
SVE-06	202102042	3.0688	3.4 ± 0.1	295.8 ± 3.6	-45.26 ± 0.2	3.3142 ± 0.0928	3.3154 ± 0.0978	4.7315 ± 0.1742	1.5418 ± 0.0568 ^f
VID-04	202201467	3.0290	5.0 ± 0.1	293.1 ± 3.6	-44 ± 0.2	1.8253 ± 0.0582	1.7492 ± 0.0615	2.1979 ± 0.1196	0.7256 ± 0.0395 ^g
VID-06	202102050	3.0481	7.4 ± 0.1	292.4 ± 3.6	-45.36 ± 0.2	5.0749 ± 0.1525	5.1676 ± 0.1606	7.5347 ± 0.2704	2.472 ± 0.0887 ^f
STR-01	202102039	5.0364	4.8 ± 0.1	293.6 ± 3.6	-45.58 ± 0.2	5.1994 ± 0.1242	5.2975 ± 0.1308	7.7400 ± 0.2315	1.5368 ± 0.0460 ^f
STR-07	202201466	5.0342	3.6 ± 0.1	295.9 ± 3.6	-46.04 ± 0.2	5.5541 ± 0.1061	5.6675 ± 0.116	8.2171 ± 0.2116	1.6323 ± 0.0420 ^g
STR-09	202102047	2.8125	3.9 ± 0.1	296.3 ± 3.6	-45.33 ± 0.2	4.6471 ± 0.1166	4.7177 ± 0.1229	6.8556 ± 0.2166	2.4376 ± 0.0770 ^f
HUD-03	202201470	4.9937	6.2 ± 0.1	294.6 ± 3.6	-45.81 ± 0.2	3.1461 ± 0.0770	3.1368 ± 0.0811	4.3488 ± 0.1528	0.8709 ± 0.0306 ^g
HUD-04	202201471	2.3697	7.2 ± 0.1	297.2 ± 3.6	-45.76 ± 0.2	2.3191 ± 0.0601	2.2679 ± 0.0634	3.0683 ± 0.1268	1.2948 ± 0.0535 ^g
17BN-03	202102046	5.0599	30.0 ± 0.4	270.5 ± 3.3	-41.47 ± 0.2	6.2579 ± 0.1401	6.4394 ± 0.1481	9.5002 ± 0.3115	1.8776 ± 0.0616 ^h
17BN-04	202102045	5.0545	31.0 ± 0.4	269 ± 3.3	-42.89 ± 0.2	6.1811 ± 0.1554	6.3482 ± 0.1640	9.2681 ± 0.3273	1.8336 ± 0.0648 ^h
17BN-08	202101475	5.0684	24.7 ± 0.3	275.1 ± 3.4	-42.0 ± 0.2	6.6216 ± 0.1150	6.8197 ± 0.1215	8.9343 ± 0.3858	1.7628 ± 0.0761 ^d
17FR-02	202102043	4.9608	25.5 ± 0.4	271.3 ± 3.3	-43.59 ± 0.2	5.5277 ± 0.1439	5.6548 ± 0.1518	8.2149 ± 0.3088	1.656 ± 0.0622 ^h
17FR-03	202101476	4.8045	24.4 ± 0.3	276.7 ± 3.4	-41.05 ± 0.2	7.5605 ± 0.1144	7.8191 ± 0.1210	10.5280 ± 0.3923	2.1913 ± 0.0817 ^d
17MFE01	202101648	5.0211	28.6 ± 0.4	275.1 ± 3.4	-42.15 ± 0.2	16.7946 ± 0.1755	17.5590 ± 0.1854	24.3960 ± 0.4396	4.8587 ± 0.0875 ^e
17VK-01	202102033	4.9103	41.9 ± 0.6	257 ± 3.1	-40.25 ± 0.2	13.4604 ± 0.2097	14.0660 ± 0.2219	21.13800 ± 0.4631	4.3049 ± 0.0943 ^h
17VK02	202201468	5.0445	48.7 ± 0.6	252.6 ± 3.1	-39.79 ± 0.2	16.2513 ± 0.1565	17.0250 ± 0.1656	25.71100 ± 0.4112	5.0969 ± 0.0815 ^g
17CJ-01	202102035	5.1150	13.9 ± 0.2	286 ± 3.5	-44.27 ± 0.2	17.0214 ± 0.2453	17.7590 ± 0.2585	26.9100 ± 0.5453	5.2609 ± 0.1066 ^h
17RH-01	202102038	5.0106	5.3 ± 0.1	293.4 ± 3.6	-45.37 ± 0.2	30.7884 ± 0.3152	32.2240 ± 0.3317	48.4530 ± 0.8008	9.6702 ± 0.1598 ^h

Table 3.3 continued

17RH-02	202101477	5.0494	5.1 ± 0.1	294.2 ± 3.6	-43.57 ± 0.2	30.7112 ± 0.3328	32.2030 ± 0.3509	47.6390 ± 0.8614	9.4345 ± 0.1706 ^d
17MAB01	202101642	5.0245	15.7 ± 0.2	287.6 ± 3.5	-43.05 ± 0.2	22.2951 ± 0.2478	23.3440 ± 0.2615	33.3690 ± 0.5966	6.6412 ± 0.1187 ^e
17MAB02	202101645	5.0410	16.6 ± 0.2	286.1 ± 3.5	-43.06 ± 0.2	24.6202 ± 0.2180	25.7960 ± 0.2300	37.0360 ± 0.5998	7.3471 ± 0.1190 ^e
17MAB04	202201469	5.0452	37.8 ± 0.5	262.7 ± 3.2	-41.11 ± 0.2	19.0326 ± 0.1909	19.9410 ± 0.2018	30.3090 ± 0.4881	6.0076 ± 0.0968 ^g
17BRA01	202101646	5.0391	12.5 ± 0.2	288.6 ± 3.5	-43.84 ± 0.2	24.3532 ± 0.2184	25.4940 ± 0.2303	36.2900 ± 0.5941	7.2017 ± 0.1179 ^e
17MH02	202101657	3.8174	26.8 ± 0.4	272.2 ± 3.3	-42.87 ± 0.2	23.7312 ± 0.2168	24.8630 ± 0.2288	35.3640 ± 0.5837	9.264 ± 0.1529 ^e
17MH03	202101655	5.0209	26.1 ± 0.4	280.1 ± 3.4	-43.28 ± 0.2	26.1754 ± 0.2398	27.4310 ± 0.2529	40.2670 ± 0.6597	8.0199 ± 0.1314 ^e
Procedural blank data									
PB1-032321	202101468	-	4.1 ± 0.1	307.7 ± 3.7	-43.82	1.2488 ± 0.0737	1.1455 ± 0.0779	1.8138 ± 0.1252	
PB1-032521	202101469	-	4.0 ± 0.1	298.0 ± 3.6	-44.6	1.2531 ± 0.0644	1.1479 ± 0.0680	1.7716 ± 0.1071	
PB1-040321	202101473	-	5.9 ± 0.1	293.9 ± 3.6	-43.73	0.9846 ± 0.0052	0.8654 ± 0.0554	1.3157 ± 0.0857	
PB1-040621	202101474	-	3.5 ± 0.1	296.2 ± 3.6	-43.91	1.1538 ± 0.0484	1.0437 ± 0.0513	1.5920 ± 0.0806	
PB1-041521	202101478	-	2.6 ± 0.1	297.4 ± 3.6	-44.41	0.7731 ± 0.0054	0.6423 ± 0.0566	0.9825 ± 0.0874	
PB1-042921	202101479	-	4.2 ± 0.1	297.5 ± 3.6	-44.37	1.1447 ± 0.0466	1.0340 ± 0.0493	1.5958 ± 0.0785	
<i>Meanⁱ</i>								<i>1.5119 ± 0.3133^d</i>	
PB1-052521	202101639	-	6.9 ± 0.1	303.4 ± 3.7	-44.81	1.7682 ± 0.0572	1.6911 ± 0.0605	2.68532 ± 0.1016	
PB1-060121	202101640	-	6.3 ± 0.1	299.3 ± 3.6	-45.72	1.8171 ± 0.0637	1.7401 ± 0.0672	2.72047 ± 0.1101	
PB1-061921	202101649	-	6.7 ± 0.1	296.9 ± 3.6	-42.33	1.8025 ± 0.0573	1.7309 ± 0.0607	2.67745 ± 0.0995	
PB1-072421	202101661	-	6.5 ± 0.1	294.0 ± 3.6	-45.16	1.7384 ± 0.0544	1.6577 ± 0.0575	2.55091 ± 0.0937	
<i>Meanⁱ</i>								<i>2.6590 ± 0.0742^e</i>	
PB1-102221	202102037	-	2.7 ± 0.1	295.7 ± 3.6	-45.11	0.3905 ± 0.0514	0.2389 ± 0.0544	0.3654 ± 0.0833	
PB1-111921	202102056	-	1.6 ± 0.1	297.8 ± 3.6	-45.83	0.3348 ± 0.0320	0.1796 ± 0.0341	0.2721 ± 0.0518	
<i>Meanⁱ</i>								<i>0.3187 ± 0.0660^f</i>	
PB1-042922	202201453	-	2.1 ± 0.1	296.3 ± 3.6	-46.14	0.4434 ± 0.0259	0.2940 ± 0.0278	0.4492 ± 0.0428	
PB1-052722	202201457	-	2.2 ± 0.1	299.8 ± 3.6	-45.97	0.49266 ± 0.0572	0.3468 ± 0.0305	0.5417 ± 0.0481	
<i>Meanⁱ</i>								<i>0.4954 ± 0.0654^g</i>	
PB2-102621	202102040	-	1.9 ± 0.1	296.6 ± 3.6	-45.4	0.4763 ± 0.0398	0.3287 ± 0.0422	0.4981 ± 0.0643	
PB2-112321	202102057	-	1.3 ± 0.1	300.7 ± 3.7	-45.59	0.3183 ± 0.0541	0.1627 ± 0.0572	0.2483 ± 0.0873	
<i>Meanⁱ</i>								<i>0.3732 ± 0.1766^h</i>	

^aAMS PRIME Lab ID (PLID) numbers^bMean procedural blank was subtracted based on the letter corresponding to the average blank below

^c Values are corrected for mass-dependent graphitization blank
ⁱ TF1 = Tube furnace 1; TF2 = Tube furnace 2 (see Appendix A)

Table 3.4. *In situ* ^{10}Be and ^{26}Al measurements for selected samples from western DML

Sample ID	PLID (^{10}Be) ^a	Sample Mass (g)	^9Be Carrier (mg)	Measured ^{10}Be Ratio (10^{-15})	[^{10}Be] (10^5 atoms g^{-1}) ^b
STR-10	202001605	18.606	0.2689	92.9765 ± 5.4698	0.9841 ± 0.8963
GRU04	202001603	12.085	0.2635	444.318 ± 10.1239	6.4719 ± 0.1476
GRU10	202001604	20.099	0.2689	961.263 ± 19.0289	8.5933 ± 0.1702
HUD07	202001606	11.782	0.2685	1282.7900 ± 17.6153	19.5345 ± 0.2683
SCH04B	202001607	6.082	0.2686	1977.5400 ± 22.2056	58.3616 ± 0.6554
COQTZ-5304	202001608	5.078	0.2689	697.5760 ± 12.3386	24.6807 ± 0.4368
Cblk5304-1	202001609	-	0.2693	0.1821 ± 0.2624	-

Table 3.4 continued

PLID (^{26}Al) ^a	Native Aluminum ^c (mg)	^{27}Al Carrier ^d (mg)	Measured ^{26}Al Ratio (10^{-15})	[^{26}Al] (10^6 atoms g^{-1}) ^e
202001605	3.288	-	188.5250 ± 11.7894	0.7437 ± 0.0465
202001603	1.709	-	1372.1200 ± 36.4001	4.3315 ± 0.1149
202001604	3.311	-	1546.6100 ± 40.1999	5.6874 ± 0.1478
202001606	2.935	-	1276.6700 ± 31.9319	7.0993 ± 0.1776
202001607	1.649	-	5671.9399 ± 137.8640	34.3283 ± 0.8344
202001608	0.084	1.8279	1909.4399 ± 48.7365	16.0482 ± 0.4096
202001609	-	1.8529	0.0000 ± 0.6401	-

^aAMS PLID numbers from PRIME Lab

^bBlank corrected with $0.1217 \pm 0.1754 \times 10^5$ atoms.

^cNative aluminum is measured with Inductively-coupled plasma optical emissions spectrometer (ICP-OES) at PRIME Lab

^dAluminum carrier is added if native aluminum is < 1.5 mg.

^eBlank corrected with $0.0000 \pm 1.4389 \times 10^4$ atoms.

Table 3.5. Apparent exposure age results from field sites in Antarctica.

ID	Type	Elevation	Latitude	Longitude	^{14}C age	^{10}Be age ^a	^{26}Al age ^a
		(m)	(DD)	(DD)	(ka \pm 1 σ (2 σ))	(ka \pm 1 σ (2 σ))	(ka \pm 1 σ (2 σ))
GRO-01	BR	1083	-71.9495	-2.0043	3.5 \pm 0.2 (0.6)	57.1 \pm 1.0 (3.6)	44.8 \pm 1.2 (4.1)
GRO-02	ER	1067	-71.95061	-2.005607	2.9 \pm 0.1 (0.4)	-	-
GRO-03	BR	890	-71.97177	-1.99038	1.0 \pm 0.1 (0.1)	35.2 \pm 0.8 (2.2)	29.0 \pm 1.1 (2.8)
MID-03	ER	1630	-72.7364	-2.0842	4.6 \pm 0.2 (0.8)	93.2 \pm 1.3 (5.8)	77.4 \pm 1.9 (7.2)
MID-05	ER	1551	-72.7348	-2.0713	2.3 \pm 0.1 (0.3)	2.7 \pm 0.2 (0.3)	2.6 \pm 0.1 (0.2)
YST-06	ER	1670	-72.4917984	-2.827147	9.6 \pm 0.3 (2.2)	92.8 \pm 1.8 (5.9)	89.0 \pm 2.4 (8.4)
SVE-02	ER	830	-72.0951	-0.4016	1.6 \pm 0.1 (0.2)	106.6 \pm 2.4 (6.9)	95.1 \pm 2.8 (9.0)
SVE-03	BR	830	-72.0951	-0.4016	1.9 \pm 0.2 (0.3)	67.1 \pm 1.5 (4.3)	40.0 \pm 1.1 (3.7)
SVE-04	ER	866	-72.0977936	-0.405136	2.1 \pm 0.1 (0.3)	121.5 \pm 2.4 (7.8)	91.5 \pm 2.3 (8.6)
SVE-06	BR	889	-72.0993	-0.4075	4.3 \pm 0.2 (0.7)	91.6 \pm 2.5 (6.1)	54.7 \pm 1.7 (5.1)
VID-04	ER	1159	-72.4169235	-2.2987721	1.3 \pm 0.1 (0.2)	5.2 \pm 0.3 (0.4)	4.9 \pm 0.3 (0.5)
VID-06	ER	1260	-72.4185	-2.3064	5.4 \pm 0.3 (0.9)	58.5 \pm 1.6 (3.8)	53.6 \pm 1.6 (5.0)
STR-01	BR	741	-71.5653	-1.1732	5.0 \pm 0.2 (0.8)	130.5 \pm 2.3 (8.3)	87.3 \pm 2.3 (8.2)
STR-07	BR	780	-71.5677567	-1.17837	5.3 \pm 0.2 (0.9)	-	-
STR-09	BR	929	-71.58659	-1.1913	8.4 \pm 0.5 (1.8)	-	-
STR-10	ER	929	-71.5865936	-1.1913	-	7.0 \pm 0.4 (0.6)	8.2 \pm 0.5 (0.9)
HUD-03	ER	1970	-72.954483	-3.766469	0.8 \pm 0.03 (0.1)	-	-
HUD-04	BR	1968	-72.954483	-3.766469	1.2 \pm 0.1 (0.2)	-	-
KUL-03	ER	1351	-72.0555496	-2.647042	-	11.0 \pm 0.3 (0.7)	10.9 \pm 0.3 (1.0)
17BN-03	ER	587	-73.02774	-13.41977	8.7 \pm 0.5 (1.9)	86.0 \pm 2.1 (5.6)	69.5 \pm 1.9 (6.5)
17BN-04	ER	562	-73.026	13.415	8.8 \pm 0.6 (2.0)	109.2 \pm 3.1 (7.3)	74.7 \pm 2.3 (7.0)
17BN-08	ER	549	-73.02307	-13.39206	8.1 \pm 0.6 (1.7)	87.9 \pm 1.8 (5.6)	65.1 \pm 1.6 (6.0)
17FR-02	ER	735	-73.391	13.040	5.7 \pm 0.3 (1.0)	3.8 \pm 0.2 (0.3)	-
17FR-03	ER	736	-73.39103	-13.04132	9.0 \pm 0.6 (2.0)	6.3 \pm 0.3 (0.5)	-
17MFE01	ER	1742	-74.314453	-9.387043	11.3 \pm 0.4 (2.9)	155.4 \pm 2.8 (9.9)	128.1 \pm 3.3 (12.2)
17VK-01	BR	1561	-75.02011	-12.75514	8.7 \pm 0.3 (1.9)	701.3 \pm 19.5 (53.3)	410.9 \pm 9.5 (44.6)

Table 3.5 continued

17VK02	BR	1561	-75.02011	-12.75514	13.0 ± 0.5 (3.8)	695.9 ± 15.3 (51.4)	427.5 ± 9.3 (46.6)
17CJ-01	BR	1609	-75.05076	-12.66977	12.4 ± 0.6 (3.5)	305.7 ± 6.0 (20.4)	293.9 ± 8.7 (30.6)
17RH-01	BR	2215	-74.925645	-11.337693	19.3 ± 1.3 (9.2)	2681.2 ± 131.1 (357.7)	1507.3 ± 59.3 (303.3)
17RH-02	BR	2214	-74.926107	-11.339867	16.5 ± 0.9 (6.3)	2698.4 ± 100.9 (351.5)	1438.4 ± 54.4 (277.7)
17MAB01	BR	1581	-74.868265	-12.264	Saturated	604.3 ± 18.7 (45.6)	375.1 ± 9.2 (40.1)
17MAB02	BR	1729	-74.8714	-12.2391	Saturated	2846.8 ± 97.7 (384.3)	1876.6 ± 111.6 (479.2)
17MAB04	ER	1640	-74.866834	-12.247551	17.6 ± 1.0 (7.1)	679.4 ± 13.0 (49.5)	483.2 ± 15.3 (55.3)
17BRA01	BR	1679	-74.89899	-12.23493	Saturated	1250.4 ± 33.3 (107.8)	929.0 ± 26.3 (133.2)
17MH02	BR	1959	-74.299316	-9.586166	Saturated	2676.9 ± 94.9 (345.1)	2138.0 ± 221.0 (662.6)
17MH03	ER	1939	-74.3036	-9.605483	23.2 ± 2.1 (15.5)	748.0 ± 15.1 (55.6)	619.1 ± 17.5 (75.4)

^a Original ¹⁰Be and ²⁶Al exposure ages were published in Andersen et al. (2020). See Andersen et al. (2020) for analytical details. The exposure ages were recalculated for this study following the procedures outlined in Appendix A.

Table 3.6. Modern day ice stream elevations and their latitude and longitude points compared to LGM best-fit model estimates.

Sample name	Type	Sample Latitude	Sample Longitude	Elevation	Ice Stream Latitude	Ice Stream Longitude	Ice stream elevation	Elevation above ice stream	LGM maximum model estimates from best-fit model
		DD	DD	(m)	DD	DD	(m)	(m)	[25th - 75th] (m) ^a
GRO-01	BR	-71.9495	-2.0043	1083	-72.01473	-1.32434	490	593	797 - 867
GRO-02	ER	-71.9506	-2.00561	1067	-72.01473	-1.32434	490	577	797 - 867
GRO-03	BR	-71.9718	-1.99038	890	-72.01473	-1.32434	490	400	797 - 867
MID-03	ER	-72.7364	-2.0842	1630	-72.69135	-2.53421	1345	285	373 - 435
MID-05	ER	-72.7348	-2.0713	1551	-72.69135	-2.53421	1345	206	373 - 435
YST-06	ER	-72.4918	-2.82715	1670	-72.50561	-2.58231	1159	511	505 - 579
SVE-02	ER	-72.0951	-0.4016	830	-72.01473	-1.32434	490	340	842 - 902
SVE-03	BR	-72.0951	-0.4016	830	-72.01473	-1.32434	490	340	842 - 902
SVE-04	ER	-72.0978	-0.40514	866	-72.01473	-1.32434	490	376	842 - 902
SVE-06	BR	-72.0993	-0.4075	889	-72.01473	-1.32434	490	399	842 - 902
VID-04	ER	-72.4169	-2.29877	1159	-72.44378	-1.72075	991	168	546 - 609
VID-06	ER	-72.4185	-2.3064	1260	-72.44378	-1.72075	991	269	546 - 609
STR-01	BR	-71.5653	-1.1732	741	-71.65305	-0.66613	80	661	802 - 872
STR-07	BR	-71.5678	-1.17837	780	-71.65305	-0.66613	80	700	802 - 872
STR-09	BR	-71.5866	-1.1913	929	-71.65305	-0.66613	80	849	802 - 872
STR-10	ER	-71.5866	-1.1913	929	-71.65305	-0.66613	80	849	802 - 872
HUD-03	ER	-72.955	-3.76679	1970	-72.9686	-3.08486	1616	354	452 - 511
HUD-04	BR	-72.9545	-3.76647	1968	-72.9686	-3.08486	1616	352	452 - 511
KUL-03	ER	-72.0555	-2.64704	1351	-72.13382	-1.56772	625	726	767 - 833
17BN-03	ER	-73.0277	-13.4198	587	-73.12661	-13.749	160	427	740 - 799
17BN-04	ER	-73.0263	-13.4149	562	-73.12661	-13.749	160	402	740 - 799
17BN-08	ER	-73.0231	-13.3921	549	-73.12661	-13.749	160	389	740 - 799
17FR-02	ER	-73.3905	-13.0404	735	-73.44556	-13.37321	555	180	535 - 585
17FR-03	ER	-73.391	-13.0413	736	-73.44556	-13.37321	555	181	535 - 585
MFE01	ER	-74.3145	-9.38704	1742	-74.35095	-8.71998	1725	17	14 - 74
17VK-01	BR	-75.0201	-12.7551	1561	-74.99324	-12.58602	1482	79	119 - 168

Table 3.6 continued

17VK-02	BR	-75.0201	-12.7551	1561	-74.99324	-12.58602	1482	79	119 - 168
17CJ-01	BR	-75.0508	-12.6698	1609	-75.01013	-12.45016	1542	67	78 - 120
17RH-01	BR	-74.9256	-11.3377	2215	-74.95574	-11.49819	1908	329	169 - 261
17RH-02	BR	-74.9261	-11.3399	2214	-74.95574	-11.49819	1908	325	169 - 261
MAB01	BR	-74.8683	-12.264	1581	-74.89868	-12.38811	1401	180	199 - 256
MAB02	BR	-74.8714	-12.2391	1729	-74.89868	-12.38811	1401	328	199 - 256
MAB04	ER	-74.8668	-12.2476	1640	-74.89868	-12.38811	1401	239	199 - 256
BRA01	BR	-74.899	-12.2349	1679	-74.91281	-12.30709	1430	249	162 - 215
MH02	BR	-74.2993	-9.58617	1959	-74.35095	-8.71998	1725	234	14 - 74
MH03	ER	-74.3036	-9.60548	1939	-74.35095	-8.71998	1725	214	14 - 74

^a The 25th – 75th elevation difference is the frequency distribution calculated from the data constrained ensemble (n=27)

CHAPTER 4. A SOFTWARE FRAMEWORK FOR CALCULATING COMPOSITIONALLY DEPENDENT *IN SITU* ¹⁴C PRODUCTION RATES

4.1 Introduction

Rare nuclides produced *in situ* in minerals near the Earth's surface by cosmic-ray bombardment (*in situ* cosmogenic nuclides or CNs) have revolutionized studies of geomorphology and Quaternary geology. CNs build predictably over time in an exposed surface through nucleon spallation and muon reactions (e.g., Gosse and Phillips, 2001). As such, the time at which geomorphic surfaces formed by glacial, fluvial, or marine activity often can be constrained with CNs, an application known as surface exposure dating. In addition, CNs can be used to constrain rates of surficial processes with appropriate interpretive models. These applications rely on measuring the concentrations (atoms g⁻¹, hereafter at g⁻¹) of CNs in a sample and calculating an exposure age or erosion rate based on the production rate (at g⁻¹ yr⁻¹). The most-commonly measured CNs, ¹⁰Be and ²⁶Al (t_{1/2} 1.39 My - Korschinek et al. (2010); Chmeleff et al. (2010); and t_{1/2} 0.705 My - Nishiizumi (2004), respectively), are typically extracted from quartz, due to its simple composition and corresponding resistance to weathering under a wide range of environmental conditions. Their long half-lives make these nuclides useful in dating surfaces that have been exposed up to millions of years. However, their half-lives also render their concentrations insensitive to periods of burial and re-exposure of less than ca. 100 ky – this can lead to problems with exposure dating due to nuclide inventories remaining from prior periods of exposure.

In situ cosmogenic ¹⁴C (*in situ* ¹⁴C) is also produced in quartz, but its 5.7 ky half-life limits its utility for simple exposure dating because its concentration reaches secular equilibrium between production and decay after 25-30 ky of continuous exposure. However, its rapid decay also makes it sensitive to complex periods of burial and exposure since ca. 25-30 ka (e.g., Briner et al., 2014). In addition, its short half-life means measured concentrations are sensitive only to very rapid erosion rates (e.g., Gosse and Phillips, 2001; von Blanckenburg, 2005; Hippe, 2017; Hippe et al., 2021), making many eroding landscape elements good targets for *in situ* ¹⁴C studies. *In situ* ¹⁴C is thus emerging as a powerful addition to the CN toolkit.

Several techniques for extracting *in situ* ¹⁴C from sand-sized quartz grains have been established (Lifton et al., 2001, 2015b; Hippe et al., 2013; Goehring et al., 2019; Fülöp et al., 2019;

Lupker et al., 2019) but while coarse-grained quartz is common, it is not ubiquitous. Landscapes dominated by mafic or intermediate lithologies generally lack quartz, and fine-grained lithologies can limit the efficacy of quartz purification techniques, thus applying *in situ* ^{14}C to such rock types is currently problematic. However, the ability to extract and interpret *in situ* ^{14}C concentrations reliably from quartz-poor and fine-grained lithologies would significantly broaden its applications to additional landscapes and enable pairing with additional nuclides such as ^{36}Cl . Indeed, early studies of *in situ* ^{14}C in terrestrial rocks utilized whole-rock samples (e.g., Jull et al., 1992, 1994), until procedural difficulties shifted the focus to the simpler quartz production and extraction systematics (Lifton, 1997; Lifton et al., 2001).

As a first step in expanding the range of available sample targets, we have developed a software framework that estimates the production of *in situ* ^{14}C from major elements found in typical rocks and potential mineral separates. We modified the MATLAB[®] code from Lifton et al. (2014) to calculate compositionally dependent, site-specific production rates using nuclide-specific scaling, major-element oxide compositions, and measured and modeled nucleon excitation functions, referenced to geologically calibrated *in situ* ^{14}C spallogenic production rates in quartz. Anticipating that appropriate extraction and CO_2 purification procedures can be developed, this new framework thus provides a critical first step for potential future applications incorporating quartz-poor or fine-grained samples.

4.2 Constraining compositionally dependent *in situ* ^{14}C production rates

4.2.1 Geologic and experimental production rate calibrations

In situ CN applications require accurate estimates of the rate at which a given nuclide of interest is produced in the target mineral or rock. This is typically achieved by calibrating the production rate with CN measurements in samples from one or more sites with an independently well-constrained exposure history (e.g., Lifton et al., 2015a; Phillips et al., 2016; Borchers et al., 2016), or for radionuclides only demonstrable surface stability such that measured CN concentrations can be inferred to have reached a secular equilibrium between production and decay, at which point the concentration is only a function of time-integrated production rate and the decay constant (e.g., Jull et al., 1992; Borchers et al., 2016). Production rates can also be calibrated experimentally by exposing high-purity, low background targets to the secondary cosmic-ray flux

at given sites for a known duration under well-constrained conditions (e.g., Nishiizumi et al., 1996; Brown et al., 2000; Vermeesch et al., 2009).

Since production rates cannot be calibrated at every place on Earth, these site-specific estimates are typically scaled to other sites of interest using an appropriate scaling framework that accounts for spatial and temporal variations in the secondary cosmic-ray flux, arising from fluctuations in the geomagnetic field (parameterized by effective vertical cutoff rigidity, R_c , in GV), atmospheric depth (X , in g cm^{-2}), and solar modulation (described by the parameter Φ , in MeV) (e.g., Lifton et al., 2014). Such scaling frameworks are typically referenced to conditions corresponding to sea-level and high geomagnetic latitude (SLHL).

Geologic calibrations are generally preferable for minerals with specific compositions since samples from well-constrained sites should incorporate natural variability relevant over geologic time spans. Such calibrations for *in situ* ^{14}C have focused on quartz to date, given its simple chemistry and weathering resistance (e.g., Schimmelpfennig et al., 2012; Young et al., 2014; Lifton et al., 2015a; Borchers et al., 2016; Phillips et al., 2016), yet variable compositions require more complicated consideration of the compositional dependence of CN production (e.g., ^{36}Cl ; Marrero et al., 2016a). It is often useful in such cases to utilize theoretical production rate estimates based on integrals of the differential cosmic-ray flux and the relationship between reaction probability and incident particle energy.

4.2.2 Theoretical production rate estimates

The probability that a given nuclear reaction will occur at a given kinetic energy E of an incident particle is described by the reaction cross-section (σ), in units of barns ($1 \text{ barn} = 10^{-24} \text{ cm}^2$). With the advent of accelerator mass spectrometry (AMS), cross-section measurements for reactions producing CNs have become relatively common, and knowledge of the variation of σ as a function of E for those reactions (known as an excitation function) are continuing to improve (e.g., Reedy, 2013). Proton-induced reactions are simpler to measure than those induced by neutrons because it is easier to accelerate protons into a mono-energetic beam. Mono-energetic (or quasi-mono-energetic) neutron reaction cross-sections are more difficult to obtain, however, and thus are often estimated from analogous proton cross-sections (Reedy, 2013).

Measured or modeled excitation functions can then be used to estimate theoretical production rates for a CN of interest using Eq. (4.1) below (e.g., Masarik and Beer, 2009),

$$P_j(X, R_C, \Phi) = \sum_i ND_i \sum_k \int_0^\infty \sigma_{ijk}(E_k) J_k(E_k, X, R_C, \Phi) dE_k \quad (4.1)$$

where ND_i is the target number density, or number of atoms of the target element i per gram of sample material (at g^{-1}), $\sigma_{ijk}(E_k)$ is the cross-section for the production of nuclide j (cm^2) by particles of type k with energy E_k (MeV), and $J_k(E_k, X, R_C, \Phi)$ is the differential flux of atmospheric cosmic-ray particles ($\text{cm}^{-2} \text{yr}^{-1} \text{MeV}^{-1}$) of type k with energy E_k at a location and time specified by X , R_C , and Φ .

The production of *in situ* ^{14}C in silicates is dominantly from spallation of O, and theoretical simulations suggest minor spallogenic production from Mg, Al, and Si (Masarik and Reedy, 1995; Masarik, 2002). Production of *in situ* ^{14}C from muons also occurs, either via slow negative muon capture or by fast muon interactions (Heisinger et al., 2002a,b). The muogenic component of *in situ* ^{14}C production in surficial quartz at SLHL is significant, on the order of 20% of total production (e.g., Lupker et al., 2015; Balco, 2017). However, muogenic production of *in situ* ^{14}C has only been estimated experimentally from ^{16}O (Heisinger et al., 2002a; 2002b). Further work is needed in this area to better understand production from other muogenic reactions. We therefore focus on the dominant spallogenic pathways for the purposes of this initial study.

4.3 Methods

4.3.1 Software framework

Our MATLAB[®]-based compositionally dependent *in situ* ^{14}C production rate software framework builds on the LSDn nuclide-dependent scaling formulation of Lifton et al. (2014), which uses the analytical approximations to Monte Carlo calculations of atmospheric differential flux spectra of neutrons, protons, and muons as a function of X , R_C , and Φ (Sato and Niita, 2006; Sato et al., 2008). We also incorporate the gridded R_C (global grids of cutoff rigidity) and dipolar R_{CD} (geocentric dipolar cutoff rigidity) models of Lifton (2016), based on the SHA.DIF.14k paleomagnetic model (Pavón-Carrasco et al., 2014). This work accounts for effects of variable sample compositions on *in situ* ^{14}C production by incorporating relevant reaction excitation functions and number densities for elements in the standard suite of major-element oxide compositions. Output from this new framework should complement current web-based cosmogenic nuclide calculators incorporating the LSDn scaling framework and *in situ* ^{14}C ,

including version 3 of the University of Washington cosmogenic-nuclide calculators (herein UWv3: hess.ess.washington.edu) (Balco et al., 2008) and the Cosmic-Ray-produced NUclide Systematics on Earth project (CRONUS-Earth) calculator (CRONUSCalc; <http://cronus.cosmogenicnuclides.rocks/>; Marrero et al., 2016).

Reaction excitation functions for neutrons and protons were compiled from Reedy (2007, 2013) and the JENDL/HE-2007 database (Fukahori et al., 2002; Watanabe et al., 2011) found in the online Evaluated Nuclear Data File (ENDF, <https://www-nds.iaea.org/exfor/endl.htm>, accessed April 2020; Brown et al., 2018), for each of the major elements included in typical elemental oxide analyses. We consider empirical excitation functions to be generally more reliable than those derived from nuclear reaction models, and thus, we use measured functions, if available. Five neutron and proton excitation functions are based on measurements from Reedy (2007, 2013) (O, Mg, Al, Si, Fe), while we used modeled neutron and proton reaction excitation functions from JENDL/HE-2007 for the most abundant isotopes of the remaining elements considered (^{23}Na , ^{31}P , ^{39}K , ^{40}Ca , ^{48}Ti , ^{55}Mn). Apart from the measured excitation function for *in situ* ^{14}C production by neutron spallation from oxygen (Reedy, 2013), it is important to note that most of the Reedy (2007, 2013) neutron excitation functions are not directly measured but instead are derived from measured proton excitation functions. We utilized the JENDL/HE-2007 database because the relevant excitation functions extended to a maximum energy of 10 GeV considered by Sato and Niita (2006) and Sato et al. (2008); a version of that nuclear data library was also utilized by those studies. The exceptions were the excitation functions for ^{31}P , extending only to 0.2 GeV. Each excitation function was interpolated into logarithmic energy bins from 1 MeV to 200 GeV for both neutron ($\text{XX}(n,x)^{14}\text{C}$) and proton ($\text{XX}(p,x)^{14}\text{C}$) reactions, where XX is the target nuclide (Fig. 4.1). The cross-section at the highest measured or modeled energy reported for each excitation function is assumed to be constant beyond that energy up to 200 GeV, the maximum energy we consider.

We incorporate sample compositions using common major elemental oxide analyses (e.g., from X-Ray Fluorescence (XRF) measurements) to calculate ND for each element considered in Eq. 1. The ND value for each target element in a sample is then calculated per Eq. (4.2), for input to Eq. 4.1:

$$ND = \frac{E_{Fr} * E_{Ox} * N_A}{100 * A_m}, \quad (4.2)$$

where E_{Fr} is the elemental fraction in each oxide (formula mass of each element in its oxide divided by the total formula mass of the oxide (e.g., Mg/MgO or 2Al/Al₂O₃)), E_{Ox} is the measured

major elemental oxide weight percent input by the user, N_A is Avogadro's number ($6.02214076 \times 10^{23}$ atoms mol⁻¹) and A_m is the molar mass of the element in g. This approach works for any silicate major elemental oxide composition input by the user.

4.3.2 Predicted compositionally dependent production rates

Theoretical compositionally dependent site-specific *in situ* ¹⁴C production rates are reported relative to the SLHL *in situ* ¹⁴C production rate in quartz, geologically calibrated as part of the CRONUS-Earth project (e.g., Phillips et al., 2016; Borchers et al., 2016) and supplemented with a subsequent production rate calibration dataset (Young et al., 2014), using the LSDn scaling framework (Lifton et al., 2014, Lifton 2016; Table 4.1). All *in situ* ¹⁴C measurements in these studies were recalculated following Hippe and Lifton (2014). SLHL estimates are referenced to the year 2010 (Lifton et al., 2014; Lifton, 2016) assuming an atmospheric pressure of 1013.25 hPa (converted to atmospheric depth, g cm⁻²), an R_c value of 0 GV, a Φ_{2010} value of 624.5718 MV, and a fractional water content value, 'w', of 0.066 (Sato and Niita, 2006; Phillips et al., 2016). We recalibrated the *in situ* ¹⁴C spallogenic production rate at SLHL in quartz from the studies above by first calculating the unweighted mean and standard deviation of replicate analyses of samples at each site (to avoid biasing the results toward sites with more analyses). Best-fitting SLHL production rate estimates for each site were determined using a χ^2 minimization procedure. The unweighted mean and standard deviation of all sites were then calculated from the site-specific SLHL production rate estimates, yielding global SLHL values for quartz of 13.5 ± 0.9 atoms g⁻¹ yr⁻¹ and 13.7 ± 1.2 atoms g⁻¹ yr⁻¹ for the gridded R_C and geocentric dipolar R_{CD} records of Lifton (2016), respectively, as noted above. The latter is comparable to the calibrated value generated by the UWv3 calculator from the same dataset (Table 4.1). In the following discussion we focus on the gridded R_C value (referenced below as P_{Qcal}), as it provides a somewhat better fit to the global calibration dataset. Corresponding geocentric dipolar values are included in Table 4.3).

For comparison, the purely theoretical *in situ* ¹⁴C production rate by nucleon spallation predicted at SLHL in quartz using Eq. 4.1 is 15.8 atoms g⁻¹ yr⁻¹ (P_{Qref}). This discrepancy with the calibrated value likely reflects uncertainties in both the excitation functions and the nucleon fluxes considered (Reedy, 2013; Sato and Niita, 2006; Sato et al., 2008). Giving more credence to the geologically calibrated quartz values, we account for this discrepancy similarly to Lifton et al. (2014), deriving a compositionally dependent site-specific production rate (P_{CD}) by normalizing

the predicted compositionally dependent production rate at the site of interest (P_{CDpred}) by the ratio of P_{Qcal} to P_{Qref} , per Eq. 4.3. Another way to think of this is that the ratio of P_{CDpred} to P_{Qref} is the compositionally dependent scaling factor, multiplied by the geologically calibrated production rate in quartz, P_{Qcal} .

$$P_{CD} = P_{Qcal} \frac{P_{CDpred}}{P_{Qref}} \text{ at } g^{-1} \text{ yr}^{-1} \quad (4.3)$$

We compare P_{CD} values at SLHL to P_{Qcal} for compositions reflecting both individual minerals (Barthelmy, 2014)(i.e., mineral separates) and a broad range of silicate rock types (Parker, 1967; Fabryka-Martin, 1988) (i.e., whole-rock analyses) (Table 4.2). A pure calcite composition ($CaCO_3$) is assumed for limestone and $MgCa(CO_3)_2$ is assumed for dolomite. Spallation production is only possible from Ca and O, although we included the O number density contribution from CO_2 in the software framework. Thermal neutron production of *in situ* ^{14}C from ^{12}C or ^{13}C is expected to be negligible and is not considered here (e.g., Wright et al., 2019).

4.4 Results and Discussion

4.4.1 Predicted compositionally dependent production rates

Predicted SLHL modern (i.e., 2010) spallogenic production rates for *in situ* ^{14}C in the silicates considered here are generally lower than that from pure quartz (Fig. 4.2; Table 4.3), but spallation production from O dominates throughout the compositional range we explored (Table 4.4). As expected from reaction systematics, ^{14}C production rates tend to decline rapidly with progressively increasing atomic mass of the target nuclide (Fig. 4.2). Interestingly, the production rate predicted for albite using the excitation functions from JENDL/HE-2007 for spallation reactions on ^{23}Na is comparable to that of quartz. We note that the JENDL/HE-2007 model $^{23}Na(n,x)^{14}C$ excitation function exhibits a broad peak between ca. 30-350 MeV with cross-sections comparable to that of the empirical $O(n,x)^{14}C$ excitation function of Reedy (2013) (Fig. 4.1), suggesting similar production magnitudes for the two reactions. To our knowledge, no comparable empirical excitation functions for the $^{23}Na(n,x)^{14}C$ or $^{23}Na(p,x)^{14}C$ reactions have been published to date, making the model reactions difficult to validate. Predicted production rates for Mg-rich silicates such as forsterite and enstatite are ca. 7-10% lower than in quartz, while Al-rich minerals such as Ca- and K-feldspars yield production rates 12-13% below quartz. Ca-rich

wollastonite exhibits less than 1% of its total ^{14}C production from Ca, yielding a production rate more than 20% below that of quartz, while Fe-rich minerals such as ferrosilite and fayalite suggest SLHL production rates ca. 32% and 41% less than quartz, respectively. Predicted production rates for two carbonate minerals considered, calcite and dolomite, are 12% and 3% less than quartz, respectively.

The P_{CD} values for selected rock types (ultramafic, basalt, high-Ca granite, low-Ca granite, and granodiorite; Fabryka-Martin, 1988) follow a similar pattern to the individual minerals, with total production rates less than that of quartz but with less overall variation (Fig. 4.2; Table 4.3). Predicted whole-rock production rates tend to increase with decreasing Fe and Mg content, with P_{CD} values ranging from nearly 15% less than quartz for ultramafic compositions to ca. 5-7% below that of quartz for more felsic compositions. As with the idealized mineral compositions, spallation from O dominates *in situ* ^{14}C production (>90% for all compositions considered), with lesser production from Si, Al, Na, and Mg. Only minor production contributions from Ca and Fe are predicted (typically <1%).

4.4.2 Assessing uncertainty in predicted compositionally dependent production rates

There are three main sources of uncertainty in our predicted production rates, associated with the particle spectra, the geologic production rate calibration for *in situ* ^{14}C in quartz, and the excitation functions. We note that these are not entirely independent, as the LSDn-based production rate calibration utilizes both the particle spectra of Sato et al. (2008) and excitation functions of Reedy (2013). Sato et al. (2008) quote statistical uncertainties in their modeled particle fluxes on the order of 5-20% between ca. 10 km altitudes and sea level, respectively, although Lifton et al. (2014) note that predictions within this altitude range show good agreement with measured differential fluxes and no evidence of systematic errors. The conservative uncertainty in the recalibrated *in situ* ^{14}C global production rate in quartz is on the order of 6-7% using the gridded R_C geomagnetic framework and LSDn scaling. Reedy (2013) suggests uncertainties on the order of 10% for the empirical excitation functions presented. However, Reedy (2013) also suggests that modeled cross-sections may differ from empirical ones for a given nuclide by a factor of ≈ 2 . Thus, assessing the uncertainty in the modeled functions of JENDL/HE-2007 is more difficult.

We attempted to assess this latter uncertainty by comparing results using JENDL/HE-2007 to predictions incorporating the more recent TENDL-2019 database (Koning et al., 2019). We

focused on the proton and neutron excitation functions for ^{14}C production from ^{23}Na , since our predictions using the JENDL/HE-2007 ^{23}Na excitation functions suggest comparable production to that from O (Fig. 4.1; Table 4.3). However, TENDL-2019 excitation functions only extend to an energy of 200 MeV, although at higher resolution than JENDL/HE-2007. We thus compared albite production rates predicted using the JENDL/HE-2007 excitation function alone (Na_J) with those incorporating spliced neutron and proton excitation functions using TENDL-2019 for $E \leq 200$ MeV and JENDL/HE-2007 for $E > 200$ MeV (Na_{TJ}) (Fig. 4.3).

Neutron and proton excitation functions for ^{23}Na have similar thresholds of ca. 30-35 MeV in both JENDL/HE-2007 and TENDL-2019 (Fig. 4.3). Of note, the low-energy peaks in the TENDL-2019 excitation functions are narrower, ca. 30% lower, and occur at a slightly higher energy than those of JENDL/HE-2007 (ca. 150 MeV vs. ca. 90 MeV, respectively). However, the predicted production rate for albite using the spliced Na_{TJ} excitation functions is only ca. 3% less than that using the Na_J excitation functions alone (Table 4.3) which is also reflected in the lower production proportion from Na of ca. 5% in the spliced version, vs. ca. 9% in Na_J version (Table 4.4).

Apart from the modeled ^{23}Na excitation functions, the remaining modeled excitation functions have only a minor impact on the overall production rates we predict. The percentages of total production of *in situ* ^{14}C from ^{55}Mn , ^{48}Ti , ^{40}Ca , ^{39}K , and ^{31}P range from <0.001 to 0.2% for the compositions considered (Table 4.4). Even if the modeled reaction cross sections are off by a factor of 2, as suggested by Reedy (2013), the impact to overall production is small. For instance, doubling the percentage of ^{14}C production from Ca for wollastonite would only increase predicted production to 0.4%. In addition, we argue that calculating production using modeled excitation functions for only the most abundant isotope of each of these elements, instead of excitation functions reflecting their natural isotopic abundances, introduces negligible additional uncertainty. For example, we assume 100% of production of *in situ* ^{14}C from ^{48}Ti , even though ^{48}Ti comprises only 73% of Ti isotopes. However, ^{48}Ti contributes <0.001 % of total production for the compositions we considered; it is unlikely that including excitation functions for other common Ti isotopes would change that prediction significantly. Similar arguments can be made for the other isotopes referenced above. We therefore argue that the overall additional uncertainty in our predictions that might be introduced by using more conservative estimates of potential errors in the modeled reaction cross-sections would be insignificant relative to other uncertainties in the

calculations for the compositions considered. That said, future additional empirical excitation functions for neutron and proton reactions using these elements in their natural abundances would likely improve our predictions.

Based on these results, we suggest assuming a 10% uncertainty for the JENDL/HE-2007 excitation functions overall, pending empirical validation. Thus, considering the three sources of uncertainty above, we suggest a reasonable estimate of current uncertainty on our theoretical production rates might be on the order of 10-15%, also pending validation with geologic calibrations, assuming extraction and CO₂ purification hurdles can ultimately be overcome.

4.4.3 Comparisons with previous studies

We compare output of our software framework to two earlier studies that also calculated theoretical *in situ* ¹⁴C production rates from targets of varying composition (Fabryka-Martin, 1988; Masarik, 2002), without adjusting our predictions to the geologically calibrated production rate in quartz. First, Fabryka-Martin (1988) estimated SLHL secular equilibrium *in situ* ¹⁴C concentrations at depths of ~20 cm for ultramafic rock, basalt, high-Ca granite, low-Ca granite, and limestone compositions, following Parker (1967) (Table 4.5). The equilibrium concentrations were calculated assuming neutron spallation production only from oxygen and a SLHL production rate of 26 atoms g⁻¹ yr⁻¹ from oxygen (Yokoyama et al., 1977) based on excitation functions from Reedy and Arnold (1972). We derived secular equilibrium SLHL production rates from Fabryka-Martin (1988) by multiplying the concentrations by the ¹⁴C decay constant of 1.216 x 10⁻⁴ y⁻¹ (Table 4.5 – P_{O-FM}). Considering only theoretical production from O in our results (Total P_{CDpred} in Table 4.3 multiplied by the corresponding O production proportion in Table 4.4), our P_O values in Table 4.5 are ca. 40-45% below those derived from Fabryka-Martin (1988). However, it should be pointed out that Yokoyama et al. (1977) suggest ±35% uncertainty (1σ) on their *in situ* ¹⁴C production rate estimate used by Fabryka-Martin (1988), so our theoretical P_O values using more accurate particle fluxes and excitation functions lie well within that range.

The second study we considered (Masarik, 2002) is a conference abstract that presents formulas for estimating compositional dependence of *in situ* cosmogenic nuclide SLHL production rates by neutron spallation, including ¹⁴C, derived from numerical simulations. For *in situ* ¹⁴C production, Masarik (2002) considers the target elements O, Mg, Al, Si, and Fe, parameterized in terms of weight fractions of each (Table 4.6). Total production rates from Masarik (2002) (P_{M02})

in Table 4.6 are typically ca. 10-20% higher than neutron-only theoretical production rates for rock and mineral compositions considered in this study (Neutron P_{CDpred} , Table 4.3). Being an abstract, details underlying the simulations and calculations in Masarik (2002) are sparse, but we suggest a combination of differences in the differential neutron flux spectra (Masarik and Beer, 1999 vs. Sato et al., 2008) and excitation functions (e.g., Masarik and Reedy, 1995) vs. Reedy, 2013) used in the two studies, as well as unstated uncertainties in the Masarik (2002) coefficients, may be the sources of the discrepancies in the predictions of the respective studies.

We derived a similar elemental parameterization to that of Masarik (2002) for SLHL *in situ* ^{14}C production in atoms $\text{g-element}^{-1} \text{yr}^{-1}$. We include production from both neutrons and protons for each element we consider, given by

$$P_{CDpred} = 29.01[\text{O}] + 15.59[\text{Na}] + 2.199[\text{Mg}] + 1.67[\text{Al}] + 0.84[\text{Si}] + 0.22[\text{P}] + 0.10[\text{Fe}] + 0.08[\text{K}] + 0.06[\text{Ca}] + 0.05[\text{Ti}] + 0.03[\text{Mn}], \quad (4.4)$$

where the bracketed values are the respective elemental fractions derived from the measured major elemental analysis. *In situ* ^{14}C production rates predicted using this equation for the compositions considered in Table 4.2 are identical to the P_{CDpred} values in Table 4.3, since both are derived using the same software framework.

In addition to the theoretical studies, Handwerger et al. (1999) measured *in situ* ^{14}C concentrations in carbonate deposits (limestone bedrock and tufa) from well-preserved Provo-level shoreline features associated with Pleistocene Lake Bonneville, Utah, to calibrate *in situ* ^{14}C spallogenic production rates in calcite. The late Pleistocene lake-level history of Lake Bonneville is well constrained by traditional radiocarbon dates and has been used for geological calibration of a number of cosmogenic nuclides (Lifton et al., 2015a). *In situ* ^{14}C measurements in Handwerger et al. (1999) were reduced according to standard methods for radiocarbon in organic materials, but Hippe and Lifton (2014) subsequently developed comprehensive data reduction procedures specifically for *in situ* ^{14}C . Unfortunately, Handwerger et al. (1999) do not present full details of their analytical results and calculations – we thus cannot correct their data to current standards using the Hippe and Lifton (2014) protocols. If we assume such corrections would be small relative to the resulting *in situ* ^{14}C concentrations in their calibration samples, neglecting three anomalous results, and using the age of initial Provo shoreline formation from Lifton et al. (2015a) of 18.3 ± 0.3 cal ka BP, their mean *in situ* ^{14}C concentration is $(3.75 \pm 0.26) \times 10^5$ atoms $\text{g}^{-1} \text{CaCO}_3$. This corresponds to a local production rate of ca. 51 atoms $\text{g}^{-1} \text{yr}^{-1}$. In contrast, the theoretical local production rate calculated with our software framework is ca. 43.9 atoms $\text{g}^{-1} \text{yr}^{-1}$, ~15% lower than

the derived local production rate. In addition, the predicted value normalized to P_{Qcal} yields 37.5 atoms $\text{g}^{-1} \text{yr}^{-1}$, 27% lower than Handwerger et al. (1999). Given the uncertainties in the uncorrected Handwerger et al. (1999) dataset, and the suggested uncertainties in our method, we find reasonable agreement between our production rate estimates and that of Handwerger et al. (1999).

4.5 Conclusions

As a first step in exploring potential applications of *in situ* ^{14}C to quartz-poor or fine-grained rock types, we have extended the functionality of the MATLAB[®]-based LSDn nuclide-specific scaling framework (Lifton et al., 2014; Lifton, 2016) to estimate spallogenic production of *in situ* ^{14}C in rock and mineral compositions other than pure quartz at sites of interest. We account for compositionally dependent production by using measured and modeled nucleon excitation functions for target elements in major element oxide analyses (e.g., XRF), in concert with secondary cosmic-ray differential fluxes per Lifton et al. (2014). The ratio of resulting theoretical compositionally dependent *in situ* ^{14}C production rates to the corresponding theoretical quartz production rate are then multiplied by the geologically calibrated production rate in quartz, placing the theoretical production rates in a calibrated context. Exploring a broad range of mineral and rock compositions indicates production is dominated by oxygen spallation as expected (>90% at SLHL), but with a general decrease in total production rate with more mafic (particularly Fe-rich) compositions. Although this study confirms previous work identifying Si, Mg, and Al as important targets, we also find for the first time that Na appears to contribute significantly. Future nucleon excitation function measurements, particularly for Na reactions, should improve the robustness of this software tool further. This framework is thus an important initial step forward in applying *in situ* ^{14}C to a broader array of landscapes.

4.6 Data availability

All MATLAB[®] scripts referenced in this chapter are available at <https://doi.org/10.5281/zenodo.7331947> (Koester and Lifton, 2022).

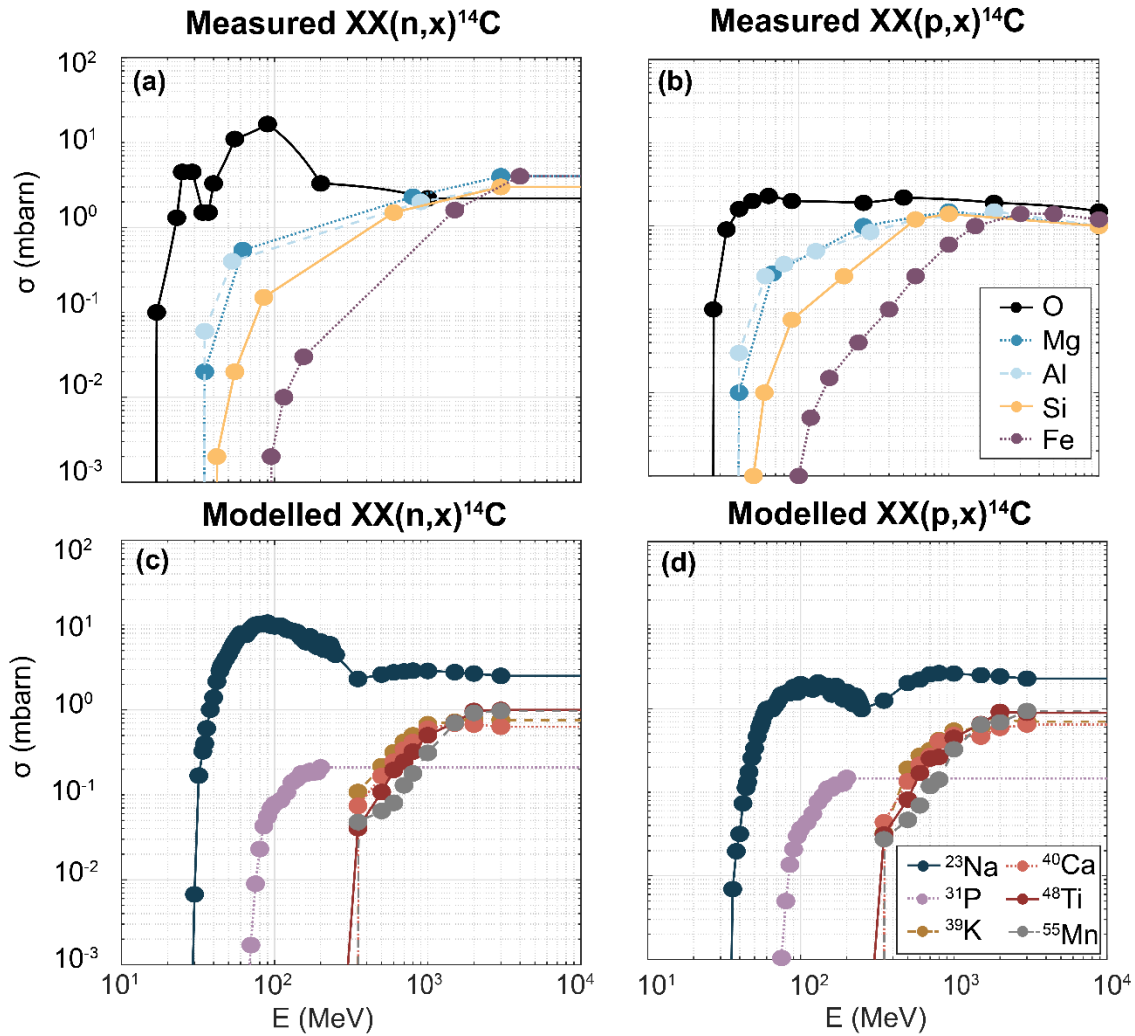


Figure 4.1. Measured (Reedy, 2013) (panels **a** and **b**) and modeled (panels **c** and **d**) neutron and proton reaction excitation functions for *in situ* ^{14}C production from various targets. The lines are linearly interpolated between points. Note that modeled predictions for ^{23}Na (JENDL/HE-2007; Fukahorit et al., 2002; Watanabe et al., 2011) suggest the highest production of all nuclides considered.

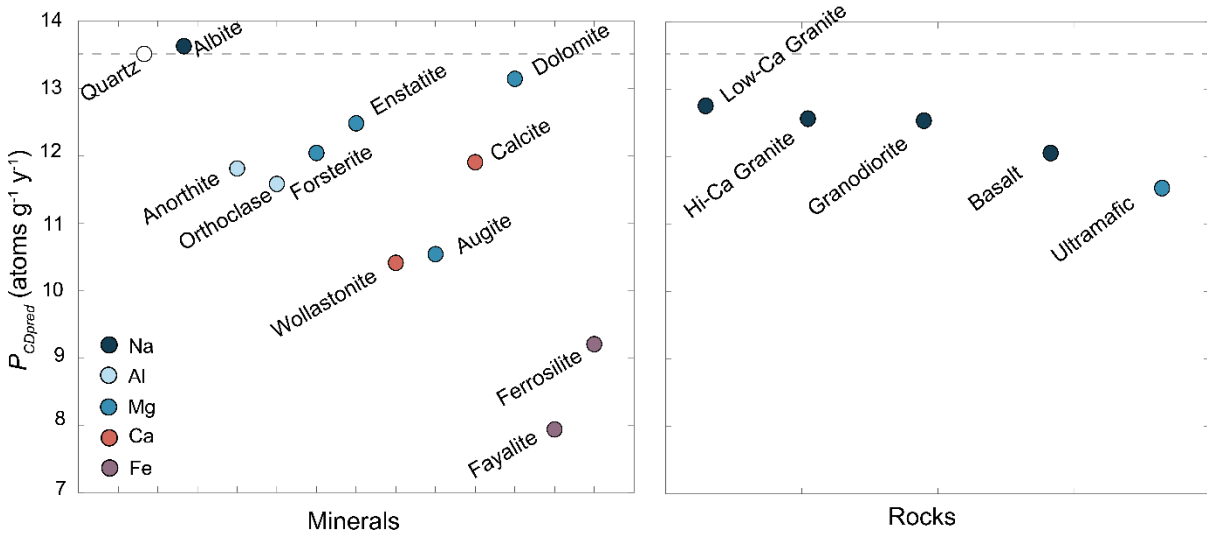


Figure 4.2. Predicted theoretical SLHL production of *in situ* ^{14}C (P_{CDpred}) in minerals (a) and rocks (b) relative to that in pure quartz (dashed grey line). The color of each symbol reflects the element that contributes the highest proportion of production after oxygen and silica.

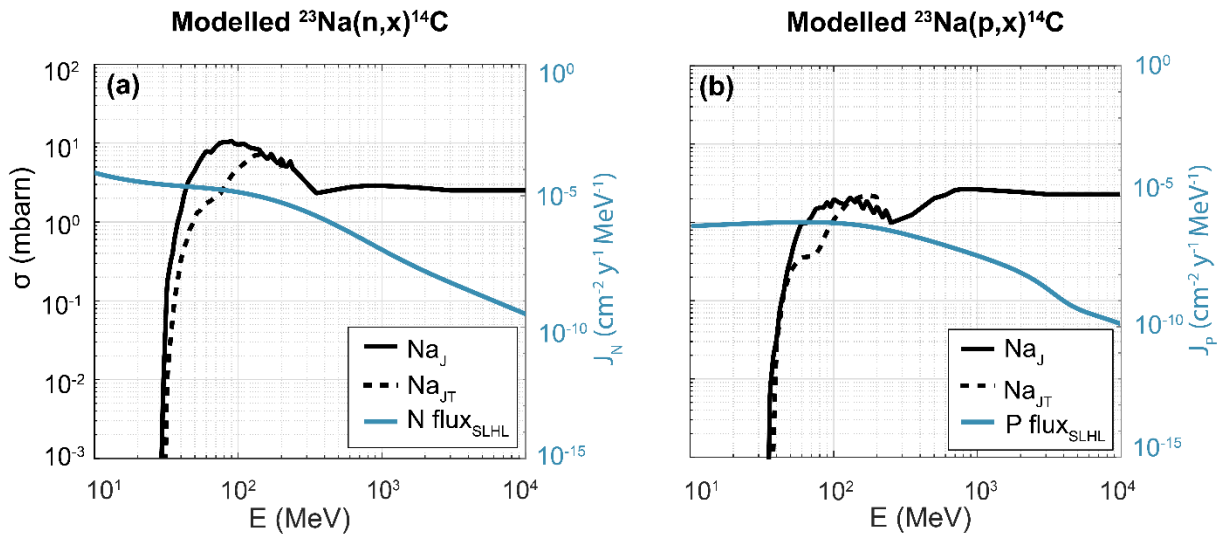


Figure 4.3. Modelled neutron (a) and proton (b) cross-sections for ^{23}Na from JENDL/HE-2007 (Na_J , solid line) compared to the spliced TENDL-2019 at energies ≤ 0.2 GeV and JENDL/HE-2007 > 0.2 GeV ($^{23}\text{Na}_{JT}$, dashed line). Differential neutron and proton fluxes at SLHL (J_N and J_P , respectively; Sato et al., 2008) are plotted in their respective panes to illustrate the combined effect of excitation function and flux on *in situ* ^{14}C production.

Table 4.1. *In situ* ¹⁴C global calibration dataset formatted for production rate calibration input to University of Washington online calculator, version 3 (Balco et al., 2008; http://hess.ess.washington.edu/math/v3/v3_cal_in.html). This dataset can be copied and pasted directly into the input data block field. Data from Borchers et al. (2016), Phillips et al. (2016), Schimmelpfennig et al. (2012), and Young et al. (2014). NL gratefully acknowledges the following colleagues for providing samples from surfaces at secular equilibrium, as part of the CRONUS-Earth project (NSF EAR-0345150): Tibor Dunai (CA-05A, northern Chile), Jay Quade (SPN samples, northern Chile), John Stone (98-PCM and WBC samples, Antarctica).

05PPT-01	41.26367	-112.47527	1603	std	3	2.65	0.978	0	2005	;	05PPT-01	C-14	quartz		
	344740	10630	;	05PPT-01	true_t	Bonneville	18300	300	;						
05PPT-02	41.26367	-112.47527	1603	std	3	2.65	0.994	0	2005	;	05PPT-02	C-14	quartz		
	327590	6700	;	05PPT-02	true_t	Bonneville	18300	300	;						
05PPT-03	41.26356	-112.4758	1600	std	5	2.65	0.962	0	2005	;	05PPT-03	C-14	quartz		
	336220	18810	;	05PPT-03	true_t	Bonneville	18300	300	;						
05PPT-04	41.26362	-112.47693	1598	std	2.5	2.66	0.982	0	2005	;	05PPT-04	C-14	quartz		
	330140	8660	;	05PPT-04	true_t	Bonneville	18300	300	;						
05PPT-05	41.2639	-112.47498	1605	std	3	2.67	0.99	0	2005	;	05PPT-05	C-14	quartz	357560	
	11670	;	05PPT-05	true_t	Bonneville	18300	300	;							
05PPT-08	41.26379	-112.47476	1606	std	2.5	2.68	0.986	0	2005	;	05PPT-08	C-14	quartz		
	368590	15820	;	05PPT-08	true_t	Bonneville	18300	300	;						
06HKY-01	57.41523	-5.64637134	std	2	2.52	0.98	0	2006	;	06HKY-01	C-14	quartz	117490		
	15540	;	06HKY-01	true_t	Scotland	11700	300	;							
06HKY-03	57.4155	-5.64662131	std	6.7	2.47	0.981	0	2006	;	06HKY-03	C-14	quartz	100780	6620	
	;	06HKY-03	true_t	Scotland	11700	300	;								
06HKY-04	57.42302	-5.65808137	std	4	2.59	0.956	0	2006	;	06HKY-04	C-14	quartz	118090		
	7820	;	06HKY-04	true_t	Scotland	11700	300	;							
06HKY-05	57.48743	-5.44933521	std	3.5	2.55	0.987	0	2006	;	06HKY-05	C-14	quartz	144320		
	12210	;	06HKY-05	true_t	Scotland	11700	300	;							
06HKY-06	57.48755	-5.44978527	std	3.5	2.53	0.987	0	2006	;	06HKY-06	C-14	quartz	155910		
	21320	;	06HKY-06	true_t	Scotland	11700	300	;							
06HKY-07	57.4878	-5.4477	500	std	6.5	2.59	0.989	0	2006	;	06HKY-07	C-14	quartz	124260	21430
	;	06HKY-07	true_t	Scotland	11700	300	;								
06HKY-08	57.48863	-5.44705502	std	3	2.58	0.988	0	2006	;	06HKY-08	C-14	quartz	146950		
	15000	;	06HKY-08	true_t	Scotland	11700	300	;							
06HKY-09	57.48863	-5.44705502	std	5	2.51	0.976	0	2006	;	06HKY-09	C-14	quartz	140500		
	14950	;	06HKY-09	true_t	Scotland	11700	300	;							
06HKY-10	57.48732	-5.44863510	std	6	2.59	0.987	0	2006	;	06HKY-10	C-14	quartz	128260		
	19410	;	06HKY-10	true_t	Scotland	11700	300	;							
06HKY-11	57.48747	-5.44995528	std	4.5	2.58	0.987	0	2006	;	06HKY-11	C-14	quartz	157140		
	14940	;	06HKY-11	true_t	Scotland	11700	300	;							

Table 4.1 continued

MR-08-03	-43.5754551	170.60803	1029	std	2.55	2.65	0.988	0	2008	;	MR-08-03	C-14	quartz		
	227200	9000	;	MR-08-03	true_t	NewZealand	9692	50	;						
MR-08-05	-43.57434507	170.607625	1032	std	2.39	2.65	0.991	0	2008	;	MR-08-05	C-14	quartz		
	194880	8770	;	MR-08-05	true_t	NewZealand	9692	50	;						
MR-08-13	-43.577517	170.606959	1028	std	1.41	2.65	0.991	0	2008	;	MR-08-13	C-14	quartz		
	213480	8830	;	MR-08-13	true_t	NewZealand	9692	50	;						
MR-08-14	-43.57789	170.60494	1032	std	2.35	2.65	0.991	0	2008	;	MR-08-14	C-14	quartz		
	200310	8920	;	MR-08-14	true_t	NewZealand	9692	50	;						
11QOO-01	69.2844	-50.7569350	std	1.5	2.65	0.995	0	2011	;	11QOO-01	C-14	quartz	133900	8030	
	;	11QOO-01	true_t	Greenland	9235	45	;								
11QOO-02	69.2844	-50.7569350	std	1.5	2.65	0.995	0	2011	;	11QOO-02	C-14	quartz	152640	7980	
	;	11QOO-02	true_t	Greenland	9235	45	;								
11QOO-03	69.2844	-50.7569350	std	1	2.65	0.995	0	2011	;	11QOO-03	C-14	quartz	146510	8010	
	;	11QOO-03	true_t	Greenland	9235	45	;								
11QOO-04	69.2844	-50.7569350	std	1.25	2.65	0.995	0	2011	;	11QOO-04	C-14	quartz	142790	7820	
	;	11QOO-04	true_t	Greenland	9235	45	;								
11QOO-05	69.2844	-50.7569350	std	1	2.65	0.995	0	2011	;	11QOO-05	C-14	quartz	146970	7740	
	;	11QOO-05	true_t	Greenland	9235	45	;								
DV-19	36.21825	-116.90151	69	std	4.5	2.65	0.999	0	2000	;	DV-19	C-14	quartz	118710	19620
	;	DV-19	true_t	DeathValley	50000	500	;								
DV-18	36.2185	-116.90119	76	std	3	2.65	0.999	0	2000	;	DV-18	C-14	quartz	135710	10210
	;	DV-18	true_t	DeathValley	50000	500	;								
DV-9	36.5272	-117.2208	480	std	4	2.65	0.999	0	2000	;	DV-9	C-14	quartz	144350	4100
	;	DV-9	true_t	DeathValley	50000	500	;								
DV-6	36.23231	-117.24528	805	std	3	2.65	0.998	0	2000	;	DV-6	C-14	quartz	189330	11430
	;	DV-6	true_t	DeathValley	50000	500	;								
DV-25	36.80958	-116.90952	1191	std	3	2.65	0.999	0	2000	;	DV-25	C-14	quartz	309670	11990
	;	DV-25	true_t	DeathValley	50000	500	;								
DV-3	36.34425	-117.13612	1576	std	1	2.65	0.998	0	2000	;	DV-3	C-14	quartz	348130	10940
	;	DV-3	true_t	DeathValley	50000	500	;								
WHM-25	37.91078	-118.3672154	std	2	2.65	0.985	0	2000	;	WHM-25	C-14	quartz	490850		
	13330	;	WHM-25	true_t	WhiteMtns	50000	500	;							
BNR-4	37.72652	-118.57617	2337	std	3	2.65	0.975	0	2000	;	BNR-4	C-14	quartz	560300	9680
	;	BNR-4	true_t	WhiteMtns	50000	500	;								
BNR-3	37.73315	-118.56721	2431	std	3	2.65	0.967	0	2000	;	BNR-3	C-14	quartz	661280	6290
	;	BNR-3	true_t	WhiteMtns	50000	500	;								
WHM-1	37.53481	-118.15325	2834	std	4	2.65	0.946	0	2000	;	WHM-1	C-14	quartz	779070	12440
	;	WHM-1	true_t	WhiteMtns	50000	500	;								

Table 4.1 continued

WHM-6	37.49138	-118.16898	3200	std	4	2.65	0.944	0	2000	;	WHM-6 C-14	quartz	106148015190		
	;	WHM-6 true_t	WhiteMtns	50000	500	;									
WHM-7	37.49062	-118.1712	3210	std	4	2.65	0.945	0	2000	;	WHM-7 C-14	quartz	100594017210		
	;	WHM-7 true_t	WhiteMtns	50000	500	;									
WHM-11	37.55066	-118.22295	3556	std	3	2.65	0.932	0	2000	;	WHM-11	C-14	quartz		
	1139770138490	;	WHM-11	true_t	WhiteMtns	50000	500	;							
WHM-10	37.55066	-118.22295	3556	std	5	2.65	0.932	0	2000	;	WHM-10	C-14	quartz		
	130371017900	;	WHM-10	true_t	WhiteMtns	50000	500	;							
WHM-19	37.59107	-118.2412	3879	std	6	2.65	0.92	0	2000	;	WHM-19	C-14	quartz		
	129607017830	;	WHM-19	true_t	WhiteMtns	50000	500	;							
WHM-15	37.59094	-118.24037	3885	std	6	2.65	0.92	0	2000	;	WHM-15	C-14	quartz		
	127232022010	;	WHM-15	true_t	WhiteMtns	50000	500	;							
WHM-16	37.59094	-118.24037	3885	std	6	2.65	0.92	0	2000	;	WHM-16	C-14	quartz		
	121798024370	;	WHM-16	true_t	WhiteMtns	50000	500	;							
CA03-5A	-27.32	-70.7603889	224	std	4	2.65	1	0	2003	;	CA03-5A	C-14	quartz	110620	
	2060	;	CA03-5A	true_t	Chile	50000	500	;							
SPN-699	-23.95698	-70.2858699		std	2	2.65	0.988	0	2002	;	SPN-699	C-14	quartz	127220	
	8720	;	SPN-699	true_t	Chile	50000	500	;							
SPN-977	-24.07313	-70.20565	977	std	3	2.65	0.977	0	2002	;	SPN-977	C-14	quartz		
	210260	42600	;	SPN-977	true_t	Chile	50000	500	;						
SPN-1921	-24.47725	-69.40802	1921	std	2	2.65	0.997	0	2002	;	SPN-1921	C-14	quartz		
	331590	19490	;	SPN-1921	true_t	Chile	50000	500	;						
SPN-3	-24.3113-68.8014333	3098	std	2.5	2.65	0.997	0	2002	;	SPN-3	C-14	quartz	571490	19260	;
	SPN-3 true_t	Chile	50000	500	;										
SPN-7D	-24.5424-68.70927	3689	std	4	2.65	0.997	0	2002	;	SPN-7D	C-14	quartz	928560	16330	;
	SPN-7D true_t	Chile	50000	500	;										
SPN-11c	-24.56542	-68.63415	4035	std	2.5	2.7	0.997	0	2002	;	SPN-11c	C-14	quartz		
	983240	51810	;	SPN-11c	true_t	Chile	50000	500	;						
98-PCM-010-SRDK	-70.86	68.13	225	std	3	2.7	1	0	1998	;	98-PCM-010-SRDK	C-14	quartz		
	183030	8420	;	98-PCM-010-SRDK	true_t	Antarctica	50000	500	;						
WBC-UVP	-77.75	160.8	2160	std	5	2.5	1	0	1999	;	WBC-UVP	C-14	quartz	968970	15770
	;	WBC-UVP	true_t	Antarctica	50000	500	;								
98-PCM-002-BVLK	-70.82	68.17	100	std	3	2.8	1	0	1998	;	98-PCM-002-BVLK	C-14	quartz		
	160050	12860	;	98-PCM-002-BVLK	true_t	Antarctica	50000	500	;						
WBC-2020	-77.75	160.8	2020	std	5.5	2.5	1	0	1999	;	WBC-2020	C-14	quartz	974370	19180
	;	WBC-2020	true_t	Antarctica	50000	500	;								
98-PCM-105-MNZ	-73.44	61.9	2538	std	3	2.7	1	0	1998	;	98-PCM-105-MNZ	C-14	quartz		
	117793019490	;	98-PCM-105-MNZ	true_t	Antarctica	50000	500	;							

Table 4.1 continued

98-PCM-067-MNZ	-73.39	61.72	2137	std	3	2.7	1	0	1998	;	98-PCM-067-MNZ	C-14	quartz
103801020640	;	98-PCM-067-MNZ		true_t	Antarctica		50000	500		;			
CRONUS-A	-77.88302	160.94308	1666	std	4	2.1	0.999	0	2004	;	CRONUS-A	C-14	quartz
713510	13360	;	CRONUS-A	true_t	Antarctica		50000	500		;			

Table 4.2. Elemental oxide compositions (weight %) for selected silicate minerals (Barthelmy, 2014; Morimoto, 1988) and rock types (Parker, 1967) used to calculate number densities (Eq. 4.2).

Mineral	Composition	SiO ₂	TiO ₂	Al ₂ O ₃	FeO	Fe ₂ O ₃	MnO	MgO	CaO	Na ₂ O	K ₂ O	P ₂ O ₅	LOI ²
<i>Quartz</i>	SiO ₂	100	-	-	-	-	-	-	-	-	-	-	-
<i>Albite</i>	NaAlSi ₃ O ₈	68.74	-	19.44	-	-	-	-	-	11.82	-	-	-
<i>Anorthite</i>	CaAl ₂ Si ₂ O ₈	43.19	-	36.65	-	-	-	-	20.16	-	-	-	-
<i>Orthoclase</i>	KAlSi ₃ O ₈	64.76	-	18.32	-	-	-	-	-	-	16.92	-	-
<i>Forsterite</i>	Mg ₂ SiO ₄	42.71	-	-	-	-	-	57.30	-	-	-	-	-
<i>Fayalite</i>	Fe ₂ SiO ₄	29.49	-	-	70.52	-	-	-	-	-	-	-	-
<i>Wollastonite</i>	Ca ₂ Si ₂ O ₆	51.73	-	-	-	-	-	-	48.28	-	-	-	-
<i>Augite</i> ¹	(Ca,Na,Fe)(Mg,Fe)Si ₂ O ₆	51.73	-	-	21.65	-	-	12.14	14.48	-	-	-	-
<i>Ferrosilite</i>	Fe ₂ Si ₂ O ₆	45.54	-	-	54.46	-	-	-	-	-	-	-	-
<i>Enstatite</i>	Mg ₂ Si ₂ O ₆	59.85	-	-	-	-	-	40.15	-	-	-	-	-
<i>Calcite</i> ²	CaCO ₃	-	-	-	-	-	-	-	56.03	-	-	-	43.97
<i>Dolomite</i> ²	CaMg(CO ₃) ₂	-	-	-	-	-	-	21.86	30.41	-	-	-	47.73
Rock type ³													
<i>Ultramafic</i>	-	40.64	0.05	0.66	-	14.09	0.19	42.94	0.98	0.77	0.04	0.04	-
<i>Basalt</i>	-	51.34	1.50	16.55	-	12.24	0.26	7.46	9.40	2.62	1.00	0.32	-
<i>Hi-Ca Granite</i>	-	67.16	0.57	15.49	-	4.23	0.07	1.56	3.54	3.83	3.04	0.21	-
<i>Low-Ca Granite</i>	-	74.22	0.20	13.60	-	2.03	0.05	0.27	0.71	3.48	5.06	0.14	-
<i>Granodiorite</i>	-	69.09	0.57	14.55	-	3.86	0.08	0.93	2.21	3.73	4.02	0.16	-

¹ Assumed empirical composition of augite (Morimoto, 1988; <https://www.mindat.org/min-419.html>, last access 18 October 2022): (Ca_{0.6}Mg_{0.2}Fe_{0.2})(Mg_{0.5}Fe_{0.5})Si₂O₆

² LOI = Loss on ignition, used in oxygen number density calculations for carbonates; assumed to be entirely CO₂ in those cases.

³ Compositions from Parker (1967)

Table 4.3. Predicted modern *in situ* ^{14}C spallogenic production rates (at $\text{g}^{-1} \text{y}^{-1}$) at SLHL from neutrons and protons in minerals and rock types considered, both theoretical (P_{CDpred}) and normalized to calibrated production in quartz (P_{CD}) using the gridded R_{C} record of Lifton (2016) and the ($P_{\text{CD,GD}}$) using the geocentric dipolar R_{CD} record of Lifton (2016).

Mineral	Neutron P_{CDpred}	Proton P_{CDpred}	Total P_{CDpred}	P_{CD}	$P_{\text{CD,GD}}$	% Diff $P_{\text{CD}} & \text{CD,GD}$ vs. P_{Qcal}
	at $\text{g}^{-1} \text{y}^{-1}$					
Quartz	15.37	0.47	15.84	13.50	13.71	0.0
Albite	15.49	0.48	15.97	13.61	13.82	0.8
Albite ¹	14.95	0.48	15.43	13.15	13.35	-2.6
Anorthite	13.43	0.42	13.85	11.80	11.98	-12.6
Orthoclase	13.20	0.39	13.60	11.59	11.77	-14.2
Forsterite	13.67	0.46	14.12	12.03	12.22	-10.9
Fayalite	9.01	0.27	9.28	7.91	8.03	-41.4
Wollastonite	11.85	0.36	12.21	10.41	10.57	-22.9
Augite	12.00	0.37	12.38	11.54	10.71	-21.9
Ferrosilite	10.46	0.32	10.78	9.18	9.33	-32.0
Enstatite	14.18	0.46	14.64	12.47	12.67	-7.6
Calcite	13.55	0.38	13.94	11.88	12.06	-12.0
Dolomite	14.96	0.44	15.40	13.12	13.33	-2.8
Rock						
Ultramafic	13.11	0.43	13.54	11.54	11.69	-14.5
Basalt	13.72	0.43	14.15	12.06	12.22	-10.7
Hi-Ca Granite	14.30	0.44	14.75	12.57	12.73	-6.9
Low-Ca Granite	14.52	0.45	14.97	12.76	12.93	-5.5
Granodiorite	14.27	0.44	14.71	12.54	12.70	-7.1

¹Production is calculated using the spliced TENDL-2019 and JENDL/HE-2007 proton and neutron excitation functions (NaTJ in text). All other Na production rates use JENDL/HE-2007 exclusively.

Table 4.4. Percentage of total theoretical predicted modern SLHL *in situ* ^{14}C production (P_{CDpred}) by element for each mineral and rock type considered.

	O	Si	Ti	Al	Fe²⁺	Fe³⁺	Mn	Mg	Ca	Na	K	P
Minerals												
<i>Quartz</i>	97.51	2.49	-	-	-	-	-	-	-	-	-	-
<i>Albite</i>	88.67	1.70	-	1.08	-	-	-	-	-	8.56	-	-
<i>Albite¹</i>	91.76	1.75	-	1.11	-	-	-	-	-	5.37	-	-
<i>Anorthite</i>	96.37	1.23	-	2.34	-	-	-	-	0.06	-	<0.01	-
<i>Orthoclase</i>	98.11	0.63	-	1.19	-	-	-	-	-	-	0.08	-
<i>Forsterite</i>	93.45	1.19	-	-	-	-	-	5.36	-	-	-	-
<i>Fayalite</i>	98.14	1.25	-	-	0.61	-	-	-	-	-	-	-
<i>Wollastonite</i>	98.16	1.67	-	-	-	-	-	-	0.17	-	-	-
<i>Augite</i>	96.87	1.65	-	-	0.14	-	-	1.30	0.05	-	-	-
<i>Ferrosilite</i>	97.93	1.66	-	-	0.41	-	-	-	-	-	-	-
<i>Enstatite</i>	94.77	1.61	-	-	-	-	-	3.62	-	-	-	-
<i>Calcite</i>	99.82	-	-	-	-	-	-	-	0.18	-	-	-
<i>Dolomite</i>	98.04	-	-	-	-	-	-	1.87	0.09	-	-	-
Rock type												
<i>Ultramafic</i>	93.84	1.18	<0.01	0.04	<0.01	0.08	<0.01	4.20	<0.01	0.66	<0.01	<0.01
<i>Basalt</i>	94.60	1.43	<0.01	1.08	<0.01	0.07	<0.01	0.70	0.03	2.14	<0.01	<0.01
<i>Hi-Ca Granite</i>	94.09	1.79	<0.01	1.01	<0.01	0.02	<0.01	0.14	0.01	3.00	0.01	<0.01
<i>Low-Ca Granite</i>	94.50	1.95	<0.01	0.89	<0.01	0.01	<0.01	0.02	<0.01	2.69	0.02	<0.01
<i>Granodiorite</i>	94.22	1.85	<0.01	0.95	<0.01	0.02	<0.01	0.08	0.01	2.93	0.02	<0.01

¹Production is calculated using the spliced TENDL-2019 and JENDL/HE-2007 proton and neutron excitation functions (Na_{TJ} in text).

All other Na production rates use JENDL/HE-2007 exclusively.

Table 4.5. Predicted modern *in situ* ^{14}C production rates at SLHL for neutron spallation from O derived from secular equilibrium concentrations (N_{SE}) at ca. 20 cm depth for different rock types (Fabryka-Martin, 1988) compared to our software framework. Note that these estimates are not normalized relative to P_{Qcal} , for straightforward comparison to Fabryka-Martin's (1988) predictions.

Rock Type	Depth¹	Density	N_{SE}^1	P_{O-FM}^1	P_{O}^2
	(m)	(g cm ⁻³)	(at g ⁻¹)	(at g ⁻¹)	(at g ⁻¹)
<i>Ultramafic</i>	0.18	2.85	135706	16.4	9.0
<i>Basalt</i>	0.18	3.0	132621	16.0	9.3
<i>Hi-Ca Granite</i>	0.19	2.75	148043	17.9	9.7
<i>Low-Ca Granite</i>	0.19	2.75	151127	18.3	9.9
<i>Limestone</i>	0.19	2.5	151127	18.3	10.1

¹Data from Fabryka-Martin (1988), assumes SLHL production rate from oxygen in Yokoyama et al. (1977).

²Data from this study assuming only production from neutron spallation of O and an attenuation length of 160 g cm⁻².

Table 4.6. Neutron-only SLHL *in situ* ^{14}C production based on Masarik (2002; P_{M02}) theoretical predictions for compositions considered in this work, compared to modern SLHL neutron-only production predicted here (also see Table 4.3). Note that these estimates are not normalized relative to P_{Qcal} , to enable direct comparison to Masarik's (2002) predictions.

Mineral	P_{M02} (at $g^{-1} y^{-1}$)	P_{CDn} (at $g^{-1} y^{-1}$)
Quartz	18.72	15.37
Albite	17.20	15.49
Anorthite	16.25	13.43
Orthoclase	16.20	13.20
Forsterite	16.43	13.67
Fayalite	11.06	9.01
Wollastonite	14.42	11.85
Augite	14.59	12.00
Ferrosilite	12.80	10.46
Enstatite	17.11	14.18
Calcite	16.48	13.55
Dolomite	18.12	14.96
Rock		
Ultramafic	15.27	13.11
Basalt	15.38	13.72
Hi-Ca Granite	17.15	14.30
Low-Ca Granite	17.15	14.52
Granodiorite	17.14	14.27

CHAPTER 5. CONCLUSIONS

This thesis examined the applications of cosmogenic nuclides in polar landscapes to reconstruct past ice sheet histories. Polar regions typically have low erosion rates and cold-based ice, that can preserve nuclides produced during prior periods of exposure (i.e., inheritance). Inheritance can be problematic for long-lived cosmogenic nuclides like ^{10}Be and ^{26}Al in polar regions. However, the application of *in situ* ^{14}C in polar regions can more reliably constrain the post-LGM exposure history due to its 5.7 kyr half-life. Therefore, the work of this thesis further demonstrates the significance of the application of *in situ* ^{14}C in polar regions to date glacial retreat.

Chapter 2 examined the hypothesis that the Riukojietna ice cap in Sweden disappeared completely during the Holocene Thermal Maximum (HTM; 8 – 5 ka) when summer temperatures were 1.5 – 2 °C higher in this region than present. Reconstructions of Norway glaciers indicate that many disappeared during the mid-Holocene due to either increased summer temperatures or reduced winter precipitation (e.g., Bjune et al., 2005; Nesje et al., 2008). Previous literature suggested that Swedish glaciers retreated and advanced multiple times during the HTM (Karlén, 1976, 1981; Karlén et al., 1995). However, more recent work has shown that some glaciers in Sweden disappeared in the mid-Holocene and reformed ~5 ka (Rosqvist et al., 2004) or ~3 ka (Snowball and Sandgren, 1996). Paired ^{14}C - ^{10}Be - ^{26}Al measurements from bedrock samples adjacent to the Riukojietna Ice Cap were collected to determine the relative size of the ice cap during the Holocene and compared to downstream proglacial sediment to indicate when the ice cap was active/inactive. Proglacial lake sediments imply the Riukojietna ice cap was active until c. 4.5 cal ka. The shift towards a cooler climate around 5 ka likely increased mass balance of glaciers, leading to glacial advance recorded in Sweden and Norway. However, Riukojietna likely retreated and thinned significantly after 4.5 cal ka because there is no input of glacier derived sediments in the lake until 1.8 cal ka, in contrast to other nearby glaciers. The response of the Riukojietna ice cap relative to other valley glaciers in the vicinity could be due to its low surface gradient, which makes it sensitive to small changes in climate. Although proglacial lake sediment can reconstruct when a glacier was active/inactive, cosmogenic nuclide samples adjacent to the ice cap can constrain relative glacier size. Our cosmogenic nuclide inventories are consistent with continuous exposure at our sampled sites between ca. 8 and 1.8 cal ka. Due to laminations in the

proglacial sediment, the Riukojietna ice cap could have persisted with a modern configuration (or smaller) until c. 4.5 cal ka.

Chapter 3 examined Holocene ice surface lowering in western Dronning Maud Land (DML) utilizing *in situ* ^{14}C exposure ages from mountains protruding through the East Antarctic Ice Sheet along two marine-terminating ice streams. The Holocene history is poorly constrained in western DML due to reliance on long-lived cosmogenic nuclides that can contain nuclides from previous periods of exposure. A previous study in DML along Jutulstraumen relying on long-lived nuclides such as ^{10}Be , ^{26}Al , and ^{36}Cl reported exposure ages between ~2 and 1450 ka, with 25% of exposure ages younger than the LGM (Andersen et al., 2020). Due to a small subset of post-LGM exposure ages ($n = 4$), the study could only interpret ~35 – 120 m of ice surface lowering during the Holocene (~ 2 – 11 ka). *In situ* ^{14}C data presented in Chapter 3 corroborates the conclusions in Andersen et al. (2020), but further refines Holocene ice surface lowering along Jutulstraumen to have occurred between 9.5 and 1 ka. In addition, *in situ* ^{14}C exposure ages from the coast inland indicate significant coastal thickening up to 850 m and up to 400 m inland at the LGM. Previous geomorphic evidence from scattered nunataks near Jutulstraumen indicate a thicker than present LGM ice sheet between 800 and 1000 m (e.g., Swithinbank, 1959; Lunde, 1961), within the range interpreted from our geochronological constraints. Exposure data from Veststraumen give supporting evidence for a thicker than present LGM ice sheet, albeit spatially scattered. Previous geological constraints in Veststraumen relied on radiocarbon dated muyimo mounds from stormy petrel colonies, while geomorphic evidence suggested the LGM ice sheet was up to 700 m thicker over coastal mountains (Lintinen, 1996; Lintinen and Nenonen, 1997). A recent study applied *in situ* ^{14}C to nunataks surrounding the Wedell Sea Embayment southwest of Veststraumen found the ice sheet was up to >310 – 655 m thicker at the LGM (Nichols et al., 2019). Our *in situ* ^{14}C data in Veststraumen indicates the ice sheet was 400 m thicker at the coast and >100 m thicker inland at the LGM, within the range of previous studies. In addition, we constrain Holocene ice surface lowering at the coast between 9 and 5 ka. This study demonstrates the importance of using *in situ* ^{14}C in Antarctica to prevent issues with inheritance.

Chapter 3 also highlights the importance of utilizing *in situ* ^{14}C exposure data as a robust way to determine combinations of model parameters and climate forcing best represents LGM conditions over the study area. Large ensemble models of Antarctica indicate little thickening of the LGM ice sheet in DML over our sample sites, likely because they rely on coarse resolution

(>20 km) that cannot properly represent the complex topography of sampled nunataks. (e.g., Whitehouse et al., 2012a; Abe-Ouchi et al., 2015; Pittard et al., 2022). However, Chapter 3 demonstrates an irregular finite-element mesh can scale down to individual nunataks to better estimate ice thickness at the LGM. LGM high-resolution ensemble model runs compared to our exposure data and ice core reconstructions constrained 27 plausible simulations out of the original 100. High resolution ensemble models that predict ice sheet geometries at the LGM indicate a spatial pattern of a thickening gradient below the escarpment to the coast while the polar plateau was thinner than present. This study reveals the importance of evaluating climate models that reconstruct the LGM configuration of the Antarctic Ice Sheet utilizing *in situ* ^{14}C exposure data to assess under or over prediction of ice sheet thickness.

Chapter 4 sought to expand the potential applications of *in situ* ^{14}C to non-quartz-bearing and fine-grained materials by estimating compositionally dependent spallogenic production of *in situ* ^{14}C . This work is a first step toward applying *in situ* ^{14}C to landscapes lacking quartz, such as landscapes dominated by mafic or intermediate rock types, and to fine-grained lithologies in which effective separation of quartz from other mineral components is difficult. This chapter extends the functionality of the LSDn nuclide-specific scaling framework. Results from this study exploring a broad range of mineral and rock compositions indicates production of *in situ* ^{14}C is dominated by oxygen spallation at sea-level high latitude (SLHL), as expected, and confirms previous work identifying Si, Mg, and Al as important targets. However, this study identifies Na contributes significantly to production of *in situ* ^{14}C .

The studies that comprise this thesis focus on the application of *in situ* ^{14}C in polar landscapes. The rapid decay of *in situ* ^{14}C due to the short half-life (5.7 kyr), makes it sensitive to complex periods of burial and exposure since 25-30 ka. The ability to extract, purify, and measure *in situ* ^{14}C has become reliable within the last few decades due to the construction of automated carbon extraction systems (i.e., Lifton et al., 2015). As such, the total number of *in situ* ^{14}C measurements has grown worldwide. *In situ* ^{14}C is specifically advantageous in polar regions where prevalent minimally erosive cold-based ice can preserve prior nuclides from long-lived radionuclides (i.e., ^{10}Be , ^{26}Al). Thus, *in situ* ^{14}C can more closely reflect the post-LGM deglacial signal. Overall, these results demonstrate the importance of *in situ* ^{14}C in polar regions to reconstruct ice retreat and ice surface lowering from the LGM into today.

APPENDIX A. COSMOGENIC NUCLIDE PROCESSING

Mineral separation

Quartz was separated at Purdue University following the standard mineral separation Purdue Rare Isotope Measurement Laboratory (PRIME lab) procedures. Samples were crushed, sieved to 250-500 μm , and magnetic minerals removed using a Carpco magnetic separator. Micas and feldspars were removed with froth flotation, and the remaining quartz separate was subsequently leached in weak hydrofluoric and nitric acids to remove meteoric ^{10}Be (Kohl and Nishiizumi, 1992). Quartz purity was assessed with inductively coupled plasma–optical emission spectrometry (ICP-OES) at Purdue University (Al target: <200 ppm). Riuko-16-002 and Riuko-16-005 had high Al and Na contents, indicating the presence of feldspars, and were therefore subjected to an additional separation step using heavy liquids followed by an extra day of etching in 1% HF/HNO₃ acid.

Cosmogenic nuclide chemistry – ^{10}Be and ^{26}Al

^{10}Be and ^{26}Al were extracted at PRIME lab following the procedures outlined in Andersen et al. (2020). Beryllium samples were spiked with ca. 260 μg of Be carrier and aluminum samples were spiked with ~1-1.5 mg of Al carrier (if needed) before digestion in HF acid. The samples were prepared in one batch with a blank and an aliquot of the intercomparison material CoQtz-N (Binnie et al., 2019). Be and Al were precipitated through anion and cation column chromatography, precipitated, oxidized, mixed with niobium powder, and pressed into cathodes for measurement. Isotopic ratios ($^{10}\text{Be}/^9\text{Be}$ and $^{26}\text{Al}/^{27}\text{Al}$) were measured by accelerator mass spectrometry at PRIME Lab. Be analyses were normalized to standard 07KNSTD3110 (Nishiizumi et al., 2007) and Al analyses were normalized to KNSTD9919.

Extraction of in situ ^{14}C

Carbon was extracted at Purdue University with a fully automated extraction system similar to that of Goehring et al. (2019), following a two-day procedure similar to that of Lifton et al (2015) (Lifton and Koester, 2022). Day 1 procedures involve degassing the lithium metaborate (LiBO₂) flux, while the second day is the extraction/purification/graphitization procedure. The system contains two tube furnaces (TF1 – tube furnace 1; TF2 – tube furnace 2) connected to the purification/graphitization line (Fig. A1). On the first day, approximately 5 g of quartz is pretreated

with 50:50 (V:V) nitric acid:18 MΩ water for 3 hours, rinsed thoroughly in DI water, then dried in a vacuum oven over-night. A reusable Pt-Rh boat (90% Pt, 10% Rh) containing 20 g of LiBO₂ is placed inside a flame-cleaned fused quartz sleeve in the mullite tube furnace. The tube furnace is evacuated to $<5 \times 10^{-3}$ torr, isolated, and then 50 torr of Research Purity (RP) O₂ is added. The furnace is then heated to 1100 °C for 1 hour while O₂ is bled through with a mass flow controller and automated metering valve to maintain the tube pressure and to flush out any evolved contaminants to the vacuum pump. Once cooled overnight, approximately 5 g of the pretreated quartz sample is evenly distributed over the now-solid LiBO₂ in the boat and returned to the furnace, evacuated to $<5 \times 10^{-3}$ torr, isolated, and ca. 50 torr RP O₂ is added again. The sample is then heated to 500°C for one hour to combust and remove atmospheric/organic contaminants, while bleeding O₂ across the sample as before. After that hour, the tube furnace is evacuated to $<5 \times 10^{-3}$ torr. Subsequently, ca. 50 torr of RP O₂ is admitted into the tube furnace and the sample/flux is heated to 1100 °C for three hours to dissolve the quartz and release any trapped carbon species.

After sample extraction, the evolved gas is bled with RP O₂ through a secondary combustion furnace filled with quartz beads at ca. 950 °C to ensure any carbon species released during the extraction step are completely oxidized to CO₂. Subsequently, the collected gas is transferred to a glass coil trap held at liquid nitrogen temperature (-196 °C). The condensed gases are then transferred to the purification section to remove water, halogens, and nitrogen and sulfur oxides. The gas is first transferred into a variable temperature trap (VTT) and held at -196 °C while O₂ and incondensable gases such as SO₂ are evacuated. Next, the CO₂ gas is passed through a Cu mesh/Ag wool reactor held at 600 °C to remove halogens and nitrogen species and subsequently transferred to a measurement chamber of known volume to quantify the CO₂ yield. The sample CO₂ is typically diluted to ca. 300 μg C-equivalent with ¹⁴C-free CO₂, then transferred to a graphite reactor. The sample undergoes hydrogen reduction to filamentous C (graphite) on an Fe catalyst following (Southon, 2007). Once the graphite reduction is complete, the sample is packed into an Al cathode for measurement by Accelerator Mass Spectrometry (AMS).

Sample ¹⁴C/¹³C ratios were measured by AMS relative to Oxalic Acid II (NIST-4990C) at Purdue University. Stable carbon isotopic ratios were measured at the University of California Davis Stable Isotope Facility using isotope ratio mass spectrometry (Lifton et al., 2015). The ¹⁴C concentration is calculated from the measured ¹⁴C/C_{total} after subtracting out representative procedural background ¹⁴C, per Hippe and Lifton (2014). Representative procedural blank (full

process without adding quartz sample) ^{14}C atoms were subtracted from total ^{14}C atoms from each sample, before ^{14}C concentrations were calculated.

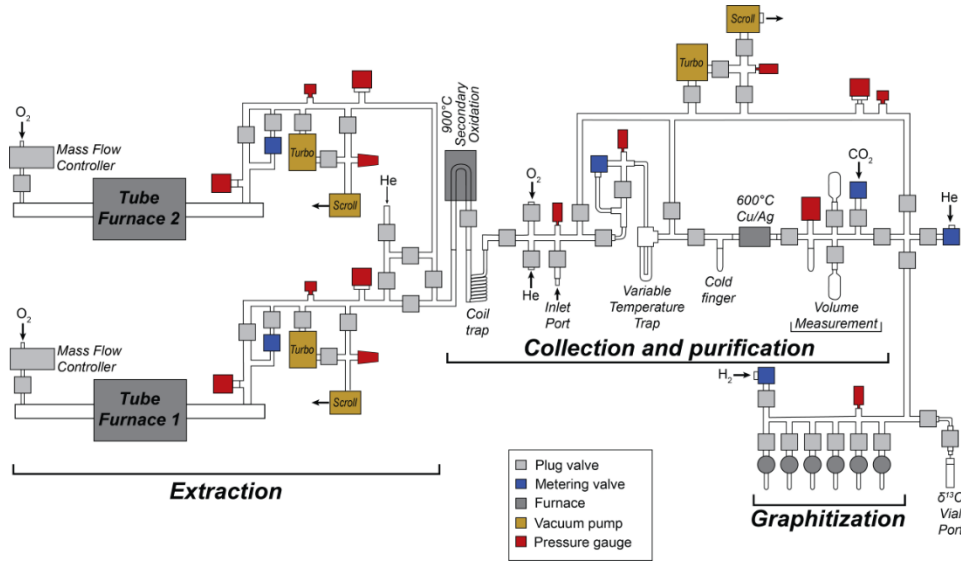


Figure A1: Schematic of the Purdue Carbon Extraction and Graphitization system (Lifton and Koester, 2022).

Calculation of *in situ* ^{14}C exposure ages

All calculations assume the CRONUS-Earth global calibration production rates for ^{10}Be ($3.9 \pm 0.3 \text{ at g}^{-1} \text{ yr}^{-1}$), ^{26}Al ($28.5 \pm 3.1 \text{ at g}^{-1} \text{ yr}^{-1}$) and *in situ* ^{14}C ($13.5 \pm 0.9 \text{ at g}^{-1} \text{ yr}^{-1}$) exposure age and forward model calculations (Lifton et al., 2014; Borchers et al., 2016; Lifton et al., 2016; Phillips et al., 2016) – the latter updated with the Young et al. (2014) *in situ* ^{14}C calibration dataset (Koester and Lifton, 2023; Chapter 4). All calculations utilize nuclide-specific LSDn scaling (Lifton et al., 2014; Lifton, 2016) and the muon production formulation from Balco (2017). Where appropriate, apparent exposure ages (i.e., assuming constant exposure with no erosion and/or burial) were calculated using the online University of Washington cosmogenic calculator, v.3 (wrapper script 3.0.2, constants: 2020-08-26, muons: 1A; <https://hess.ess.washington.edu/>) (Balco et al., 2008).

APPENDIX B. SWEDEN SITE DESCRIPTIONS



Figure B1: Riuko 16-001 and Riuko 16-002 bedrock site at Riukojietna Ice Cap in 2016. Riuko 16-001 bedrock was collected about ~1 m from the ice cap edge. Riuko 16-002 was collected ~2 m from the ice margin, ca. 50 cm above the current ice margin.



Figure B2: Riuko 16-003 (left) and Riuko 16-004 (right) are taken from the same bedrock knob site at Riukojietna Ice Cap in 2016. Site Riuko 16-003 is a glacially molded bedrock knob that recently emerged from the ice cap since 2008. The surface contained abundant striae. Site Riuko 16-004 is glacially polished and striated ~1 m from the ice edge.



Figure B3: Riuko 16-005 bedrock site adjacent to Lake 1063. The site had moderate to light lichen cover. The sampled surface was above the lichen kill zone.

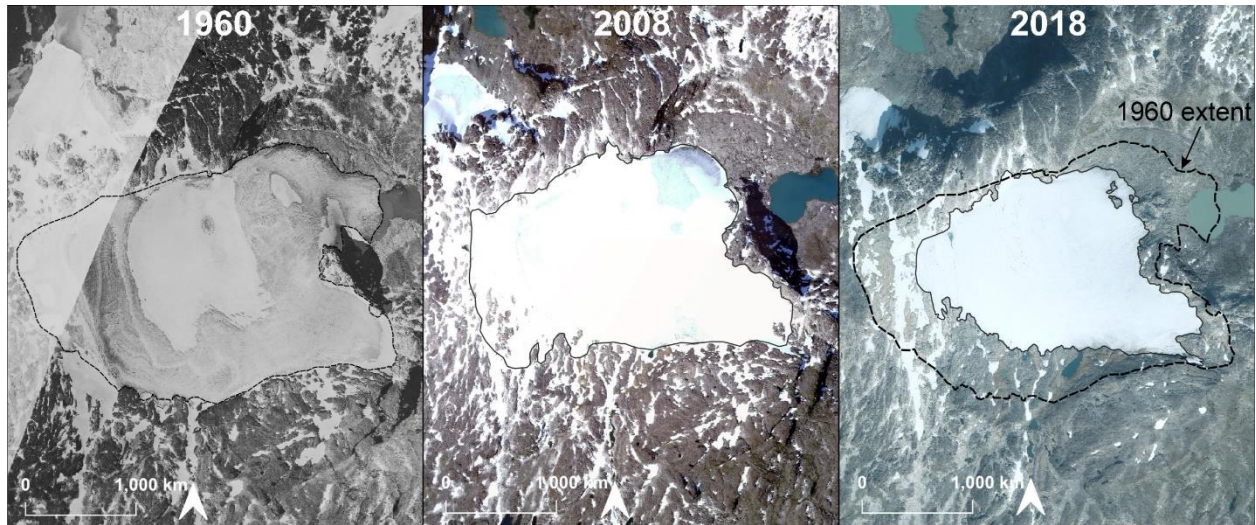


Figure B4: Aerial photographs of Riukojetna Ice Cap from 1960 (left), 2008 (middle), and 2018 (right).

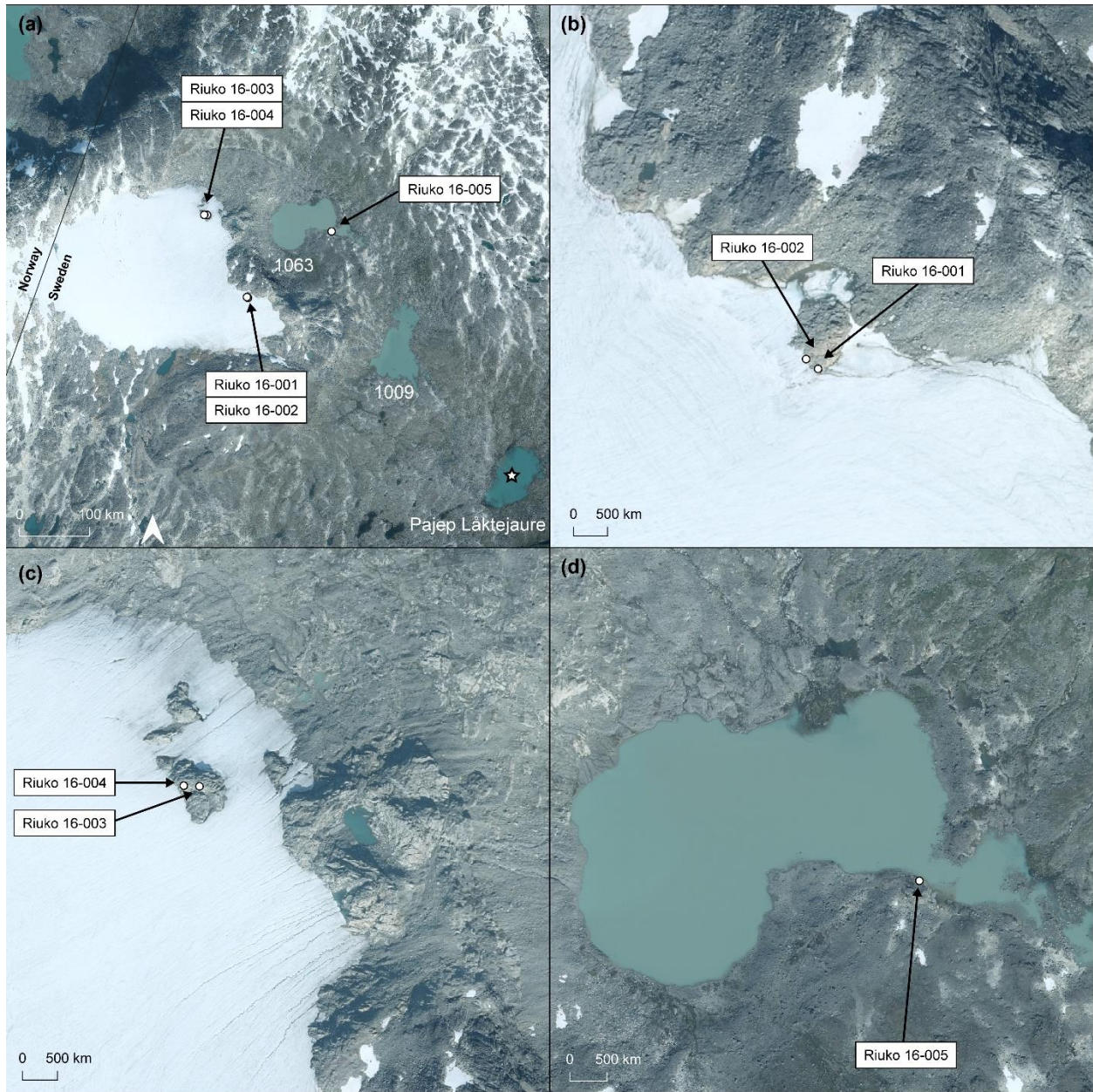


Figure B5: Google satellite images from 2018 showing the locations of sampling sites (a) (as in Fig. 2.2). Zoomed in locations are shown for each site (b – d).

APPENDIX C. FORWARD MODELING OF COSMOGENIC NUCLIDE PRODUCTION UNDER ICE

This MATLAB code calculates the glacial history of bedrock samples with respect to ice cover duration, ice thickness, and subglacial erosion. The code calls the function ‘forward_CN_bedrock.m’ which calculates the concentrations of ^{10}Be , ^{26}Al , and ^{14}C in a sample over time based on these parameters. This function calls scripts from Balco et al. (2008) and Balco (2017) muon production MATLAB code. The script produces a plot of ice thickness change and cosmogenic nuclide build-up as a function of time.

The ice cover is defined using a function that calls ‘define_ice_history.m’, which loads some pre-defined potential ice cover histories. The user can choose between three different ice sheet model outputs (ice_model) between 20 and 10 ka: (1) University of Maine Ice Sheet Model; UMISM (2) ANU ice sheet model (3) Patton (2016) ice sheet model. The Holocene ice cover model can be chosen from a variety of pre-defined ice models, such as the HTM model and EXP model described in Chapter 2.

show_CN_Ice_MC.m:

```
% Developed by Allie Koester, Purdue University (koestea@purdue.edu) and  
% Jane Lund Andersen, Aarhus University (jane.lund@geo.au.dk), 2021-23
```

```
clear, close all  
set(groot,'defaulttextinterpreter','latex');  
set(groot,'defaultAxesTickLabelInterpreter','latex');  
set(groot,'defaultLegendInterpreter','latex');
```

```
load RiukoProduction.mat consts samples %file will be available once study is published
```

```
%% a few variables  
dt = 100; %time step, annual years  
Esubgla = 0; %No subglacial erosion  
Esubgla1 = 0.01; %Subglacial erosion = 0.01cm/yr = 0.1 mm yr-1 (Hallet et al., 1996).  
Tstart = 12; %Sets the time-range for plotting (ka BP), but does not control the model start
```

```
%% initiate figures and plot sample data  
figure(1)  
t = tiledlayout(3,2,'TileSpacing','compact');
```

```

ax1 = nexttile(1); % 14C samples 1 and 2
sIDs=1:2; %sample index's
tname=['Riuko-' char(samples{sIDs(1)}.name) ' and Riuko-' char(samples{sIDs(2)}.name)];
title(tname,'interpreter','latex','FontSize',16)

colororder([.1 .1 .1; .3 .4 1]) % colororder({'k','b'})
yyaxis left
hold on
cols=[.5 .2 .2] [.2 .2 .5];
for i=1:2 %sample index's
    patch([0 Tstart Tstart 0],[samples{i}.N14-samples{i}.dN14.*2 ...
        samples{i}.N14-samples{i}.dN14.*2 samples{i}.N14+samples{i}.dN14.*2. ...
        samples{i}.N14+samples{i}.dN14.*2 ],cols{i},'EdgeColor',cols{i},'FaceAlpha',.5)
    if i==1, text(5.5,samples{i}.N14-3e4,samples{i}.name,'Color',cols{i})
    else, text(5.5,samples{i}.N14+3e4,samples{i}.name,'Color',cols{i})
    end
end
xlim([0 Tstart]), ylim([0 3e5])
set(gca,'FontSize',12)
ylabel("[$^{14}$C] (at g$^{-1}$)",'fontsize',16) % ylabel("C-14 (at g$^{-1}$)",'fontsize',16)
text(.3,2.8e5,'a','fontsize',20)

ax2 = nexttile(3); %sample 1 and 2, 10Be
hold on
for i=1:2 %sample index's
    patch([0 Tstart Tstart 0],[samples{i}.N10-samples{i}.dN10.*2 ...
        samples{i}.N10-samples{i}.dN10.*2 samples{i}.N10+samples{i}.dN10.*2. ...
        samples{i}.N10+samples{i}.dN10.*2 ],cols{i},'EdgeColor',cols{i},'FaceAlpha',.5)
    if i==1, text(5.5,samples{i}.N10-2.5e4,samples{i}.name,'Color',cols{i})
    else, text(5.5,samples{i}.N10+2.5e4,samples{i}.name,'Color',cols{i})
    end
end
xlim([0 Tstart]), ylim([0 3e5])
set(gca,'FontSize',12)
ylabel("[$^{10}$Be] (at g$^{-1}$)",'FontSize',16) % ylabel("Be-10 (at g$^{-1}$)",'FontSize',16)
text(.3,2.8e5,'c','fontsize',20)

ax5 = nexttile(5); %sample 1 and 2, 26Al
hold on
for i=1:2 %sample index's
    patch([0 Tstart Tstart 0],[samples{i}.N26-samples{i}.dN26.*2 ...
        samples{i}.N26-samples{i}.dN26.*2 samples{i}.N26+samples{i}.dN26.*2. ...
        samples{i}.N26+samples{i}.dN26.*2 ],cols{i},'EdgeColor',cols{i},'FaceAlpha',.5)
    if i==1, text(5.5,samples{i}.N26-2.5e5,samples{i}.name,'Color',cols{i})
    else, text(5.5,samples{i}.N26+2.5e5,samples{i}.name,'Color',cols{i})
    end
end

```

```

end
xlim([0 Tstart]), ylim([0 2e6])
set(gca,'FontSize',12,'YTick',0:1e6:2e6)
ylabel("$g^{26}$AI (at $g^{-1}$)",'FontSize',16) %ylabel("AI-26 (at $g^{-1}$)",'FontSize',16)
text(.3,1.8e6,'e','fontsize',20)

ax3 = nexttile(2); %14C
sIDs=3:4; %sample index's
tname=['Riuko-' char(samples{sIDs(1)}.name) ' and Riuko-' char(samples{sIDs(2)}.name)];
title(tname,'interpreter','latex','FontSize',16)

colororder([.1 .1 .1; .3 .4 1]) % colororder({'k','b'})
yyaxis left
hold on
cols={[.5 .2 .2] [.2 .2 .5]};
for i=1:length(sIDs) %sample index's
    patch([0 Tstart Tstart 0],[samples{sIDs(i)}.N14-samples{sIDs(i)}.dN14.*2 ...
        samples{sIDs(i)}.N14-samples{sIDs(i)}.dN14.*2
        samples{sIDs(i)}.N14+samples{sIDs(i)}.dN14.*2. ...

samples{sIDs(i)}.N14+samples{sIDs(i)}.dN14.*2 ],cols{i},'EdgeColor',cols{i},'FaceAlpha',.5)
    if i==2, text(5.5,samples{sIDs(i)}.N14-3e4,samples{sIDs(i)}.name,'Color',cols{i})
    else, text(5.5,samples{sIDs(i)}.N14+3e4,samples{sIDs(i)}.name,'Color',cols{i})
    end
end
end
xlim([0 Tstart]), ylim([0 3e5])
text(.3,2.7e5,'b','fontsize',20)
yyaxis right
set(gca,'FontSize',12)
ylabel("Ice thickness (m)",'FontSize',16)

ax4 = nexttile(4); %10Be
hold on
for i=1:length(sIDs) %sample index's
    patch([0 Tstart Tstart 0],[samples{sIDs(i)}.N10-samples{sIDs(i)}.dN10.*2 ...
        samples{sIDs(i)}.N10-samples{sIDs(i)}.dN10.*2
        samples{sIDs(i)}.N10+samples{sIDs(i)}.dN10.*2. ...

samples{sIDs(i)}.N10+samples{sIDs(i)}.dN10.*2 ],cols{i},'EdgeColor',cols{i},'FaceAlpha',.5)
    if i==1, text(5.5,samples{sIDs(i)}.N10-2e4,samples{sIDs(i)}.name,'Color',cols{i})
    else, text(5.5,samples{sIDs(i)}.N10+2e4,samples{sIDs(i)}.name,'Color',cols{i})
    end
end
end
% xlim([0 Tstart]), ylim([0 1.5e5])
xlim([0 Tstart]), ylim([0 3.0e5])
set(gca,'FontSize',12)

```

```

text(.3,13.5e4,'d','fontsize',20)

ax6 = nexttile(6); %26Al
hold on
for i=1:length(sIDs) %sample index's
    patch([0 Tstart Tstart 0],[samples{sIDs(i)}.N26-samples{sIDs(i)}.dN26.*2 ...
        samples{sIDs(i)}.N26-samples{sIDs(i)}.dN26.*2
samples{sIDs(i)}.N26+samples{sIDs(i)}.dN26.*2. ...

samples{sIDs(i)}.N26+samples{sIDs(i)}.dN26.*2 ],cols{i},'EdgeColor',cols{i},'FaceAlpha',.5)
    if i==1, text(5.5,samples{sIDs(i)}.N26-1.5e5,samples{sIDs(i)}.name,'Color',cols{i})
    else, text(5.5,samples{sIDs(i)}.N26+1.5e5,samples{sIDs(i)}.name,'Color',cols{i})
    end
end
% xlim([0 Tstart]), ylim([0 1e6])
xlim([0 Tstart]), ylim([0 2e6])
set(gca,'FontSize',12)
text(.3,9e5,'f','fontsize',20)

xlabel(t,"Time (ka BP)",'fontsize',16,'interpreter','latex')

%% Define ice-cover scenarios and calculate nuclide build-up
% choose between Method 1 and Method 2.
% Method 1: Regular Model; Method 2: MC Model
method=2; %two different methods implemented;
switch method
case 1 % Method #1
    %choose a pre-defined scenario from 'define_ice_history.m'
    ice_model=1; %1=UMISM, 2=EUR17, 3=Patton
    mode=2; %1=HTM model with 33 m max 2=EXP model,
    %3=HTM with 10 m max, 4=HTM with 1 m max, 5=deglac at 8ka, HTM=33m,
    %6=deglac at 8ka, HTM=15m,7=deglac at 8ka, HTM=10m,
    %8=deglac at 8ka, HTM=5m
    [ice_hist,ts] = define_ice_history(ice_model,mode,dt);

    % Calculate cosmogenic nuclide inventories over time, note calculated with
    % production profile from first sample only, but they are very similar

% sample 1 and 2
E=Esubgla; %Choose subglacial erosion rate for samples 1 and 2
[b14C,b10Be,b26Al] = forward_CN_bedrock(ts,ice_hist,E,samples{1},consts,0);
[b14C_up,b14C_lo] = forward_bounds_C(ts,ice_hist,E,samples{1},consts,2);
axes(ax1), plot(ts/1e3,b14C,'k','LineWidth',2,'LineStyle','-');
plot(ts/1e3,b14C_up,'k--','LineWidth',1); %plot upper bounds of C14 PR uncert
plot(ts/1e3,b14C_lo,'k--','LineWidth',1); %plot lowers bounds of C14 PR uncert
%ylim([0 2.5e5])

```

```

%Show info on subgl. erosion
%text(2,2.78e5,['Subglacial erosion: ' num2str(E) ' cm a$^{-1}$'],...
% 'fontsize',14,'Color',.5*[1 1 1])
yyaxis right
plot(ts/1e3,(ice_hist./100),'LineWidth',2,'LineStyle','-')
ylim([0 100]);
plot(ax2,ts/1e3,b10Be,'k','LineWidth',2,'LineStyle','-');
plot(ax5,ts/1e3,b26Al,'k','LineWidth',2,'LineStyle','-');
% sample 3 and 4
E=Esubgl; %Choose subglacial erosion rate for samples 3 and 4
[b14C,b10Be,b26Al] = forward_CN_bedrock(ts,ice_hist,E,samples{3},consts,0);
[b14C_up,b14C_lo] = forward_bounds_C(ts,ice_hist,E,samples{3},consts,2);
axes(ax3), yyaxis left
plot(ts/1e3,b14C,'k','LineWidth',2,'LineStyle','-');
%plot upper bounds of C14 PR uncert
plot(ts/1e3,b14C_up,'k--','LineWidth',1);
%plot lowers bounds of C14 PR uncert
plot(ts/1e3,b14C_lo,'k--','LineWidth',1);
%Show info on subglacial erosion, can turn on or off
% text(2,2.7e5,['Subglacial erosion: ' num2str(E) ' cm a$^{-1}$'],...
% 'fontsize',14,'Color',.5*[1 1 1])
% ylim([0 2e5]) %set limits for the y axis
yyaxis right
plot(ts/1e3,(ice_hist./100),'LineWidth',2,'LineStyle','-')
ylim([0 100]);
plot(ax4,ts/1e3,b10Be,'k','LineWidth',2,'LineStyle','-');
plot(ax6,ts/1e3,b26Al,'k','LineWidth',2,'LineStyle','-');

case 2 % Method #2: Monte Carlo - quasi-bootstrap
ice_model=1; %1=UMISM, 2=EUR17, 3=Patton
mode=2; %1=HTM model with 33 m max 2=EXP model,
%3=HTM with 10 m max, 4=HTM with 1 m max, 5=deglac at 8ka, HTM=33m,
%6=deglac at 8ka, HTM=15m,7=deglac at 8ka, HTM=10m,
%8=deglac at 8ka, HTM=5m
nMC = 100; %number of MC iterations to run
iceHistErr = 0.1; %uncertainty in ice thickness history
[ice_hist,ts] = define_ice_history(ice_model,mode,dt);
rng('shuffle') %creates a different seed each time
%samples 1 and 2
E=Esubgl1; %Choose subglacial erosion rate for sample 1 and 2
for i = 1:1:nMC %run n amount of simulations
%generate noise in the ice history vector
n = length(ice_hist);
m = ice_hist.*iceHistErr; %ice history, 10% error
ice_histX = ice_hist + (rand(1,n)*2-1).*m;
q = 1:length(ice_histX);

```

```

    if ice_histX(q) > 0 %check for negative numbers
        ice_histX(q) = 0; %replace negative numbers with 0
    end
    % Calculate cosmogenic nuclide inventories over time
    [b14CMC,b10BeMC,b26AIMC] =
forward_CN_bedrock(ts,ice_histX,E,samples{1},consts,1);
    %save the end result for each iteration into a new vector
    MC_14(i) = b14CMC(end);
    MC_10(i) = b10BeMC(end);
    MC_26(i) = b26AIMC(end);
end
%mean and standard deviation at 2 sigma
me_14MC = mean(MC_14); std_14MC = 2*std(MC_14);
me_10MC = mean(MC_10); std_10MC = 2*std(MC_10);
me_26MC = mean(MC_26); std_26MC = 2*std(MC_26);
%calculate the forward model once
[b14C,b10Be,b26Al] = forward_CN_bedrock(ts,ice_hist,E,samples{1},consts,0);
%plot forward model
axes(ax1), plot(ts/1e3,b14C,'k','LineWidth',2,'LineStyle','-');
% plot the error
errorbar(0,me_14MC,std_14MC,'k','LineWidth',2);
%Show info on subgl. erosion
%text(2,2.78e5,['Subglacial erosion: ' num2str(E) ' cm a$^{-1}$'],...
%'fontsize',14,'Color',.5*[1 1 1])
yyaxis right
plot(ts/1e3,(ice_hist./100),'LineWidth',2,'LineStyle','-')
ylim([0 100]);
plot(ax2,ts/1e3,b10Be,'k','LineWidth',2,'LineStyle','-');
errorbar(ax2,0,me_10MC,std_10MC,'k','LineWidth',2);
plot(ax5,ts/1e3,b26Al,'k','LineWidth',2,'LineStyle','-');
errorbar(ax5,0,me_26MC,std_26MC,'k','LineWidth',2);

E=Esubgl1; %Choose subglacial erosion rate for sample 3 and 4
%sample 3 and 4
for i = 1:1:nMC %run 1000 simulations
    %generate noise in the ice history vector
    n = length(ice_hist);
    m = ice_hist.*iceHistErr; %ice history, 10% error
    ice_histX = ice_hist + (rand(1,n)*2-1).*m;
    q = 1:length(ice_histX);
    %check for negative numbers in the ice history
    if ice_histX(q) > 0
        ice_histX(q) = 0; %replace negative numbers with 0
    end
    % Calculate cosmogenic nuclide inventories over time

```

```

    [b14CMC,b10BeMC,b26AlMC] =
forward_CN_bedrock(ts,ice_histX,E,samples{3},consts,1);
    %save the end result for each iteration into a new vector
    MC_14(i) = b14CMC(end);
    MC_10(i) = b10BeMC(end);
    MC_26(i) = b26AlMC(end);
end
%mean and standard deviation at 2 sigma
me_14MC = mean(MC_14); std_14MC = 2*std(MC_14);
me_10MC = mean(MC_10); std_10MC = 2*std(MC_10);
me_26MC = mean(MC_26); std_26MC = 2*std(MC_26);
%calculate model once, no error.
[b14C,b10Be,b26Al] = forward_CN_bedrock(ts,ice_hist,E,samples{3},consts,0);
%plot 14C forward model
axes(ax3), yyaxis left, plot(ts/1e3,b14C,'k','LineWidth',2,'LineStyle','-');
%plot error on the model
errorbar(0,me_14MC,std_14MC,'k','LineWidth',2);
%Show info on subgl. erosion
%text(2,2.7e5,['Subglacial erosion: ' num2str(E) ' cm a$^{-1}$'],...
% 'fontsize',14,'Color',.5*[1 1 1])
yyaxis right
%plot ice history
plot(ts/1e3,(ice_hist./100),'LineWidth',2,'LineStyle','-')
ylim([0 100]);
%plot Be10 forward model output
plot(ax4,ts/1e3,b10Be,'k','LineWidth',2,'LineStyle','-');
errorbar(ax4,0,me_10MC,std_10MC,'k','LineWidth',2);
%plot 26Al forward model
plot(ax6,ts/1e3,b26Al,'k','LineWidth',2,'LineStyle','-');
errorbar(ax6,0,me_26MC,std_26MC,'k','LineWidth',2);
end

set(gcf,'units','normalized','position',[.2,.3,.6,.6]);
% print -painters -depsc lake1_5ero.eps
%%
set(groot,'defaulttextinterpreter','default');
set(groot,'defaultAxesTickLabelInterpreter','default');
set(groot,'defaultLegendInterpreter','default');

```

forward_CN_bedrock.m

```
function [N14C,N10Be,N26Al] =
forward_CN_bedrock(ts,ice_hist,Esubgla,sampledata,consts,flag)

% This function returns the calculated cosmogenic nuclide inventory
% (10Be-26Al-14C) in a surface sample over time as it is subaerially
% exposed or covered by (thin) ice (with or without subglacial erosion).
% The function uses the LSDn scaling scheme by Lifton et al., 2014

% Input variables: consts: constants file for production generated from
% running the compile_production.m file (saved in RiukoProduction.mat);
% sampledata: sample and production parameters compiled when running the
% compile_production.m file (saved in RiukoProduction.mat); ts: time
% vector; ice_hist: ice thickness for times in ts

% Output variables: N14C, N10Be, N26Al are calculated
% nuclide inventories in bedrock samples at times in ts

% Developed by Allie Koester, Purdue University (koestea@purdue.edu) and
% Jane Lund Andersen, Aarhus University (jane.lund@geo.au.dk), 2021-22

%% Load and define constants
dc14 = consts.l14; %decay constant for 14C
dc10 = consts.l10; %decay constant for 10Be
dc26 = consts.l26; %decay constant for 26Al
Lspi = 140; %attenuation length under ice for spallation at high latitude,
% per Lifton et al., 2014 Table 1 and Marrero et al., 2016, Table 4 and Eqs 5&6
Lspr = 150;%attenuation length under rock for spallation at high latitude,
% per Lifton et al., 2014 Table 1 and Marrero et al., 2016, Table 4 and Eqs 5&6
Lnmc = 1500; %attenuation length for negative muon capture
Lfm = 4320; %attenuation length for fast muons
rho_ice = 0.92; %g/cm3 density of ice
rho_br = sampledata.rho; %g/cm3 density of bedrock

%% define spallation and muon surface production
P14_sp = interp1(sampledata.c_results.tv,sampledata.c_results.P_LS,ts); %spallation production
at surface - sampledata.c_results.P_LS
P10_sp = interp1(sampledata.be_results.tv,sampledata.be_results.P_LS,ts); %spallation
production at surface - sampledata.be_results.P_LS;
P26_sp = interp1(sampledata.al_results.tv,sampledata.al_results.P_LS,ts); %spallation
production at surface - sampledata.al_results.P_LS;

if flag == 1 %calculate uncertainties on PR for each nuclide for MC
    rng('shuffle') %creates a different seed each time
    y = 0.9.*randn(1,1)+13.5; %random error on the C14 PR, SLHL PR: 13.5 +/- 0.9
    for i = 1:length(P14_sp) %C14
```

```

    P14_sp_i(i) = P14_sp(i) + P14_sp(i).*(y/13.5-1); %Nat's way
end
y = 0.22.*randn(1,1)+4.1; %random error on the 10Be PR, SLHL PR: 4.1 +/- 0.22
for i = 1:length(P10_sp) %Be10
    P10_sp_i(i) = P10_sp(i) + P10_sp(i).*(y/4.1-1);
end
y = 2.*randn(1,1)+28.6; %random error on the 26Al PR, SLHL PR: 28.6 +/- 2
for i = 1:length(P26_sp) %Al26
    P26_sp_i(i) = P26_sp(i) + P26_sp(i).*(y/28.6-1);
end
end

%% Calculate depth of sample over time as a function of the subglacial
erosiveIce=30; %Threshold value for erosive ice (m)

Ise=find(diff(sign(ice_hist/1e2-erosiveIce))); %find indices for subglacial erosion on/off
temp=sign(ice_hist/1e2-erosiveIce); Ise=Ise(abs(temp(Ise))>0); %remove exact zero's
Tse=[ts(1) ts(Ise) ts(end)]; %times for subglacial erosion on/off
dT=abs(diff(Tse)); %length of periods
dtGE=dT(end-1:-2:1); %length of glac. erosive periods assuming exposure during most recent
period
Zs=Esubgla*sum(dtGE); %depths for subglacial erosion on/off extended below
for i=1:length(dtGE)-1
    Zs=[Zs Esubgla*sum(dtGE(1:end-i)) Esubgla*sum(dtGE(1:end-i))];
end
Zs=[Zs 0 0]; %Assuming exposure during most recent period
burial=interp1(Tse,Zs,ts); %Tse and Zs need to be the same length

%% calculate pressure at each site for muon code

if (strcmp(sampledata.aa,'std'))
    sampledata.pressure = ERA40atm(sampledata.lat,sampledata.long,sampledata.elv);
elseif (strcmp(sampledata.aa,'ant'))
    sampledata.pressure = antatm(sampledata.elv);
end

%% preallocate for simulation
N14C = zeros(size(ts)); %preallocate
N10Be = zeros(size(ts)); %preallocate
N26Al = zeros(size(ts)); %preallocate

%% Define muon production with depth for Be10
% Muon calculation code is borrowed from Greg Balco's get_age_LSDLal.m code.
% It relies on P_mu_total_alpha1_ice.m to calculate the muon production
% The output combines the fast and negative muon capture in one output
% array

```

```

% constants structure for muon production rate
mconsts.Natoms = consts.NatomsQtzO;
mconsts.sigma0.St = consts.sigma010.St;
mconsts.fstar.St = consts.fstar10.St;
mconsts.k_negpartial = consts.k_negpartial_10;
mconsts.mfluxRef = consts.mfluxRef;

for i = 1:length(ice_hist)' %calculate muon production with depth under proscribed ice thickness
P10_muSt_dep(i) =
P_mu_total_alpha1((ice_hist(i).*rho_ice+rho_br*burial(i)),sampledata.pressure,mconsts,'no'); %
corrected for ice thickness
end

if flag == 1 %add 10% error for MC
    y = 0.0003.*randn(1,1)+0.00157; %random error on the Be10 muon PR, SLHL PR: 0.00157
    +/- ? Balcon, 2017
    for i = 1:length(P10_muSt_dep)
        P10_muSt_dep(i) = P10_muSt_dep(i) + P10_muSt_dep(i).*(y/0.199-1);
    end
end

%% Define muon production with ice depth for 26Al
% Muon calculation code is borrowed from Greg Balco's get_age_LSDLa1.m code.
% It relies on P_mu_total_alpha1_ice.m to calculate the muon production

% constants structure for muon production rate
mconsts.Natoms = consts.NatomsQtzSi;
mconsts.sigma0.St = consts.sigma026.St;
mconsts.fstar.St = consts.fstar26.St;
mconsts.k_negpartial = consts.k_negpartial_26;
mconsts.mfluxRef = consts.mfluxRef;

for i = 1:length(ice_hist)' %calculate muon production with depth under proscribed ice thickness
    P26_muSt_dep(i) =
P_mu_total_alpha1((ice_hist(i).*rho_ice+rho_br*burial(i)),sampledata.pressure,mconsts,'no'); %
corrected for ice thickness
end

if flag == 1 %add error for MC
    y = 0.002.*randn(1,1)+0.0118; %random error on the Al26 muon PR, SLHL PR: 0.0118 +/- ?
    Balco, 2017
    for i = 1:length(P26_muSt_dep)
        P26_muSt_dep(i) = P26_muSt_dep(i) + P26_muSt_dep(i).*(y/1.52-1);
    end
end

%% Define muon production with depth for C14

```

```

% Muon calculation code is borrowed from Greg Balco's get_age_LSDLal.m code.
% It relies on P_mu_total_alpha1_ice.m to calculate the muon production

% constants structure for muon production rate
mconsts.Natoms = consts.NatomsQtzO;
mconsts.sigma0.St = consts.sigma014.St;
mconsts.fstar.St = consts.fstar14.St;
mconsts.k_negpartial = consts.k_negpartial_14;
mconsts.mfluxRef = consts.mfluxRef;

for i = 1:length(ice_hist)' %calculate muon production with depth under proscribed ice thickness
    P14_muSt_dep(i) =
P_mu_total_alpha1((ice_hist(i).*rho_ice+rho_br*burial(i)),sampledata.pressure,mconsts,'no'); %
corrected for ice thickness
end

if flag == 1 %add error for MC
    y = 0.75.*randn(1,1)+3.31; %random error on the C14 muon PR, SLHL PR: 3.31 +/- 0.75
    Lupker et al., 2015.
    %Lupker's uncertainty is asymmetric (+0.43, -1.07). Change to 0.75 ((0.43+1.07)/2).
    for i = 1:length(P14_muSt_dep)
        P14_muSt_dep(i) = P14_muSt_dep(i) + P14_muSt_dep(i).*(y/3.31-1);
    end
end

%% calculate total production corrected for ice thickness and burial over time
dt=ts(end-1)-ts(end); %time step length

if flag == 1 %MC, correct the spallation production for the ice and burial history
    P10_sp_dep = P10_sp_i.*exp(-(rho_ice.*ice_hist./Lspi+rho_br*burial./Lspr)); %spallation
    P26_sp_dep = P26_sp_i.*exp(-(rho_ice.*ice_hist./Lspi+rho_br*burial./Lspr)); %spallation
    P14_sp_dep = P14_sp_i.*exp(-(rho_ice.*ice_hist./Lspi+rho_br*burial./Lspr)); %spallation
    %total production
    P10_tot = P10_sp_dep + P10_muSt_dep;
    P26_tot = P26_sp_dep + P26_muSt_dep;
    P14_tot = P14_sp_dep + P14_muSt_dep;
else %regular model, no extra uncertainty
    P10_sp_dep = P10_sp.*exp(-(rho_ice.*ice_hist./Lspi+rho_br*burial./Lspr)); %spallation
    P26_sp_dep = P26_sp.*exp(-(rho_ice.*ice_hist./Lspi+rho_br*burial./Lspr)); %spallation
    P14_sp_dep = P14_sp.*exp(-(rho_ice.*ice_hist./Lspi+rho_br*burial./Lspr)); %spallation
    %total production
    P10_tot = P10_sp_dep + P10_muSt_dep;
    P26_tot = P26_sp_dep + P26_muSt_dep;
    P14_tot = P14_sp_dep + P14_muSt_dep;
end

```

```

%% Calculate the surface production over time with prescribed ice thickness
for j = 1:length(ts)
    if j == 1 %first time step (starts at zero -> no decay)
        N14C(j) = (P14_tot(j)/dc14).*(1-exp(-dc14.*dt));
        N10Be(j) = (P10_tot(j)/dc10).*(1-exp(-dc10.*dt));
        N26Al(j) = (P26_tot(j)/dc26).*(1-exp(-dc26.*dt));
    else % decay since last timestep plus production in this time step
        N14C(j) = (N14C(j-1).*exp(-dc14.*dt)) + (P14_tot(j)/dc14).*(1-exp(-dc14.*dt));
        N10Be(j) = (N10Be(j-1).*exp(-dc10.*dt)) + (P10_tot(j)/dc10).*(1-exp(-dc10.*dt));
        N26Al(j) = (N26Al(j-1).*exp(-dc26.*dt)) + (P26_tot(j)/dc26).*(1-exp(-dc26.*dt));
    end
end
end

```

define_ice_history.m

```
function [ice_hist,ts] = define_ice_history(ice_model,mode,dt)

% This function loads some pre-defined potential ice-cover scenarios for
% Riukojietna Ice Cap, Northern Sweden.

% Developed by Allie Koester, Purdue University (koestea@purdue.edu) and
% Jane Lund Andersen, Aarhus University (jane.lund@geo.au.dk), 2021-22
if ice_model == 1 %UMISM
    M_t = [20000 18000 16000 14000 12900 12500 11000 10800 10700 10600 10500 10400
10300 10000];
    M_c = [901 943 917 608 613 741 506 437 376 258 171 95 40 40];
elseif ice_model == 2 %ANU
    M_t = [20000 19000 18000 17000 16500 15000 14000 12800 12000 11500 10000];
    M_c = [1556 1443 1313 1062 920 954 764 777 794 637 40];
elseif ice_model == 3 %Patton, 2017
    M_t = [20000 19000 18000 17000 16000 15000 14000 13000 12000 11000 10500 10000
9500];
    M_c = [956 938 917 962 966 979 936 959 937 687 255 88 63];
end

if mode == 1 %HTM model with 33 m during HTM
    mode_t = [8000 6600 6500 5600 5500 5400 4500 4400 1900 1800 105 55 37 0];
    mode_c = [33 33 0 0 0 33 33 0 0 33 33 32 30 0];
elseif mode == 2 %EXP model
    mode_t = [8000 7900 1900 1800 105 55 37 0];
    mode_c = [33 0 0 33 33 32 30 0];
elseif mode == 3 %HTM model with 10 m during HTM
    mode_t = [8000 6600 6500 5600 5500 5400 4500 4400 1900 1800 105 55 37 0];
    mode_c = [33 33 0 0 0 10 10 0 0 33 33 32 30 0];
elseif mode == 4 %HTM model with 1 m during HTM
    mode_t = [8000 6600 6500 5600 5500 5400 4500 4400 1900 1800 105 55 37 0];
    mode_c = [33 33 0 0 0 1 1 0 0 33 33 32 30 0];
elseif mode == 5 %HTM model, ice gone by 8 ka
    mode_t = [8000 7900 5500 5400 4500 4400 1900 1800 105 55 37 0];
    mode_c = [33 0 0 33 33 0 0 33 33 32 30 0];
elseif mode == 6 %HTM model with 15 m during HTM, ice gone by 8 ka
    mode_t = [8000 7900 5500 5400 4500 4400 1900 1800 105 55 37 0];
    mode_c = [33 0 0 15 15 0 0 33 33 32 30 0];
elseif mode == 7 %HTM model with 10 m during HTM, ice gone by 8 ka
    mode_t = [8000 7900 5500 5400 4500 4400 1900 1800 105 55 37 0];
    mode_c = [33 0 0 10 10 0 0 33 33 32 30 0];
elseif mode == 8 %HTM model with 5 m during HTM, ice gone by 8 ka
    mode_t = [8000 7900 5500 5400 4500 4400 1900 1800 105 55 37 0];
    mode_c = [33 0 0 5 5 0 0 33 33 32 30 0];
elseif mode == 9 %deglaciation at 10 ka, burial at 3 ka
```

```

mode_t = [9900 7900 3900 3800 105 55 37 0];
mode_c = [0 0 0 33 33 32 30 0];
end

ice_times = [M_t mode_t];
ice_cover = [M_c mode_c].*100;

ts = (ice_times(1)-1):-dt:0; %time vector for calculations
%make sure ts vecctor ends in 0, if it doesn't, add a 0 at the end
if ts(end) == 0
    ts(end) = ts(end);
elseif ts(end) > 0
    ts = [ts 0];
end
ice_hist=interp1(ice_times,ice_cover,ts); %interpolate ice-thickness at times in time vector

```

APPENDIX D. ANTARCTIC SITE DESCRIPTIONS, MODEL SET UP, AND MODEL OUTPUTS

SITE DESCRIPTIONS

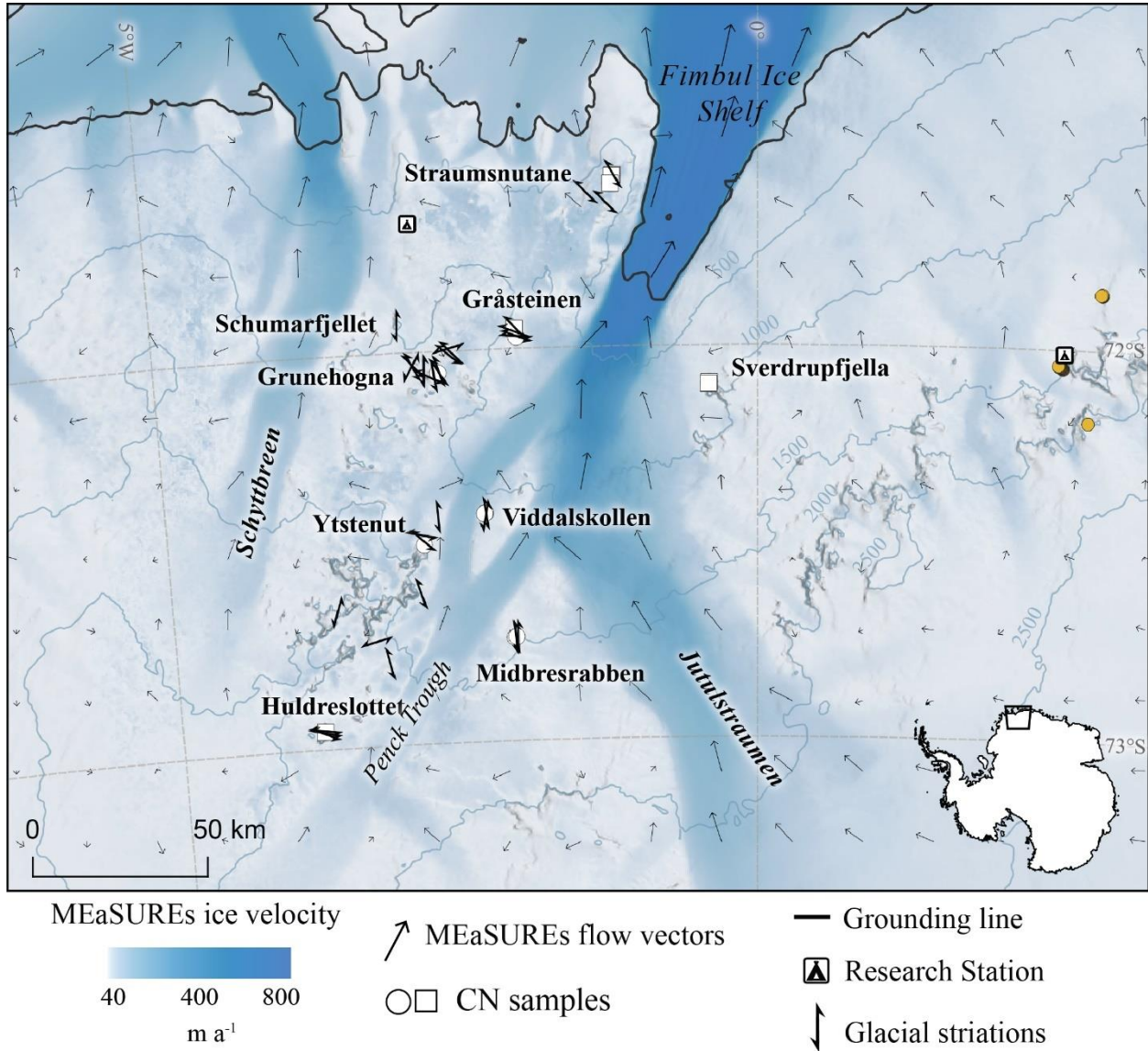


Figure D1: Map of Jutulstraumen samples showing the MEaSUREs flow vectors (Rignot and Scheuchl, 2017) and glacial striations.

Jutulstraumen Drainage Area

We collected samples along the western side of the Jutulstraumen ice stream (analyzed n=14) plus one site on the eastern side (analyzed n=4). Geomorphic descriptions of each nunatak

were also presented in Andersen et al. (2020). Glacial striations were noted in the field when present at each sampled nunatak (Fig. 3.2; Table 3.2). Most striations near the grounding line were oriented NW-SE, though there were exceptions at Gråsteinen where recent striae appeared to be oriented E-W. Striations surrounding the Penck Trough typically trend NW-SE or N-S. The following discussion of sampled nunataks moves from north to south shown in Fig. D1.

Straumsnutane consists of a series of three N-S orientated nunataks on the western side of Jutulstraumen closest to the grounding line. The area was covered in deep, soft snow which was not observed elsewhere in the field area. The bedrock consists of slightly weathered andesitic to basaltic lavas with intermittent quartz veins. The striations along the bedrock surfaces were dominantly N-S, indicating ice flow along Jutulstraumen.



Figure D2: STR-07 (left) and STR-01 (right) sample sites at Staumsnutane.

Gråsteinen consists of four small nunataks on the western side of the Jutulstraumen. The bedrock consists of meta-sedimentary rocks capped with andesite and quartz veins. The northern and southern nunatak sampled displayed striations from N-S crosscut by more recent striate oriented E-W directions, and contained erratics.



Figure D3: GRO-01 (left) and GRO-03 (right) sample sites at Gråsteinen

Sverdrupfjella was the only site sampled on the eastern side of Jutulstraumen, which was accessed by helicopter. Erratics were present up to ~100 m above the present ice surface, but few were observed at higher elevations. The syenite and banded gneiss bedrock was mostly intact but neither glacial striae nor polish were observed in the field.



Figure D4: SVE-03 (left) and SVE-04 (right) sample sites at Sverdrupfjella

We also sampled areas between Jutulstraumen and the neighboring Schyttbreen ice stream to the west which contains a broad region of nunataks that are more distal to Jutulstraumen (Fig.

3.2b). Kullen is an elongated nunatak orientated N-S. Erratics on the nunatak became less frequent moving to the north. Grunehogna is directly west of Kullen and is split into two sections by a saddle. The eastern section contains erratics sitting on shattered bedrock. The lower portions of the saddle contains a till drape. The western section had chatter marks and striations oriented NW-SE although no erratics were found. Schumarfjellet is a N-S orientated nunatak located northwest of Grunehogna and Kullen. Striations on the bedrock were oriented N-S.

Penck Trough Assemblage

Nunataks along the southwestern portion in our study area are more heavily influenced by the Penck glacier, therefore we describe them separately (Fig D1). Viddalskollen is located between Jutulstraumen and the Penck Trough on a NW-SE oriented horst. Small erratics (<10 cm) were present on the nunatak and a patchy till is present on the northern slope. The bedrock is predominantly diorite and capped by a meta-sedimentary sequence. Glacial striations are oriented N-S.



Figure D5: VID-04 (left) and VID-06 (right) sample sites from Viddalskollen

Ystenut is located on the western side of Penck Glacier (Fig. 3.2b). The regolith is diorite but contains intact striations trending NNW-SSE.



Figure D6: YST-01 (left) and YST-06 (right) sample sites from Ystenut

Midbresrabben is a crescent-shaped nunatak located on the southeastern margin of the Penck Glacier (Fig. D1). The bedrock is a mix of metamorphic lithologies, and many erratics appeared to be locally derived. Samples were collected from the stoss side that faces south.

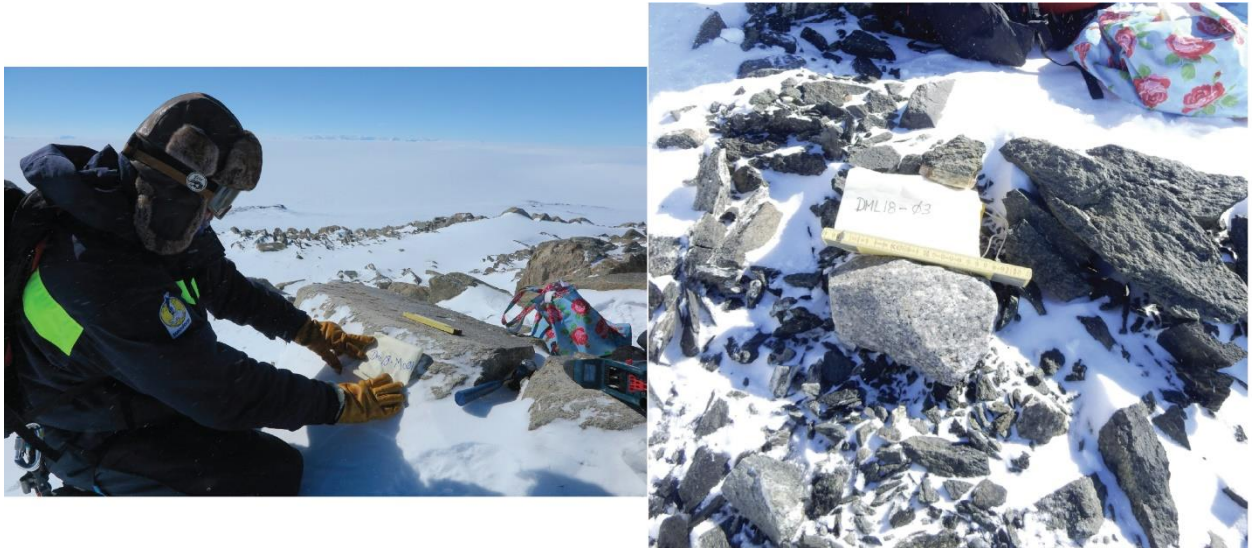


Figure D7: MID-01 (left) and MID-03 (right) sample sites from Midbresrabben.

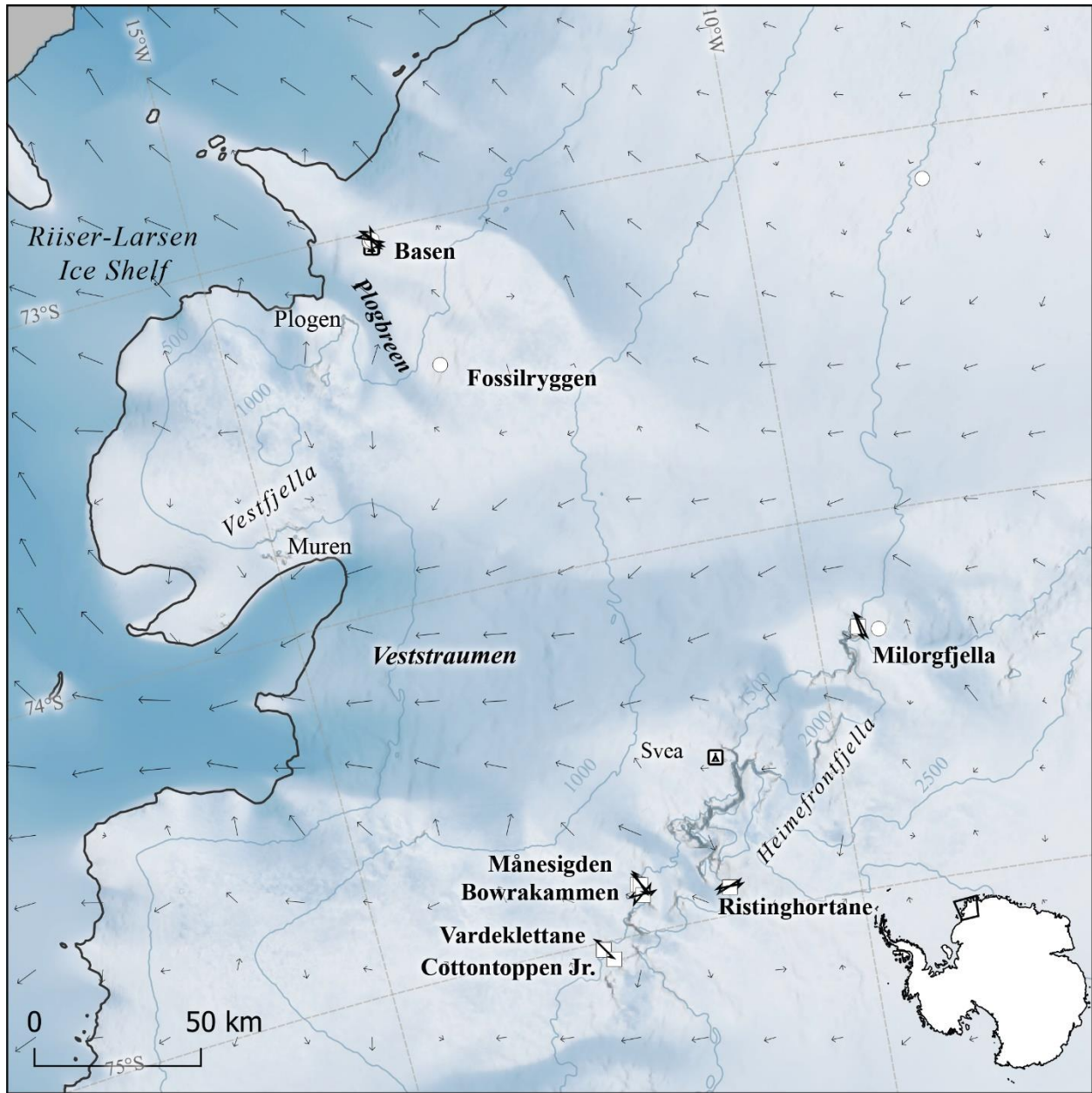
Huldreslottet is our furthest southern sample location influenced by the Penck Glacier. Striations trend E-W, perpendicular to the ridge. Blue ice was present along the southeastern C-shaped ridge.



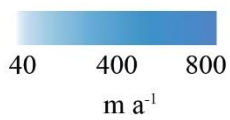
Figure D8: HUD-03 (left) and HUD-04 (right) sample sites from Huldreslottet

Veststraumen Drainage Area

The samples in the Veststraumen field area were collected both above and below a high escarpment (~500 m) that separates coastal ice streams from the high polar plateau ice. We have split up site descriptions into coastal nunataks near the grounding line, inland below the escarpment, and on top of the escarpment. Descriptions of geomorphology from satellite imagery can be found in Newall et al. (2020).



MEaSUREs ice velocity



↗ MEaSUREs flow vectors

○ □ CN samples

— Grounding line

▴ Research Station

↓ Glacial striations

Figure D9: Veststraumen field area showing the MEaSUREs flow vectors compared to glacial striations.

Vestfjella coastal nunataks – Basen and Fossilryggen

Vestfjella is a 130 km long coastal mountain range of basaltic nunataks near the Riser-Larsenisen ice shelf and has been described in Lintinen (1996). Basen lies ~20 km from the grounding line in the field area and protrudes up to ~400 m above the present-day ice sheet. Today, ice flows northwest around the nunatak and into the trough of Plogbreen. The bedrock is basaltic but hosts sandstone and quartzite erratic cobbles and boulders. Locally abundant striations were found on Basen in directions ranging from 280-355°, with the most prevalent being NW-SE (Fig. 3). Previous field studies have documented till cover on Basen and other Vestfjella nunataks, such as the nearby Plogen to the west of Basen (Lintinen and Nenonen, 1997).



Figure D10: BN-03 (left) and BN-04 (right) at Basen.

Fossilryggen lies ~40 km southeast of Basen and protrudes between 5 and 40 m above the current ice surface. The nunatak is a broad rounded ridge that is predominantly meta-sedimentary, and hosts erratics of mixed lithologies. No glacial striations were recorded in the field, although Jonsson (1988) describes NW-SE striations 5 km east of the main ridge. Modern ice flow vectors from MeASURES (Rignot and Scheuchl, 2017) indicate ice flow inland from the coast across the nunatak. It is likely that ice overrode the NW-SE oriented ridge along its short axis into Plogbreen.



Figure D11: FR-02 (left) and FR-03 (right) at Fossilryggen.

Inland below escarpment – Vardeklettane, Cottontoppen Junior, Bowrakammen, Månesigden, Milorgfjella low

About 150 km inland from Vestfjella are the Heimefrontfjella nunataks that trend sub-parallel to the coastline and comprise a portion of the high escarpment separating the polar plateau from coastal ice streams. The highest summits reach altitudes of ca. 2600 m a.s.l., though some smaller nunataks crop out below the high summit.

Vardeklettane is located near the southwestern end of our study area along the Heimefrontfjella mountain range below the escarpment. The site contains glacially molded quartzite bedrock that displayed faint striations trending 315° and crescentic gouges.



Figure D12: VK-01 (left) and VK-02 (right) at Vardeklettane.

Cottontoppen Junior is an informal name for a small nunatak ~4 km southeast of Vardeklettane. The bedrock sampled consists of augen gneiss intruded by a granitic dike that has

likely been polished by the wind. Modern ice flow vectors from MEaSURES (Rignot and Scheuchl, 2017) indicate ice flows away from the escarpment into Veststraumen for both sites, but the local ice flow direction is difficult to determine.



Figure D13: CJ-01 sample site at Cottentoppen Junior.

The north end of Bowrakammen (1679 m a.s.l.) is comprised of quartzite bedrock with weakly developed striations that range from 220-255°.



Figure D14: BRA-01 (left) BRA-02 (right) from Bowrakammen.

Månesigden is located ~3.5 km to the north of Bowrakammen. The bedrock is quartz-rich orthogneiss that is heavily weathered in some areas. We sampled an intact bedrock outcrop (MAB-01) that protruded ~4 m from the crumbly orthogneiss regolith slope. The second bedrock outcrop (MAB-02) displayed faint short striae trending 318° and had glacial polish.



Figure D15: MAB-01 (left) and MAB-04 (right) sample sites from Månesigden.

Milorgfjella low is the furthest eastern sample location in our field area located along an outlet glacier to the east of the Heimfrontfjella escarpment. The local bedrock is amphibolite gneiss that has been jointed. One erratic cobble (MFE-01) lodged in a bedrock joint was collected and requires significant shielding correction.

Heimefrontfjella escarpment – Ristinghortane, Månesigden, Milorgfjella high

The highest elevation site on the escarpment is Ristinghortane (2215 m a.s.l.) and is located along an outlet glacier that cuts through the escarpment. The quartzite bedrock contains faint striae at 258° and sits ~40-50 m above nearby ice, but 200 m above the nearby outlet glacier.



Figure D16: RH-01 (left) and RH-02 (right) at Ristinghortane.

The high-altitude samples from Milorgfjella were collected along the top edge of the escarpment ridge. The bedrock in the area was predominantly gneiss and quartz-vein-rich orthogneiss with numerous well-preserved striations trending 340° . We sampled bedrock that is ~ 0.5 m above till/drift bedrock near the summit ridge (MH-02) as well as a gneissic cobble that was sitting on weathered sandstone (MH-03).



Figure D17: MH-02 (left) and MH-03 (right) collected along the escarpment.

NUMERICAL MODELING SETUP

This section was written by Dr. M. Mas e Braga as a supplemental section to the manuscript preprint. The writing and figures in this section are M. Mas e Braga's work.

Ice Sheet model

We use the ice-flow model *Úa* (Gudmundsson, 2020), a depth-integrated numerical model that solves for the Shallow Shelf Approximation (SSA) of the Stokes momentum equations on a finite-element mesh (Fig. S1). *Úa* has been successfully applied to model the ice flow of the entire Antarctic Ice Sheet (Gudmundsson et al., 2012, 2019) as well as regional catchments for modern and palaeo timescales (Hill et al., 2021; Jones et al., 2021; Suganuma et al., 2022). *Úa* implicitly accounts for ice thermodynamics and anisotropy by using a spatially variable strain-rate coefficient (*A*) in Glen's Flow Law. The modelled domain encompasses the area of DML between the catchments of Veststraumen and Jutulstraumen (Fig. 3.1). We modify the ice-front boundary by extending it to the continental-shelf break, which allows the ice to advance beyond its present-day position. The domain is covered by an irregular mesh with initial resolution of 10 km in the ice sheet interior, and a refinement of up to ~500 m and ~1 km over critical regions of interest: the 500 m refinement is applied where the subglacial topography is steepest, while the 1 km refinement is applied within a 4 km buffer zone on each side of the grounding line (Fig. C1). The mesh refinement is adjusted during simulation time (also known as dynamic adaptive mesh refinement), so that the refinement criteria still hold as the ice geometry evolves.

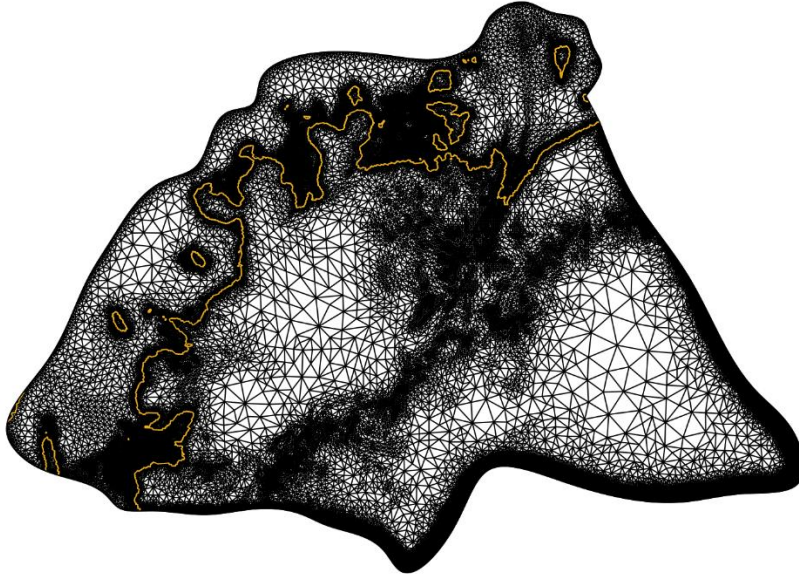


Figure D18: The high-resolution finite element mesh used over our model domain. The orange line depicts the modern grounding line.

Basal friction is calculated through a Weertman-type sliding law (using $m=3$), which, due to the higher mesh resolution at the grounding line, yields a satisfactory representation of the transition in the stress regime between grounded and floating ice (Gladstone et al., 2017). Ice creep is computed through Glen’s flow law. A first guess of the ice rheology distribution in Glen’s flow law (A) and the basal sliding coefficient in Weertman’s sliding law (C) is obtained through an inversion procedure, penalizing for changes in ice thickness in order to minimize model drift at the start of time-dependent runs (Rosier et al., 2021). The inversion procedure obtains a best fit of the spatial distribution of A and C that minimizes the error between modelled and observed surface velocities (Rignot et al., 2011), based on the modern BedMachine-Antarctica (BMA) bedrock topography (Morlighem et al., 2020). We obtain this first guess based on the modern ice sheet because no observations for ice surface velocity are available for the LGM. Because the ice is currently afloat over the modern continental shelf, and hence there is no friction at the ice base, the inversion procedure cannot estimate values of basal sliding over the continental shelf. Since there are signs of grounded ice over this region during the LGM (Mackintosh et al., 2014), a distribution of basal sliding coefficients needs to be prescribed, so that realistic sliding over the continental shelf can be reproduced. Similarly, the ice sheet was colder during the LGM, and hence

it should have been stiffer than at present. To address these two differences between the inverted model parameters, and their likely (yet uncertain) behavior during the LGM, we test for a combination of different basal sliding distributions over the continental shelf, and different degrees of ice stiffening compared to present day, which are described in the next section.

All experiments start from the modern geometry from BMA and are evolved until equilibrium with the climate forcing is attained, following the same step-procedure as in Suganuma et al., (2022) assuming no ice-shelf basal melting, and an LGM sea level 134 m below present-day values.

Sensitivity to model parameters

Regardless of the basal sliding law adopted, models use a spatial distribution of basal sliding coefficients in combination with the adopted sliding law. These can be obtained by an iterative adjustment so that the ice sheet matches modern geometries (e.g., Pollard and DeConto, 2012; Bernales et al., 2017), be prescribed as a function of bed elevation (Åkesson et al., 2018; Albrecht et al., 2020), or, as in our study, inverted based on modern observations of the ice sheet geometry and velocity. The latter process, however, cannot obtain basal sliding coefficients over the continental shelf where the ice sheet is currently afloat. To produce estimates of basal sliding over the modern continental shelf, we fit a third-degree polynomial curve that best fits the variation of inverted basal sliding under ice that is grounded below sea level in the domain's modern ice sheet configuration, as a function of depth. Because the substrate at the continental shelf is softer than where the ice is currently grounded due to a larger amount of sediment deposited (Pollard and DeConto, 2020), we multiply the best-fit curve by factors of 4, 6, 8, and 10 (Fig. D19), producing four different estimates of the basal sliding distribution (Fig. D20). Our fields qualitatively match the likelihood of sedimentary basins distribution determined by Li et al. (2022), and we constrain which distributions yield realistic ice sheet geometries when comparing our ensemble with the exposure ages presented in this study (see below).

As for the rheology parameter A , we “stiffen” the ice by reducing A by factors of 2 (sitff_2) and 10 (sitff_{10}). To test for the effect of these two parameters (A and C), we combine three different basal sliding distributions (sld_{06} , sld_{08} , and sld_{10}) with the two different rheology distributions. Considering the original rheology distribution using the four basal sliding distributions, we test up to 10 different combinations of A and C for a given climate forcing. While the modern ice-rheology distribution was tested using all 4 basal sliding distributions for all 15 climate forcings, we only

test the different rheology distributions for five climate models, four chosen among the ones that yielded inland thinning values close to those reconstructed by ice cores (Parrenin et al., 2007; Buizert et al., 2021), and TraCE-21ka, because of its unique coupled-model transient setup for an entire deglaciation (Liu et al., 2009). In total, 100 experiments were performed, which we compare with the cosmogenic-nuclide samples presented in chapter 3 to determine which ensemble members can represent plausible ice sheet geometries at the LGM.

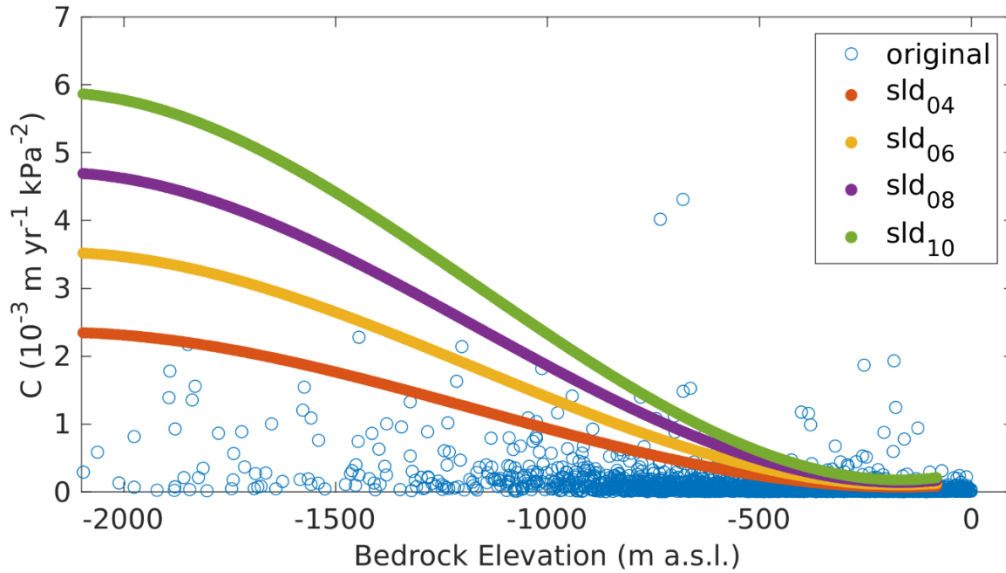


Figure D19: Distribution of basal sliding coefficient values (C) for the inverted area where ice is grounded below sea level (original), and the different curves used when creating the distributions of basal sliding for the areas under present-day floating ice (Fig. D20). These curves were obtained by multiplying the best-fit curve by 4, 6, 8, and 10 (sld_{04} , sld_{06} , sld_{08} , and sld_{10} respectively).

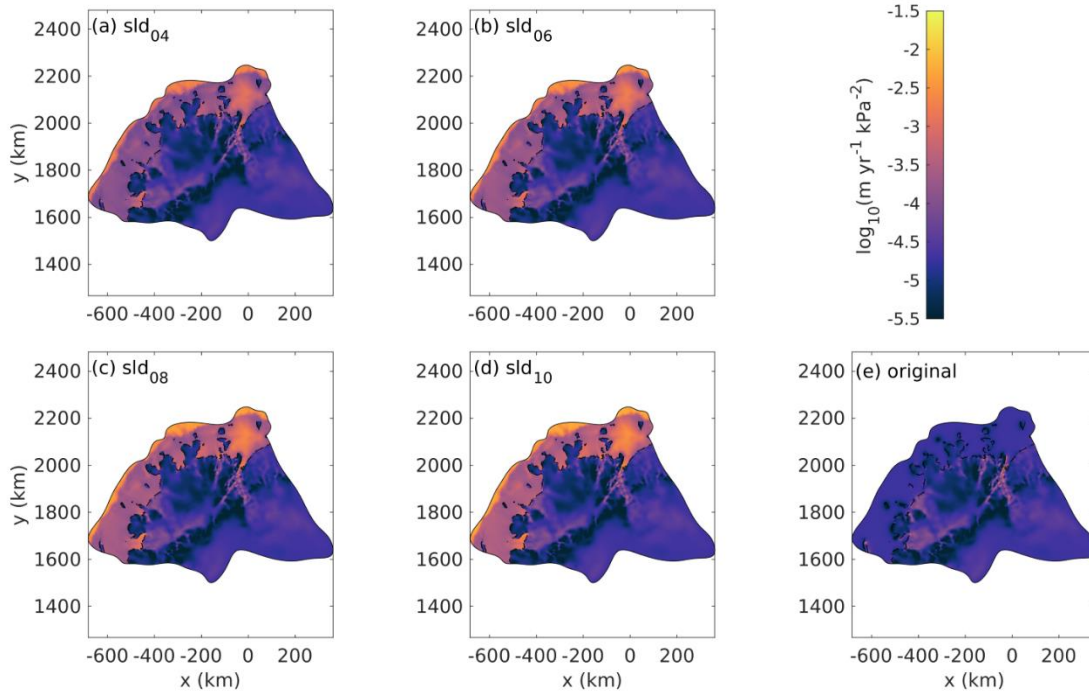


Figure D20: Spatial distribution of C, with enhanced sliding over the continental shelf by factors of (a) 4, (b) 6, (c) 8, and (d) 10. Panel (e) shows the original field based on inversions from surface velocities (Rignot et al., 2011) and subglacial topography (Morlighem et al., 2020).

MODEL VALIDATION BASED ON THE GEOLOGICAL RECORD

We assess the performance of each experiment by evaluating how many of the younger-than-LGM (i.e., 21 ka or less) samples presented in this study were covered by ice, and how close the thinning at the upstream end of the domain (i.e., within the polar plateau) is to an elevation-change estimate of -130 m (Parrenin et al., 2007; Buizert et al., 2021). We consider a model experiment to satisfactorily represent a LGM configuration if inland thinning at the upstream end of the domain is between -100 and -160 m, and if at least 90% of the samples were covered (i.e., $n < 5$ in Fig. D21a). Applying these criteria yields a constrained ensemble of 27 simulations, out of the original 100 (Fig. 3.8).

In general, our model setup was most sensitive to the choice of climate forcing, followed by basal sliding, and ice rheology. In most cases, the climate models that performed well did so for most combination of model parameters (e.g., IPSLCM5A2, IPSL-CM5A-LR, and MIROC-ESM), while the climate models that yielded results furthest from the constraints did so regardless of the choice of model parameters. Climate models that create an ice sheet that is too thin (CNRM-CM5, GISS-E2-R, HadCM3, TraCE-21ka) do not thicken enough even when under the less

slippery sld_{04} distribution, as a lesser amount of basal sliding over the continental shelf results in a thicker geometry from the margin to the ice divide. Similarly, those that thickened over the polar plateau (e.g., FGOALS-g2, INM-CM4-8, MIROC-ES2L) did so even under the most slippery basal sliding distribution (sld_{10}), which is able to produce an overall thinner ice sheet geometry. For the climate models that performed best, the sld_{06} and sld_{08} distributions seemed to achieve the best balance between marginal thickening and inland thinning, while the two “stiffening ratios” tested acted mainly as a fine tuning of the climate forcing-basal sliding combination, producing a slightly thicker ice sheet than under the present-day rheology. Although we make this assessment in this work with the main goal to find the most likely estimates of LGM ice cover over the sampled nunataks, our validation also proves useful to inform which climate models can best represent our study region, which might be relevant for further studies.

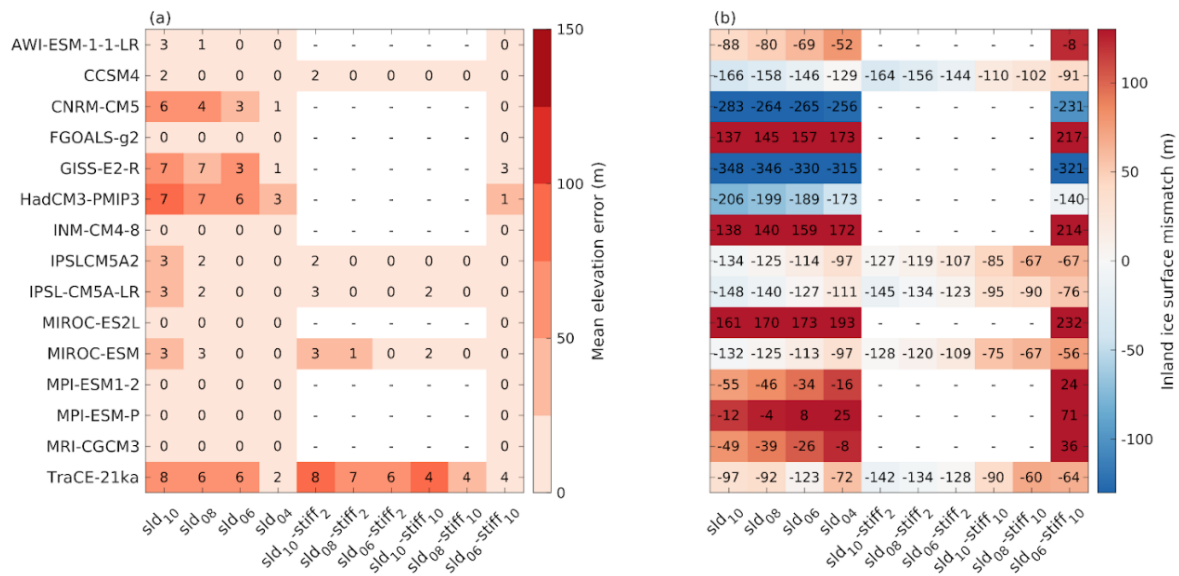


Figure D21: Summary of the performance of all model experiments performed, using different climate-model forcing (rows) and combination of model parameters (columns; basal sliding and ice rheology). (a) Number of samples that should have been covered during the LGM according to their apparent exposure age, but that are ice free in the given model experiment. Colors show the mean elevation error, i.e., the average elevation below the sampled site that the modelled ice surface is. (b) Difference in ice-surface elevation between each LGM experiment and present-day at the upstream end of the domain (numbers). Colors show their departure from the -130 m difference reconstructed for the Dome Fuji ice core (Buizert et al., 2021). Dashes indicate the combination of parameters for which no experiment was performed. In summary, the best experiments are those which show the lightest colors in both panels, and lowest number in panel (a).

DETERMINING ELEVATION CHANGES OF THE ICE SURFACE

Changes in ice-surface elevation were computed as the LGM ice-surface elevation at the sample site minus the present-day ice-surface elevation at the reference point (Table 3.6). This difference was computed for each sample in each model experiment, and the results for select nunataks (white markers in Fig. 3.5) are presented as frequency distributions (Fig. 3.5), where light grey bars represent the full ensemble ($n=100$), and blue bars represent the constrained ensemble ($n=27$) based on the criteria listed above. The elevation-change interval presented in Fig. 3.5 is computed as the 25th – 75th percentiles of the constrained ensemble frequency distribution, and greyed zones denote the minimum thickening according to ^{14}C exposure ages. Among the constrained ensemble, experiment IPSL-CM5A-LR_sld06 was the one to perform the best (i.e., all samples are covered during the LGM, and its inland elevation change is the closest to 130 m thinning). Therefore, it is the experiment chosen to display the spatial distribution of elevation differences (Fig. D22).

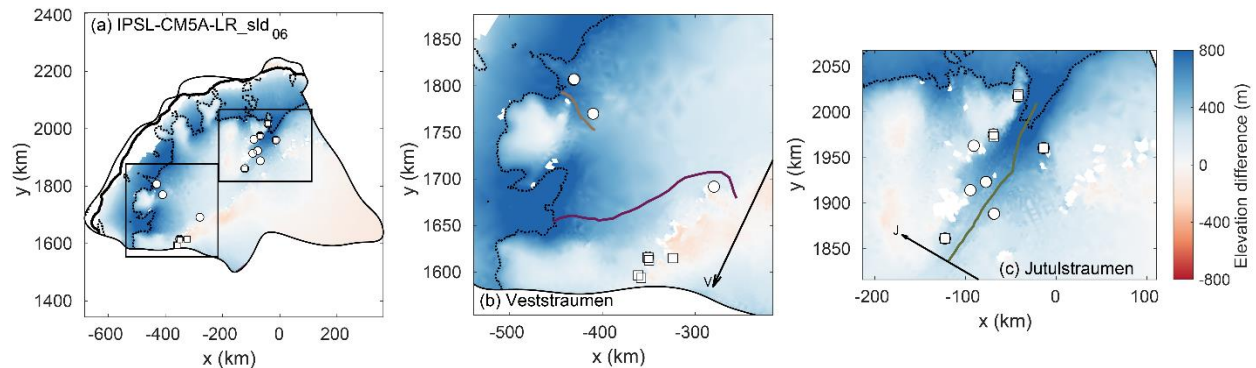


Figure D22. Ice surface elevation difference between LGM and present day for (a) the entire modeled region and zoomed in for the (b) Veststraumen and (c) Jutulstraumen regions. Nunataks are those for which the elevation-change estimates are presented in Figs. 3.5. Circles and squares denote the different sample types as in Fig. 3.2. Colored lines show the ice stream trunks of Fig. 3.6. Black arrows show the line from which distances were computed in Fig. 3.6 for Veststraumen (V) and Jutulstraumen (J).

REFERENCES

- Abe-Ouchi, A., Saito, F., Kageyama, M., Braconnot, P., Harrison, S.P., Lambeck, K., Otto-Bliesner, B.L., Peltier, W.R., Tarasov, L., Peterschmitt, J.Y., Takahashi, K., 2015. Ice-sheet configuration in the CMIP5/PMIP3 Last Glacial Maximum experiments. *Geoscientific Model Development* 8, 3621–3637. <https://doi.org/10.5194/gmd-8-3621-2015>
- Åkesson, H., Morlighem, M., Nisancioglu, K.H., Svendsen, J.I., Mangerud, J., 2018. Atmosphere-driven ice sheet mass loss paced by topography: Insights from modelling the south-western Scandinavian Ice Sheet. *Quaternary Science Reviews* 195, 32–47. <https://doi.org/10.1016/j.quascirev.2018.07.004>
- Albrecht, T., Winkelmann, R., Levermann, A., 2020. Glacial-cycle simulations of the Antarctic Ice Sheet with the Parallel Ice Sheet Model (PISM) – Part 1: Boundary conditions and climatic forcing. *The Cryosphere* 14, 599–632. <https://doi.org/10.5194/tc-14-599-2020>
- Alley, R.B., Brook, E.J., Anandkrishnan, S., 2002. A northern lead in the orbital band: North-south phasing of Ice-Age events. *Quaternary Science Reviews* 21, 431–441. [https://doi.org/10.1016/S0277-3791\(01\)00072-5](https://doi.org/10.1016/S0277-3791(01)00072-5)
- Altmaier, M., Herpers, U., Delisle, G., Merchel, S., Ott, U., 2010. Glaciation history of Queen Maud Land (Antarctica) reconstructed from in-situ produced cosmogenic ^{10}Be , ^{26}Al and ^{21}Ne . *Polar Science* 4, 42–61. <https://doi.org/10.1016/j.polar.2010.01.001>
- Andersen, J.L., Newall, J.C., Blomdin, R., Sams, S.E., Fabel, D., Koester, A.J., Lifton, N.A., Fredin, O., Caffee, M.W., Glasser, N.F., Rogozhina, I., Suganuma, Y., Harbor, J.M., Stroeven, A.P., 2020. Ice surface changes during recent glacial cycles along the Jutulstraumen and Penck Trough ice streams in western Dronning Maud Land, East Antarctica. *Quaternary Science Reviews* 249. <https://doi.org/10.1016/j.quascirev.2020.106636>
- Anderson, J.B., Shipp, S., Lowe, A.L., Wellner, J., Mosola, A.B., 2002. The Antarctic Ice Sheet during the Last Glacial Maximum and its subsequent retreat history: a review. *Quaternary Science Reviews* 21, 49–70. [https://doi.org/10.1016/S0277-3791\(01\)00083-X](https://doi.org/10.1016/S0277-3791(01)00083-X)
- Anderson, R.K., Miller, G.H., Briner, J.P., Lifton, N.A., DeVogel, S.B., 2008. A millennial perspective on Arctic warming from ^{14}C in quartz and plants emerging from beneath ice caps. *Geophysical Research Letters* 35. <https://doi.org/10.1029/2007GL032057>
- Andersson, C., Pausata, F.S.R., Jansen, E., Risebrobakken, B., Telford, R.J., Centre, B., 2010. Holocene trends in the foraminifer record from the Norwegian Sea and the North Atlantic Ocean. *Climate of the Past* 6, 179–193.
- Argus, D.F., Peltier, W.R., Drummond, R., Moore, A.W., 2014. The Antarctica component of postglacial rebound model ICE-6G_C (VM5a) based on GPS positioning, exposure age dating of ice thicknesses, and relative sea level histories. *Geophysical Journal International* 198, 537–563. <https://doi.org/10.1093/gji/ggu140>

- Arias, P.A., Bellouin, N., Jones, R.G., Naik, V., Plattner, G.-K., Rogelj, J., Sillmann, J., Storelvmo, T., Thorne, P.W., Trewin, B., Rao, K.A., Adhikary, B., Allan, R.P., Armour, K., Barimalala, R., Canadell, J.G., Cassou, C., Cherchi, A., Collins, W., Corti, S., Cruz, F., Dentener, F.J., Dereczynski, C., Luca, A.D., Diongue, A., Doblus-Reyes, F.J., Dosio, A., Douville, H., Engelbrecht, F., Fyfe, J.C., Gillett, N.P., Goldfarb, L., 2021. Technical Summary. *Climate Change 2021: The Physical Science Basis. Contribution of Working Group I to the Sixth Assessment Report of the Intergovernmental Panel on Climate Change* 33–144. <https://doi.org/10.1017/9781009157896.002>
- Bakke, J., Dahl, S.O., Paasche, Ø., Riis Simonsen, J., Kvisvik, B., Bakke, K., Nesje, A., 2010. A complete record of Holocene glacier variability at Austre Okstindbreen, northern Norway: an integrated approach. *Quaternary Science Reviews* 29, 1246–1262. <https://doi.org/10.1016/j.quascirev.2010.02.012>
- Balco, G., 2017. Production rate calculations for cosmic-ray-muon-produced ^{10}Be and ^{26}Al benchmarked against geological calibration data. *Quaternary Geochronology* 39, 150–173. <https://doi.org/10.1016/j.quageo.2017.02.001>
- Balco, G., Stone, J.O., Lifton, N.A., Dunai, T.J., 2008. A complete and easily accessible means of calculating surface exposure ages or erosion rates from ^{10}Be and ^{26}Al measurements. *Quaternary Geochronology* 3, 174–195. <https://doi.org/10.1016/j.quageo.2007.12.001>
- Balco, G., Stone, J.O.H., Porter, S.C., Caffee, M.W., 2002. Cosmogenic-nuclide ages for New England coastal moraines, Martha's Vineyard and Cape Cod, Massachusetts, USA. *Quaternary Science Reviews* 21, 2127–2135. [https://doi.org/10.1016/S0277-3791\(02\)00085-9](https://doi.org/10.1016/S0277-3791(02)00085-9)
- Balter, A., Bromley, G., Balco, G., Thomas, H., Jackson, M., 2020. A 14.5 million-year record of East Antarctic Ice Sheet fluctuations from the central Transantarctic Mountains, constrained with cosmogenic ^3He , ^{10}Be , ^{21}Ne , and ^{26}Al . *The Cryosphere Discussions* 1–41. <https://doi.org/10.5194/tc-2020-57>
- Barnekow, L., 2000. Holocene regional and local vegetation history and lake-level changes in the Tornetrask area, northern Sweden. *Journal of Paleolimnology* 23, 399–420. <https://doi.org/10.1023/A:1008171418429>
- Barthelmy, D., 2014. Mineralogy Database [WWW Document]. Mineralogy Database. URL <http://www.webmineral.com> (accessed 7.8.14).
- Benn, D.I., Hulton, N.R.J., 2010. An Excel™ spreadsheet program for reconstructing the surface profile of former mountain glaciers and ice caps. *Computers and Geosciences* 36, 605–610. <https://doi.org/10.1016/j.cageo.2009.09.016>

- Bentley, M.J., Ocofaigh, C., Anderson, J.B., Conway, H., Davies, B., Graham, A.G.C., Hillenbrand, C.D., Hodgson, D.A., Jamieson, S.S.R., Larter, R.D., Mackintosh, A., Smith, J.A., Verleyen, E., Ackert, R.P., Bart, P.J., Berg, S., Brunstein, D., Canals, M., Colhoun, E.A., Crosta, X., Dickens, W.A., Domack, E., Dowdeswell, J.A., Dunbar, R., Ehrmann, W., Evans, J., Favier, V., Fink, D., Fogwill, C.J., Glasser, N.F., Gohl, K., Golledge, N.R., Goodwin, I., Gore, D.B., Greenwood, S.L., Hall, B.L., Hall, K., Hedding, D.W., Hein, A.S., Hocking, E.P., Jakobsson, M., Johnson, J.S., Jomelli, V., Jones, R.S., Klages, J.P., Kristoffersen, Y., Kuhn, G., Leventer, A., Licht, K., Lilly, K., Lindow, J., Livingstone, S.J., Massé, G., McGlone, M.S., McKay, R.M., Melles, M., Miura, H., Mulvaney, R., Nel, W., Nitsche, F.O., O'Brien, P.E., Post, A.L., Roberts, S.J., Saunders, K.M., Selkirk, P.M., Simms, A.R., Spiegel, C., Stollendorf, T.D., Sugden, D.E., van der Putten, N., van Ommen, T., Verfaillie, D., Vyverman, W., Wagner, B., White, D.A., Witus, A.E., Zwart, D., 2014. A community-based geological reconstruction of Antarctic Ice Sheet deglaciation since the Last Glacial Maximum. *Quaternary Science Reviews* 100, 1–9. <https://doi.org/10.1016/j.quascirev.2014.06.025>
- Bernales, J., Rogozhina, I., Greve, R., Thomas, M., 2017. Comparison of hybrid schemes for the combination of shallow approximations in numerical simulations of the Antarctic Ice Sheet. *The Cryosphere* 11, 247–265. <https://doi.org/10.5194/tc-11-247-2017>
- Binnie, S.A., Dewald, A., Heinze, S., Voronina, E., Hein, A., Wittmann, H., von Blanckenburg, F., Hetzel, R., Christl, M., Schaller, M., Léanni, L., ASTER Team, Hippe, K., Vockenhuber, C., Ivy-Ochs, S., Maden, C., Fülöp, R.H., Fink, D., Wilcken, K.M., Fujioka, T., Fabel, D., Freeman, S.P.H.T., Xu, S., Fifield, L.K., Akçar, N., Spiegel, C., Dunai, T.J., 2019. Preliminary results of CoQtz-N: A quartz reference material for terrestrial in-situ cosmogenic ^{10}Be and ^{26}Al measurements. *Nuclear Instruments and Methods in Physics Research, Section B: Beam Interactions with Materials and Atoms* 456, 203–212. <https://doi.org/10.1016/j.nimb.2019.04.073>
- Bjune, A.E., Bakke, J., Nesje, A., Birks, H.J.B., 2005. Holocene mean July temperature and winter precipitation in western Norway inferred from palynological and glaciological lake-sediment proxies. *Holocene* 15, 177–189. <https://doi.org/10.1191/0959683605hl798rp>
- Blaauw, M., Christen, J.A., 2011. Flexible paleoclimate age-depth models using an autoregressive gamma process. *Bayesian Analysis* 6, 457–474. <https://doi.org/10.1214/11-BA618>
- Borchers, B., Marrero, S., Balco, G., Caffee, M., Goehring, B., Lifton, N., Nishiizumi, K., Phillips, F., Schaefer, J., Stone, J., 2016. Geological calibration of spallation production rates in the CRONUS-Earth project. *Quaternary Geochronology* 31, 188–198. <https://doi.org/10.1016/j.quageo.2015.01.009>
- Briggs, R.D., Pollard, D., Tarasov, L., 2014. A data-constrained large ensemble analysis of Antarctic evolution since the Eemian. *Quaternary Science Reviews* 103, 91–115. <https://doi.org/10.1016/j.quascirev.2014.09.003>
- Briner, J.P., Lifton, N.A., Miller, G.H., Refsnider, K., Anderson, R., Finkel, R., 2014. Using in situ cosmogenic ^{10}Be , ^{14}C , and ^{26}Al to decipher the history of polythermal ice sheets on Baffin Island, Arctic Canada. *Quaternary Geochronology* 19, 4–13. <https://doi.org/10.1016/j.quageo.2012.11.005>

- Bromley, G.R.M., Schaefer, J.M., Hall, B.L., Rademaker, K.M., Putnam, A.E., Todd, C.E., Hegland, M., Winckler, G., Jackson, M.S., Strand, P.D., 2016. A cosmogenic ^{10}Be chronology for the local last glacial maximum and termination in the Cordillera Oriental, southern Peruvian Andes: Implications for the tropical role in global climate. *Quaternary Science Reviews* 148, 54–67. <https://doi.org/10.1016/j.quascirev.2016.07.010>
- Brown, D.A., Chadwick, M.B., Capote, R., Kahler, A.C., Trkov, A., Herman, M.W., Sonzogni, A.A., Danon, Y., Carlson, A.D., Dunn, M., Smith, D.L., Hale, G.M., Arbanas, G., Arcilla, R., Bates, C.R., Beck, B., Becker, B., Brown, F., Casperson, R.J., Conlin, J., Cullen, D.E., Descalle, M.A., Firestone, R., Gaines, T., Guber, K.H., Hawari, A.I., Holmes, J., Johnson, T.D., Kawano, T., Kiedrowski, B.C., Koning, A.J., Kopecky, S., Leal, L., Lestone, J.P., Lubitz, C., Márquez Damián, J.I., Mattoon, C.M., McCutchan, E.A., Mughabghab, S., Navratil, P., Neudecker, D., Nobre, G.P.A., Noguere, G., Paris, M., Pigni, M.T., Plompen, A.J., Pritychenko, B., Pronyaev, V.G., Roubtsov, D., Rochman, D., Romano, P., Schillebeeckx, P., Simakov, S., Sin, M., Sirakov, I., Sleaford, B., Sobes, V., Soukhovitskii, E.S., Stetcu, I., Talou, P., Thompson, I., van der Marck, S., Welsch-Sherrill, L., Wiarda, D., White, M., Wormald, J.L., Wright, R.Q., Zerkle, M., Žerovnik, G., Zhu, Y., 2018. ENDF/B-VIII.0: The 8th Major Release of the Nuclear Reaction Data Library with CIELO-project Cross Sections, New Standards and Thermal Scattering Data. *Nuclear Data Sheets* 148, 1–142. <https://doi.org/10.1016/j.nds.2018.02.001>
- Brown, E.T., Trull, T.W., Jean-baptiste, P., Raisbeck, G., Bourles, D., Yiou, F., Marty, B., 2000. Determination of cosmogenic production rates of ^{10}Be , ^3He and ^3H in water. *Nuclear Instruments and Methods in Physics Research B* 172, 873–883.
- Buizert, C., Fudge, T.J., Roberts, W.H.G., Steig, E.J., Sherriff-Tadano, S., Ritz, C., Lefebvre, E., Edwards, J., Kawamura, K., Oyabu, I., Motoyama, H., Kahle, E.C., Jones, T.R., Abe-Ouchi, A., Obase, T., Martin, C., Corr, H., Severinghaus, J.P., Beaudette, R., Epifanio, J.A., Brook, E.J., Martin, K., Chappellaz, J., Aoki, S., Nakazawa, T., Sowers, T.A., Alley, R.B., Ahn, J., Sigl, M., Severi, M., Dunbar, N.W., Svensson, A., Fegyveresi, J.M., He, C., Liu, Z., Zhu, J., Otto-Bliesner, B.L., Lipenkov, V.Y., Kageyama, M., Schwander, J., 2021. Antarctic surface temperature and elevation during the Last Glacial Maximum. *Science* 372, 1097–1101. <https://doi.org/10.1126/science.abd2897>
- Chmeleff, J., von Blanckenburg, F., Kossert, K., Jakob, D., 2010. Determination of the ^{10}Be half-life by multicollector ICP-MS and liquid scintillation counting. *Nuclear Inst. and Methods in Physics Research, B* 268, 192–199. <https://doi.org/10.1016/j.nimb.2009.09.012>
- Clark, P.U., Dyke, A.S., Shakun, J.D., Carlson, A.E., Clark, J., Wohlfarth, B., Mitrovica, J.X., Hostetler, S.W., McCabe, A.M., 2009. The Last Glacial Maximum. *Science (New York, N.Y.)* 325, 710–714. <https://doi.org/10.1126/science.1172873>
- Corbett, L.B., Bierman, P.R., Stone, B.D., Caffee, M.W., Larsen, P.L., 2017. Cosmogenic nuclide age estimate for Laurentide Ice Sheet recession from the terminal moraine, New Jersey, USA, and constraints on latest Pleistocene ice sheet history. *Quaternary Research* 87, 482–498. <https://doi.org/10.1017/qua.2017.11>
- Cuzzone, J.K., Clark, P.U., Carlson, A.E., Ullman, D.J., Rinterknecht, V.R., Milne, G.A., Lunkka, J.P., Wohlfarth, B., Marcott, S.A., Caffee, M., 2016. Final deglaciation of the Scandinavian Ice Sheet and implications for the Holocene global sea-level budget. *Earth and Planetary Science Letters* 448, 34–41. <https://doi.org/10.1016/j.epsl.2016.05.019>

- De Rydt, J., Reese, R., Paolo, F.S., Gudmundsson, G.H., 2021. Drivers of Pine Island Glacier speed-up between 1996 and 2016. *The Cryosphere* 15, 113–132. <https://doi.org/10.5194/tc-15-113-2021>
- DeConto, R.M., Pollard, D., 2016. Contribution of Antarctica to past and future sea-level rise. *Nature* 531, 591–597. <https://doi.org/10.1038/nature17145>
- DeConto, R.M., Pollard, D., Alley, R.B., Velicogna, I., Gasson, E., Gomez, N., Sadai, S., Condrón, A., Gilford, D.M., Ashe, E.L., Kopp, R.E., Li, D., Dutton, A., 2021. The Paris Climate Agreement and future sea-level rise from Antarctica. *Nature* 593, 83–89. <https://doi.org/10.1038/s41586-021-03427-0>
- Fabel, D., Fink, D., Fredin, O., Harbor, J., Land, M., Stroeven, A.P., 2006. Exposure ages from relict lateral moraines overridden by the Fennoscandian ice sheet. *Quaternary Research* 65, 136–146. <https://doi.org/10.1016/j.yqres.2005.06.006>
- Fabel, D., Stroeven, A.P., Harbor, J., Kleman, J., Elmore, D., Fink, D., 2002. Landscape preservation under fennoscandian ice sheets determined from in situ produced ^{10}Be and ^{26}Al . *Earth and Planetary Science Letters* 201, 397–406. [https://doi.org/10.1016/S0012-821X\(02\)00714-8](https://doi.org/10.1016/S0012-821X(02)00714-8)
- Fabryka-Martin, J.T., 1988. Production of radionuclides in the earth and their hydrogeologic significance, with emphasis on chlorine-36 and iodine-129. Ph.D. thesis. The University of Arizona.
- Fastook, D.J.L., Prentice, M.L., 1994. A Finite-element Model of Antarctica: Sensitivity Test for Meteorological Mass Balance Relationship. *Journal of Glaciology* 40, 167–175.
- Fastook, J.L., 1994. Modeling the ice age: the finite-element method in glaciology. *IEEE Comput. Sci. Eng.* 1, 55–67. <https://doi.org/10.1109/99.295374>
- Fastook, J.L., Chapman, J.E., 1989. A Map-plane Finite-element Model: Three Modeling Experiments. *J. Glaciol.* 35, 48–52. <https://doi.org/10.3189/002214389793701464>
- Fretwell, P., Pritchard, H.D., Vaughan, D.G., Bamber, J.L., Barrand, N.E., Bell, R., Bianchi, C., Bingham, R.G., Blankenship, D.D., Casassa, G., Catania, G., Callens, D., Conway, H., Cook, A.J., Corr, H.F.J., Damaske, D., Damm, V., Ferraccioli, F., Forsberg, R., Fujita, S., Gim, Y., Gogineni, P., Griggs, J.A., Hindmarsh, R.C.A., Holmlund, P., Holt, J.W., Jacobel, R.W., Jenkins, A., Jokat, W., Jordan, T., King, E.C., Kohler, J., Krabill, W., Riger-Kusk, M., Langley, K.A., Leitchenkov, G., Leuschen, C., Luyendyk, B.P., Matsuoka, K., Mouginot, J., Nitsche, F.O., Nogi, Y., Nost, O.A., Popov, S.V., Rignot, E., Rippin, D.M., Rivera, A., Roberts, J., Ross, N., Siegert, M.J., Smith, A.M., Steinhage, D., Studinger, M., Sun, B., Tinto, B.K., Welch, B.C., Wilson, D., Young, D.A., Xiangbin, C., Zirizzotti, A., 2013. Bedmap2: Improved ice bed, surface and thickness datasets for Antarctica. *Cryosphere* 7, 375–393. <https://doi.org/10.5194/tc-7-375-2013>
- Fukahori, T., Watanabe, Y., Yoshizawa, N., Maekawa, F., Meigo, S.I., Konno, C., Yamano, N., Konobeyev, A.Y., Chiba, S., 2002. JENDL high energy file. *Journal of Nuclear Science and Technology* 39, 25–30. <https://doi.org/10.1080/00223131.2002.10875031>
- Fülöp, R.H., Fink, D., Yang, B., Codilean, A.T., Smith, A., Wacker, L., Levchenko, V., Dunai, T.J., 2019. The ANSTO – University of Wollongong in-situ ^{14}C extraction laboratory. *Nuclear Instruments and Methods in Physics Research, Section B: Beam Interactions with Materials and Atoms* 438, 207–213. <https://doi.org/10.1016/j.nimb.2018.04.018>
- Gladstone, R.M., Warner, R.C., Galton-Fenzi, B.K., Gagliardini, O., Zwinger, T., Greve, R., 2017. Marine ice sheet model performance depends on basal sliding physics and sub-shelf melting. *The Cryosphere* 11, 319–329. <https://doi.org/10.5194/tc-11-319-2017>

- Goehring, B.M., Brook, E.J., Linge, H., Raisbeck, G.M., Yiou, F., 2008. Beryllium-10 exposure ages of erratic boulders in southern Norway and implications for the history of the Fennoscandian Ice Sheet. *Quaternary Science Reviews* 27, 320–336. <https://doi.org/10.1016/j.quascirev.2007.11.004>
- Goehring, B.M., Schaefer, J.M., Schluechter, C., Lifton, N.A., Finkel, R.C., Jull, A.J.T., Akçar, N., Alley, R.B., 2011. The Rhone Glacier was smaller than today for most of the Holocene. *Geology* 39, 679–682. <https://doi.org/10.1130/G32145.1>
- Goehring, B.M., Wilson, J., Nichols, K., 2019. A fully automated system for the extraction of in situ cosmogenic carbon-14 in the Tulane University cosmogenic nuclide laboratory. *Nuclear Instruments and Methods in Physics Research, Section B: Beam Interactions with Materials and Atoms* 1–9. <https://doi.org/10.1016/j.nimb.2019.02.006>
- Golledge, N.R., Menviel, L., Carter, L., Fogwill, C.J., England, M.H., Cortese, G., Levy, R.H., 2014. Antarctic contribution to meltwater pulse 1A from reduced Southern Ocean overturning. *Nature Communications* 5, 5107. <https://doi.org/10.1038/ncomms6107>
- Gosse, J.C., Phillips, F.M., 2001. Terrestrial in situ cosmogenic nuclides: theory and application. *Quaternary Science Reviews* 20, 1475–1560. [https://doi.org/10.1016/S0277-3791\(00\)00171-2](https://doi.org/10.1016/S0277-3791(00)00171-2)
- Granger, D.E., 2006. A review of burial dating methods using ^{26}Al and ^{10}Be . *Geological Society of America Special Paper* 415 2415, 1–16. [https://doi.org/10.1130/2006.2415\(01\)](https://doi.org/10.1130/2006.2415(01))
- Groenewald, P.B., Moyes, A.B., Grantham, G.H., Krynauw, J.R., 1995. East Antarctic crustal evolution: geological constraints and modelling in western Dronning Maud Land. *Precambrian Research* 75, 231–250. [https://doi.org/10.1016/0301-9268\(95\)80008-6](https://doi.org/10.1016/0301-9268(95)80008-6)
- Grudd, H., 1990. Small Glaciers as Sensitive Indicators of Climatic Fluctuations. *Geografiska Annaler, Series A: Physical Geography* 119–123. <https://doi.org/10.1080/04353676.1990.11880305>
- Gudmundsson, G.H., 2020. Ua2019b.
- Gudmundsson, G.H., Krug, J., Durand, G., Favier, L., Gagliardini, O., 2012. The stability of grounding lines on retrograde slopes. *The Cryosphere* 6, 1497–1505. <https://doi.org/10.5194/tc-6-1497-2012>
- Gudmundsson, G.H., Paolo, F.S., Adusumilli, S., Fricker, H.A., 2019. Instantaneous Antarctic ice sheet mass loss driven by thinning ice shelves. *Geophysical Research Letters* 46, 13903–13909. <https://doi.org/10.1029/2019GL085027>
- Gulev, S.K., Thorne, P.W., Ahn, J., Dentener, F.J., Domingues, C.M., Gerland, S., Gong, D., Kaufman, D.S., Nnamchi, H.C., Quaas, J., Rivera, J.A., Sathyendranath, S., Smith, S.L., Trewin, B., von Schuckmann, K., Vose, R.S., 2021. Changing State of the Climate System, in: *Climate Change 2021: The Physical Science Basis. Contribution of Working Group I to the Sixth Assessment Report of the Intergovernmental Panel on Climate Change*. Cambridge University Press, Cambridge, United Kingdom and New York, NY, USA, pp. 287–422.
- Hall, B.L., 2009. Holocene glacial history of Antarctica and the sub-Antarctic islands. *Quaternary Science Reviews* 28, 2213–2230. <https://doi.org/10.1016/j.quascirev.2009.06.011>
- Hallet, B., Hunter, L., Bogen, J., 1996. Rates of erosion and sediment evacuation by glaciers: A review of field data and their implications. *Global and Planetary Change* 12, 213–235. [https://doi.org/10.1016/0921-8181\(95\)00021-6](https://doi.org/10.1016/0921-8181(95)00021-6)

- Hammarlund, D., Björck, S., Buchardt, B., Israelson, C., Thomsen, C.T., 2003. Rapid hydrological changes during the Holocene revealed by stable isotope records of lacustrine carbonates from Lake Igelsjön, southern Sweden. *Quaternary Science Reviews* 22, 353–370. [https://doi.org/10.1016/S0277-3791\(02\)00091-4](https://doi.org/10.1016/S0277-3791(02)00091-4)
- Handwerker, D.A., Cerling, T.E., Bruhn, R.L., 1999. Cosmogenic ^{14}C in carbonate rocks. *Geomorphology* 27.
- Hays, J.D., Imbrie, J., Shackleton, N.J., 1976. Variations in the Earth's Orbit: Pacemaker of the Ice Ages. *Science* 194, 1121–1132.
- Heisinger, B., Lal, D., Jull, A.J.T., Kubik, P., Ivy-Ochs, S., Knie, K., Nolte, E., 2002a. Production of selected cosmogenic radionuclides by muons: 2. Capture of negative muons. *Earth and Planetary Science Letters* 200, 357–369. [https://doi.org/10.1016/S0012-821X\(02\)00641-6](https://doi.org/10.1016/S0012-821X(02)00641-6)
- Heisinger, B., Lal, D., Jull, A.J.T., Kubik, P., Ivy-Ochs, S., Neumaier, S., Knie, K., Lazarev, V. and Nolte, E., 2002b. Production of selected cosmogenic radionuclides by muons 1. Fast muons. *Earth and Planetary Science Letters* 200, 345–355. [https://doi.org/10.1016/S0012-821X\(02\)00640-4](https://doi.org/10.1016/S0012-821X(02)00640-4)
- Heyman, J., Stroeven, A.P., Harbor, J.M., Caffee, M.W., 2011. Too young or too old: Evaluating cosmogenic exposure dating based on an analysis of compiled boulder exposure ages. *Earth and Planetary Science Letters* 302, 71–80. <https://doi.org/10.1016/j.epsl.2010.11.040>
- Hill, E.A., Rosier, S.H.R., Gudmundsson, G.H., Collins, M., 2021. Quantifying the potential future contribution to global mean sea level from the Filchner–Ronne basin, Antarctica. *The Cryosphere* 15, 4675–4702. <https://doi.org/10.5194/tc-15-4675-2021>
- Hippe, K., 2017. Constraining processes of landscape change with combined in situ cosmogenic ^{14}C - ^{10}Be analysis. *Quaternary Science Reviews* 173, 1–19. <https://doi.org/10.1016/j.quascirev.2017.07.020>
- Hippe, K., Jansen, J.D., Skov, D.S., Lupker, M., Ivy-ochs, S., Kober, F., Zeilinger, G., Capriles, J.M., Christl, M., Maden, C., Vockenhuber, C., Egholm, D.L., 2021. Cosmogenic in situ ^{14}C - ^{10}Be reveals abrupt Late Holocene soil loss in the Andean Altiplano. *Nature Communications* 12, 1–9. <https://doi.org/10.1038/s41467-021-22825-6>
- Hippe, K., Kober, F., Baur, H., Ruff, M., Wacker, L., Wieler, R., 2009. The current performance of the in situ ^{14}C extraction line at ETH. *Quaternary Geochronology* 4, 493–500. <https://doi.org/10.1016/j.quageo.2009.06.001>
- Hippe, K., Kober, F., Wacker, L., Fahrni, S.M., Ivy-Ochs, S., Akçar, N., Schlüchter, C., Wieler, R., 2013. An update on in situ cosmogenic ^{14}C analysis at ETH Zürich. *Nuclear Instruments and Methods in Physics Research, Section B: Beam Interactions with Materials and Atoms* 294, 81–86. <https://doi.org/10.1016/j.nimb.2012.06.020>
- Hippe, K., Lifton, N.A., 2014. Calculating Isotope Ratios and Nuclide Concentrations for In Situ Cosmogenic ^{14}C Analyses. *Radiocarbon* 56, 1167–1174. <https://doi.org/10.2458/56.17917>
- Hock, R., Rasul, G., Adler, C., Cáceres, B., Gruber, S., Hirabayashi, Y., Jackson, M., Kääb, A., Kang, S., Kutuzov, S., Milner, A., Molau, U., Morin, S., Orlove, B., Steltzer, H.I., 2019. Chapter 2: High Mountain Areas. IPCC Special Report on the Ocean and Cryosphere in a Changing Climate. IPCC Special Report on the Ocean and Cryosphere in a Changing Climate 131–202.
- Holmlund, P., Karlén, W., Grudd, H., 1996. Fifty Years of Mass Balance and Glacier Front Observations at the Tarfala Research Station. *Geografiska Annaler. Series A, Physical Geography* 78, 105–114.

- Howat, I., Porter, C., Noh, M.-J., Husby, E., Khuvis, S., Danish, E., Tomko, K., Gardiner, J., Negrete, A., Yadav, B., Klassen, J., Kelleher, C., Cloutier, M., Bakker, J., Enos, J., Arnold, G., Bauer, G., Morin, P., 2022. The Reference Elevation Model of Antarctica – Mosaics, Version 2.
- Huang, X., Jokat, W., 2016. Sedimentation and potential venting on the rifted continental margin of Dronning Maud Land. *Marine Geophysical Research* 37, 313–324. <https://doi.org/10.1007/s11001-016-9296-x>
- Huybrechts, P., Payne, T., EISMINT Intercomparison Group, 1996. The EISMINT benchmarks for testing ice-sheet models. *Annals of Glaciology* 23, 1–12.
- IPCC, 2022. Global Warming of 1.5°C: IPCC Special Report on Impacts of Global Warming of 1.5°C above Pre-industrial Levels in Context of Strengthening Response to Climate Change, Sustainable Development, and Efforts to Eradicate Poverty, 1st ed. Cambridge University Press. <https://doi.org/10.1017/9781009157940>
- Jansen, H.L., Simonsen, J.R., Dahl, S.O., Bakke, J., Nielsen, P.R., 2016. Holocene glacier and climate fluctuations of the maritime ice cap Høgtuvbreen, northern Norway. *The Holocene* 26, 736–755. <https://doi.org/10.1177/0959683615618265>
- Jansson, P., Rosqvist, G., Schneider, T., 2005. Glacier Fluctuations, Suspended Sediment Flux and Glacio-Lacustrine Sediments. *Geografiska Annaler* 87, 37–50.
- Johnson, J.S., Nichols, K.A., Goehring, B.M., Balco, G., Schaefer, J.M., 2019. Abrupt mid-Holocene ice loss in the western Weddell Sea Embayment of Antarctica. *Earth and Planetary Science Letters* 518, 127–135. <https://doi.org/10.1016/j.epsl.2019.05.002>
- Jones, R.S., Gudmundsson, G.H., Mackintosh, A.N., McCormack, F.S., Whitmore, R.J., 2021. Ocean-Driven and Topography-Controlled Nonlinear Glacier Retreat During the Holocene: Southwestern Ross Sea, Antarctica. *Geophysical Research Letters* 48. <https://doi.org/10.1029/2020GL091454>
- Jones, R.S., Small, D., Cahill, N., Bentley, M.J., Whitehouse, P.L., 2019. iceTEA: Tools for plotting and analysing cosmogenic-nuclide surface-exposure data from former ice margins. *Quaternary Geochronology* 51, 72–86. <https://doi.org/10.1016/j.quageo.2019.01.001>
- Jonsson, C.E., Andersson, S., Rosqvist, G.C., Leng, M.J., 2010. Reconstructing past atmospheric circulation changes using oxygen isotopes in lake sediments from Sweden. *Climate of the Past* 6, 49–62. <https://doi.org/10.5194/cp-6-49-2010>
- Jonsson, S., 1988. Observations on the physical geography and glacial history of the Vestfjella nunataks in western Dronning Maud Land, Antarctica. *Forskningsrapport* 57 pp.
- Jull, A.J.T., Lifton, N.A., Phillips, W.M., Quade, J., 1994. Studies of the production rate of cosmic-ray produced ^{14}C in rock surfaces. *Nuclear Instruments and Methods in Physics Research B* 92, 308–310.
- Jull, A.J.T., Wilson, A.E., Burr, G.S., Toolin, L.J., Donahue, D.J., 1992. Measurements of Cosmogenic ^{14}C Produced by Spallation in High-Altitude Rocks. *Radiocarbon* 34, 737–744. <https://doi.org/10.1017/S003382220006402X>
- Karlén, W., 1988. Scandinavian glacial and climate fluctuations during the Holocene. *Quaternary Science Reviews* 7, 199–209.
- Karlén, W., 1981. Lacustrine Sediment Studies. *Geografiska Annaler: Series A, Physical Geography* 63, 273–281. <https://doi.org/10.1080/04353676.1981.11880042>
- Karlén, W., 1976. Lacustrine Sediments and Tree-Limit Variations as Indicators of Holocene Climatic Fluctuations in Lappland, Northern Sweden. *Geografiska Annaler: Series A, Physical Geography* 58, 1–34. <https://doi.org/10.1080/04353676.1976.11879921>

- Karlén, W., 1975. Lichenometrisk datering i norra Skandinavien – metodens tillförlitlighet och regionala tillämpning. *Naturgeografiska institutionen* 22, 1–70.
- Karlén, W., Bodin, A., Kuylenstierna, J., Naslund, J.-O., 1995. Climate of Northern Sweden During the Holocene. *Journal of Coastal Research* 17, 49–54.
- Karlén, W., Denton, G.H., 1973. Holocene glacial variations in Sarek National Park, northern Sweden. *Boreas* 5, 25–56.
- Kawamata, M., Suganuma, Y., Doi, K., Misawa, K., Hirabayashi, M., Hattori, A., Sawagaki, T., 2020. Abrupt Holocene ice-sheet thinning along the southern Soya Coast, Lützow-Holm Bay, East Antarctica, revealed by glacial geomorphology and surface exposure dating. *Quaternary Science Reviews* 247, 106540. <https://doi.org/10.1016/j.quascirev.2020.106540>
- Kawamura, K., Parrenin, F., Lisiecki, L., Uemura, R., Vimeux, F., Severinghaus, J.P., Hutterli, M.A., Nakazawa, T., Aoki, S., Jouzel, J., Raymo, M.E., Matsumoto, K., Nakata, H., Motoyama, H., Fujita, S., Goto-Azuma, K., Fujii, Y., Watanabe, O., 2007. Northern Hemisphere forcing of climatic cycles in Antarctica over the past 360,000 years. *Nature* 448, 912–916. <https://doi.org/10.1038/nature06015>
- Kleman, J., Hättstrand, C., Borgström, I., Stroeven, A., 1997. Fennoscandian palaeoglaciology reconstructed using a glacial geological inversion model. *J. Glaciol.* 43, 283–299. <https://doi.org/10.3189/S0022143000003233>
- Knudsen, M.F., Egholm, D.L., Jansen, J.D., 2019. Time-integrating cosmogenic nuclide inventories under the influence of variable erosion, exposure, and sediment mixing. *Quaternary Geochronology*. <https://doi.org/10.1016/j.quageo.2019.02.005>
- Koester, A.J., Lifton, N.A., 2023. Technical note: A software framework for calculating compositionally dependent in situ ^{14}C production rates. *Geochronology* 5, 21–33. <https://doi.org/10.5194/gchron-5-21-2023>
- Koester, A.J., Lifton, N.A., 2022. nlifton/CD14C: CD14C (v1.0.0).
- Koester, A.J., Shakun, J.D., Bierman, P.R., Davis, P.T., Corbett, L.B., Goehring, B.M., Vickers, A.C., Zimmerman, S.R., 2020. Laurentide ice sheet thinning and erosive regimes at Mount Washington, New Hampshire, inferred from multiple cosmogenic nuclides, in: Waitt, R.B., Thackray, G.D., Gillespie, A.R. (Eds.), *Untangling the Quaternary Period - A Legacy of Stephen C. Porter*. Geological Society of America Special Paper 548, pp. 295–310. [https://doi.org/10.1130/2020.2548\(15\)](https://doi.org/10.1130/2020.2548(15))
- Koning, A.J., Rochman, D., Sublet, J., Dzysiuk, N., Fleming, M., Marck, S.V.D., 2019. TENDL: Complete Nuclear Data Library for Innovative Nuclear Science and Technology. *Nuclear Data Sheets* 155, 1–55. <https://doi.org/10.1016/j.nds.2019.01.002>
- Korschinek, G., Bergmaier, A., Faestermann, T., Gerstmann, U.C., Knie, K., Rugel, G., Wallner, A., Dillmann, I., Dollinger, G., Lierse von Gostomski, Ch., Kossert, K., Maiti, M., Poutivtsev, M., Remmert, A., 2010. A new value for the half-life of ^{10}Be by Heavy-Ion Elastic Recoil Detection and liquid scintillation counting. *Nuclear Inst. and Methods in Physics Research, B* 268, 187–191. <https://doi.org/10.1016/j.nimb.2009.09.020>
- Lambeck, K., Purcell, A.P., 2001. Sea-level change in the Irish Sea since the Last Glacial Maximum: constraints from isostatic modelling. *J. Quaternary Sci.* 16, 497–506. <https://doi.org/10.1002/jqs.638>
- Lambeck, K., Rouby, H., Purcell, A., Sun, Y., Sambridge, M., 2014. Sea level and global ice volumes from the Last Glacial Maximum to the Holocene. *Proceedings of the National Academy of Sciences* 111, 15296–15303. <https://doi.org/10.1073/pnas.1411762111>

- Larocca, L.J., Axford, Y., 2022. Arctic glaciers and ice caps through the Holocene: a circumpolar synthesis of lake-based reconstructions. *Clim. Past* 18, 579–606. <https://doi.org/10.5194/cp-18-579-2022>
- Leonard, E.M., 1986. Use of lacustrine sedimentary sequences as indicators of Holocene glacial history, Banff National Park, Alberta, Canada. *Quaternary Research* 26, 218–231. [https://doi.org/10.1016/0033-5894\(86\)90106-7](https://doi.org/10.1016/0033-5894(86)90106-7)
- Leong, W.J., Horgan, H.J., 2020. DeepBedMap: a deep neural network for resolving the bed topography of Antarctica. *The Cryosphere* 14, 3687–3705. <https://doi.org/10.5194/tc-14-3687-2020>
- Li, D., DeConto, R.M., Pollard, D., 2023. Climate model differences contribute deep uncertainty in future Antarctic ice loss. *Sci. Adv.* 9, eadd7082. <https://doi.org/10.1126/sciadv.add7082>
- Li, L., Aitken, A.R.A., Lindsay, M.D., Kulesa, B., 2022. Sedimentary basins reduce stability of Antarctic ice streams through groundwater feedbacks. *Nat. Geosci.* 15, 645–650. <https://doi.org/10.1038/s41561-022-00992-5>
- Lifton, N., 2016. Implications of two Holocene time-dependent geomagnetic models for cosmogenic nuclide production rate scaling. *Earth and Planetary Science Letters* 433, 257–268. <https://doi.org/10.1016/j.epsl.2015.11.006>
- Lifton, N., Caffee, M., Finkel, R., Marrero, S., Nishiizumi, K., Phillips, F.M., Goehring, B., Gosse, J., Stone, J., Schaefer, J., Theriault, B., Jull, A.J.T., Fifield, K., 2015a. In situ cosmogenic nuclide production rate calibration for the CRONUS-Earth project from lake Bonneville, Utah, shoreline features. *Quaternary Geochronology* 26, 56–69. <https://doi.org/10.1016/j.quageo.2014.11.002>
- Lifton, N., Goehring, B., Wilson, J., Kubley, T., Caffee, M., 2015b. Progress in automated extraction and purification of in situ ^{14}C from quartz: Results from the Purdue in situ ^{14}C laboratory. *Nuclear Instruments and Methods in Physics Research, Section B: Beam Interactions with Materials and Atoms* 361, 381–386. <https://doi.org/10.1016/j.nimb.2015.03.028>
- Lifton, N., Jull, A.J.T., Quade, J., 2001. A new extraction technique and production rate estimate for in situ cosmogenic ^{14}C in quartz. *Geochimica et Cosmochimica Acta* 65, 1953–1969. [https://doi.org/10.1016/S0016-7037\(01\)00566-X](https://doi.org/10.1016/S0016-7037(01)00566-X)
- Lifton, N., Sato, T., Dunai, T.J., 2014. Scaling in situ cosmogenic nuclide production rates using analytical approximations to atmospheric cosmic-ray fluxes. *Earth and Planetary Science Letters* 386, 149–160. <https://doi.org/10.1016/j.epsl.2013.10.052>
- Lifton, N.A., 1997. A new extraction technique and production rate estimate for in situ cosmogenic ^{14}C in quartz. [https://doi.org/10.1016/S0016-7037\(01\)00566-X](https://doi.org/10.1016/S0016-7037(01)00566-X)
- Lifton, N.A., Koester, A.J., 2022. Studying LiBO_2 fluxes and low-temperature combustion systematics with a fully automated in situ cosmogenic ^{14}C processing system at PRIME Lab. Presented at the 24th Radiocarbon Conference and 10th Archaeology Conference, Zurich, Switzerland.
- Lintinen, P., 1996. Evidence for the former existence of a thicker ice sheet on the Vestfjella nunataks in western Dronning Maud Land, Antarctica. *Bulletin of the Geological Society of Finland* 68, 85–98. <https://doi.org/10.17741/bgsf/68.1.007>
- Lintinen, P., Nenonen, J., 1997. Glacial History of the Vestfjella and Heimefrontfjella Nunatak Ranges in Western Dronning Maud Land, Antarctica, in: *The Antarctic Region: Geological Evolution and Processes*. pp. 845–852.

- Liu, A.Z., He, F., Brady, E.C., Tomas, R., Clark, P.U., Carlson, A.E., Curry, W., Brook, E., Erickson, D., Jacob, R., Kutzbach, J., Cheng, J., Clark, P.U., Brady, E.C., 2009. Transient Simulation of Last a New Mechanism with Deglaciation for Bolling-Allerod Warming 325, 310–314.
- Lunde, T., 1961. On the snow accumulation in Dronning Maud Land. *Norsk Polarinstitutt Skrifter* 123, 48.
- Lupker, M., Hippe, K., Wacker, L., Kober, F., Maden, C., Braucher, R., Bourlès, D., Romani, J.R.V., Wieler, R., 2015. Depth-dependence of the production rate of in situ ^{14}C in quartz from the Leymon High core, Spain. *Quaternary Geochronology* 28, 80–87. <https://doi.org/10.1016/j.quageo.2015.04.004>
- Lupker, M., Hippe, K., Wacker, L., Steinemann, O., Tikhomirov, D., Maden, C., Haghypour, N., Synal, H.A., 2019. In-situ cosmogenic ^{14}C analysis at ETH Zürich: Characterization and performance of a new extraction system. *Nuclear Instruments and Methods in Physics Research, Section B: Beam Interactions with Materials and Atoms* 457, 30–36. <https://doi.org/10.1016/j.nimb.2019.07.028>
- Mackintosh, A., White, D., Fink, D., Gore, D.B., Pickard, J., Fanning, P.C., 2007. Exposure ages from mountain dipsticsk in Mac. Robertson Land, East Antarctica, indicate little change in ice-sheet thickness since the Last Glacial Maximum. *Geology* 35, 551–554. <https://doi.org/10.1130/G23503A.1>
- Mackintosh, A.N., Verleyen, E., O'Brien, P.E., White, D.A., Jones, R.S., McKay, R., Dunbar, R., Gore, D.B., Fink, D., Post, A.L., Miura, H., Leventer, A., Goodwin, I., Hodgson, D.A., Lilly, K., Crosta, X., Golledge, N.R., Wagner, B., Berg, S., van Ommen, T., Zwartz, D., Roberts, S.J., Vyverman, W., Masse, G., 2014. Retreat history of the East Antarctic Ice Sheet since the Last Glacial Maximum. *Quaternary Science Reviews* 100, 10–30. <https://doi.org/10.1016/j.quascirev.2013.07.024>
- Marcott, S.A., Shakun, J.D., Clark, P.U., Mix, A.C., 2013. A Reconstruction of Regional and Global Temperature for the Past 11,300 Years. *Science* 339, 1198–1201. <https://doi.org/10.1126/science.1228026>
- Marrero, S.M., Hein, A.S., Naylor, M., Attal, M., Shanks, R., Winter, K., Woodward, J., Dunning, S., Westoby, M., Sugden, D., 2018. Controls on subaerial erosion rates in Antarctica. *Earth and Planetary Science Letters* 501, 56–66. <https://doi.org/10.1016/j.epsl.2018.08.018>
- Marrero, S.M., Phillips, F.M., Borchers, B., Lifton, N., Aumer, R., Balco, G., 2016. Cosmogenic nuclide systematics and the CRONUScal program. *Quaternary Geochronology* 31, 160–187. <https://doi.org/10.1016/j.quageo.2015.09.005>
- Marsella, K. a., Bierman, P.R., Thompson Davis, P., Caffee, M.W., 2000. Cosmogenic ^{10}Be and ^{26}Al ages of the Last Glacial Maximum, Eastern Baffin Island, Arctic Canada. *Bulletin of the Geological Society of America* 112, 1296–1312. [https://doi.org/10.1130/0016-7606\(2000\)112<1296:CBAAAF>2.0.CO;2](https://doi.org/10.1130/0016-7606(2000)112<1296:CBAAAF>2.0.CO;2)
- Mas e Braga, M., Selwyn Jones, R., Newall, J., Rogozhina, I., Andersen, J., Lifton, N., Stroeven, A., 2021. Nunataks as barriers to ice flow: implications for palaeo ice-sheet reconstructions. *The Cryosphere Discussions* 1–27. <https://doi.org/10.5194/tc-2021-173>
- Masarik, J., 2002. Numerical simulation of in-situ production of cosmogenic nuclides, in: *Goldschmidt Conference Abstracts*. p. A491.
- Masarik, J., Beer, J., 2009. An updated simulation of particle fluxes and cosmogenic nuclide production in the Earth ' s atmosphere. *Journal of Geophysical Research* 114, 1–9. <https://doi.org/10.1029/2008JD010557>

- Masarik, J., Beer, J., 1999. Simulation of particle fluxes and cosmogenic nuclide production in the Earth's atmosphere. *Journal of Geophysical Research: Atmospheres* 104, 12099–12111. <https://doi.org/10.1029/1999JD200091>
- Masarik, J., Reedy, R.C., 1995. Terrestrial cosmogenic-nuclide production systematics calculated from numerical simulations. *Earth and Planetary Science Letters* 136, 381–395.
- Matthews, J.A., Dresser, P.Q., 2008. Holocene glacier variation chronology of the Smørstabbtindan massif, Jotunheimen, southern Norway, and the recognition of century- to millennial-scale European Neoglacial Events. *The Holocene* 18, 181–201. <https://doi.org/10.1177/0959683607085608>
- Miller, G.H., Briner, J.P., Lifton, N.A., Finkel, R.C., 2006. Limited ice-sheet erosion and complex exposure histories derived from in situ cosmogenic ^{10}Be , ^{26}Al , and ^{14}C on Baffin Island, Arctic Canada. *Quaternary Geochronology* 1, 74–85. <https://doi.org/10.1016/j.quageo.2006.06.011>
- Morlighem, M., Rignot, E., Binder, T., Blankenship, D., Drews, R., Eagles, G., Eisen, O., Ferraccioli, F., Forsberg, R., Fretwell, P., Goel, V., Greenbaum, J.S., Gudmundsson, H., Guo, J., Helm, V., Hofstede, C., Howat, I., Humbert, A., Jokat, W., Karlsson, N.B., Lee, W.S., Matsuoka, K., Millan, R., Mouginot, J., Paden, J., Pattyn, F., Roberts, J., Rosier, S., Ruppel, A., Seroussi, H., Smith, E.C., Steinhage, D., Sun, B., Broeke, M.R. van den, Ommen, T.D. van, Wessem, M. van, Young, D.A., 2020. Deep glacial troughs and stabilizing ridges unveiled beneath the margins of the Antarctic ice sheet. *Nature Geoscience* 13, 132–137. <https://doi.org/10.1038/s41561-019-0510-8>
- Nesje, A., 2009. Latest Pleistocene and Holocene alpine glacier fluctuations in Scandinavia. *Quaternary Science Reviews* 28, 2119–2136. <https://doi.org/10.1016/j.quascirev.2008.12.016>
- Nesje, A., Bakke, J., Dahl, S.O., Lie, Ø., Matthews, J.A., 2008. Norwegian mountain glaciers in the past, present and future. *Global and Planetary Change* 60, 10–27. <https://doi.org/10.1016/j.gloplacha.2006.08.004>
- Nesje, A., Olaf Dahl, S., Andersson, C., Matthews, J.A., 2000. The lacustrine sedimentary sequence in Syngneskardvatnet, western Norway: A continuous, high-resolution record of the Jostedalbreen ice cap during the Holocene. *Quaternary Science Reviews* 19, 1047–1065. [https://doi.org/10.1016/S0277-3791\(99\)00090-6](https://doi.org/10.1016/S0277-3791(99)00090-6)
- Newall, J.C.H., Dymova, T., Serra, E., Blomdin, R., Fredin, O., Glasser, N.F., Suganuma, Y., Harbor, J.M., Stroeven, A.P., 2020. The glacial geomorphology of western Dronning Maud Land, Antarctica. *Journal of Maps* 16, 468–478. <https://doi.org/10.1080/17445647.2020.1761464>
- Nichols, K.A., Goehring, B.M., Balco, G., Johnson, J.S., Hein, A.S., Todd, C., 2019. New Last Glacial Maximum ice thickness constraints for the Weddell Sea Embayment, Antarctica. *Cryosphere* 13, 2935–2951. <https://doi.org/10.5194/tc-13-2935-2019>
- Nishiizumi, K., 2004. Preparation of ^{26}Al AMS standards. *Nuclear Instruments and Methods in Physics Research Section B: Beam Interactions with Materials and Atoms* 223–224, 388–392. <https://doi.org/10.1016/j.nimb.2004.04.075>
- Nishiizumi, K., Rinkel, R.C., Klein, J., Kohl, C.P., 1996. Cosmogenic production of ^7Be and ^{10}Be in water targets. *Journal of Geophysical Research* 101, 22,225–22,232.
- Oerlemans, J., 2005. Extracting a climate signal from 169 glacier records. *Science* 308, 675–677. <https://doi.org/10.1126/science.1107046>

- Oerlemans, J., Anderson, B., Hubbard, A., Huybrechts, P., Jóhannesson, T., Knap, W.H., Schmeits, M., Stroeven, A.P., Van De Wal, R.S.W., Wallinga, J., Zuo, Z., 1998. Modelling the response of glaciers to climate warming. *Climate Dynamics* 14, 267–274. <https://doi.org/10.1007/s003820050222>
- Oerlemans, J., Fortuin, J.P.F., 1992. Sensitivity of Glaciers and Small Ice Caps to Greenhouse Warming. *Science* 258, 115–118.
- Parker, R.L., 1967. Data of Geochemistry, in: Fleischer, M. (Ed.), U. S. Geological Survey Professional Paper 440-D. p. 12. [https://doi.org/10.1016/S0016-0032\(20\)90415-5](https://doi.org/10.1016/S0016-0032(20)90415-5)
- Parrenin, F., Dreyfus, G., Durand, G., Fujita, S., Gagliardini, O., Gillet, F., Jouze, J., Kawamura, K., Lhomme, N., Masson-Delmotte, V., Ritz, C., Schwander, J., Shoji, H., Uemura, R., Watanabe, O., Yoshida, N., 2007. 1-D-ice flow modelling at EPICA Dome C and Dome Fuji, East Antarctica. *Climate of the Past* 3, 243–259. <https://doi.org/10.5194/cp-3-243-2007>
- Patton, H., Hubbard, A., Andreassen, K., Auriac, A., Whitehouse, P.L., Stroeven, A.P., Shackleton, C., Winsborrow, M., Heyman, J., Hall, A.M., 2017. Deglaciation of the Eurasian ice sheet complex. *Quaternary Science Reviews* 169, 148–172. <https://doi.org/10.1016/j.quascirev.2017.05.019>
- Patton, H., Hubbard, A., Andreassen, K., Winsborrow, M., Stroeven, A.P., 2016. The build-up, configuration, and dynamical sensitivity of the Eurasian ice-sheet complex to Late Weichselian climatic and oceanic forcing. *Quaternary Science Reviews* 153, 97–121. <https://doi.org/10.1016/j.quascirev.2016.10.009>
- Pavón-Carrasco, F.J., Osete, M.L., Torta, J.M., De Santis, A., 2014. A geomagnetic field model for the Holocene based on archaeomagnetic and lava flow data. *Earth and Planetary Science Letters* 388, 98–109. <https://doi.org/10.1016/j.epsl.2013.11.046>
- Payne, A.J., Huybrechts, P., Abe-Ouchi, A., Calov, R., Fastook, J.L., Greve, R., Marshall, S.J., Marsiat, I., Ritz, C., Tarasov, L., Thomassen, M.P.A., 2000. Results from the EISMINT model intercomparison: the effects of thermomechanical coupling. *J. Glaciol.* 46, 227–238. <https://doi.org/10.3189/172756500781832891>
- Pendleton, S.L., Miller, G.H., Lifton, N., Lehman, S.J., Southon, J., Crump, S.E., Anderson, R.S., 2019. Rapidly receding Arctic Canada glaciers revealing landscapes continuously ice-covered for more than 40,000 years. *Nature Communications* 10, 445. <https://doi.org/10.1038/s41467-019-08307-w>
- Phillips, F.M., Argento, D.C., Balco, G., Caffee, M.W., Clem, J., Dunai, T.J., Finkel, R., Goehring, B., Gosse, J.C., Hudson, A.M., Jull, A.J.T., Kelly, M.A., Kurz, M., Lal, D., Lifton, N., Marrero, S.M., Nishiizumi, K., Reedy, R.C., Schaefer, J., Stone, J.O.H., Swanson, T., Zreda, M.G., 2016. The CRONUS-Earth Project: A synthesis. *Quaternary Geochronology* 31, 119–154. <https://doi.org/10.1016/j.quageo.2015.09.006>
- Pittard, M.L., Whitehouse, P.L., Bentley, M.J., Small, D., 2022. An ensemble of Antarctic deglacial simulations constrained by geological observations. *Quaternary Science Reviews* 298, 107800. <https://doi.org/10.1016/j.quascirev.2022.107800>
- Pohjola, V.A., Cole-Dai, J., Rosqvist, G., Stroeven, A.P., Thompson, L.G., 2005. Potential to recover climatic information from Scandinavian ice cores: An example from the small ice cap Riukojietna. *Geografiska Annaler, Series A: Physical Geography* 87, 259–270. <https://doi.org/10.1111/j.0435-3676.2005.00257.x>

- Pollard, D., DeConto, R.M., 2020. Continuous simulations over the last 40 million years with a coupled Antarctic ice sheet-sediment model. *Palaeogeography, Palaeoclimatology, Palaeoecology* 537, 109374. <https://doi.org/10.1016/j.palaeo.2019.109374>
- Pollard, D., DeConto, R.M., 2012. A simple inverse method for the distribution of basal sliding coefficients under ice sheets, applied to Antarctica. *The Cryosphere* 6, 953–971. <https://doi.org/10.5194/tc-6-953-2012>
- Prentice, M.L., Matthews, R.K., 1991. Tertiary ice sheet dynamics: the snow gun hypothesis. *Journal of Geophysical Research* 96, 6811–6827. <https://doi.org/10.1029/90JB01614>
- Rand, C., Goehring, B.M., 2019. The distribution and magnitude of subglacial erosion on millennial timescales at Engabreen, Norway. *Annals of Glaciology* 60, 73–81. <https://doi.org/10.1017/aog.2019.42>
- Reedy, R.C., 2013. Cosmogenic-nuclide production rates: Reaction cross section update. *Nuclear Instruments and Methods in Physics Research, Section B: Beam Interactions with Materials and Atoms* 294, 470–474. <https://doi.org/10.1016/j.nimb.2011.08.034>
- Reedy, R.C., 2007. Proton cross sections for producing cosmogenic radionuclides, in: *Lunar and Planetary Science Conference XXXVIII*. pp. 1329–1330.
- Reedy, R.C., Arnold, J.R., 1972. Interaction of solar and galactic cosmic-ray particles with the Moon. *Journal of Geophysical Research* 77, 537–555. <https://doi.org/10.1029/ja077i004p00537>
- Reimer, P.J., Austin, W.E.N., Bard, E., Bayliss, A., Blackwell, P.G., Bronk Ramsey, C., Butzin, M., Cheng, H., Edwards, R.L., Friedrich, M., Grootes, P.M., Guilderson, T.P., Hajdas, I., Heaton, T.J., Hogg, A.G., Hughen, K.A., Kromer, B., Manning, S.W., Muscheler, R., Palmer, J.G., Pearson, C., Van Der Plicht, J., Reimer, R.W., Richards, D.A., Scott, E.M., Southon, J.R., Turney, C.S.M., Wacker, L., Adolphi, F., Büntgen, U., Capano, M., Fahrni, S.M., Fogtmann-Schulz, A., Friedrich, R., Köhler, P., Kudsk, S., Miyake, F., Olsen, J., Reinig, F., Sakamoto, M., Sookdeo, A., Talamo, S., 2020. The IntCal20 Northern Hemisphere Radiocarbon Age Calibration Curve (0-55 cal kBP). *Radiocarbon* 62, 725–757. <https://doi.org/10.1017/RDC.2020.41>
- Rignot, E., Mouginot, J., Scheuchl, B., 2011. Ice flow of the Antarctic Ice Sheet. *Science* 333, 1427–1430.
- Rignot, E., Mouginot, J., Scheuchl, B., van den Broeke, M.R., van Wessem, M.J., Morlighem, M., 2019. Four decades of Antarctic Ice Sheet mass balance from 1979-2017. *Proceedings of the National Academy of Sciences* 1–9. <https://doi.org/10.1073/pnas.1812883116>
- Rignot, E., Scheuchl, B., 2017. MEaSUREs InSAR-Based Antarctica Ice Velocity Map. National Snow & Ice Data Center, version 2.
- Rosier, S.H.R., Reese, R., Donges, J.F., De Rydt, J., Gudmundsson, G.H., Winkelmann, R., 2021. The tipping points and early warning indicators for Pine Island Glacier, West Antarctica. *The Cryosphere* 15, 1501–1516. <https://doi.org/10.5194/tc-15-1501-2021>
- Rosqvist, G., Jonsson, C., Yam, R., Karlén, W., Shemesh, A., 2004. Diatom oxygen isotopes in pro-glacial lake sediments from northern Sweden: A 5000 year record of atmospheric circulation. *Quaternary Science Reviews* 23, 851–859. <https://doi.org/10.1016/j.quascirev.2003.06.009>
- Rosqvist, G., Østrem, G., 1989. The Sensitivity of a Small Icecap to Climatic Fluctuations. *Geografiska Annaler. Series A, Physical Geography* 71, 99–103.

- Rosqvist, G.C., Leng, M.J., Jonsson, C., 2007. North Atlantic region atmospheric circulation dynamics inferred from a late-Holocene lacustrine carbonate isotope record, northern Swedish Lapland. *Holocene* 17, 867–873. <https://doi.org/10.1177/0959683607080508>
- Rubensdotter, L., Rosqvist, G., 2003. The effect of geomorphological setting on Holocene lake sediment variability, northern Swedish Lapland. *J. Quaternary Sci.* 18, 757–767. <https://doi.org/10.1002/jqs.800>
- Sato, T., Niita, K., 2006. Analytical functions to predict cosmic-ray neutron spectra in the atmosphere. *Radiation Research* 166, 544–555. <https://doi.org/10.1667/RR0610.1>
- Sato, T., Yasuda, H., Niita, K., Endo, A., Sihver, L., Sato, T., Yasuda, H., Niita, K., Endo, A., Sihver, L., 2008. Development of PARMA : PHITS-Based Analytical Radiation Model in the Atmosphere. *Radiation Research* 170, 244–259.
- Schimmelpfennig, I., Schaefer, J., Lamp, J., Godard, V., Schwartz, R., Bard, E., Tuna, T., Akçar, N., Schlüchter, C., Zimmerman, S., 2022. Glacier response to Holocene warmth inferred from in situ ^{10}Be and ^{14}C bedrock analyses in Steingletscher's forefield (central Swiss Alps). *Climate of the Past Discussions* 18, 1–27. <https://doi.org/10.5194/cp-2021-110>
- Schimmelpfennig, I., Schaefer, J.M., Goehring, B.M., Lifton, N., Putnam, A.E., Barrell, D.J.A., 2012. Calibration of the in situ cosmogenic ^{14}C production rate in New Zealand's Southern Alps. *Journal of Quaternary Science* 27, 671–674. <https://doi.org/10.1002/jqs.2566>
- Seppä, H., Hammarlund, D., Antonsson, K., 2005. Low-frequency and high-frequency changes in temperature and effective humidity during the Holocene in south-central Sweden: Implications for atmospheric and oceanic forcings of climate. *Climate Dynamics* 25, 285–297. <https://doi.org/10.1007/s00382-005-0024-5>
- Shemesh, A., Rosqvist, G., Rietti-Shati, M., Rubensdotter, L., Bigler, C., Yam, R., Karlén, W., 2001. Holocene climatic change in Swedish Lapland inferred from an oxygen-isotope record of lacustrine biogenic silica. *Holocene* 11, 447–454. <https://doi.org/10.1191/095968301678302887>
- Sjögren, P.J.E., 2021. An overview of Holocene climate reconstructions in northernmost Fennoscandia. *SapReps.* <https://doi.org/10.7557/7.5747>
- Snowball, I., Sandgren, P., 1996. Lake sediment studies of Holocene glacial activity in the Karsa valley, northern Sweden: Contrasts in interpretation. *Holocene* 6, 367–372. <https://doi.org/10.1177/095968369600600312>
- Southon, J., 2007. Graphite reactor memory – Where is it from and how to minimize it? *Nuclear Instruments and Methods in Physics Research Section B: Beam Interactions with Materials and Atoms* 259, 288–292. <https://doi.org/10.1016/j.nimb.2007.01.251>
- Stenni, B., Masson-Delmotte, V., Selmo, E., Oerter, H., Meyer, H., Röthlisberger, R., Jouzel, J., Cattani, O., Falourd, S., Fischer, H., Hoffmann, G., Iacumin, P., Johnsen, S.J., Minster, B., Udisti, R., 2010. The deuterium excess records of EPICA Dome C and Dronning Maud Land ice cores (East Antarctica). *Quaternary Science Reviews* 29, 146–159. <https://doi.org/10.1016/j.quascirev.2009.10.009>
- Stokes, C.R., Abram, N.J., Bentley, M.J., Edwards, T.L., England, M.H., Foppert, A., Jamieson, S.S.R., Jones, R.S., King, M.A., Lenaerts, J.T.M., Medley, B., Miles, B.W.J., Paxman, G.J.G., Ritz, C., van de Flierdt, T., Whitehouse, P.L., 2022. Response of the East Antarctic Ice Sheet to past and future climate change. *Nature* 608, 275–286. <https://doi.org/10.1038/s41586-022-04946-0>

- Stone, J.O., Balco, G.A., Sugden, D.E., Caffee, M.W., Sass, L.C., Cowdery, S.G., Siddoway, C., 2003. Holocene deglaciation of Marie Byrd Land, West Antarctica. *Science* (New York, N.Y.) 299, 99–102. <https://doi.org/10.1126/science.1077998>
- Stroeven, A.P., Fabel, D., Harbor, J.M., Fink, D., Caffee, M.W., Dahlgren, T., 2011. Importance of sampling across an assemblage of glacial landforms for interpreting cosmogenic ages of deglaciation. *Quaternary Research* 76, 148–156. <https://doi.org/10.1016/j.yqres.2011.04.004>
- Stroeven, A.P., Hättestrand, C., Kleman, J., Heyman, J., Fabel, D., Fredin, O., Goodfellow, B.W., Harbor, J.M., Jansen, J.D., Olsen, L., Caffee, M.W., Fink, D., Lundqvist, J., Rosqvist, G.C., Strömberg, B., Jansson, K.N., 2016. Deglaciation of Fennoscandia. *Quaternary Science Reviews* 147, 91–121. <https://doi.org/10.1016/j.quascirev.2015.09.016>
- Stuiver, M., Reimer, P.J., 1993. Extended ^{14}C Data Base and Revised CALIB 3.0 ^{14}C Age Calibration Program. *Radiocarbon* 35, 215–230. <https://doi.org/10.1017/S0033822200013904>
- Suganuma, Y., Kaneda, H., Mas e Braga, M., Ishiwa, T., Koyama, T., Newall, J.C., Okuno, J., Obase, T., Saito, F., Rogozhina, I., Andersen, J.L., Kawamata, M., Hirabayashi, M., Lifton, N.A., Fredin, O., Harbor, J.M., Stroeven, A.P., Abe-Ouchi, A., 2022. Regional sea-level highstand triggered Holocene ice sheet thinning across coastal Dronning Maud Land, East Antarctica. *Commun Earth Environ* 3, 273. <https://doi.org/10.1038/s43247-022-00599-z>
- Suganuma, Y., Miura, H., Zondervan, A., Okuno, J., 2014. East Antarctic deglaciation and the link to global cooling during the Quaternary: Evidence from glacial geomorphology and ^{10}Be surface exposure dating of the Sør Rondane Mountains, Dronning Maud Land. *Quaternary Science Reviews* 97, 102–120. <https://doi.org/10.1016/j.quascirev.2014.05.007>
- Sugden, D.E., Marchant, D.R., Potter, N., Souchez, R.A., Denton, G.H., Swisher III, C.C., Tison, J.-L., 1995. Preservation of Miocene glacier ice in East Antarctica. *Nature* 376, 412–414. <https://doi.org/10.1038/376412a0>
- Swithinbank, C., 1959. The morphology of the inland ice sheet and nunatak areas of Western Dronning Maud Land. *Glaciology, Norwegian-British-Swedish Antarctic Expedition* 1, 99–117.
- Todd, C., Stone, J., Conway, H., Hall, B., Bromley, G., 2010. Late Quaternary evolution of Reedy Glacier, Antarctica. *Quaternary Science Reviews* 29, 1328–1341. <https://doi.org/10.1016/j.quascirev.2010.02.001>
- van de Berg, W.J., van den Broeke, M.R., Reijmer, C.H., Meijgaard, E.V., 2006. Reassessment of the Antarctic surface mass balance using calibrated output of a regional atmospheric climate model. *Journal of Geophysical Research* 111, 1–15. <https://doi.org/10.1029/2005JD006495>
- Vermeesch, P., Baur, H., Heber, V.S., Kober, F., Oberholzer, P., Schaefer, J.M., Schlüchter, C., Strasky, S., Wieler, R., 2009. Cosmogenic ^3He and ^{21}Ne measured in targets after one year of exposure in the Swiss Alps. *Earth and Planetary Science Letters* 284, 417–425. <https://doi.org/10.1016/j.epsl.2009.05.007>
- von Blanckenburg, F., 2005. The control mechanisms of erosion and weathering at basin scale from cosmogenic nuclides in river sediment. *Earth and Planetary Science Letters* 237, 462–479. <https://doi.org/10.1016/j.epsl.2005.06.030>
- Wahlström, C.-A., 2016. A century of volume reduction of a small ice cap; Riukojietna Northern Sweden. Stockholm University.

- Wastegård, S., 2022. The Holocene of Sweden – a review. *GFF* 144, 126–149. <https://doi.org/10.1080/11035897.2022.2086290>
- Watanabe, Y., Kosako, K., Kunieda, S., Chiba, S., Fujimoto, R., Harada, H., Kawai, M., Maekawa, F., Murata, T., Nakashima, H., Niita, K., Shigyo, N., Shimakawa, S., Yamano, N., Fukahori, T., 2011. Status of JENDL high energy file. *Journal of the Korean Physical Society* 59, 1040–1045. <https://doi.org/10.3938/jkps.59.1040>
- Weber, M.E., Clark, P.U., Ricken, W., Mitrovica, J.X., Hostetler, S.W., Kuhn, G., 2011. Interhemispheric Ice-Sheet Synchronicity During the Last Glacial Maximum 1265. <https://doi.org/10.1126/science.1209299>
- WGMS, 2022. Fluctuations of Glacier Database. World Glacier Monitoring Service (WGMS). Zurich, Switzerland. <https://doi.org/10.5904/wgms-fog-2022-09>
- White, D.A., Fink, D., 2014. Late Quaternary glacial history constrains glacio-isostatic rebound in Enderby Land, East Antarctica. *Journal of Geophysical Research: Earth Surface* 119, 401–413. <https://doi.org/10.1002/2013JF002870>
- White, D.A., Fink, D., Gore, D.B., 2011. Cosmogenic nuclide evidence for enhanced sensitivity of an East Antarctic ice stream to change during the last deglaciation. *Geology* 39, 23–26. <https://doi.org/10.1130/G31591.1>
- Whitehouse, P.L., Bentley, M.J., Le Brocq, A.M., 2012a. A deglacial model for Antarctica: Geological constraints and glaciological modelling as a basis for a new model of Antarctic glacial isostatic adjustment. *Quaternary Science Reviews* 32, 1–24. <https://doi.org/10.1016/j.quascirev.2011.11.016>
- Whitehouse, P.L., Bentley, M.J., Milne, G.A., King, M.A., Thomas, I.D., 2012b. A new glacial isostatic adjustment model for Antarctica: Calibrated and tested using observations of relative sea-level change and present-day uplift rates. *Geophysical Journal International* 190, 1464–1482. <https://doi.org/10.1111/j.1365-246X.2012.05557.x>
- Wirsig, C., Ivy-Ochs, S., Akçar, N., Lupker, M., Hippe, K., Wacker, L., Vockenhuber, C., Schluechter, C., 2016. Combined cosmogenic ^{10}Be , in situ ^{14}C and ^{36}Cl constrain Holocene history and erosion depth of Grueben glacier (CH). *Swiss Journal of Geoscience* 379–388. <https://doi.org/10.1007/s00015-016-0227-2>
- Wittmeier, H.E., Bakke, J., Vasskog, K., Trachsel, M., 2015. Reconstructing Holocene glacier activity at Langfjordjøkelen, Arctic Norway, using multi-proxy fingerprinting of distal glacier-fed lake sediments. *Quaternary Science Reviews* 114, 78–99. <https://doi.org/10.1016/j.quascirev.2015.02.007>
- Wright, T., Bennett, S., Heintz, S., Köster, U., Mills, R., Soldner, T., Steier, P., Wallner, A., Wieninger, T., 2019. Measurement of the $^{13}\text{C}(n,\gamma)$ thermal cross section via neutron irradiation and AMS. *Eur. Phys. J. A* 55, 200. <https://doi.org/10.1140/epja/i2019-12893-0>
- Yamane, M., Yokoyama, Y., Abe-Ouchi, A., Obrochta, S., Saito, F., Moriwaki, K., Matsuzaki, H., 2015. Exposure age and ice-sheet model constraints on Pliocene East Antarctic ice sheet dynamics. *Nature Communications* 6, 1–8. <https://doi.org/10.1038/ncomms8016>
- Yamane, M., Yokoyama, Y., Miura, H., Maemoku, H., Iwasaki, S., Matsuzaki, H., 2011. The last deglacial history of Lützow-Holm Bay, East Antarctica. *Journal of Quaternary Science* 26, 3–6. <https://doi.org/10.1002/jqs.1465>
- Yokoyama, Y., Reys, J.L., Guichard, F., 1977. Production of radionuclides by cosmic rays at mountain altitudes. *Earth and Planetary Science Letters* 36, 44–50. [https://doi.org/10.1016/0012-821X\(77\)90186-8](https://doi.org/10.1016/0012-821X(77)90186-8)

- Young, N., Lesnek, A., Cuzzone, J., Briner, J., Badgeley, J., Balter-Kennedy, A., Graham, B., Cluett, A., Lamp, J., Schwartz, R., Tuna, T., Bard, E., Caffee, M., Zimmerman, S., Schaefer, J., 2021. In situ cosmogenic ^{10}Be - ^{14}C - ^{26}Al measurements from recently deglaciated bedrock as a new tool to decipher changes in Greenland Ice Sheet size. *Climate of The Past Discussions* 17, 1–47. <https://doi.org/10.5194/cp-2020-111>
- Young, N.E., Schaefer, J.M., Goehring, B., Lifton, N., Schimmelpfennig, I., Briner, J.P., 2014. West Greenland and global in situ ^{14}C production-rate calibrations. *Journal of Quaternary Science* 29, 401–406. <https://doi.org/10.1002/jqs.2717>

VITA

Alexandria (Allie) J. Koester (she/her)

Department of Earth, Atmospheric, and Planetary Sciences
550 Stadium Mall Drive
Purdue University
West Lafayette, IN 47906

Education

Purdue University, West Lafayette, IN
Ph.D in Geology (expected May 2023)

Advisor: Dr. Nat Lifton
nlifton@purdue.edu

Boston College, Boston, MA
M.S. in Geology

Advisor: Dr. Jeremy Shakun
jeremy.shakun@bc.edu

Pacific Lutheran University, Tacoma, WA
B.A. in Geosciences & Environmental Studies

Advisor: Dr. Claire Todd
claire.todd@sub.edu

Professional Experience

Purdue University

Graduate Student Researcher

West Lafayette, IN

Aug 2018 to present

- Designing and managing multiple research projects with 5 to 12+ collaborators per project. Research focused on how past climate variability has affected ice sheets/glaciers.
- Independent laboratory work at Purdue Rare Isotope Measurement Laboratory (PRIME Lab) including crushing rocks, mineral separation, mineral acid digestion, extraction of isotopes (^{10}Be , ^{26}Al , ^{14}C)
- Communicating research findings through scientific publications and professional presentations at conferences using Adobe Illustrator, Microsoft Word, and MATLAB

Purdue University

Teaching Assistant

West Lafayette, IN

Aug 2019 to May 2020; Jan 2022 to May 2022

- Taught introductory Earth Science topics to laboratory classes of 16-25 students
- Designed and presented introductory lectures using Microsoft PowerPoint each week
- Graded exercises and tutored students when questions arose during office hours

Boston College

Clean Lab Technician

Boston, MA

Sept 2014 to May 2017

- Maintained clean room standards and practices
- Managed strontium columns including set up of strontium resin, cleaning columns, and eluting strontium at the Center for Isotope Geochemistry

Boston College

Teaching Assistant

Boston, MA

Sept 2014 to May 2017

- Managed laboratory classes of 10-25 students each week by introducing the lab exercises, answered questions effectively and proficiently to resolve confusion
- Organized laboratory exercises for multiple courses (introductory Earth Science, climate change) by writing and/or editing lab handouts

Boston, MA

Boston College

June 2015 to Aug 2015

Graduate Research Fellow

- Coordinated and managed field excursions to New England mountains in groups of 3-7 collaborators to collect rock samples for geochemical analysis
- Analyzed and interpreted data and communicated findings through scientific writing and presentations

Pacific Lutheran University

Tacoma, WA

Undergraduate Research Intern

June 2012 to Aug 2012

- Designed a research plan to investigate downstream aggradation in Mount Rainier National Park
- Water quality monitoring focused on suspended sediment load

Publications

- Koester, A.J.**, & Lifton, N.A., 2023, Technical Note: A software framework for calculating compositionally dependent *in situ* ¹⁴C production rates, *Geochronology*, v. 5, p. 21-33.
- Andersen, J.L., Newall, J.C., Blomdin, R., Sams, S.E., Fabel, D., **Koester, A.J.**, Lifton, N.A., Fredin, O., Caffee, M.W., Glasser, N.F., Rogozhina, I., Suganuma, Y., Harbor, J.M., Stroeven, A.P., 2020, Ice surface changes during recent glacial cycles along the Jutulstraumen and Penck Trough ice streams in western Dronning Maud Land, East Antarctica: *Quaternary Science Reviews*, v. 249, doi:10.1016/j.quascirev.2020.106636.
- Koester, A.J.**, Shakun, J.D., Bierman, P.R., Davis, P.T., Corbett, L.B., Goehring, B.M., Vickers, A.C., and Zimmerman, S.R., 2020, Laurentide ice sheet thinning and erosive regimes at Mount Washington, New Hampshire, inferred from multiple cosmogenic nuclides, *in* Waitt, R.B., Thackray, G.D., and Gillespie, A.R. eds., *Untangling the Quaternary Period - A Legacy of Stephen C. Porter*, Geological Society of America Special Paper 548, p. 295–310, doi:10.1130/2020.2548(15).
- Corbett, L.B., Bierman, P.R., Wright, S.F., Shakun, J.D., Davis, P.T., Goehring, B.M., Halsted, C.T., **Koester, A.J.**, Caffee, M.W., Zimmerman, S.R., 2019. Analysis of multiple cosmogenic nuclides constrains Laurentide Ice Sheet history and process on Mt. Mansfield, Vermont's highest peak. *Quaternary Science Reviews*, v. 205, p. 234-246.
- Davis, P.T., **Koester, A.J.**, Shakun, J.D., Bierman, P.R., and Corbett, L.B., 2017, Applying the Cosmogenic Nuclide Dipstick Model for Deglaciation of Mt. Washington in Johnson, B. and Eusden, J.D., ed., *Guidebook for Field Trips in Western Maine and Northern New Hampshire: New England Intercollegiate Geological Conference*, Bates College, p. 247-272.
- Koester, A.J.**, Shakun, J.D., Bierman, P.R., Davis, P.T., Corbett, L.B., Braun, D., Zimmerman, S.R., 2017, Rapid Thinning of the Laurentide Ice Sheet in coastal Maine, USA during late Heinrich Stadial 1, *Quaternary Science Reviews*, v. 163, p. 180–192.

Presentations

- Koester, A.J.**, Sams, S.E., Lifton, N.A., Andersen, J.L., Mas e Braga, M., Fredin, O., Glasser, N., Saganuma, Y., Caffee, M.W., Harbor, J.M., Stroeven, A.P., Holocene ice surface lowering in western Dronning Maud Land, East Antarctica, Poster presented at AGU, Chicago, IL.
- Koester, A.J.**, Lifton, N.A., 2022, A software framework for calculating compositionally dependent *in situ* ^{14}C production rates, Abstract presented at Radiocarbon, Zurich, Switzerland.
- Koester, A.J.**, Stroeven, A.P., Lifton, N.A., Rosqvist, G.C., 2022, Investigating the deglacial history of a Swedish ice cap using combined *in situ* ^{14}C - ^{10}Be - ^{26}Al , Poster presented at AGU, New Orleans, LA.
- Koester, A.J.**, Shakun, J.D., Bierman, P.R., Davis, P.T., Corbett, L.B., Goehring, B.M., Vickers, A.C., Zimmerman, S.H., 2017, Rapid thinning of the Laurentide Ice Sheet at Mount Washington, N.H. during the Bølling Warming, constrained by analysis of cosmogenic ^{14}C and ^{10}Be , Abstract presented at GSA, Seattle, WA
- Koester, A.J.**, Shakun, J.D., Bierman, P.R., Davis, P.T., Corbett, L.B., Braun, D., Zimmerman, S.R., 2016. Rapid Thinning of the Laurentide Ice Sheet in coastal Maine, USA during late Heinrich Stadial 1, Abstract presented at AGU, San Francisco, CA
- Koester, A.J.**, Todd, C.E., Lapo, K., 2012, Tracking Suspended Sediment Transport in Mount Rainier National Park, Washington, Poster presented at GSA, Charlotte, NC

Memberships and Affiliations

Earth Science Women's Network
Geological Society of America
American Geophysical Union

Volunteer Work and Science Communication

2021 – 2022: EAPS Graduate Mentor for incoming graduate students
2021 – 2022: Educational outreach, Lilly Nature Center
2021: 1 minute science (video: <https://www.youtube.com/watch?v=WeO5pIfpDGI>)
2018 – 2021: Women in Science Programs Departmental President
2017 – 2018; 2021: Volunteer at Passport Day (science discovery for kids)
2017 – 2018: Volunteer at U.S.G.S. Water Science Center
2012: Ocean Ecology Lead at Sound View Camp

Awards and Grants

Bisland Fellowship, Purdue University	2022-2023
Henry Silver Award, Purdue University	2022-2023
Terry R. West Scholarship, Purdue University	2020-2021
Mobil Oil Award, Purdue University	2020-2021
GSA Graduate Student Research Grant	2020
Michael C. Gardner Memorial Award, Purdue University	2019
Ross Fellowship, Purdue University	2018-2019
NSF GRFP, Honorable Mention	2015